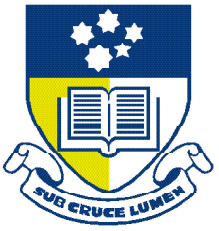

THE UNIVERSITY OF ADELAIDE

Department of Geology & Geophysics

METHODS FOR UNDERSTANDING POORLY EXPOSED TERRANES:

THE INTERPRETIVE GEOLOGY AND TECTONOTHERMAL EVOLUTION OF THE WESTERN GAWLER CRATON

Jonathan Teasdale, BSc (Hons.)

December, 1997

Thesis submitted for the degree of Doctor of Philosophy
in the University of Adelaide, Faculty of Science

TABLE OF CONTENTS

LIST OF FIGURES

ABSTRACT

Over 80% of the Earth's continental crust is concealed beneath a thin veneer of sediment, regolith or ice, therefore our understanding of the crust is heavily biased towards continuously exposed terranes whose exposure is largely caused by recent tectonism. However, a large proportion of the continents comprise stable, cratonic regions which only outcrop sporadically and remain poorly understood. Such areas constitute the major hurdle to any explanation for the evolution and behaviour of the continents through time. Clearly the challenge is to develop an integrated scientific approach that facilitates geological understanding in poorly exposed terranes. Such an approach will necessarily rely on methods that "see through" the veneer to characterise the underlying crust.

Recent technological advances have revolutionised the acquisition, processing and display of airborne geophysical data, principally aeromagnetic data. Such data provides continuous, high-resolution, high-precision geophysical coverage which is not often affected by regolith or thin sedimentary cover. In order to characterise the geology of poorly exposed terranes, it is vital to understand the geological features and processes that control geophysical signatures. Observations likely to be useful include magnetic petrology and susceptibility, gravimetric data, structural observations, metamorphic grade, geochronology and geochemistry. The precise correlation of this information with airborne geophysical data provides a sound basis for developing a regional geological framework in poorly exposed terranes, via both two- and three-dimensional spatial geophysical interpretations. The principal means for visualising such interpretations is via interpretive geological maps, which act as a proxy for continuous geological exposure.

The Gawler Craton, in South Australia, only outcrops sporadically, and is poorly understood in both a local and Australian context. The recent aquisition of high resolution aeromagnetic data over most of the Gawler Craton by Mines and Energy, South Australia, provides an effective tool to "see through" the thin regolith which blankets over 90% of the area. This study focuses on the geological evolution of the western Gawler Craton, less than 1% of which outcrops. Using the integrated approach described above, the following tectonothermal synthesis has been determined:

The geology of the western Gawler Craton is dominated by major, northeast-trending, transpressional, crustal-scale shear zones which juxtapose five subdomains of significantly different geological character:

- The ***Nawa Subdomain*** contains ultra-high temperature, high pressure granulites (>950°C, >10kb) metamorphosed and highly deformed during the late Palaeoproterozoic (1650-1690 Ma), synchronous with plutonism in the Christie Subdomain. These granulites are the highest grade metamorphic rocks yet reported in Australia.
- The ***Christie Subdomain*** comprises a late Archaean - early Paleoproterozoic, low-medium pressure granulite terrane metamorphosed at around 2420 Ma (the Mulgathing Complex). During the late Palaeoproterozoic (~1670 Ma), voluminous, I-type magmatism occurred (the Ifould Complex). Subsequently the terrane has been extensively reworked by major shear zones.
- The ***Fowler Subdomain*** comprises voluminous late Palaeoproterozoic mafic-intermediate intrusives (~1700 Ma) interlayered with metasedimentary material, which underwent high pressure (up to 10kb) granulite-amphibolite facies metamorphism in the Mesoproterozoic (~1530 Ma) and subsequently reworked at progressively lower grades.
- The ***Wilgena and Nuyts Subdomains*** are dominated by voluminous, upper crustal Mesoproterozoic felsic intrusives and localised, low grade shear zones. Both subdomains have resided in the upper crust since the Palaeoproterozoic; as evidenced by numerous Palaeo-Mesoproterozoic clastic sedimentary basins and undeformed volcanics (e.g. the Gawler Range Volcanics).

Five major tectonothermal cycles have been identified the western Gawler Craton: (i) a late Archaean-early Palaeoproterozoic (~3.0-2.4 Ga) cycle involving sedimentation, complex ductile deformation and granulite-facies metamorphism (the Sleafordian Orogeny), (ii) magmatism, high grade metamorphism and deformation during a late Palaeproterozoic orogeny (~1.74-1.65 Ga), (iii) massive, anorogenic, felsic magmatism at ~1.63-1.58 Ga, (iv) high grade metamorphism and deformation during a compressional orogeny at ~1-54-1.49 Ga, and (v) the amalgamation and reworking of the western Gawler Craton along major shear zones at ~1.2-1.1 Ga. Importantly, these tectonothermal cycles are not "seen" by every subdomain.

Three generations of major, "framework" shear zones have effected the western Gawler Craton. Kinematic analysis of these shear zones indicates a prolonged history of transpressional deformation, culminating in brittle faulting. High grade, syn-kinematic intrusives from the Tallacootra Shear Zone yielded a zircon age of ~1175 Ma, implying that the major, northeast-trending shear zones which juxtapose these subdomains were active in the late Mesoproterozoic, synchronous with major collisional tectonism in the Musgrave Block and Albany-Fraser Province. This previously unrecognised link between the Gawler Craton and other Precambrian terranes in Australia is enormously significant and suggests that "Grenvillian" tectonism may have been much more widespread in proto-Australia than originally thought, and contrary to conventional wisdom, the ~1200Ma amalgamation of Rodinia involved extensive tectonism in the western Gawler Craton.

DISCLAIMER

This thesis contains no material which has been accepted for the award of any other degree or diploma in any university or other tertiary institution and, to the best of my knowledge and belief, contains no material previously published or written by any other person, except where due reference has been made in the text.

I give consent to this copy of my thesis, when deposited in the University Library, being available for loan and photocopying.

Jonathan Teasdale

ACKNOWLEDGMENTS

This project would not have been possible without the ongoing support, assistance and patience of my supervisor, Mike Sandiford. Thanks, Mike, for providing a stimulating, relaxed and enjoyable learning environment in which we can explore the ups and downs of science for ourselves. You are a scientific inspiration to all of us.

Martin Hand played a key role in this project. Thanks for being an "honorary" supervisor! Your ongoing friendship, support and interest in my work has been a wonderful catalyst for me. I dare not think what path my PhD would have taken had it not been for your help.

I am eternally grateful to John Parker for helping me initiate and arranging funding for this project. Thanks for your ongoing support and interest, John, it has been an immense help.

Sue Daly at Mines and Energy, South Australia has been an amazing source of information and ideas, as well as a wonderful listener. Your enthusiasm is infectious, Sue. May there be many more epic field expeditions around the Gawler Craton with you at the helm!

Without the ongoing financial support of Equinox Resources N.L. and Mines and Energy, South Australia, fieldwork would not have been possible. Thanks to Bruce Nisbet and Craig Williams at Equinox for providing this generous support. Thanks also to Tony Belperio and Stuart Robinson at MESA.

Thanks to all my colleagues at uni, especially to Bruce Schaefer for his friendship, ideas and his sympathetic ear! Thanks also to Eike, Thomas, Pete, Jo, Rob, Scotty, Gary, Paul, Betina, Jerry, Trevor, Victor, Kathy, John, Bunge, and anyone else that I've forgotten for your frienship and support over the years.

Jon Dougherty-Page was a tremendous help in teaching me the delicate art of Kober zircon dating - thanks for your patience and guidance.

Thanks to all of the support staff in this department - you make the whole place "tick" with great cheer and goodwill. In particular I'd like to thank Gerald Buttfield (management and diplomacy!), Wayne Mussared (thin sections), Geoff Trevalyn (thin sections), Sherry Proferes (computers and drafting), Ian Florance (computers), John Stanley (XRD etc.) and Sophia Craddock (just about everything else!).

The team at CEMMSA provided invaluable support (and very valuable equipment!) with microprobing - thanks in particular to Huw Rosser and John Terlet for your help.

Thanks to all the other people at MESA who assisted with this project - Brian Logan, Peta Abbot, John Bradford and Martin Fairclough all helped out when the situation demanded.

Thanks to the team at PRISE, ANU for your help on the SHRIMP - in particular to Mark Fanning for his patience in teaching me how to SHRIMP and for processing the data.

Last but not least, I could not have survived 8 years at university without the ongoing support of my parents. This has meant a tremendous amount to me which is very difficult to express in words, but THANKYOU!

Chapter 1
INTRODUCTION

1.1 Project overview and aims

Over 80% of the Earth's continental crust is concealed beneath a thin veneer of sediment, regolith, water or ice. As a result, our understanding of the evolution of the continental crust and the distribution of mineral resources within it is biased towards well exposed terranes. Because such exposure is often related to recent tectonism it is not clear how representative such terranes may be of the more numerous poorly exposed parts of the continents. One class of terrane which tend to be particularly poorly exposed are the stable cratons which occupy large, low-lying areas in most continents. Understanding these cratons is essential to any explanation for the evolution and behaviour of the continents through time. Clearly the challenge is to develop an integrated scientific approach that facilitates geological understanding in poorly exposed terranes. Such an approach will necessarily rely on methods that "see through" the veneer to characterise the underlying crust.

Recent technological advances have revolutionised the acquisition, processing and display of airborne geophysical data, principally airborne magnetic (aeromagnetic) data. Such data provide continuous, high-resolution, high-precision geophysical coverage which can "see through" the surficial veneers. One of the main aims of this study was to apply a systematic scientific approach to facilitate geological understanding in poorly exposed terranes using high resolution aeromagnetic data. The fundamental key to using aeromagnetic data is the ability to relate it to crustal geology, and the challenge is twofold: (i) to understand the rock properties that cause a magnetic signature, and (ii) to understand the geological processes that control such properties. Clearly the geological processes that control rock magnetisation are complex and diverse, and any study based on aeromagnetic data must necessarily integrate diverse geological observations. Such observations must pertain to processes likely to operate at regional scales relevant to large geophysical datasets, such as magnetic petrology and susceptibility, gravimetric data and rock density data, structural observations, metamorphic grade, geochronology and geochemistry. The correlation of such observations with aeromagnetic data provides a sound basis for developing a regional geological framework in poorly exposed terranes, via both two- and three-dimensional geophysical interpretations. Hence aeromagnetic data can be used as a proxy for geological exposure, facilitating a level of geological interpretation that can ultimately lead to the evaluation of regional tectonic models.

This study has focussed on the geology and geophysics of the western Gawler Craton, less than 1% of which outcrops (see Figures 1.1 & 1.2). Since the western Gawler Craton is largely composed of high grade gneisses, considerable attention has been devoted to understanding the tectonothermal evolution of various metamorphic and igneous rocks. The tectonothermal evolution of high grade metamorphic terranes reflects the temporal and spatial interplay between metamorphism, magmatism and deformation. Numerous studies detailing the nature of these relationships have been successfully undertaken by geologists working in well exposed terranes where detailed mapping of critical rock relationships at both regional and local scales provides a sound framework for understanding their tectonothermal evolution. In contrast, in poorly exposed terranes it has proved very difficult to correlate and synthesise seemingly disparate observations and develop a coherent understanding of their tectonothermal evolution. The use of interpretive geological maps as a proxy for outcrop observations can provide a sound basis for understanding the tectonothermal evolution of such terranes. Inevitably, observations regarding the metamorphic, magmatic and temporal evolution of such terranes necessarily rely on relatively few, widely spaced observations, therefore tectonothermal syntheses will be limited to relatively broad scales appropriate to the resolution of the geophysical and geological data. As a result it is vital to make observations of geological parameters which operate at regional, as well as local scales, such as regional metamorphic grade distributions, the distribution and nature of regionally extensive magmatism, and the geochronology of regionally representative samples. Thus the other main aims of this thesis are:

- to describe and map the geological relationships and structures within basement outcrops and available drill core in the western Gawler Craton;
- to develop a qualitative understanding of rock magnetisation in the western Gawler Craton based on magnetic susceptibility measurements and magnetic petrology;
- to produce a detailed interpretive geological map of the western Gawler Craton based on

aeromagnetic data;

- to investigate the tectonothermal evolution of the western Gawler Craton by studying the spatial and temporal distribution of metamorphism and magmatism with respect to major geological structures;
- to investigate the broader-scale relationships between the Gawler Craton and neighbouring Precambrian terranes in Australia and Antarctica and the processes that resulted in their amalgamation.

1.2 The western Gawler Craton - regional geological setting and previous work

The Gawler Craton, in South Australia, forms a large (>800x1000km) Precambrian shield which contains a rock record spanning the late Archaean to the late Mesoproterozoic. It is bound to the east by the Neoproterozoic-Cambrian Adelaide Fold Belt, and to the south by the continental margin (see Figure 3.1). The northwestern margin of the Gawler Craton has previously been loosely defined since it was thought to be concealed beneath sediments of the the Neoproterozoic-Palaeozoic Officer Basin. Recent studies of the Officer Basin

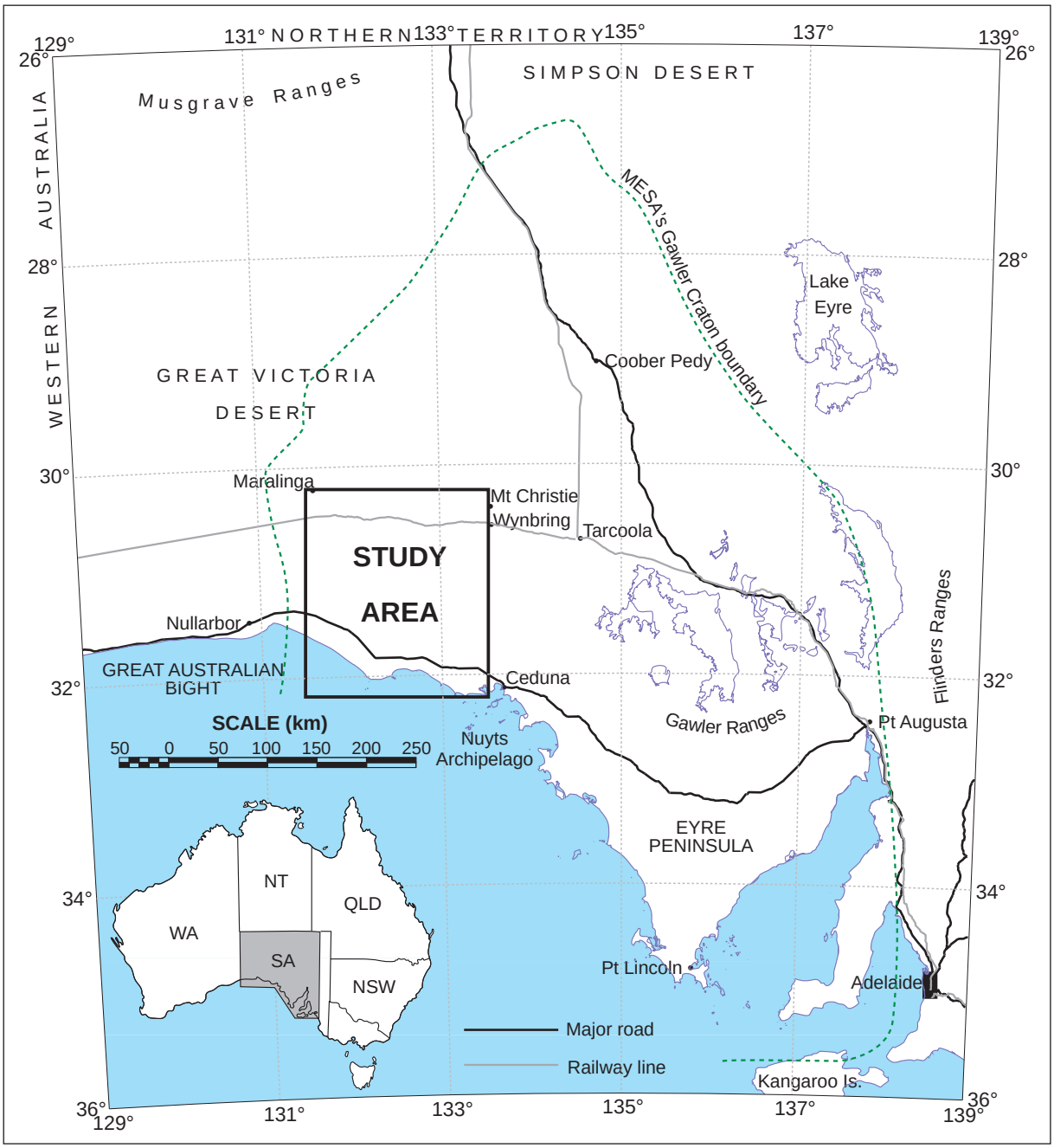

Figure 1.1 Location map showing the study area in the western Gawler Craton. Readers are encouraged to use the transparent overlays of geophysical images (in back pocket) in conjunction with this map.

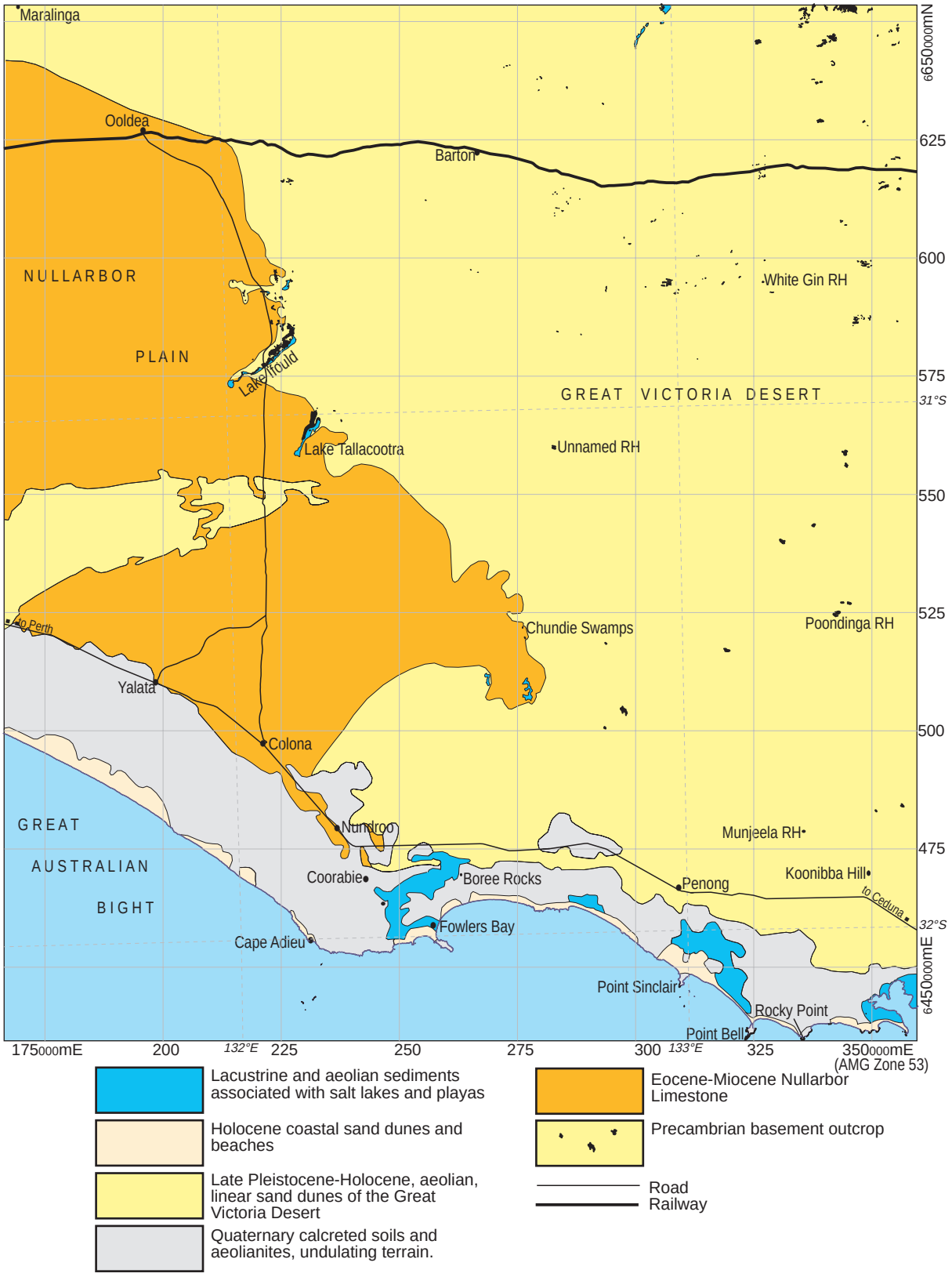

Figure 1.2 Principal physiographic features of the study area in the western Gawler Craton. Readers are encouraged to use the transperant overlays of geophysical images (in back pocket) in conjunction with this map.

indicate that it formed the southern part of the Centralian Superbasin; a regionally extensive sag basin initiated in the Neoproterozoic (Walter et al., 1995). Geophysical and seismic data show a gradual deepening of Neoproterozoic sediments to the north and west of the Gawler Craton (Preiss, 1993; Zang, 1995). As a result, basement rocks beneath the Officer Basin are continuous, and there appears to be no definite tectonic boundary between the Officer Basin and the Gawler Craton. Intact "Gawler Craton" basement probably extends as far north as the Musgrave Block (which is bound by a major, north-dipping, ~Devonian thrust fault), and west to the Albany-Fraser Orogen (see Chapter 9).

The relationship between the Gawler Craton and neighbouring Precambrian terranes in Australia and Antarctica is uncertain. Most Gondwana and Rodinia reconstructions show that Australia and Antarctica formed a continuous continental landmass at least during the Palaeozoic, indicating that the Gawler "Craton" extended well into what is now Antarctica (e.g. Veevers, 1986; Veevers & Eittreim, 1988; Willcox & Stagg, 1990). Recent geological and geochronological evidence supporting this notion has led to the definition of the *Mawson Continent* comprising the Gawler Craton and large parts of the East Antarctic Shield (Fanning et al., 1995, 1996). The Mawson Continent was probably bound by Grenvillian (1300-1000 Ma) and Pan-African (~500 Ma) mobile belts, and Neoproterozoic-Palaeozoic sedimentary basins (Fanning et al., 1996; Myers et al., 1996).

Less than 10% of the Gawler Craton outcrops and it is topographically subdued with local relief generally less than 100m (see Figure 1.2). It is largely blanketed by a thin veneer of regolith and/or sediment, and large tracts of the central and western Gawler Craton are covered by vegetated Quaternary sand dunes of the Great Victoria Desert. In the western Gawler craton outcrops constitute less than 1% of the surface area, and are confined to rocky coastal headlands, inland palaeochannels, and isolated inselbergs, bosses, platforms and saprolitic subcrop (see Figures 1.2, 1.4 & 1.5). Due to the remote, inaccessible nature of the terrain, many outcrops have not been identified or visited by geologists. Drill core provides valuable information in many unexposed areas. A geological map of the study area in the western Gawler Craton showing its principal physiographic features is shown in Figure 1.2. The distribution of basement drill holes is shown in Figure 1.3. Transparent overlays of aeromagnetic and gravimetric data for these areas can be found at the rear of this thesis, and the reader is encouraged to use these in conjunction with the thematic maps in this and subsequent chapters.

Most previous studies in the Gawler Craton have focussed on the better-exposed southeastern Gawler Craton, where more continuous outcrop has facilitated a reasonably detailed geological understanding (e.g. Drexel et al., 1993). Crystalline basement rocks in the western Gawler Craton were first described by Tate (1879), Giles (1889), Brown (1885, 1897, 1905) and George (1905). Subsequent mapping by King (1950, 1951) identified large outcrops of Precambrian gneiss in the Pidinga area (Lake Ifould) and surrounding rock holes and coastal headlands, which he subdivided into three categories: an older deformed and metamorphosed gneiss suite, mafic intrusives, and a younger granite-migmatite suite. Crawford (1957) and Whitten (1960) described ironstone outcrops in the Mount Christie-Fingerpost Hill area. Helicopter surveys by MESA and various mineral exploration companies identified and described many "new" outcrops in the sand dune areas (e.g. Forbes, 1970; Blissett & Vitols, 1973; Martin et al., 1989) resulting in the FOWLER and BARTON 1:250,000 geological map sheets (Firman, 1975; Rankin et al., 1995). Pain & Morris (1981) identified and described granitoid outcrops near several railway sidings. Potentially Archaean basement rocks were first recognised in the Tarcoola area by Webb & Thomson (1977) and Daly et al. (1978) who dated gneissic granites interlayered with banded iron formation via the Rb-Sr isochron method. Subsequent work by Daly et al. (1979), Daly (1981; 1986) and Daly & Fanning (1993) defined and described the late-Archaean to early-Palaeoproterozoic Mulgathing Complex; a series of multiply deformed metaigneous and metasedimentary rocks in the northwestern Gawler Craton. The occurrence of very high grade granulites at Ooldea was first recognised by Purvis (1981). Subsequent petrological work by Oliver & Purvis (1986), Radke & Fanning (1987), Taylor (1987) and Oliver et al. (1988) confirmed the presence of sapphirine-quartz bearing, ultrahigh temperature granulites in magnetite-rich gneiss from the Ooldea DDH2 drill core. The nature, age and tectonic setting of ultrahigh temperature metamorphism at Ooldea was not constrained prior to this study.

Fanning et al. (1988) proposed three "megacycles" of orogenic development in the Gawler Craton: (i) a late-Archaean to earliest Proterozoic megacycle (~2500-2300 Ma) involving the formation of the Mulgathing and Sleaford Complexes with subsequent tectonism during the Sleafordian Orogeny, (ii) a Palaeoproterozoic megacycle (~2000-1680 Ma) involving widespread sedimentation (Hutchison Group), magmatism (Lincoln Complex) and tectonism (Kimban Orogeny), and (iii) a Mesoproterozoic megacycle (~1590 Ma) involving extensive anorogenic magmatism (Gawler Range Volcanics and Hiltaba Suite). No post-1590 Ma tectonothermal activity was recognised in the western Gawler Craton, and "cratonisation" was thought to have occurred by ~1450 Ma (Drexel et al., 1993).

Parker (1990a, 1990b, 1993a) compiled a tectonic framework for the Gawler Craton based on the megacycles of Fanning et al. (1988) using a series of subdomains of broadly different geological and geophysical character separated by major shear zones; a spatial classification scheme adopted for this study (see Chapter 3).

Until very recently, the MESA geological framework for the Gawler Craton was largely based on the geology of the southeastern Gawler Craton

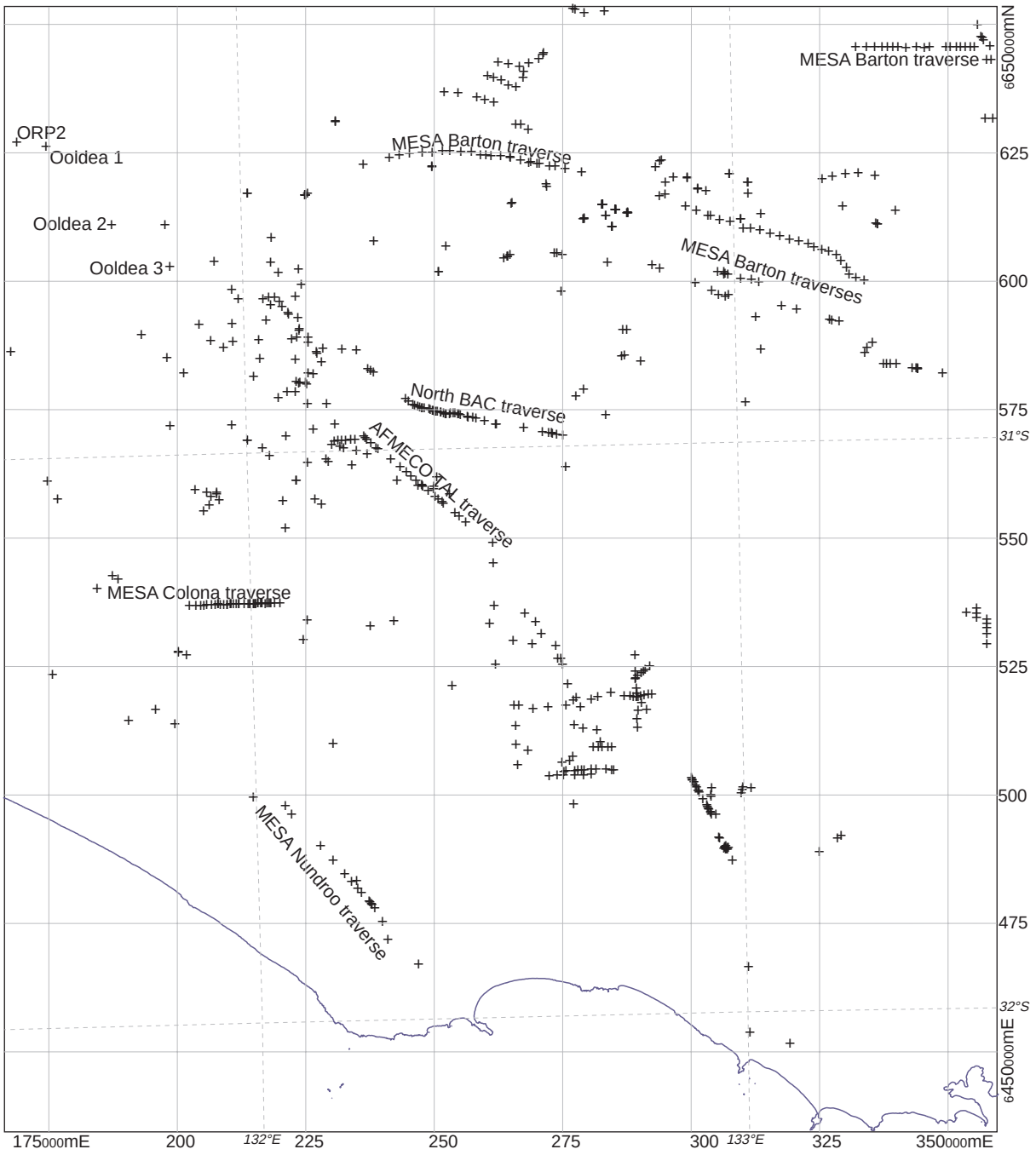

Figure 1.3 Distribution of basement-intersecting drill holes in the western Gawler Craton. Readers are encouraged to use the transparent overlays of geophysical images (in back pocket) in conjunction with this map.

(e.g. Fanning et al., 1988; Parker, 1990a, 1990b; Drexel et al., 1993; Rankin et al., 1996), whereby terms such as "Lincoln Complex", "Hutchison Group" and "Kimban Orogeny" were extrapolated to describe the geological evolution of the entire Gawler Craton. Recently Daly et al. (1995) and Rankin et al. (1996) recognised that there may have been post-Hiltaba Suite deformation in the northern and western Gawler Craton. The magnitude and extent of Mesoproterozoic tectonism in the northwestern Gawler Craton was acknowledged by Daly et al. (in press), who proposed the term *Kararan Orogeny* as a blanket term to describe tectonism between ~1650 Ma and ~1540 Ma.

In late 1993, Mines and Energy, South Australia (MESA) released data collected during the South Australian Exploration Initiative (SAEI). The SAEI was undertaken in 1992 in order to initiate geological understanding and mineral exploration in poorly exposed parts of the state, principally through aeromagnetic surveys and bedrock drilling programs. This PhD project was initiated in 1994 to use data collected during the SAEI to develop a geological framework for the western Gawler Craton.

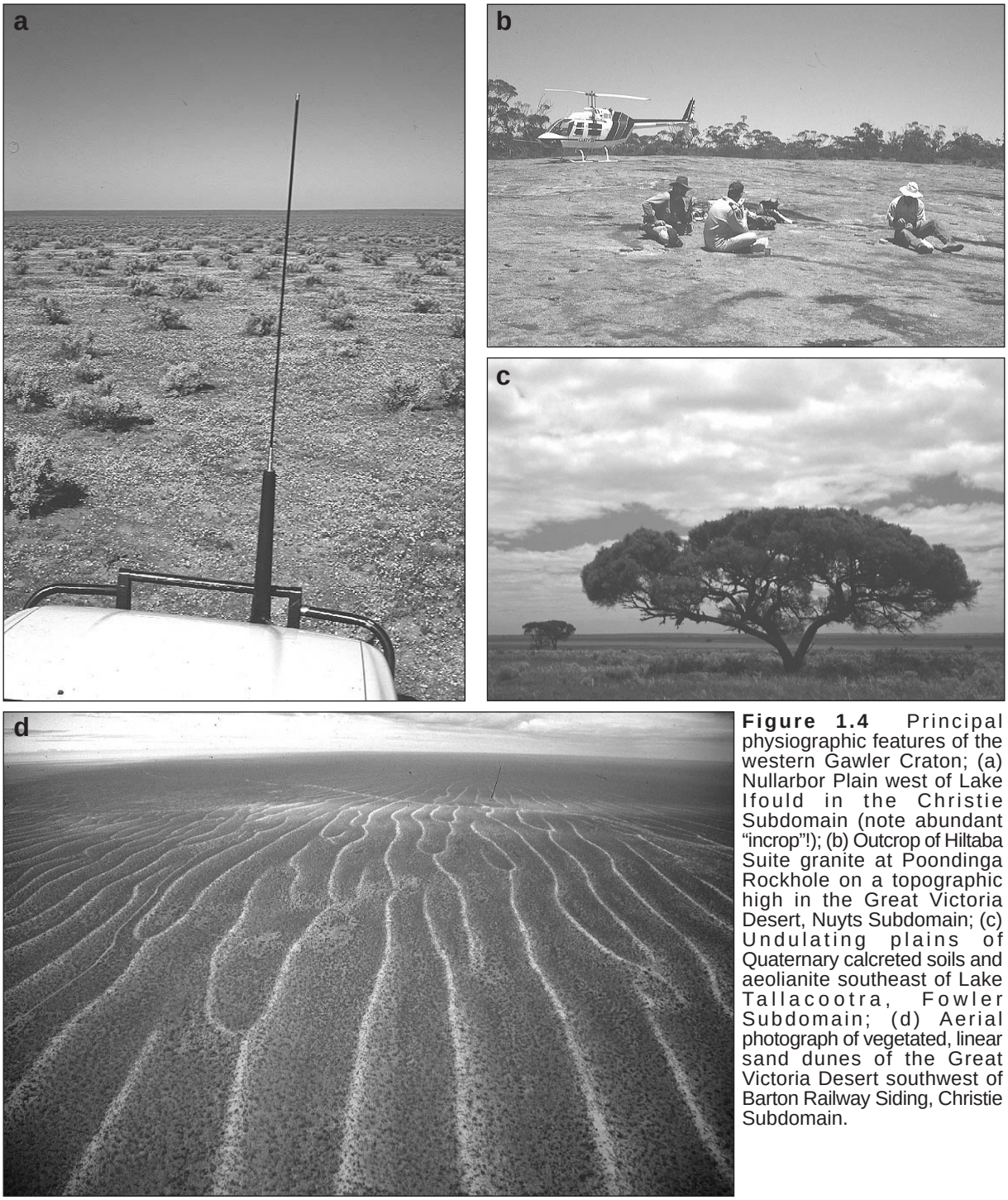

Figure 1.4 Principal physiographic features of the western Gawler Craton; (a) Nullarbor Plain west of Lake Ifould in the Christie Subdomain (note abundant "incrop"!); (b) Outcrop of Hiltaba Suite granite at Poondinga Rockhole on a topographic high in the Great Victoria Desert, Nuyts Subdomain; (c) Undulating plains of Quaternary calcreted soils and aeolianite southeast of Lake Tallacootra, Fowler Subdomain; (d) Aerial photograph of vegetated, linear sand dunes of the Great Victoria Desert southwest of Barton Railway Siding, Christie Subdomain.

1.3 Thesis outline

This thesis is divided into two parts. Part 1, entitled *Understanding poorly exposed terranes: a case study in the western Gawler Craton*, details some methods for understanding poorly exposed terranes and their application to the study area. Chapter 2 outlines the methodology used in this study, principally the geophysical approaches to understanding poorly exposed terranes, including information on rock magnetisation, and the acquisition, processing and interpretation of aeromagnetic data. Chapter 3 outlines the application of this methodology to the western Gawler Craton and the procedures and rationale used to construct the interpretive geological map (in back pocket). An outline of the geological framework of the Gawler Craton and its relationship with neighbouring terranes is presented, and is based on the notion that the Gawler Craton can be divided into discrete, structurally bound subdomains of significantly different geological character (after Parker 1990a, 1990b). The geophysical signature of the subdomains and shear zones spanned by the study area in the western Gawler Craton is discussed and related to the magnetic characteristics of the observed lithologies.

Figure 1.5 Typical coastal outcrops in the western Gawler Craton. St Peter Suite intrusives on St Peter's Island, Nuyts Subdomain.

Part 2 details the tectonothermal evolution of the western Gawler Craton with particular emphasis on the spatial and temporal distribution of metamorphic grade and style, as well as an outline of the magmatic evolution and geochronology of each subdomain in the study area. Chapter 4 outlines the tectonothermal evolution of the southern Nawa Subdomain, and focusses on the nature and possible causes of ultrahigh temperature metamorphism. Chapter 5 deals with the protracted geological history of the Christie Subdomain which has experienced multiple tectonothermal events since the late Archaean. Chapter 6 deals with the lower crustal tectonothermal evolution of the Fowler Subdomain during the Mesoproterozoic. Chapter 7 summarises the tectonothermal evolution of the Wilgena and Nuyts Subdomains which are dominated by upper crustal, felsic plutons. The tectonothermal evolution of the major shear zones that juxtapose and transect the subdomains are discussed in Chapter 8, where the overall architecture of the western Gawler Craton is also outlined.

The tectonothermal evolution of the western Gawler Craton is summarised and discussed in Chapter 9, where it is related to the broader scale evolution of the Gawler Craton. The relationship between the Gawler Craton and its neighbouring terranes is discussed in light of the new data, with particular reference to the role of the Gawler Craton in the assembly of Rodinia and Gondwana.

Relevant data used in the thesis is presented in five appendices at the rear of the thesis. A list of samples from outcrop and drillcore, including brief descriptions is provided in Appendix 1. Appendix 2 contains representative mineral analyses used in metamorphic calculations. Appendix 3 summarises thermobarometric results. Appendices 4 and 5 contain all geochronological and geochemical data.

PART 1

METHODS FOR UNDERSTANDING POORLY EXPOSED TERRANES: A CASE STUDY IN THE WESTERN GAWLER CRATON

Chapter 2
METHODS FOR UNDERSTANDING POORLY EXPOSED TERRANES

2.1 Introduction

Poorly exposed parts of the continental crust constitute a major hurdle to any explanation for the evolution and behaviour of the continents through time. As a result one of the main contemporary challenges for earth scientists is to develop integrated methods for understanding poorly exposed terranes. Such methods must rely on techniques that "see through" the surficial veneer of sediment, regolith, water or ice to characterise the underlying crust. Remotely sensed geophysical data; principally airborne magnetic (aeromagnetic) data; can provide precise, accurate, high resolution coverage that can "see through" the thin veneers that blanket most poorly exposed terranes. As outlined in Chapter 1, the fundamental key to using aeromagnetic data is the ability to relate it to crustal geology, and the challenge is twofold: (i) to understand the rock properties that cause a magnetic signature (i.e. rock magnetisation), and (ii) to understand the geological processes that control such properties (i.e. magnetic petrology).

Potential field measurements, such as magnetic and gravity data provide 3-dimensional information about the underlying lithosphere. However, since the same anomaly pattern can be caused by many different source lithologies and geometries, the inherent non-uniqueness of potential field source distributions can only be resolved with geological constraints (Grant, 1985a; Clark, 1997). Hence in order to extract the maximum amount of information from aeromagnetic data (and in particular to resolve its ambiguity) it is vital to understand the geological processes which control rock magnetisation.

Continent-scale, composite magnetic anomaly maps have proved to be a useful tool for resolving the gross geological architecture of some continents (e.g. Hinze & Zietz, 1985; Hinze & Hood, 1989; Jorgensen et al., 1995; Tarlowski et al., 1997). Such studies have provided the basis for continent-scale crustal elements maps (e.g. Wellman, 1988; Shaw et al., 1995) which may provide important information about the large scale geological framework of the continents. However, such datasets are inherently difficult to relate to observed geological features because of their low resolution. In general, terrane-scale geological features can only be resolved using higher resolution aeromagnetic data which can be correlated with outcrop-scale geological features. The most effective way of understanding continental geology in poorly exposed terranes is via the construction of interpretive geological maps based on aeromagnetic data. Such maps serve as a proxy for outcrop geology in unexposed areas, and are a very powerful tool for unravelling the geological history of poorly exposed terranes.

This chapter outlines the nature of the geophysical methods, as well as some of the types of geological observations necessary for understanding poorly exposed terranes and constructing interpretive geological maps. Section 2.2 provides an overview of current aeromagnetic data acquisition, processing and presentation technology. Section 2.3 contains a detailed summary of rock magnetisation and magnetic petrology, focussing on the geological factors that control crustal magnetisation. Section 2.4 outlines the interpretive techniques used in this project, and focuses on the geological "observables" that provide constraints on the interpretation of aeromagnetic data, thus allowing the development of an interpretive geological map of the western Gawler Craton.

2.2 Aeromagnetic data - background and methodology

2.2.1 Introduction

The generation of large, high resolution geophysical datasets is now commonplace in geological surveys and mineral exploration companies. The use of such datasets has been motivated by recent technological advances in computing and satellite navigation that allow the precise, accurate acquisition, and rapid processing and imaging of large geophysical datasets. The fast, easy manipulation and modelling of large geophysical datasets using desktop computers has provided earth scientists with extremely powerful research tools which are becoming an essential part of modern earth science. Images produced from these datasets have revolutionised our world view.

Aeromagnetic surveys provide a first-order constraint on the distribution of magnetic material

within the Earth's crust. Essentially, aircraft-mounted magnetometers measure small perturbations in the Earth's magnetic field caused by magnetic material in the crust (measured in nanoTeslas, nT). The resulting potential field data maps the 3-dimensional distribution of magnetic material in the Earth's crust. This section outlines the current methods for the acquisition, processing and presentation of aeromagnetic data.

2.2.2 Acquisition

Aeromagnetic data is acquired by flying an aircraft-mounted magnetometer along a series of equally spaced, parallel flight lines. Ideally, flight lines are oriented perpendicular to the predominant strike direction of magnetic anomalies in the crust. Flight-line spacing and flying height are determined by the amount of detail required and the cost. The important technological advances that have facilitated the acquisition of high resolution magnetic data in recent years include:

• Satellite navigation: Most pre-1990 aeromagnetic surveys relied on labour-intensive, visual flight-line recovery methods based on aerial photographs, with location errors normally in the range ±50m to ±200m (Denham, 1997; Hone et al., 1997). As a result, aeromagnetic surveys were restricted to flight line spacings in excess of 1km and often as much as 3km (Denham, 1997). Such data prohibited the recognition of many geologically relevant, map-scale phenomena, and limited the data application to very broad scale, regional studies (e.g. Hall, 1968; Lidiak, 1974; Zietz, 1980; papers in Hinze, 1985; Hinze & Hood, 1989; Teskey & Hood, 1991). The advent of Global Positioning Systems (GPS) in the late 1980's revolutionised flight-line accuracy. Modern differential GPS systems enable rapid, remarkably accurate positioning, and consequently have found widespread application in flight-line navigation (with real-time errors as low as ±2m). Similar advances in radar and GPS altimetry, and digital elevation models (DEMs) provide accurate flying height information (Denham, 1997). As a result, modern aeromagnetic surveys can operate with flight-line spacings less than 100m at a flying height as low as 40m (Horsfall, 1997). One ramification of high precision navigation is that earlier, widely spaced geophysical data can be infilled.

• Magnetometers: Modern caesium or helium vapour magnetometers provide precision of ±0.01nT, and can take measurements every 0.1 second (approximately one sample every 6-7m along the flight line) (Denham, 1997; Horsfall, 1997). This compares with the older fluxgate and proton precession magnetometers which only provided accuracy of 0.1-5nT, with sampling rates of 0.2-1 second (every 60-70m) (Hone et al., 1997; Horsfall, 1997). As a result, even weakly magnetised terranes can be accurately surveyed at high resolution.

• Computers: Modern computers enable large geophysical datasets to be stored digitally, in real time. Older analog systems were very slow and bulky.

• Aircraft: Modern light aircraft can fly further and faster, more safely and efficiently than older aircraft. Combined with lighter payloads caused by miniaturisation of computer and magnetometer components, light aeroplanes and helicopters provide a fast, cost-effective means for airborne geophysical data acquisition.

2.2.3 Processing

In order to derive the residual total magnetic intensity data relevant to geological problems, raw aeromagnetic data is traditionally processed using a series of steps which are discussed in detail by Isles et al. (1995) and Luyendyk (1997), and are briefly summarised below:

(i) Verifying and editing: Visual inspection of the raw magnetic and navigation data is carried out to remove spikes, gaps, instrument noise and any other irregularities resulting from random errors in data acquisition.

(ii) Parallax correction: Due to the finite distance between the navigation and magnetic sampling points on the aircraft (the cable length) a small parallax correction must be made.

(iii) Diurnal variation corrections: Since the Earth's magnetic field varies with time over many wavelengths (e.g. 1 second to many years, with the most pronounced variations occurring diurnally - Parkinson, 1983), aeromagnetic data are corrected for diurnal variations by comparing the measured magnetic data with data recorded at a time-synchronised base station.

(iv) IGRF removal: The International Geomagnetic Reference Field (IGRF) is a mathematical approximation of the Earth's magnetic field, which must be subtracted from the aeromagnetic data in order to provide a realistic measure of the residual magnetic anomalies caused by rocks. The IGRF is a function of position and altitude.

(v) Levelling: Aeromagnetic surveys are flown along parallel, evenly spaced flight lines, with occasional tie lines flown perpendicular to the main flight lines. At the crossover points, duplicate measurements are made. Levelling is the procedure by which discrepancies between duplicate measurements at crossover points (intersection errors) are reduced by systematically proportioning them between the flight-lines and the tie lines.

(vi) Gridding is the procedure by which flight-line data is interpolated onto a regular geometric grid. For example, high resolution aeromagnetic data collected at 10m intervals along flight lines 500m apart can be interpolated onto a 100m regular

grid using a bicubic spline gridding algorithm. Gridding is performed for three reasons: (i) to reduce the size of the dataset in order to manipulate it more efficiently via computers (in practise, raw magnetic datasets are huge [>1 gigabyte], whereas the equivalent gridded dataset is at least an order of magnitude smaller), (ii) to facilitate the display of the data (usually via pixel images) on a graphical device, and (iii) to facilitate the application of filters (see §2.2.4 below).

2.2.4 Enhancement

The enhancement of processed (either gridded or non-gridded) aeromagnetic data is principally performed using filters. There are two types of filter: *space domain* and *frequency domain* filters. Space domain filters use convolution kernels (matrices) which operate on each datapoint in gridded magnetic data. For frequency domain filters, the Fourier Transform of the magnetic data is convolved with frequency and/or amplitude filters, and the modified data is then transformed back into the space domain. Frequency domain filters can be approximated using space domain filters, a procedure commonly used by image enhancement software packages. Most filters used to enhance aeromagnetic data are frequency filters, which modify the range and amplitude of the frequency data. Filters used in this study are outlined below and illustrated in Figure 2.2a (descriptions adapted from Isles et al., 1997; Milligan & Gunn, 1997 and Tarlowski et al., 1997):

- Band-pass filters remove a specified frequency range. High-pass filters remove low frequencies and low-pass filters remove high frequencies. Low-pass filters are commonly used to remove high frequency magnetic anomalies and/or noise, in order to better visualise broader wavelength (hence deeper sourced) anomalies. Band-pass filters provide a first-order control on the depth of the displayed anomalies.
- Upward and downward continuation filters compute the magnetic field at higher or lower levels (mimicking a change in flying height). Downward continuation filters enhance high frequency anomalies, but amplify noise. Upward continuation filters smooth out high-frequency anomalies relative to low frequency anomalies, and can emphasise broader wavelength (hence deeper) magnetic sources. In effect, continuation filters are a type of band-pass filter.
- Vertical derivative filters enhance vertical changes in magnetic data (i.e. magnetic boundaries). The first vertical derivative is a measure of the rate of change of magnetic field with height, and is calculated by computing the upward continuation of the data, subtracting it from the original data and dividing by the effective "height" difference. Vertical derivative filters enhance short wavelength anomalies, including noise. In practice, vertical derivative filters are used to highlight magnetic boundaries, such as geological contacts and faults (see Figure 2.2).
- Automatic gain control (AGC) filters remove amplitude information from magnetic datasets, giving approximately equal emphasis to anomalies of both high and low amplitudes/intensities. AGC filters are useful in conjunction with first vertical derivative filters (see Figure 2.2a).

2.2.5 Presentation

Until recently, contour maps and stacked profiles were the principal means for presenting aeromagnetic data. The advent of colour graphical display devices (e.g. computer monitors and printers) facilitated the fast, accurate generation of colour and greyscale pixel image maps which have become standard way of displaying large, high resolution aeromagnetic datasets. Pixel image maps are vastly superior for visualising and interpreting regional aeromagnetic data. Contour maps and stacked profiles are not an efficient way of displaying these large datasets, although they are still very relevant to smaller scale studies. Pixel image maps usually comprise a large grid of pixels (usually corresponding to grid points in magnetic data) which are assigned a different colour depending on their magnetic intensity. Since the range of magnetic intensity is continuous, and the range of colours on the display device is finite, it is necessary to subdivide the magnetic intensity values into discrete blocks and assign colours to each block according to a colour lookup table (LUT). The colour assignment of magnetic intensity values using a lookup table can usually be enhanced for maximum visual effect by "stretching" the initial raw data histograms. Commonly implemented histogram stretches are histogram equalisation (equal quantities of grid values are assigned to each level in the lookup table), histogram normalisation (raw data is converted into a Gaussian distribution) and clipping (data outliers clipped to a 90% or 95% confidence interval).

A very commonly used image enhancement tool is the shaded relief algorithm. Shaded relief maps use an artificial sun angle routine (e.g. Pelton, 1987) which greatly enhance boundaries and textures in pixel image maps by varying the hue, saturation and intensity of the colours, according to a 3-dimensional colour LUT (e.g. Milligan & Gunn, 1997). Usually, sun angle algorithms are set up to artificially illuminate the grid surface orthogonal to the pervasive anomaly trends. Hence shaded relief maps highlight geological structures and also extract fine detail (Teskey & Hood, 1991). Shaded relief maps must be used cautiously since boundaries can be artificially displaced.

Recent advances in printing technology enable the cheap, fast production of high quality pixel image maps.

2.3 Magnetisation of rocks

2.3.1 Introduction

Aeromagnetic surveys map the distribution of magnetic minerals in the Earth's crust. They do not provide unique information about the lithology or geometry of anomaly sources. Clearly, the fundamental key to reliably interpreting aeromagnetic data is the ability to relate it to crustal geology, and as outlined in Chapter 1, the challenge is twofold: (i) to understand the rock properties that cause a magnetic signature (i.e. rock magnetisation), and (ii) to understand the geological processes that control such properties (i.e. magnetic petrology). This section outlines the types of rock magnetisation, and discusses the diverse geological processes that control them.

2.3.2 Rock magnetisation

Rock magnetisation is a collective term for the rock properties that cause a magnetic response. Magnetisation, **M** (a vector) is defined as the magnetic dipole moment per unit volume. There are two types of magnetisation; induced magnetisation ($\mathbf{M}_I$, caused by an applied field) and remanent magnetisation ($\mathbf{M}_R$, "permanent" magnetisation). The total magnetisation is the vector sum of the induced and remanent magnetisation, i.e.:

$$\mathbf{M}_{TOTAL} = \mathbf{M}_I + \mathbf{M}_R$$

Induced magnetisation is caused by an applied magnetic field (in this case, the Earth's magnetic field), and is approximately proportional to the applied field. The magnetic susceptibility, k, is the constant of proportionality between the induced and applied fields. Therefore:

$$\mathbf{M}_I = k\mathbf{F}, \text{ and } \mathbf{M}_{TOTAL} = k\mathbf{F} + \mathbf{M}_R$$

where **F** is the applied field (i.e. the geomagnetic field). Note that both **M** and **F** are vector quantities. Induced magnetisation is approximately parallel to the applied field in most rocks, therefore susceptibility is a scalar quantity which only has magnitude, not direction (Clark, 1997). The *Königsberger ratio*, Q is a measure of the ratio of the magnitude of induced to remanent magnetisation:

$$Q = \mathbf{M}_R / \mathbf{M}_I$$

2.3.2.1 Induced magnetisation

Induced magnetisation is the component of magnetisation produced in response to an applied magnetic field. In aeromagnetic surveys the Earth's magnetic field constitutes the applied field. The induced magnetisation in a rock can be measured by recording its magnetic susceptibility. Induced magnetisation in rocks can be caused by three factors (Isles et al., 1995; Clark, 1997):

(i) Diamagnetism, which is caused by orbiting electrons' resistance to an applied magnetic field. Diamagnetic materials act to *oppose* the applied field, and have weak negative magnetic susceptibility. Importantly, the contribution of diamagnetic materials to the Earth's residual magnetic field is geologically insignificant.

(ii) Paramagnetism, which is caused by magnetic elements in a material (e.g. iron and other transition metals). Paramagnetic materials have a weak positive susceptibility which is independent of the applied field. Only very high resolution, localised magnetic surveys are likely to detect paramagnetic minerals.

(iii) Ferromagnetism, which occurs in materials in which magnetic dipoles align parallel to the applied field. Ferromagnetic materials can have a very high positive susceptibility which is a function of both the applied field and temperature, and can be spontaneously magnetic (e.g. magnets). Ferromagnetic minerals are the only geologically significant contributors to regional magnetic anomalies. The most common ferromagnetic mineral is magnetite.

The susceptibility of common rock-forming minerals is shown in Table 2.1, and the susceptibility ranges of common rock types are shown in Figure 2.1, which is largely derived from a extensive, long term study undertaken by the combined Scandinavian Geological Surveys (Henkel, 1991a). Importantly, there is a strong grain-size dependence on susceptibility; coarser grained rocks have higher magnetic susceptibility (e.g. Grant, 1985a; Henkel, 1991a,b; Isles et al., 1995). Magnetite is clearly the

Mineral	Susceptibility (S.I. x 10^{-5})
Quartz	-1.5
Feldspar	-1.4
Calcite	-1.3
Dolomite	1.2
Spinel	3
Pyrite	4.3
Muscovite	4-75
Cordierite	20-110
Epidote	100
Amphibole	50-130
Hematite	50-220
Ilmenite (pure)	190
Pyroxene	12-330
Biotite	90-330
Olivine	12-540
Garnet	50-680
Titanohematite	200-100000
Pyrrhotite	4000-100000
Magnetite	100000-1000000

Table 2.1 Magnetic susceptibility of common rock-forming minerals (after Isles et al., 1995; Clark, 1997).

most magnetic mineral, and is the only significantly magnetic mineral common in crustal rocks. Hence magnetic susceptibility primarily reflects magnetite content in a rock, and aeromagnetic surveys essentially map the distribution of magnetite in the crust (e.g. Grant, 1985a; Isles et al., 1995; Clark, 1997). Induced magnetisation is roughly proportional to magnetite content.

The temperature dependence of induced magnetisation is a vital consideration, especially in thermally perturbed areas. Diamagnetic and paramagnetic minerals exhibit strongly decaying magnetic susceptibility with increasing temperature (Clark, 1997). Ferromagnetic minerals (principally magnetite) exhibit approximately constant magnetic susceptibility below a critical temperature known as the *Curie Point*, or *Curie Temperature*. Magnetite has a Curie Temperature of 578°C (Clark, 1997), which is approximately that at the moho in thermally equilibrated, isostatically balanced continental crust. Any thermal or tectonic regime which results in crustal temperatures in excess of ~600°C will demagnetise the deeper parts of the crust, with an isothermal surface (the *Curie Isotherm*) defining the boundary of magnetisation. As a result, the lower boundary of deep crustal magnetic anomalies is constrained by the Curie Isotherm (e.g. Haggerty, 1978; Gasparini et al., 1979; Schlinger, 1985). Conversely, mantle-derived mafic-ultramafic rocks may exhibit strong induced magnetisation if they are cooled below ~600°C.

2.3.2.2 Remanent magnetisation

Remanent magnetisation (remanence) is caused by the alignment of microscopic magnetic dipoles in rocks with the Earth's magnetic field. Physically, this can only occur in either low-viscosity melts cooling below the Curie Temperature, or in very low energy sedimentary environments. Remanence only occurs in fine grained rocks which contain very fine grained Fe-Ti oxides that act as magnetic dipoles. Magnetite rarely exhibits remanent magnetisation, however Fe-Ti oxides such as titanohematite and ülvospinel can exhibit strong remanence (oxides with Fe:Ti=1:1 have the strongest remanence) (Grant, 1985a; Isles et al., 1995). Remanent magnetisation varies with time when subjected to an external magnetic field. The time-varying component of remanence is known as *viscous remanent magnetisation*. The "permanent" component of remanence is known as *thermoremanent magnetisation*. There are other, minor components of remanent magnetisation which are beyond the scope of this study.

Unmetamorphosed mafic volcanics, fine grained sediments and high level mafic intrusives (e.g. sills and dykes) are the most likely carriers of remanence. The strongest carriers of remanence are highly oxidised, Fe-Ti minerals (e.g. titanohematite), which are only likely to form in highly oxidised rocks (e.g. Grant, 1985a). In fine grained sedimentary rocks the magnetic grains are detrital and are aligned with the Earth's magnetic field during sedimentation. In fine grained mafic rocks, magnetic grains will align with the Earth's magnetic field when magmas cool below the Curie Temperature. Remanence is unlikely to occur in most mid-lower crustal rocks, especially metamorphic rocks (remanence does not survive recrystallisation), and is unlikely to occur in most plutonic rocks (Grant, 1985a; Isles et al., 1995; Clark, 1997). The most dramatic terrestrial manifestation of remanent magnetisation are the parallel magnetic anomalies in oceanic crust (oceanic "stripes"), which reflect the abrupt polarity reversals in the Earth's magnetic field. Fine grained mid-ocean ridge basalts cooling below the Curie Point are responsible for these anomalies. Apparent Polar Wander (APW) paths for the continents derived from palaeomagnetic observations rely on precise preservation of remanent magnetisation directions in fine grained mafic and sedimentary rocks.

2.3.3 Magnetic Petrology

Clark (1997) defines magnetic petrology as "the integration of rock magnetism and conventional petrology to characterise the composition, abundance, microstructure and paragenesis of magnetic minerals, and to define the processes that create, alter and destroy magnetic minerals in rocks". Early workers attempted to subdivide magnetic intensity according to lithology, however it soon became apparent that this was impossible. Pioneering studies by the Scandinavian geological surveys measured the magnetic susceptibility of over 30,000 rocks, and the resulting bar graph of susceptibility versus lithology demonstrated that it is impossible to classify rocks according to their susceptibility (e.g. Henkel, 1991a) (see Figure 2.1). As a result, it is vital to understand the magnetic petrology of rocks in areas covered by aeromagnetic surveys in order to understand the causes of magnetic anomalies.

Rock magnetisation primarily reflects the partitioning of iron between strongly magnetic oxides and weakly magnetic silicates and carbonates (e.g. Clark, 1997). The geological factors that control rock magnetisation (i.e. factors that control Fe-partitioning) include initial iron concentration, oxidation state (oxygen fugacity, fO_2), metamorphic grade, grain size, crystallisation environment, major element chemistry, degree of deformation, alteration and fluid flow (Grant, 1985a; Isles et al., 1995). Clearly these factors are often genetically linked.

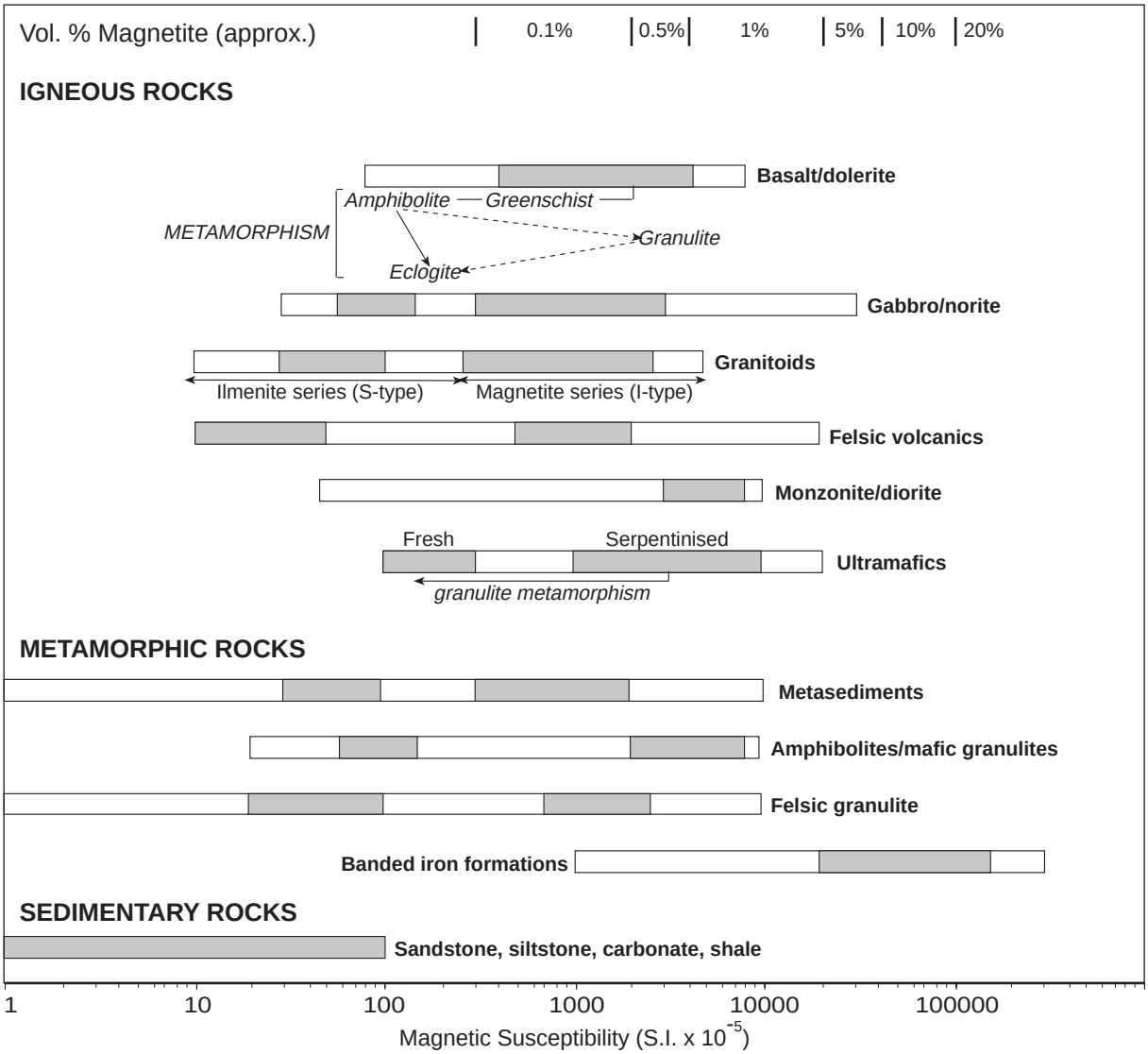

Figure 2.1 Magnetic susceptibility ranges of common rock types (after Henkel, 1991a; Isles et al., 1995; Clark, 1997). Clear rectangles = total observed susceptibility range, shaded rectangles = common susceptibility range.

In the following subsections the magnetic petrology of igneous, sedimentary and metamorphic rocks is briefly discussed. In Chapter 3, the magnetic petrology of relevant rocks from the western Gawler Craton will be discussed in light of their origin, and metamorphic, structural and alteration histories.

One of the most important controlling factors of magnetisation in magnetite-bearing rocks is grain size. As a first-order approximation, grain size is roughly proportional to magnetic susceptibility (Clark, 1997), thus coarse grained magnetite has a much higher susceptibility than fine grained magnetite. As a result the geological processes that control grain size are an important consideration in understanding rock magnetisation.

2.3.3.1 Magnetic petrology of igneous rocks

The fundamental factors controlling magnetisation in igneous rocks are the magma chemistry and grain size. The silica saturation, iron content and oxidation state of a magma determines whether iron will be partitioned into oxides or silicates during crystallisation. The crystallisation grain size of an igneous rock is a very important controlling factor on rock magnetisation. For example, very fine grained mafic igneous rocks can exhibit strong remanent magnetisation but relatively weak induced magnetisation, whereas coarse grained, magnetite-bearing intermediate rocks can exhibit very high induced magnetisation.

2.3.3.2 Magnetic petrology of sedimentary rocks

Unmetamorphosed sedimentary rocks rarely contain magnetite, since magnetite is unstable during low temperature, highly oxidising chemical weathering processes and in sedimentary environments (Grant, 1985a). Hence unmetamorphosed sedimentary rocks are rarely magnetised sufficiently to contribute to regional magnetic anomalies. One illustration of this is the apparent magnetic "transparency" of unmetamorphosed sediments. Iron-rich sedimentary rocks contain abundant hydrous iron oxides such as hematite, siderite and goethite, hence can exhibit weak remanent magnetisation. Only

magnetite-series banded iron formations can exhibit high induced magnetisation.

2.3.3.3 Magnetic petrology of metamorphic rocks

Magnetite is an important rock-forming mineral and is produced and destroyed at all grades of metamorphism (e.g. Grant, 1985a). Hence the effects of metamorphism on rock magnetisation are variable and complex, and magnetite petrogenesis in each metamorphic rock must be considered separately. However, there are two main factors which control magnetite growth during metamorphism: bulk composition and oxidation state (fO_2). Clearly iron-rich rocks can potentially grow more magnetite, especially under relatively oxidising conditions which partition iron into oxides rather than silicates. As a general rule, magnetic susceptibility increases with metamorphic grade (e.g. Lidiak, 1974; Grant, 1985a; Wasilewski & Warner, 1988; Urquhart, 1989; Olesen et al., 1991; Skilbrei et al., 1991), and retrogression (especially hydration) decreases magnetic susceptibility via the breakdown of magnetite (e.g. Henkel, 1991a; Skilbrei et al., 1991; Toft et al., 1993). One exception is the retrograde serpentinisation of ultramafic rocks, which produces magnetite and markedly increases magnetic susceptibility (e.g. Grant, 1985a; Henkel, 1991a; Isles et al., 1995; Clark, 1997).

2.4 Methods for interpreting aeromagnetic data

2.4.1 Introduction

In order to develop a regional geological framework in poorly exposed terranes based on aeromagnetic data, it is important to make diverse geological observations and inferences of processes likely to control rock magnetisation at regional scales. Clearly it is vital to understand the contribution of geological processes such as metamorphism, magmatism, deformation and alteration to the magnetisation of rocks. The precise correlation of these observations with aeromagnetic data provides a sound basis for developing a regional geological framework in poorly exposed terranes, principally via 2-dimensional interpretive geological maps.

Section 2.4.2 outlines the main "observables" used in this study to relate widely spaced geological observations to aeromagnetic data, providing a brief outline of the methods used to derive them. The qualitative geometric procedure used to generate two-dimensional interpretive geological maps is presented in Section 2.4.3. The use of power spectra to quantify aeromagnetic data is outlined in Section 2.4.4. A brief outline of the importance of Geographical Information Systems (GIS) to this study is presented in Section 2.4.5.

2.4.2 Important "observables"

Clearly, it is vitally important to make as many basic lithological observations as possible during fieldwork and drill core examination. Fundamental observations such as rock type, contact relationships and structures must be combined with a representative sampling program as in any geological mapping exercise. This section focuses on the subsequent important "observables" made during this study that were found necessary to relate basic geological observations to aeromagnetic data.

2.4.2.1 Rock magnetisation

The principal magnetic rock property measured in this study is magnetic susceptibility; a dimensionless (scalar) quantity which relates rock magnetisation to the inducing field (i.e. the Earth's magnetic field - see §2.3.2). Magnetic susceptibility measurements can be directly correlated with aeromagnetic data. Strongly magnetised rocks have a very high positive magnetic susceptibility, and visa versa. Aeromagnetic anomalies occur at scales larger than most outcrops and drill holes in the western Gawler Craton (which are effectively point data), so in order to relate magnetic susceptibility measurements to these anomalies, it is important to deduce the causative magnetic lithologies. In most cases the correlation is obvious, however ambiguity does occur, and can only be resolved by drawing information from other outcrops and drill core or other "observables". The magnetic susceptibility of all visited outcrops, samples and drill core was measured using a hand-held Geoinstruments JH-8 analog magnetic susceptibility meter. The "unit" of magnetic susceptibility used in this study is S.I. x 10^{-5}.

Remanent magnetisation was not measured in this study for two reasons: (i) in highly metamorphosed terranes (such as the western Gawler Craton) rocks are unlikely to record remanence (e.g. Clark, 1997); and (ii) the equipment used to measure remanence is expensive and not accessible in South Australia. However, remanent magnetisation is inferred for several mafic intrusive bodies in the western Gawler Craton (see Chapter 3).

2.4.2.2 Magnetic petrology

The magnetic petrology of selected samples from the western Gawler Craton was investigated in order to constrain their magnetic mineralogy and petrogenesis, and the possible geological causes of rock magnetisation. These observations are discussed case-specifically in Chapter 3. Metamorphism controls rock magnetisation via the

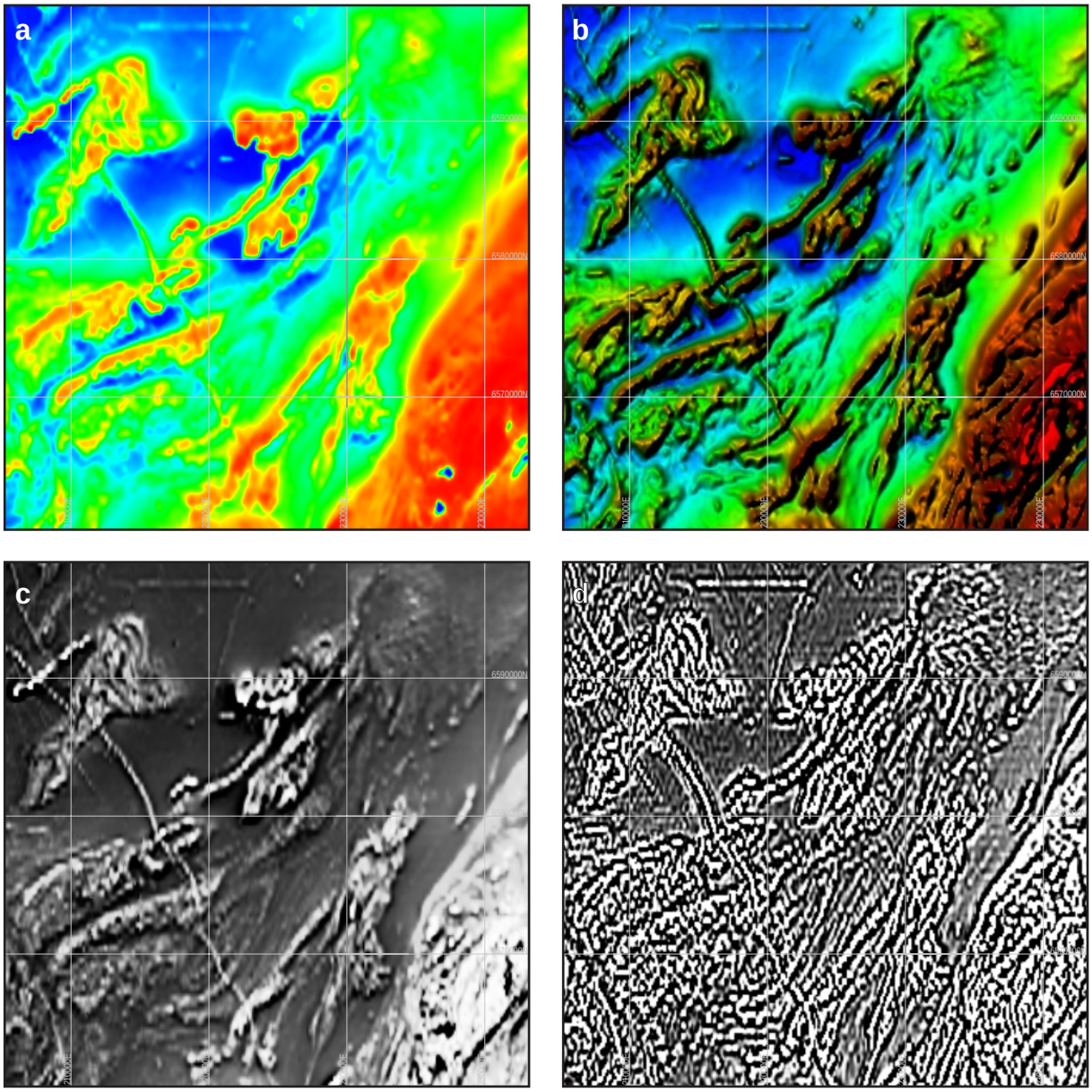

Figure 2.2a Examples of various image processing algorithms (from an area near Lake Ifould in the Christie and Fowler Subdomains); (a) pseudocolour image of total magnetic intensity; (b) shaded relief image of total magnetic intensity with northwesterly illumination; (c) greyscale image of first vertical derivative of the total magnetic intensity; (d) greyscale image of the first vertical derivative with automatic gain control.

growth and consumption of magnetic minerals in rocks, and generally occurs at regional scales relevant to aeromagnetic data. As a result it is vital to understand metamorphism and its bearing on magnetic petrology in any realistic magnetic interpretation. Hence the magnetic petrological observations presented in Chapter 3 are intricately linked with the tectonothermal evolution of the terrane (see Part 2).

2.4.2.3 Structural observations

Basic structural observations, such as the orientation of primary layering, foliations, lineations, fold axes and shear bands, combined with kinematic information, are an important part of any geological framework. The correlation of these data with aeromagnetic data by matching observed structural trends with magnetic anomaly trends is a vital part of any magnetic interpretation. In the western Gawler Craton, major crustal shear zones often exhibit large-scale linear magnetic trends which parallel observed high strain foliations. The kinematic evolution of these shear zones holds an important key to understanding the tectonic evolution of the terrane.

2.4.2.4 Gravimetric data

Regional gravimetric data is an important adjunct to aeromagnetic data. Since gravity surveys are ground-based, they are generally acquired using a much coarser grid size than magnetic surveys (usually 1-10km). As a result, they only detect longer wavelength anomalies which are generally associated with deep sources. Hence gravity data are particularly useful for delineating deep-crustal geological boundaries (Jaques et al., 1997).

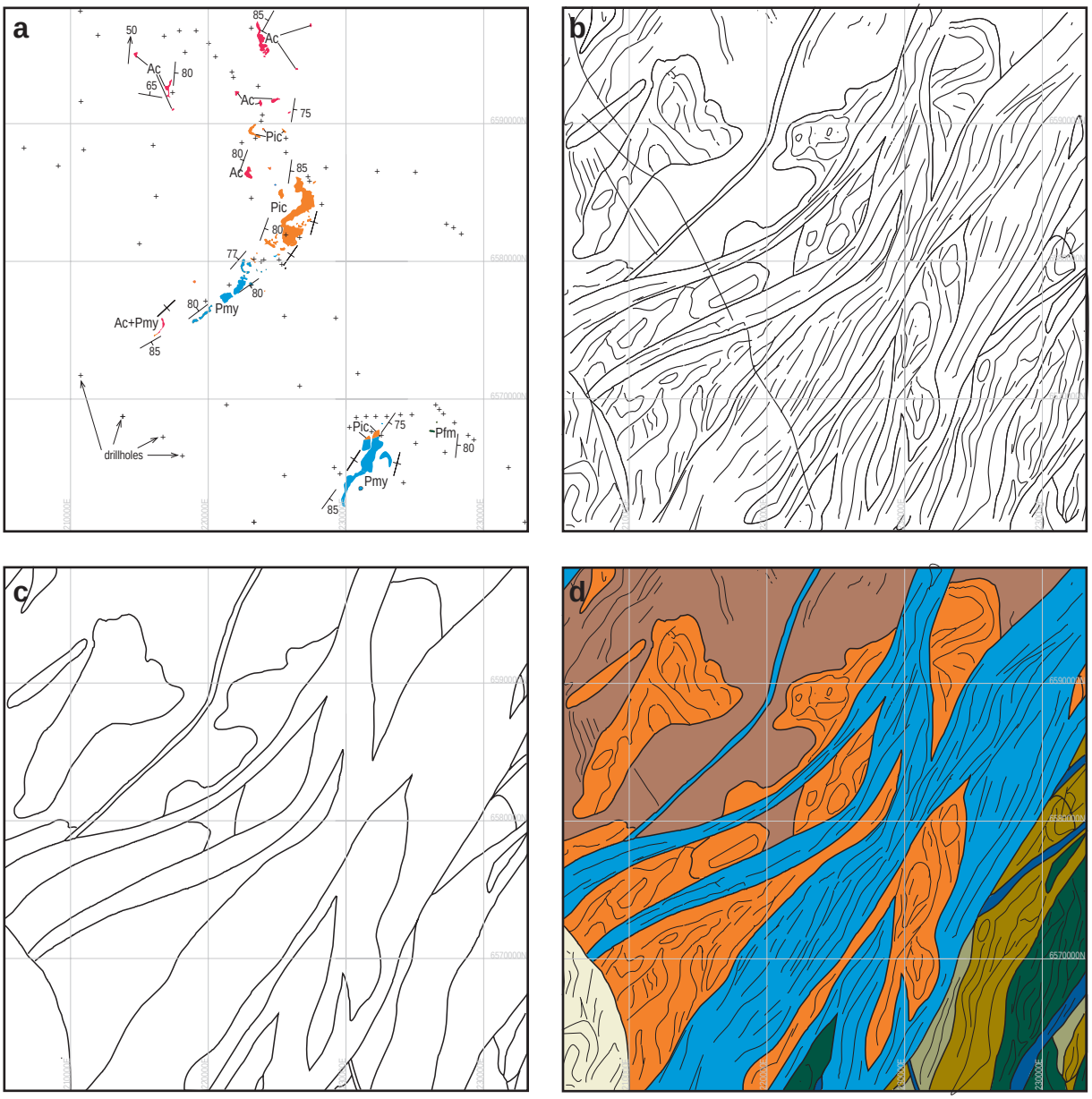

Figure 2.2b Three stage geological interpretation of the images shown in Figure 2.3a; (a) Outcrop geology and basement drill holes (see Figure I1 at rear of thesis for legend); (b) Stage 1 linear features; (c) Stage 2 polygonal features; (d) final interpretive geological map (see text for explanation and Figure I1 for legend).

2.4.3 Constructing interpretive geological maps

Two-dimensional, interpretive geological maps are the most commonly used type of aeromagnetic interpretation. However, no systematic method for interpreting high resolution aeromagnetic data has been adopted by earth scientists. This in part must reflect the diversity of geology and magnetic anomalies in the studied areas. It is very important to realise that such maps are only an interpretation, and that there is no "correct" version (in the same way that geological maps are purely interpretations). The interpretation of aeromagnetic data is strongly influenced by individual style, relevant geological problems and the required results (Isles et al., 1995). Objectivity is very important (Isles et al., 1995); it is wrong to base a magnetic interpretation on existing geological interpretations, but it is vital to incorporate geological facts as outlined in Section 2.4.2.

The mechanical procedure for interpreting aeromagnetic data derived during this project involves three stages, loosely based on the methods prescribed by Henkel (1991b), Isles et al. (1995), Gunn et al. (1997) and Jaques et al. (1997), together with conversations with Dr John Parker and Dr Rodney Hammond at Equinox Resources N.L. Stage 1 defines linear magnetic features, Stage 2 defines magnetic "areas", and Stage 3 relates the geometric interpretation to the known geology. These stages are illustrated in Figure 2.2.

Stage 1: The geometric "skeleton"

The main aim of Stage 1 is to identify linear magnetic trends and pattern breaks. Hence image enhancement procedures that emphasise short

wavelength magnetic trends and boundaries are used, such as greyscale images processed using vertical derivative and automatic gain control filters (note that shaded relief images are not used during Stage 1, since they can displace short wavelength anomalies). The resulting linear "skeleton" interpretation depicts the detailed geometric aspects of the magnetic data. Importantly, this interpretation is entirely based on the magnetic data (see Figure 2.3), and its relationship with the geology is unknown at this stage. The interpretation detail is limited by the shortest wavelength anomalies. An example of a geometric "skeleton" interpretation is shown in Figure 2.2b.

Stage 2: Pattern recognition

The main aim of Stage 2 is to identify areas of common magnetic character. Hence image enhancement procedures that emphasise magnetic textures and longer wavelength magnetic features are used, such as pseudocolour images with shaded relief. The resulting interpretation groups areas according to their magnetic character. By overlaying the Stage 1 "skeleton" interpretation, the boundaries of magnetic units can be precisely defined, and their dip may be inferred. As in Stage 1, the resulting interpretation is based entirely on the magnetic data, and its relationship with the geology is not yet qualified.

Stage 3: The interpretive geological map

The main aim of Stage 3 is to correlate the geometric interpretation generated during Stages 1 and 2 with the known geology. All relevant geological information (including the "observables" outlined in §2.4.2) is overlayed onto the Stage 1 and 2 interpretations. The ensuing interpretation involves the delineation of geological units, boundaries and structures based on the Stage 1 linear trends and the Stage 2 magnetic "areas" in geologically well-constrained areas, and to extrapolate this interpretation to unexposed areas where no geological information is available. Clearly not all of the geometric features identified in Stages 1 and 2 will appear on the resulting interpretation; many will not have any real geological meaning and may in fact be artefacts in the data. Similarly some of the geological information may be irrelevant at the regional scale of the interpretation. Clearly the main aim in Stage 3 is to produce an *internally consistent* interpretation which takes into account as many geophysical and geological observations as possible. The resulting interpretive geological map provides a 2-dimensional interpretation of the surface geology, and serves as a proxy for continuous geological exposure.

2.4.4 Quantification of aeromagnetic data

Traditionally, quantitative studies of potential field data have revolved around forward modelling of source geometries and depth. Such models can provide important geological information in the third dimension (i.e. depth), however they have not been attempted during this project. The realisation that magnetic anomalies have a form in the frequency domain (as well as the space domain) provides a way of quantitatively characterising the magnetic anomaly patterns of a given area. The principal means for displaying magnetic data in the frequency domain implements power spectra, whereby the frequency distribution (expressed in cycles per kilometre) is plotted against power (or radial energy). Power spectra quantify the intensity (i.e. amplitude) and wavelength of magnetic anomalies in a given area, and are independent of geometry and distribution of aeromagnetic anomalies. Many workers have used a method developed by Spector (1968) and Spector & Grant (1970) using power spectra to estimate depths to anomaly sources. Such calculations have little or no geological meaning, and rely heavily on assumed source geometries which can result in errors of ±50% (Gunn, 1997). In an attempt to dispel the widespread use of the method, Spector & Grant (1975) and Spector (1985) have published disclaimers recommending that it not be used for quantitative depth estimations (Gunn, 1997). Power spectra have been used in this study to in order to quantify the obvious visual differences between the subdomains in the western Gawler Craton.

2.4.5 Geographical Information Systems

Modern Geographical Information Systems (GIS) have revolutionised the visualisation, superposition and production of maps and geographical data. Effectively, GIS software integrates graphical data (e.g. maps, images) with spatial data (e.g. point data, demographic data) within a geographical reference frame. In Earth science, GIS software has enabled the precise superposition of many layers of relevant data, the ability to perform advanced multi-layer searches, and the production of high quality thematic maps containing different combinations of data layers. Global Positioning Systems (GPS) have revolutionised fieldwork in poorly exposed, geographically featureless terranes. They enable easy, fast, accurate navigation to outcrop sites which would otherwise be extremely difficult to find, and facilitate the fast, accurate input of geological point data into GIS software. All maps in this thesis have been generated using MapInfo™ and MapPublisher™ GIS software, integrated with Adobe Illustrator™, Macromedia Freehand™ and GeoBaseMap™ on a Power Macintosh 7200 computer.

As part of the SAEI, MESA generated large digital geological databases (e.g. SA_DISPLAY)

comprising many layers of geological information such as geological maps, aeromagnetic images, drill hole data, geochemical data and cultural features. These databases are incorporated into Geographical Information Systems such as MapInfo™ and ArcView™.

Chapter 3
INTERPRETIVE GEOLOGY OF THE WESTERN GAWLER CRATON

3.1 Introduction

Less than 1% of Precambrian basement in the western Gawler Craton outcrops, and as a result it has remained very poorly understood. The recent acquisition of high resolution aeromagnetic data over most of the area provides a powerful tool for understanding the geology of this little-known terrane. Aeromagnetic images of the Gawler Craton show a spectacular, complex array of anomalies of heterogeneous geometry, wavelength and amplitude. The most striking feature of the data is the distinct grouping of anomalies into areas of similar magnetic character, which are bound and dissected by an extensive network of narrow, linear anomalies. Areas of similar magnetic character have been classified as subdomains (e.g. Thomson, 1980; Parker, 1990a, 1990b, 1993). The narrow, linear anomalies which juxtapose the subdomains are caused by a series of major, craton-scale shear zones. The new geophysical data has facilitated the refinement of exisiting subdomain boundaries and the definition of several "new" subdomains in the Gawler Craton. Naturally the contrasting magnetic signatures of the subdomains directly reflects their different geological characteristics.

In this chapter, the methods outlined in Chapter 2 for understanding poorly exposed terranes are applied to the western Gawler Craton. The Gawler Craton aeromagnetic dataset is summarised in Section 3.2. Section 3.3 outlines the geophysical rationale behind the subdomain definitions, resulting in the construction of a new tectonic map of the Gawler Craton. Sections 3.4-3.9 describe the aeromagnetic interpretation of the five subdomains and the major shear zones spanned by the study area in the western Gawler Craton, resulting in the construction of a detailed interpretive geological map (Figure I1 at rear of thesis). This map is used as a basis for understanding the tectonothermal evolution of the western Gawler Craton in Part 2 of this thesis.

3.2 The Gawler Craton aeromagnetic dataset

Most of the high resolution aeromagnetic data for the Gawler Craton used in this study was acquired in 1993 by Mines and Energy, South Australia (MESA), under the South Australian Exploration Initiative (SAEI). Flight line spacing was 400m, at a height of ~80m. Data processing and gridding was carried out by MESA using the Intrepid™ software package. This data has been merged with various company datasets and older MESA datasets to produce both 100m and 200m gridded datafiles for the entire Gawler Craton. The 100m dataset incorporates only the 400m SAEI data and some high resolution company data, and provides high quality, high resolution data for these areas at scales up to ~1:100,000 (see Figure 3.4). The 200m dataset is a composite of all magnetic data in the state (including the 1987/88, 1km flight line spacing BMR data), and provides regional information at scales up to ~1:250,000 (see Figure 3.1). Gridded datasets from MESA have been processed using ERMapper™ 5.2 image processing software at the Department of Geology and Geophysics, University of Adelaide. The filters, colour lookup tables and histogram stretches described in Chapter 2 have been used selectively to highlight relevant geological features (see Figures 3.1, 3.2, 3.4 & 3.5). Figure 2.2 (in previous chapter) illustrates the effects of different image processing algorithms on high resolution aeromagnetic data from the western Gawler Craton.

3.3 Geophysical framework of the Gawler Craton

The availability of improved geophysical and geological data, combined with the recognition that the Gawler Craton does not have a well defined northwestern boundary (see Chapter 1), has facilitated the construction of a new map showing the tectonic framework of the Gawler Craton and its neighbouring terranes (see Figure 3.3). This map shows that the Gawler Craton comprises a collage of at least 14 subdomains of contrasting geophysical (hence geological) character which are mainly bound by craton-scale shear zones. The boundaries of the Nawa, Christie, Wilgena, Nuyts, Coulta, Cleve and Moonta Subdomains, as well as the Gawler Range Volcanics and the Stuart Shelf have been refined from those of Thomson (1980) and Parker (1990a, 1990b, 1993) using the new aeromagnetic data. The definition of the "new" Fowler, Coober Pedy and Lincoln Subdomains is based on their unique geological and geophysical characteristics which contrast markedly with those in the adjacent subdomains. This study has focussed on an area in the western Gawler Craton which

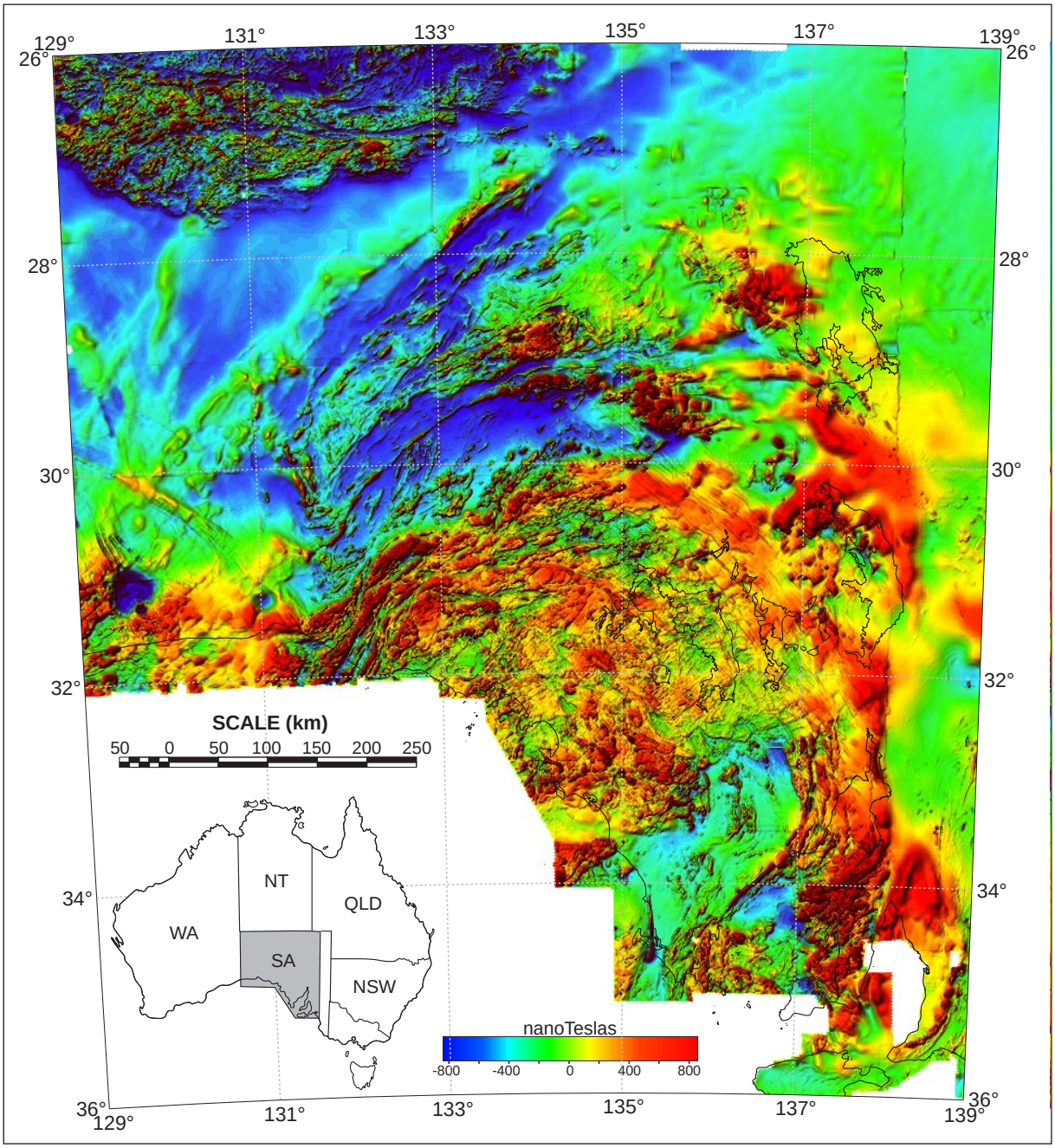

Figure 3.1a Total magnetic intensity image of the Gawler Craton and neighbouring terranes, illuminated from the northwest (MESA data).

includes the southern parts of the Nawa and Christie Subdomains, the Fowler Subdomain and the western parts of the Wilgena and Nuyts Subdomains (see Figure 3.6). The main distinguishing characteristics of each subdomain in the Gawler Craton are summarised below:

- The Moonta Subdomain is dominated by large, irregularly shaped, high magnetic intensity anomalies which exhibit a minor, north-south linear trend component and a high gravimetric signature (see Figure 3.2). The high magnetic signature is caused by voluminous, ~1.72 Ga, syn-Kimban Orogeny volcanics, intrusives and sediments and ~1.59 Ga, anorogenic Hiltaba Suite granitoids. It is separated from the Lincoln Subdomain by a major, north-south trending, linear pattern break (interpreted to be a shear zone which is stitched by Hiltaba Suite plutons), and is bound to the east by the Torrens Hinge Zone.

- The Lincoln Subdomain (*new*) is dominated by large, irregularly shaped, moderate magnetic intensity, dense bodies of the ~1.85Ga, mid-lower crustal Lincoln Batholith (B. Schaefer pers. comm., 1997). It is separated from the Cleve Subdomain by the ~1.7 Ga Kalinjala Mylonite Zone; a series of major linear magnetic anomalies which is the locus of the transpressional Kimban Orogen.

- The Cleve Subdomain is dominated by a broad spectrum of linear magnetic anomalies which

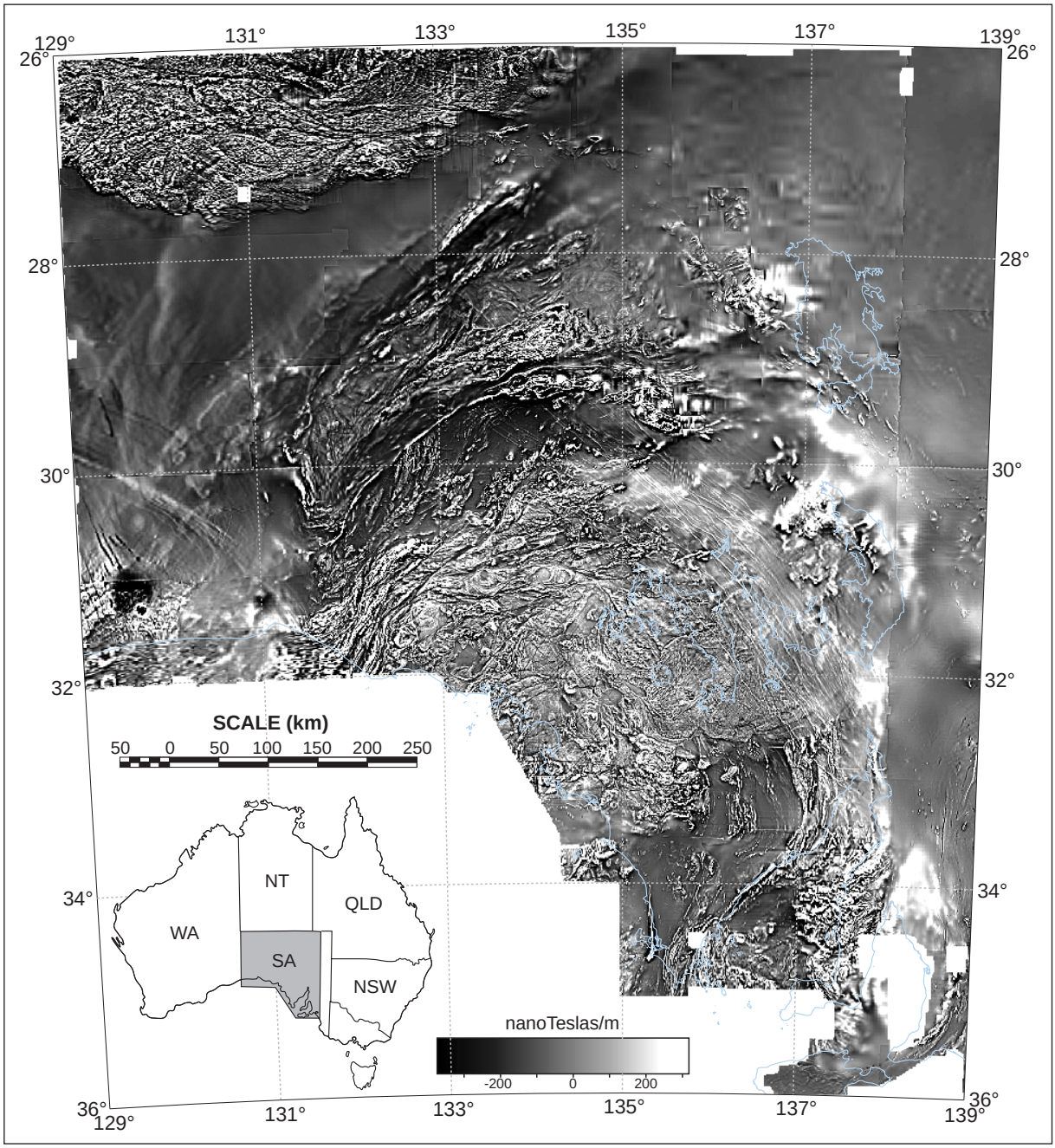

Figure 3.1b Greyscale first vertical derivative image of the total magnetic intensity of the Gawler Craton and neighbouring terranes (MESA data).

represent deformed, ~1.9-1.85 Ga Hutchison Group metasediments and >2.45 Ga, high grade Sleaford Complex supracrustals. It forms a major mobile belt which operated during the ~1.8-1.7Ga Kimban Orogeny. It is separated from the Coulta Subdomain by a major, ~northeast-trending, linear pattern break interpreted to be a major shear zone.

- The Coulta Subdomain is dominated by weakly magnetised, high level intrusives and supracrustals of the ~2.6-2.5 Ga Sleaford Complex and Dutton Suite. It exhibits localised magnetic trends which parallel those in the neighbouring Cleve Subdomain, hence is interpreted to have been reworked during the Kimban Orogeny. It is separated from the Nuyts Subdomain by a major pattern break interpreted to be a shear zone (which is stitched by ~1.59 Ga Hiltaba Suite plutons).

- The voluminous, ~1.59 Ga Gawler Range Volcanics form a large, moderate magnetic intensity, strongly textured area which masks the northern margins of the Moonta, Lincoln, Cleve, Coulta Subdomains and the eastern margin of the Nuyts Subdomain. A broad wavelength gravimetric high underlies the Gawler Range Volcanics (see Figure 3.2).

- The Stuart Shelf is dominated by long wavelength magnetic anomalies due to its thick Meso-Neoproterozoic sedimentary cover. The geology is thought to be dominated by ~1.59 Ga

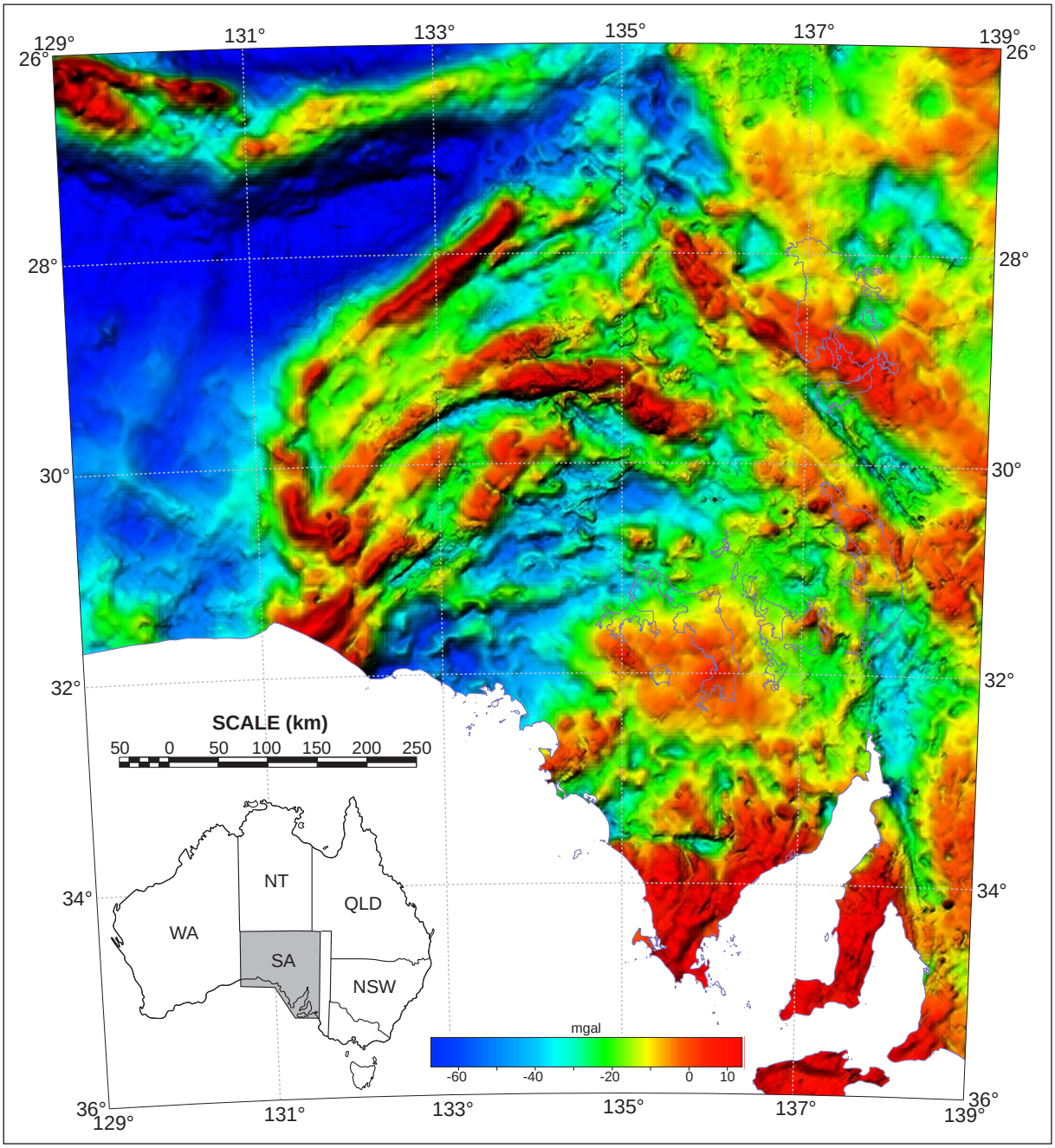

Figure 3.2 Bouger gravity image of the Gawler Craton and neighbouring terranes, with northeasterly illumination (MESA data).

Hiltaba Suite plutons which host the massive Olympic Dam Cu-Au-Ag-U-REE ore deposit. Importantly, it may be a continuation of the Wilgena Subdomain since no obvious structural discontinuity exists between them.

- The Nuyts Subdomain is dominated by large, elliptical anomalies caused by a series of Mesoproterozoic, high level plutons (see §3.8 and Chapter 7) which often exhibit coincident gravimetric lows (see Figure 3.2). It forms a large crustal block over 50,000km^2 in size which is bound to the west by the Coorabie Shear Zone, to the north by the Yerda Shear Zone, and to the south by the coastline and the Coulta Subdomain. The eastern boundary of the Nuyts Subdomain is obscured by the Gawler Range Volcanics.

- The Wilgena Subdomain has a complex magnetic signature dominated by short wavelength, high magnetic intensity anomalies (caused by low grade, localised jaspilites) and large elliptical anomalies (caused by ~1.59 Ga Hiltaba Suite plutons) which punctuate a low magnetic intensity basement comprising various ~2.5-2.6 Ga Archaean supracrustals (see §3.7 and Chapter 7). It forms a westward-narrowing wedge over 300km wide and 100km long, which is truncated to the north and west by the Coorabie Shear Zone, to the south by the Yerda Shear Zone, and obscured to the east by the Stuart Shelf.

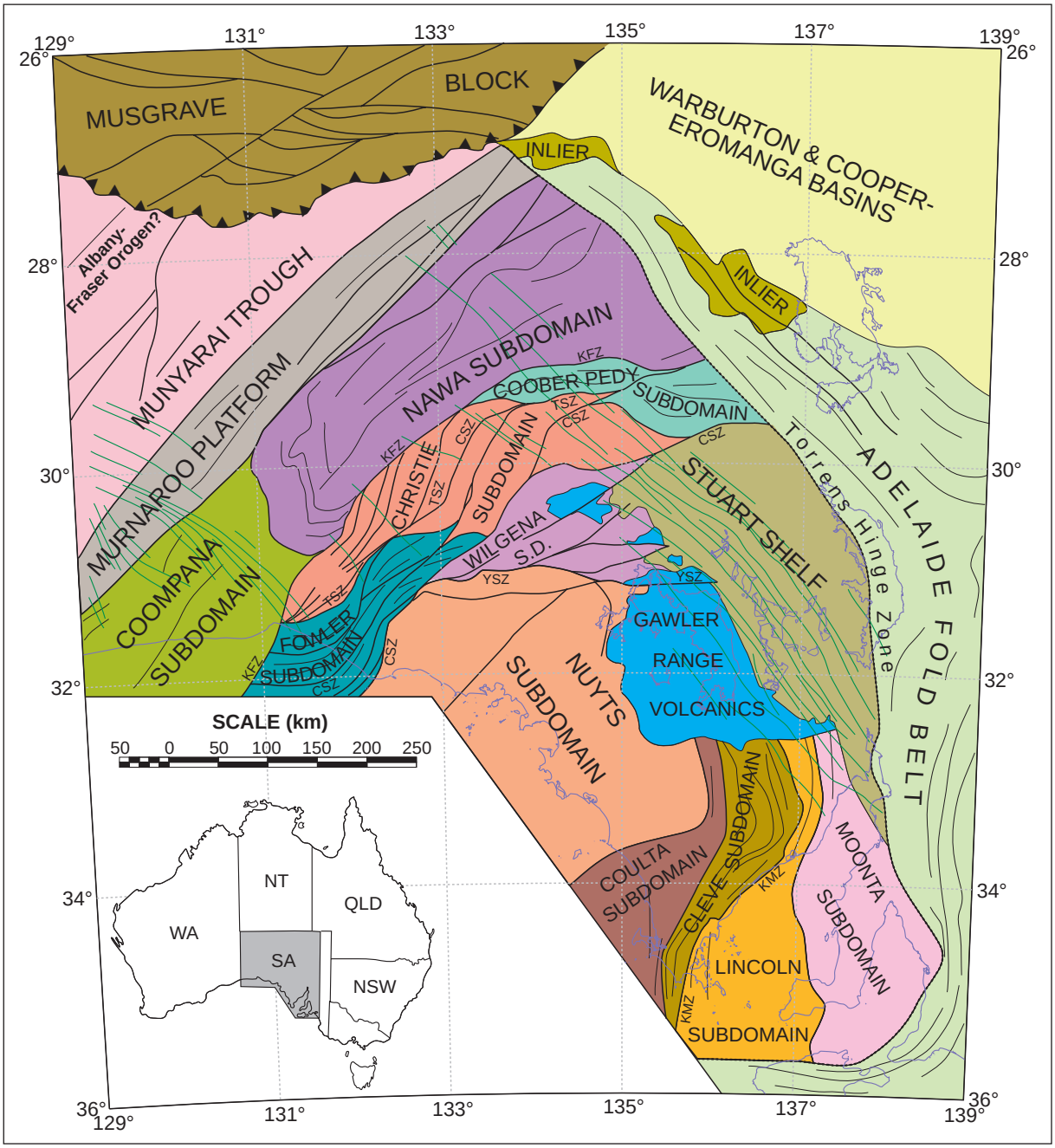

Figure 3.3 Revised tectonic framework of the Gawler Craton, with some subdomain boundaries modified from Parker (1990a, 1990b). Some major shear zones are labelled: KFZ=Karari Fault Zone, TSZ=Tallacootra Shear Zone, CSZ=Coorabie Shear Zone, YSZ=Yerda Shear Zone, and KMZ=Kalinjala Mylonite Zone. Readers are encouraged to use the transperant overlaysof geophysical images (in back pocket) in conjunction with this map. See also Figure 8.1 for a more detailed map of the shear zone systems in the western Gawler Craton.

- The Fowler Subdomain (*new*) forms a distinctive, northeast-trending, sinuous belt of elongate, high magnetic intensity anomalies dissected by numerous, anastamosing shear zones. It is bound to the east by the Coorabie Shear Zone, and to the north and west by several major shear zones, notably the Tallacootra Shear Zone and the Karari Fault Zone. The subdomain extends for over 300km at widths of up to 100km. The anastamosing magnetic highs are caused by a complex sequence of ~1.7-1.49 Ga lower crustal igneous and metamorphic rocks and are paralleled by ~20-40mgal gravimetric highs (see Figure 3.2, §3.6 and Chapter 6). The Fowler Subdomain has previously previously been termed the Fowler Suture Zone (e.g. Daly et al., 1995), and the Fowler Orogenic Belt (Daly et al., in press).

- The Christie Subdomain is dominated by large areas of low magnetic intensity (caused by ~2.5-2.4 Ga Mulgathing Complex granulites) punctuated by irregular high intensity anomalies (caused by ~1.67 Ga Ifould Complex intrusives) (see §3.5 and Chapter 5). It forms a vast sigmoidal arc that stretches over 500km from the Nullarbor coast in the southwest to the Coober Pedy Subdomain in the northeast at widths of 50-100km. It is bound to the east by various major shear zones

(principally the Coorabie and Tallacootra Shear Zones), and to the west by the Karari Fault Zone.

• The Coober Pedy Subdomain (*new*) is dominated by very high magnetic intensity, sinuous magnetic highs caused by ~1.7-1.55 Ga, iron-rich, metasedimentary granulites. It is bound by the northern parts of the Karari Fault Zone and the Tallacootra Shear Zone.

• The Nawa Subdomain forms a vast crustal block with a complex magnetic signature. It is bound to the northwest by the Murnaroo Platform and to the southeast by the Karari Fault Zone (see §3.3 and Chapter 4). It forms a seemingly intact crustal block (i.e. it is not dissected by major shear zones) over 60,000km^2 in size which extends northeast to the Torrens Hinge Zone. The southwestern boundary of the Nawa Subdomain is interpreted to be a curvilinear shear zone which separates it from the Coompana Subdomain.

• The Coompana Subdomain (originally defined as the *Coompana Block* by Thomson, 1980 and Parker, 1990a) is dominated by complex, heterogeneous magnetic anomalies and dissected by numerous, high magnetic intensity, NW trending mafic dykes. It is bound to the east by the Karari Fault Zone and to the west by a major, northeast trending shear zone which juxtaposes it with the Murnaroo Platform. Geochronological data from a granodiorite gneiss intersected by the Mallabie 1 drill hole yielded K-Ar biotite/hornblende and U-Pb zircon ages of ~1150-1200 Ma (Flint & Daly, 1993; S. Daly pers. comm., 1997).

• The Murnaroo Platform forms a narrow, northeast trending belt dominated by long wavelength magnetic highs which parallel its bounding shear zones. It is deeply buried beneath Officer Basin sediments (~0.5-2km), and is bound to the east and west by craton-scale, northeast trending shear zones.

• Deeply covered basement northwest of the Murnaroo Platform beneath the Munyarai Trough of the Officer Basin may also be considered part of the Gawler Craton. Its magnetic signature contrasts with that of the Murnaroo Platform; it only exhibits very low magnetic intensity, long wavelengh, northeast trending anomalies. It is juxtaposed with basement of the Murnaroo Platform by a major, northeast-trending pattern break interpreted to be a shear zone, and is truncated to the north by the Musgrave Block. Basement beneath the Munyarai Trough probably extends west to the Albany-Fraser Orogen, and may in fact represent the easternmost parts of the Albany Fraser Orogen (see Chapter 9).

3.4 Interpretive geology of the southern Nawa Subdomain

This study has focussed on the southern parts of the Nawa Subdomain, which are blanketed by Tertiary karst sediments of the Nullarbor Plain, Palaeozoic Officer Basin sediments and vegetated Quaternary sand dunes of the Great Victoria Desert. No basement outcrop occurs, and all information is taken from drill core and geophysical data. Only a small number of basement drill hole intersections exist in the Nawa Subdomain due to its thick sedimentary carapace, its very remote and inaccessible nature, and the radioactive contamination caused by massive nuclear bomb testing at Maralinga during the 1950's and 1960's.

Aeromagnetic data for the southern Nawa Subdomain features a series of narrow (0.1-1km), parallel, linear, high magnetic intensity anomalies which form an arcuate, roughly northwest-trending belt of high average magnetic intensity. Weakly magnetised crust southwest of this belt exhibits weak linear trends which parallel the strongly magnetised linear anomalies, indicating that they share a common structural history. The parallel, strongly and weakly magnetised belts combine to define a ~50km wide, ~120km long, ~northwest trending mobile belt which transects the southern Nawa Subdomain (the "Moondrah mobile belt" - see Figure 8.1). This belt is truncated to the east by the Karari Fault Zone, and to the west by a northeast-trending shear zone which juxtaposes it with the Murnaroo Platform. Importantly, the Moondrah mobile belt is paralleled by a coincident, >20mgal gravimetric high. The northwesterly trend of this mobile belt contrasts markedly with the dominantly northeasterly structural grain of the rest of the Nawa Subdomain, and also the other studied subdomains.

The linear magnetic highs which dominate the southern Nawa Subdomain are clearly caused by strongly magnetised, iron-rich gneiss (the Moondrah Gneiss) intersected in several drill holes, notably Ooldea DDH2. The strongly magnetised gneisses contain 2-60% magnetite associated with ultrahigh temperature metamorphic assemblages which grew prior to and during fabric develpment. The petrography and tectonothermal evolution of these unusual rocks is discussed in Chapter 4. This intensely deformed series of strongly magnetised (5000-15000x10^{-5} S.I.), mylonitic gneisses form meso- to macroscopic layers in a sequence dominated by weakly magnetised, mylonitic felsic gneisses. All gneisses exhibit a steep to subvertical high strain fabric (which is presumably compressional), as evidenced by the symmetric nature of the linear magnetic anomalies and structural observations of drill core.

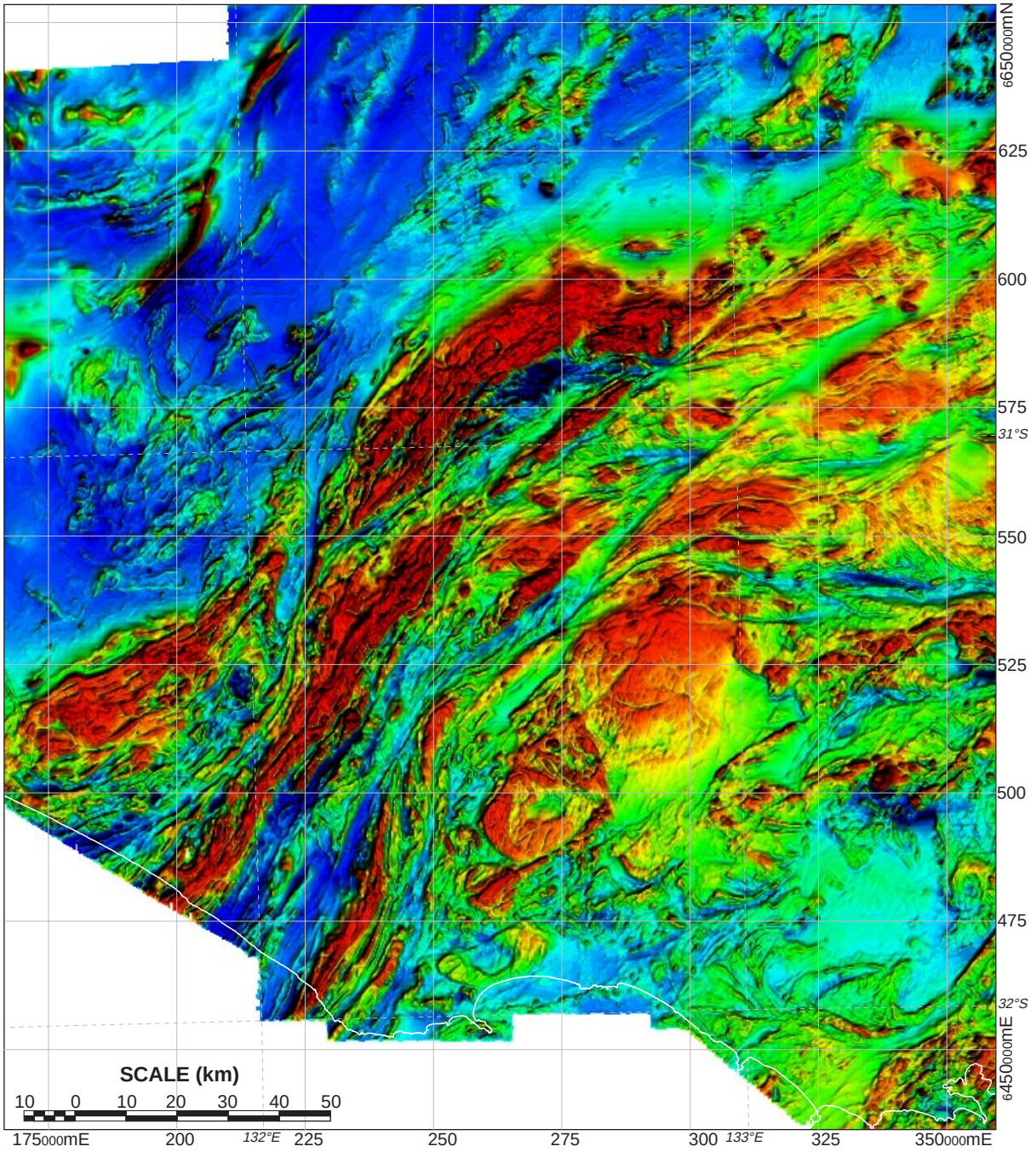

Figure 3.4a Total magnetic intensity image of the study area in the western Gawler Craton, illuminated from the northwest (MESA data).

Irregularly shaped, moderate magnetic intensity anomalies south of Ooldea are tentatively interpreted as post-kinematic intrusives since they appear to crosscut the regional magnetic fabric. No drillholes have intersected these bodies.

3.5 Interpretive geology of the Christie Subdomain

The magnetic signature of the Christie Subdomain is dominated by large areas of low magnetic intensity and minimal magnetic contrast (5300-5500nT) punctuated by numerous large (10-40km), irregularly shaped, complex, high magnetic intensity anomalies (~6300-7000nT). Craton-scale linear anomalies corresponding to major shear zones crosscut and bound the Christie Subdomain (see §3.9).

The low magnetic intensity, low contrast areas can be directly correlated with high grade gneisses of the Mulgathing Complex, which encompasses all Archaean to early Palaeoproterozoic rocks in the northwestern Gawler Craton (Daly et al., 1979). Very weak linear magnetic trends in the Mulgathing Complex can be traced in only strongly enhanced images (however at this level of enhancement the data are often too noisy to be very useful), which

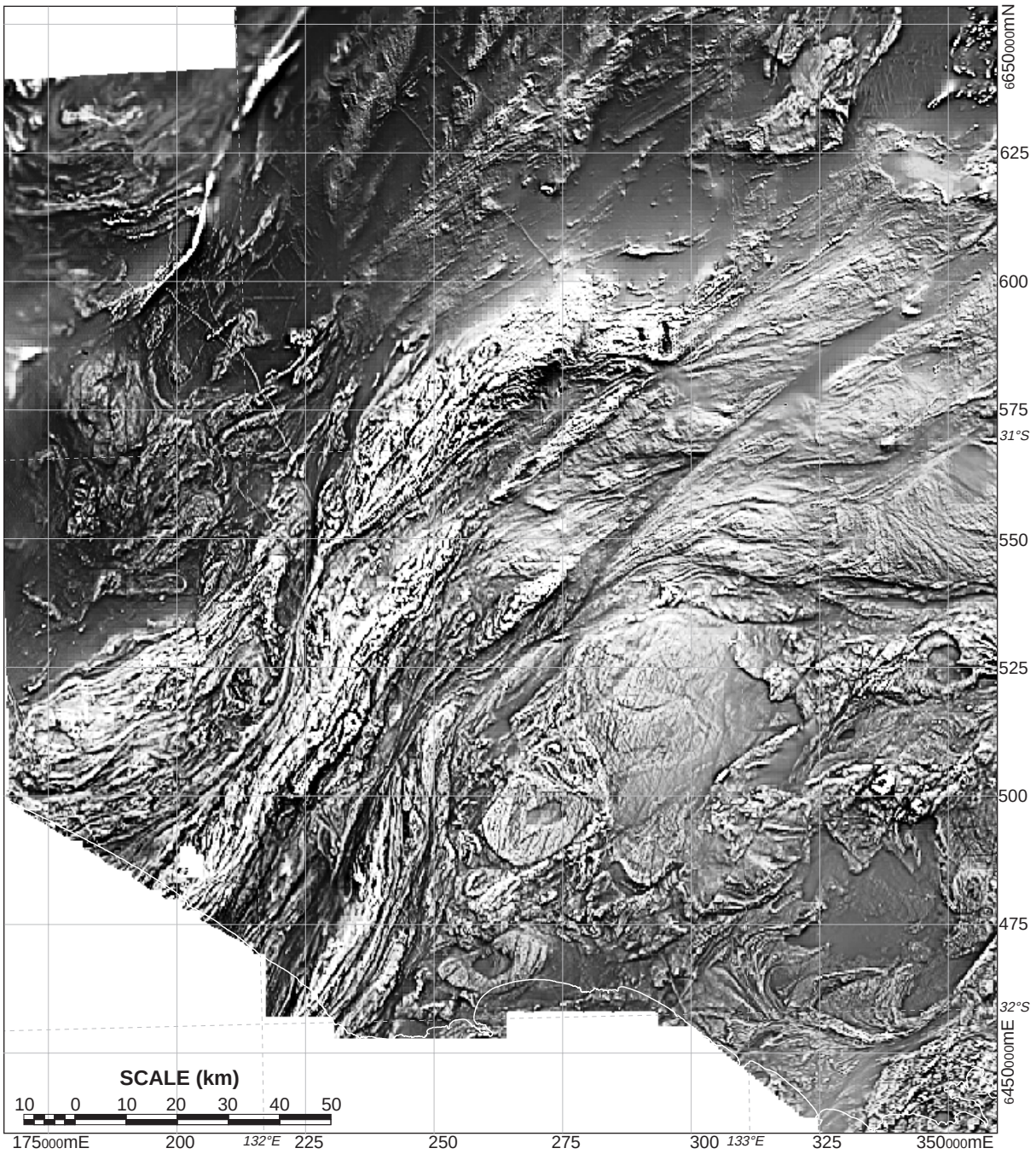

Figure 3.4b Greyscale first vertical derivative of the total magnetic intensity of the study area in the western Gawler Craton (MESA data).

are interpreted to reflect the surface projection of subtle S_0/SS_1, complexly folded and transposed lithological heterogeneities. In the Christie Subdomain, the most dominant Archaean unit is the Christie Gneiss, comprising various interlayered, high grade, metasedimentary lithologies. The Christie Gneiss is dominated by medium-coarse grained, layered, weakly foliated, migmatitic garnet-cordierite-biotite±sillimanite pelitic gneiss, which is interlayered with felsic gneiss, semi-pelitic garnet-biotite gneiss, calc-silicate, mafic gneiss and locally with banded iron formation (notably in the Mount Christie area). The compositional layering is isoclinally folded and transposed into an early foliation that has been variably overprinted by a weak-moderate foliation which parallels the axial surface of a series of open-tight folds (see Chapter 5). All lithologies are intruded by abundant pre- and post-kinematic leucosomes and pegmatites, and are weakly to intensely overprinted by a northeast-trending, retrograde foliation associated with regional reworking, especially in proximity to the major shear zones. Even though the Christie Gneiss is dominated by relatively iron-rich lithologies (metapelites and mafics) it is only very weakly magnetised and generally exhibits very low magnetic susceptibilities (0-50x10^{-5}S.I.), with the exception of the banded iron formations (up to 7000x10^{-5}S.I.). Iron is partitioned as Fe^{2+} into paramagnetic silicates such as garnet, cordierite

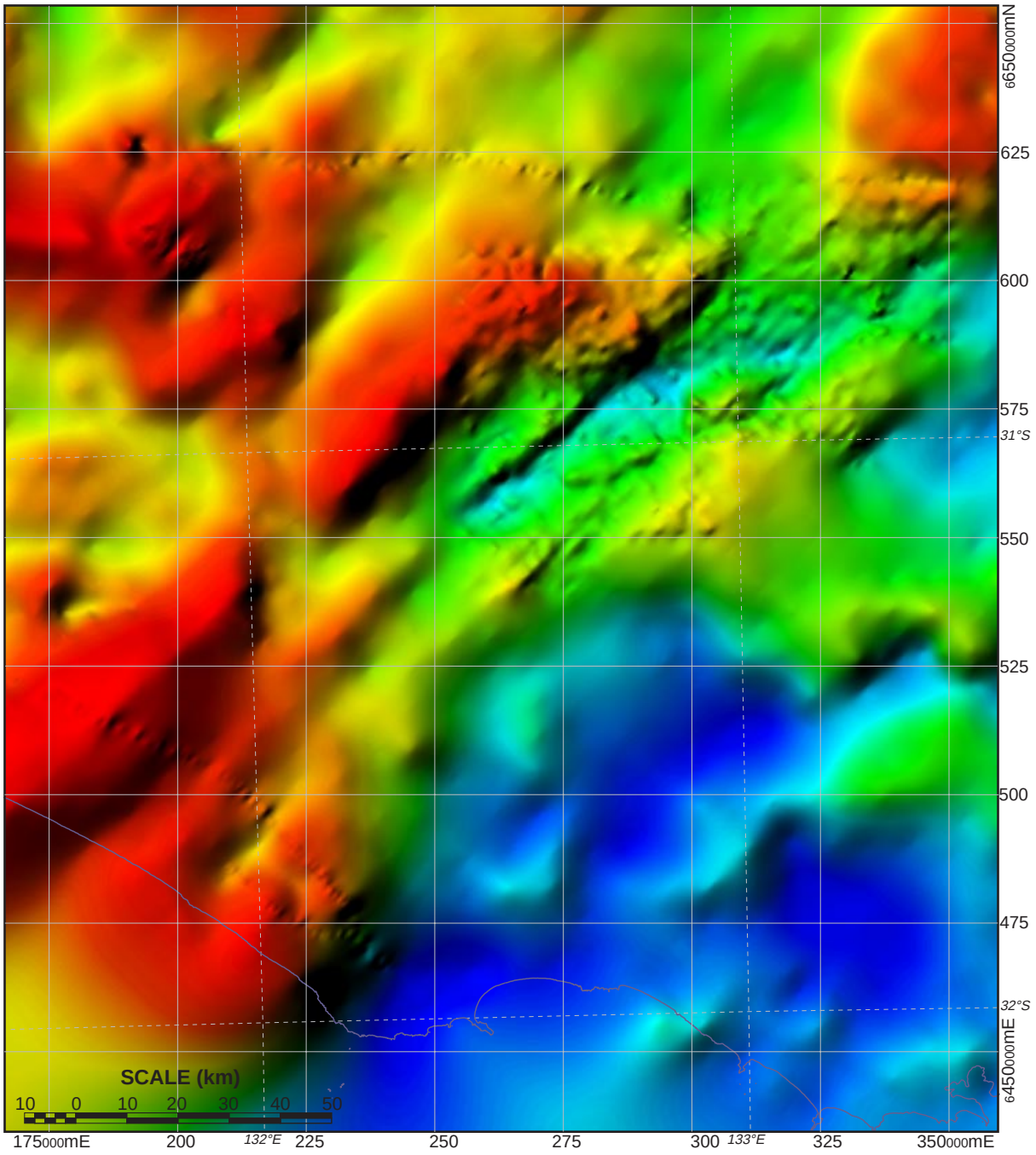

Figure 3.5 Bouger gravity image of the study area in the western Gawler Craton illuminated from the northeast (MESA data).

and pyroxene, suggesting very low fO_2 conditions at least during granulite facies metamorphism (verified by the absence of magnetite). Low-fO_2 conditions in metasedimentary rocks are thought to be inherited from the original sediments (McIntyre, 1980; Grant, 1985; Denham, 1997). The Mount Christie area is characterised by numerous narrow (<1km wide), elongate, complexly folded magnetic highs (>15000nT) which can be directly correlated with outcropping-subcropping iron formation on topographic highs. The continuation of these trends beneath the shallow cover material can also be traced, and the axial traces of at least two fold generations can be inferred (e.g. the Mulgathing Antiform - Daly & Fanning, 1993).

The irregulary shaped, complex, moderate to high magnetic intensity anomalies which punctuate the magnetically nondescript Mulgathing Complex can be directly correlated with lithologically heterogeneous, intrusives of the Ifould Complex (new name - see Chapter 5) and are interpreted to be the surficial expression of large (~3-30km), deformed plutons. The Ifould Complex encompasses all late Palaeoproterozoic (1700-1670 Ma), I-type plutonic rocks in the Christie Subdomain (see Chapter 5). The Ifould Complex is lithologically heterogeneous, ranging in composition from granite and granodiorite, through to diorite and gabbro, exhibiting a range of magnetic susceptibilities from

~400x10^{-5}S.I. to over 1000x10^{-5}S.I. (in the mafics). Outcrop to map-scale, complex igneous mixing relationships indicate that this lithologically diverse suite was comagmatic, with pluton-scale heterogeneities and zoning resulting in the observed complex and irregular magnetic anomaly patterns of the plutons (see Chapter 5). Although the margins of the Ifould Complex intrusives are often well defined, narrow offshoots of igneous material into the Mulgathing Complex are also inferred from the magnetic data (an observation consistent with the field observations discussed in Chapter 5). Strongly magnetised granitoids such as the Ifould Complex have been termed "magnetite-series" by Ishihara (1977), and can be correlated with relatively oxidised, I-type intrusives (in contrast with the "ilmenite-series", S-type intrusives). The abundance of disseminated magnetite and potentially Fe^{3+}-rich phases such as epidote, biotite and hornblende in the Ifould Complex indicate highly oxidised magmatic conditions.

Other observations in the Christie Subdomain pertinent to the interpretive geological map (Figure I1) include:

- Several large, elliptical, low magnetic intensity anomalies are also interpreted to represent Ifould Complex plutons, as verified by geochronological data from weakly magnetised granites south of Barton Siding (see §6.5).
- Both the Mulgathing Complex and Ifould Complex have been extensively elongated and disrupted during deformation associated with at least two generations of major shear zones (see §3.7).
- Two large (20-40km), circular, moderate to high magnetic intensity anomalies in the southwestern Christie Subdomain are interpreted to be late plutons. They crosscut (i.e. stitch) several major shear zones (notably the Tallacootra Shear Zone), and contain complex magnetic patterns characteristic of composite igneous bodies. Drilling reports indicate that these plutons are composed of granitoids, however the core could not be found to verify these observations. These granitoids are an important potential geochronology target.
- The structurally youngest magnetic feature observed in the Christie Subdomain are a series of parallel, northwest-trending, narrow (<400m) linear highs which can be directly correlated with the ~800 Ma Gairdner Dyke Swarm.

Power spectra for the Christie Subdomain directly reflect the dominance of the low magnetic intensity (i.e. low radial energy) areas, and have a distinctive "concave" shape, particularly at low frequencies (see Figure 3.7). Power spectra for areas dominated by the short wavelength magnetic highs (banded iron formations) show a distinct "convex" spectrum which is significantly different to those of magnetically quiescent areas, indicating that in the frequency domain, the short wavelength magnetic highs have a broad freqency response (which is somewhat counter-intuitive given their apparently short wavelength, high frequency form in the space domain). The power spectra for areas of the Christie Subdomain dominated by Ifould Complex intrusives show markedly higher power (i.e. intensity) over a broad range of frequencies which directly reflects the heterogeneous visual anomaly pattern in the space domain.

3.6 Interpretive geology of the Fowler Subdomain

The magnetic signature of the Fowler Subdomain is dominated by numerous complex, high magnetic intensity domains dissected by at least two generations of anastamosing shear zones (represented by narrow, linear magnetic lows). Power spectra for the Fowler Subdomain show a very high average power (i.e. intensity) over a broad frequency range, reflecting the broad distribution of high intensity anomalies of different wavelengths (notably the narrow, short wavelength anomalies) (see Figure 3.8).

This study has identified four major crustal blocks within the Fowler Subdomain (the Nundroo, Central, Colona and Barton Blocks), each bound by the major shear zones (see Figure 3.6). Although the four blocks exhibit similar geophysical signatures, their geological characteristics (especially metamorphic grade) differ considerably (see Chapter 6). The Nundroo, Barton and Colona Blocks all form distinctive, northeast trending magnetic and gravimetric highs. Westward offset of long wavelength magnetic and gravimetric highs with respect to the interpreted surface geology suggests that the crustal blocks in the Fowler Subdomain dip at moderate angles to the west. They have broad similarities with long wavelenth potential field anomalies in the neighbouring Christie Subdomain, suggesting that similar, dense, strongly magnetised crustal blocks may reside at mid-crustal levels beneath the current exposure level in the Christie Subdomain. The gravimetric highs are clearly bound by the major, northeast trending shear zones which dominate the geology of the western Gawler Craton (see §3.9 and Chapter 8).

The complex magnetic anomalies in the Fowler Subdomain have been ascribed to four litho-magnetic associations via careful correlation between lithological observations (see Chapter 6), magnetic petrology, magnetic susceptibility measurements and aeromagnetic data. It is important to note that these lithological associations

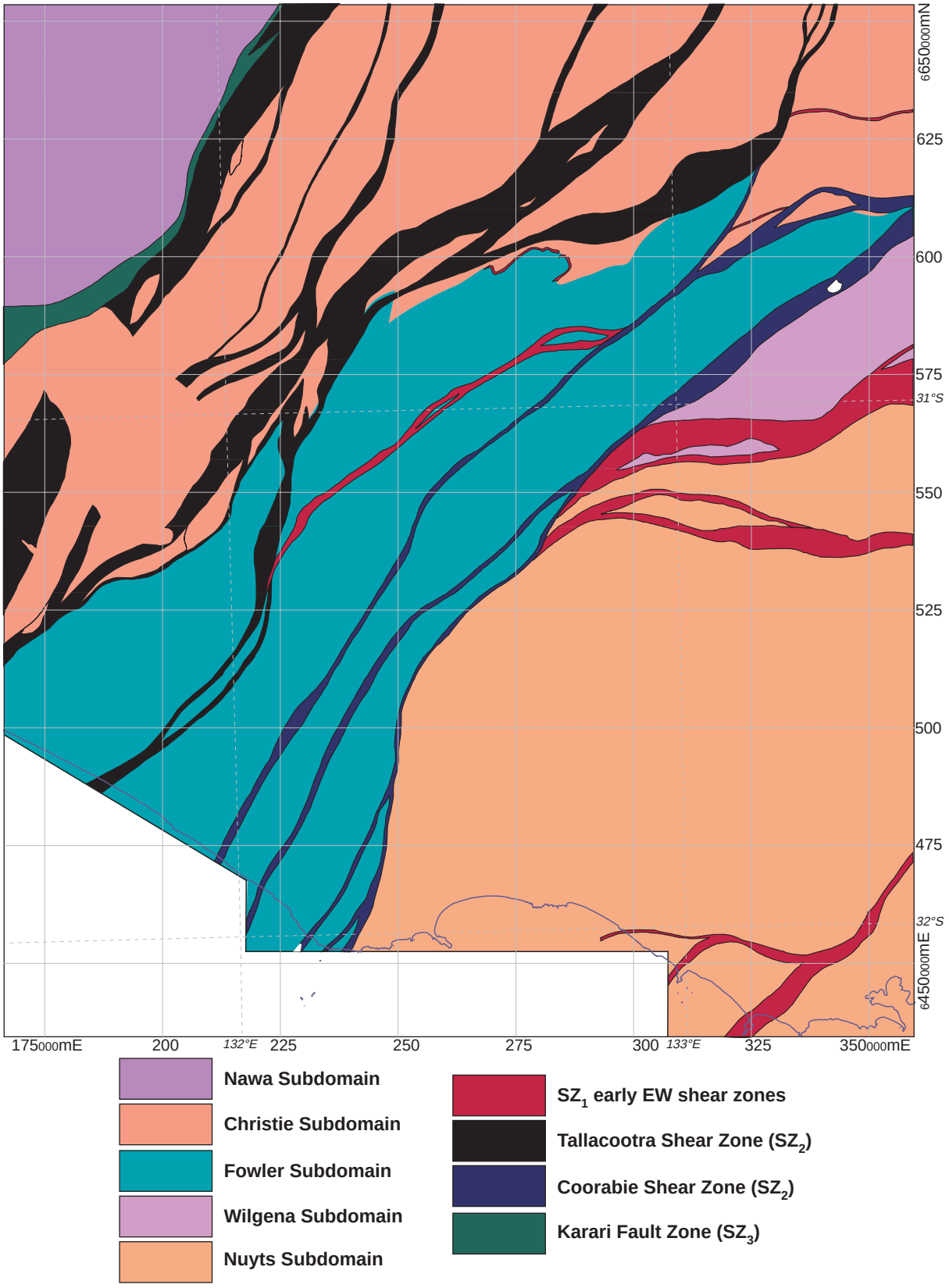

Figure 3.6 Subdomains and late "framework" shear zones in the western Gawler Craton. The reader is encouraged to use the transperant overlays of geophysical images (in back pocket) in conjunction with this map.

are defined to describe the *dominant* lithologies in a particular area, thus lithological components from other associations may still be present in varying amounts. The distribution and nature of lithologies in the Fowler Subdomain are discussed in Chapter 6.

Association 1: A high to very high magnetic intensity association dominated by strongly magnetised, weakly deformed, magnetite-rich mafic to intermediate intrusives (gabbro, diorite and tonalite) and granulite facies equivalents. The

magnetic signature is characterised by nebulous, rounded trend patterns which exhibit only weak linear trend components. The high magnetic susceptibility of these units is caused by: (i) disseminated primary igneous magnetite in the gabbros (which in some cases causes strong remenant magnetisation - e.g. the intense negative anomaly in the eastern-central Barton Block), (ii) by fine (0.2-1mm), amoeboid magnetite grains in the granulites (often associated with pyrite and chalcopyrite) which comprise ~1-10vol% of the rock, and (iii) by very fine grained magnetite exsolution lamellae in primary igneous pyroxenes (a feature that can also cause remenant magnetisation).

Association 2: A moderate to high magnetic intensity association dominated by moderately-strongly magnetised, metasedimentary gneiss/schist and retrogressed, amphibolite facies mafic gneiss. The magnetic signature is characterised by a strong, linear structural grain (caused by transposed lithological heterogeneities) which clearly overprints the nebulous trends of Association 1. The amphibolites exhibit lower magnetic susceptibility than their granulite/gabbro precursors owing to the partial breakdown of magnetite to Fe^{3+}-bearing hornblende and/or biotite. The metasediments contain moderate amounts (0.1-5%) of disseminated magnetite, often as symplectic inclusions in garnet, and exhibit a lower average magnetic susceptibility than the Association 1 mafics.

Association 3: A low to moderate magnetic intensity association dominated by weakly-moderately magnetised, relativley felsic granitoids. The magnetic signature exhibits variable texture and structural grain, no doubt reflecting the complex lithological and strain heterogeneities observed in outcrop and drill core.

Association 4: A low magnetic intensity association of highly strained, very weakly magnetised mylonites and schists which define a set of anastamosing, narrow (50-500m wide), NNE-trending, linear shear zones which dissect the above litho-magnetic associations at scales of 5-20km. These shear zones are characterised by narrow, low magnetic intensity, linear anomalies which crosscut and juxtapose the above lithological associations. Strongly magnetised mafic and pelitic lithologies are demagnetised in these retrograde shear zones, since magnetite has broken down to Fe^{3+}-bearing paramagnetic silicates such as biotite and epidote.

Contacts between the high grade Association 1 and the retrograde Association 2 are gradational and irregular, no doubt reflecting the heterogeneous nature of retrograde fabric development observed in outcrop and drill core (see Chapter 6). Associations 1, 2 and 3 are clearly interlayered on a 0.5-10km scale. Many of the contacts between the litho-magnetic associations are parallel and have clearly been transposed during deformation. Contacts have been extensively disrupted by Association 4 retrograde shear zones.

The contrast in rock magnetisation between the strongly magnetised, high grade granulites/gabbros (Association 1) and the moderately magnetised, retrograde, amphibolite facies equivalents (Association 2) is a feature commonly observed in mafic rocks, and is readily explained by the retrograde breakdown of early magnetite to Fe^{3+}-bearing silicates such as hornblende and biotite (e.g. Grant, 1985; Olesen et al., 1991; Skilbrei et al., 1991; Toft et al., 1993; Denham, 1997). Further reductions in magnetic susceptibility in the weakly magnetised, late mylonites and schists (Association 4) are explained by further breakdown of magnetite and the partitioning of Fe^{3+} into hydrous Fe-Mg phases such as biotite and epidote. In highly retrogressed and altered samples (which have near-zero magnetic susceptibility), the presence of hematite (which is paramagnetic) in favour of magnetite is testament to high-fO_2 conditions probably caused by aqueous fluids (Denham, 1997). Demagnetisation by hydration of deep-crustal rocks is a feature commonly observed in modern continental collision zones, where hydrating fluids are presumably derived from a subducting slab (Toft et al., 1993).

3.7 Interpretive geology of the Wilgena Subdomain

The Wilgena Subdomain exhibits a complex array of magnetic signatures reflecting a prolonged and diverse geological history. The Wilgena Subdomain is peripheral to the study area, and only its easternmost parts are of relevance here. In this area, the magnetic signature is dominated by large, strongly textured, moderate magnetic intensity anomalies which can be directly correlated with a series of moderately magnetised, locally deformed, high level Palaeoproterozoic granitoids (e.g. the Symon's Granite - see Chapter 7). A few ovoid, higher magnetic intensity bodies are interpreted to be Hiltaba Suite plutons. Power spectra for the Wilgena Subdomain are varied, directly reflecting the observed heterogeneous anomaly patterns, and as a result are of little use in characterising the aeromagnetic data, especially in comparison with the other subdomains in the study area.

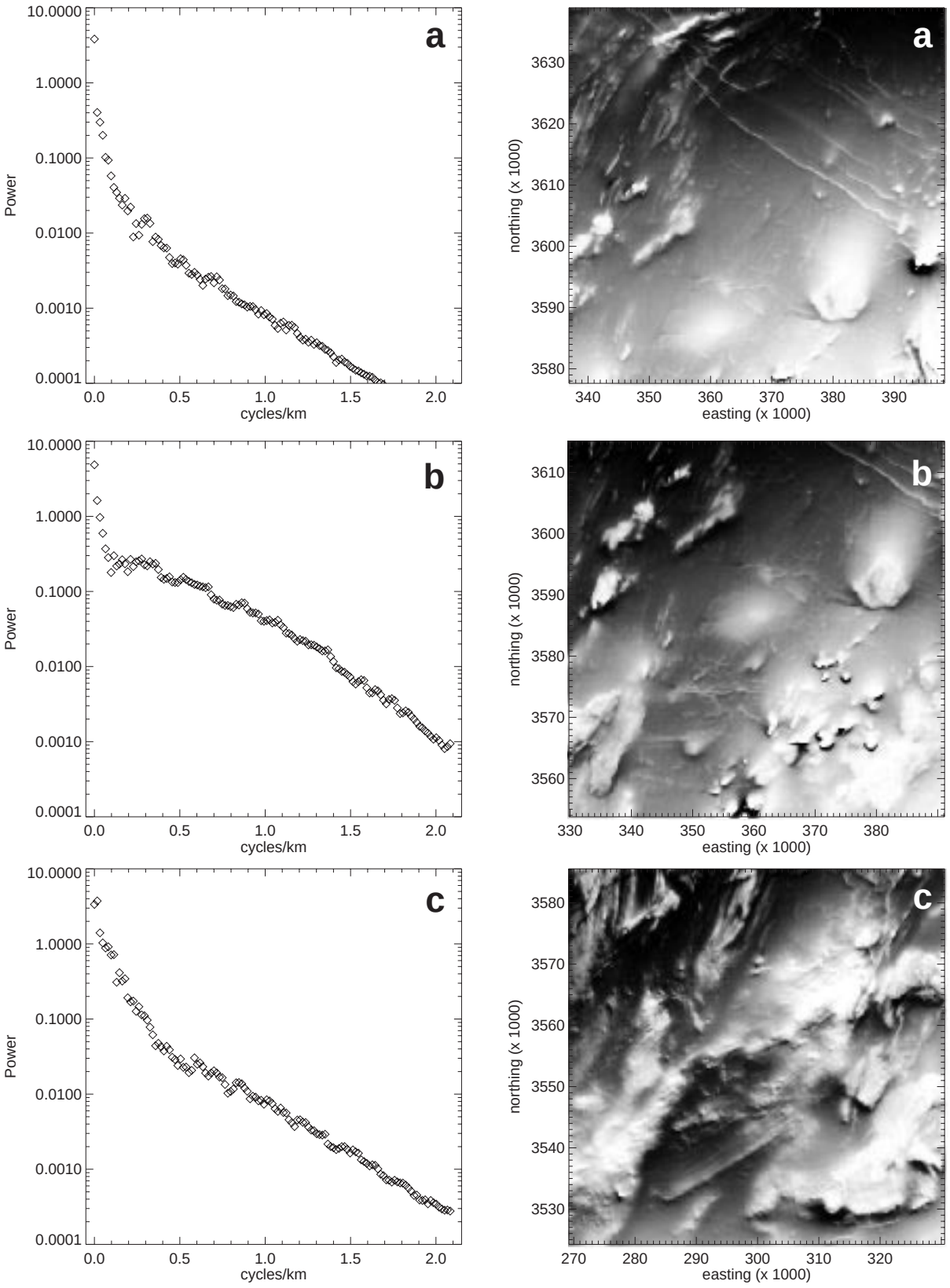

Figure 3.7 Power spectra for selected 60x60km areas in the Christie Subdomain, (a) Low magnetic intensity and contrast area dominated by Mulgathing Complex gneisses, showing low power at all frequencies and a bilinear geometry, (b) Low magnetic intensity Mulgathing Complex gneisses punctuated by short wavelength, high amplitude anomalies caused by narrow layers of banded iron formation, which significantly modifies the power spectrum across a broad range of frequencies giving it a distinctly convex geometry, (c) Low magnetic intensity, Mulgathing Complex gneisses which host moderate magnetic intensity, Ifould Complex plutons, which increase the average power across a broad range of frequencies while maintaining a bilinear geometry.

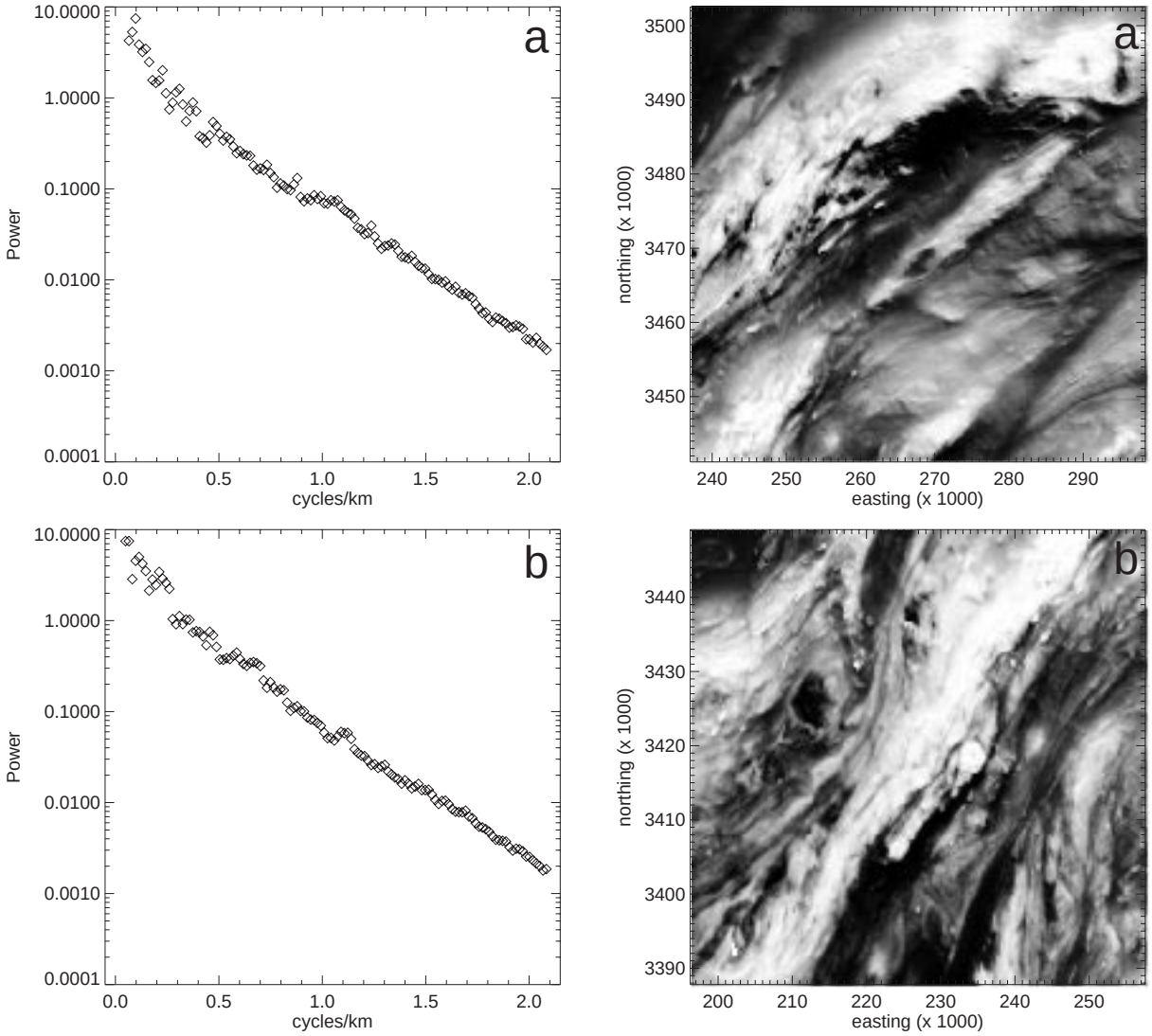

Figure 3.8 Power spectra for 60x60km areas in the Fowler Subdomain. High magnetic intensity, strongly textured, sinous anomalies in (a) the northern Fowler Subdomain and (b) the southern Fowler Subdomain show almost identical power spectra, with very high power over the entire frequency range, in marked contrast with the other subdomains.

3.8 Interpretive geology of the Nuyts Subdomain

Aeromagnetic images of the Nuyts Subdomain are dominated by large (10-50km) elliptical anomalies of varying intensity and texture, and large (2-40km), irrelularly shaped, low magnetic intensity, magnetically featureless anomalies. The elliptical anomalies correlate directly with presumed plutons of Hiltaba Suite granite; part of a regionally extensive suite of Mesoproterozoic A-type granitoids (see Chapter 7). The irregular, low magnetic intensity anomalies correlate directly with Munjeela Suite plutons; a newly recognised suite of leucocratic, S-type granites (see Chapter 7). The Hiltaba and Munjeela Suite plutons intrude undifferentiated basement material which has been divided into higher magnetic intensity and lower magnetic intensity areas in the interpretive geolgical map. The older basement has been deformed by a series of undifferentiated, pre-Hiltaba Suite shear zones. A portion of a late Palaeoproterozoic St Peter Suite pluton forms a complex, strongly textured, high magnetic intensity anomaly in the southeastern corner of the study area.

Power spectra for the Nuyts Subdomain form relatively straight lines (in contrast with the other subdomains) showing moderate average power in contrast with those of the Fowler and Christie Subdomains (see Figure 3.9).

3.9 Interpretive geology of the major shear zones

The use of aeromagnetic data to map the extent, nature and crosscutting relationships of shear zone systems provides a powerful basis for understanding the geological framework and tectonic evolution of the Earth's crust. The

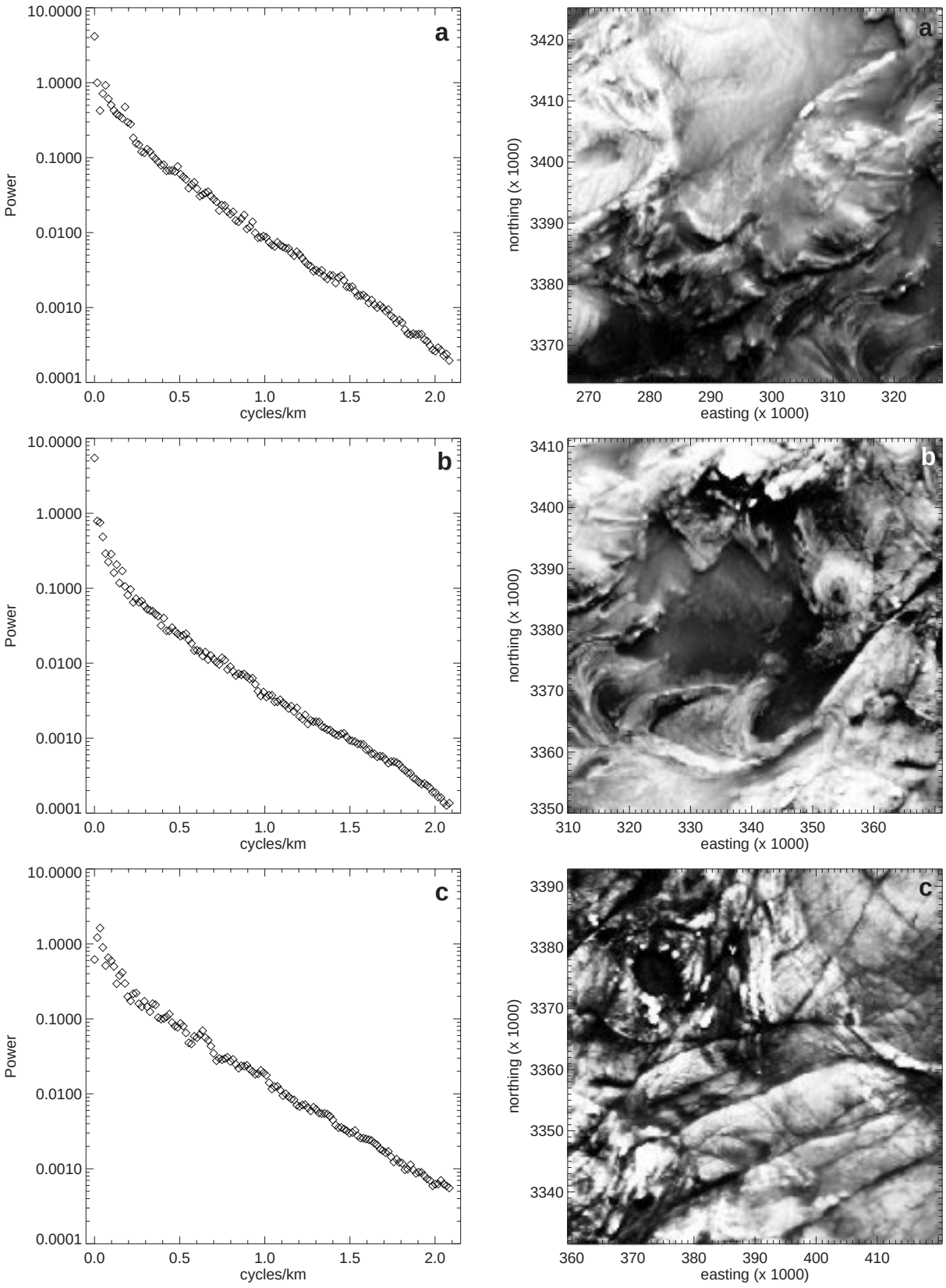

Figure 3.9 Power spectra for 60x60km areas in the Nuyts Subdomain, (a) and (b) strongly textured, moderate magnetic intensity areas in the eastern Nuyts Subdomain show distinctly linear power spectra with moderate power at all frequencies, (c) strongly textured, moderate-high average magnetic intensity area in the western Nuyts Subdomain shows higher average power. Note the concave geometry of the power spectra.

localisation of strain by shear zones at all scales fundamentally controls the crust's response to deformation, and as a result, shear zones are critical to the architecture of all orogenic belts, and are an important key to unravelling the apparently disparate tectonic histories present within terranes such as the western Gawler Craton (see Chapter 8). Three generations of late, "framework" shear zones have been identified in the western Gawler Craton; an early east-west trending set (SZ_1), a major northeast trending set (SZ_2), and the late, northeast trending Karari Fault Zone (SZ_3).

Numerous other, smaller scale shear zones which predate the above-mentioned systems occur throughout the western Gawler Craton. They range in age from early Palaeoproterozoic (Sleafordian) through to Mesoproterozoic, and are important parts of the intra-Subdomain structural evolution of the area. They have been detailed where relevant in the preceding sections. This section deals primarily with the three generations of late "framework" shear zones which dominate the geology of the western Gawler Craton.

Outcrop and drill core in all generations of shear zones shows a striking correlation with the interpreted shear zone geometry and structural trends. Measured foliations in high strain lithologies correlate precisely with the regional interpreted shear zone trends; an observation which forms the basis for understanding the kinematic evolution of the shear zones presented in Chapter 8.

3.9.1 SZ_1 shear zones

A set of early, east-west trending shear zones are responsible for some of the key subdomain juxtapositions in the western Gawler Craton. The best-preserved, most continuous, east-west trending, SZ_1 shear zone is the Yerda Shear Zone which juxtaposes the Wilgena and Nuyts Subdomains and is marked by narrow, linear, demagnetised zones which wrap around presumed Hiltaba Suite, "porphyroclastic" plutons. A set of poorly preserved, east-west trending shear zones form the original boundary between the Fowler and Christie Subdomains. They define the northern interface between strongly magnetised lithologies in the Barton Block of the Fowler Subdomain and very weakly magnetised rocks (presumed Christie Gneiss) of the Christie Subdomain, and also form the northern margin of the Wynbring pluton. Magnetic gradient data suggests that these shear zones dip at moderate angles to the north.

3.9.2 SZ_2 shear zones

The most prominent geophysical features in the western and northern Gawler Craton are a series of northeast-trending, craton-scale, anastamosing linear anomalies caused by a system of major shear zones. These shear zones are a fundamental part of the tectonic framework of the northwestern Gawler Craton, and define a mobile belt extending for over 800km at widths of 100-200km. They often juxtapose subdomains of significantly different geophysical and geological character and have clearly been responsible for the exhumation of large tracts of lower crustal rocks. The western Gawler Craton is dominated by two major, northeast-trending, anastamosing shear zone systems; the Tallacootra Shear Zone and the Coorabie Shear Zone, which juxtapose and transect the Christie, Fowler, Wilgena and Nuyts Subdomains (see Figure 3.6).

The shear zone anomalies exhibit low magnetic intensity, with strong, linear structural grains. As a result, they are very prominent in areas of high magnetic contrast where the surrounding country rock exhibits higher magnetic intensity, however in regions of low average magnetic intensity (such as the Mulgathing Complex in the Christie Subdomain) they form very subtle anomalies characterised by pattern breaks and weak, linear structural trends. In order to accurately interpret the location and width of shear zones in areas of low magnetic contrast, it is necessary to use strongly enhanced aeromagnetic images which highlight short-wavelength anomalies (first vertical derivative and automatic gain control algorithms were used in this study). The northern portions of the Tallacootra and Coorabie Shear Zones have been interpreted in this way.

The Tallacootra Shear Zone forms one of the most significant geophysical boundaries in the western Gawler Craton, and can be traced for over 700km. It comprises a set of major, ~northeast trending, curvilinear, anastamosing, ductile structures which are truncated by the Torrens Hinge Zone in the far northeastern Gawler Craton, and extend well to the west beyond the current coastline where they are truncated by the Karari Fault Zone. Two main exposures of the Tallacootra Shear Zone occur at Lake Tallacootra and Lake Ifould, which preserve a diversity of high strain, high grade, mylonitic rocks (see Chapter 8).

The Coorabie Shear Zone forms the easternmost system of major, anastamosing shear zones in the western Gawler Craton, and defines the boundary between the Fowler/Christie Subdomains and the Wilgena/Nuyts Subdomains (see Figures 3.3 and 3.6). The Colona Fault (as defined by Drexel et al., 1993) forms the westernmost limb of the Coorabie Shear Zone system. Outcrop and drillcore in the Coorabie Shear Zone is very sparse; probably due to the high "weatherability" of intensely deformed

and altered rocks. The information presented here is derived from outcrop-subcrop in the Mount Christie/Mulgathing area, beach boulders at Cape Adieu, and isolated outcrops south of Barton Railway Siding in the Great Victoria Desert (see Chapter 8). Importantly, the Coorabie Shear Zone defines the northern margin of the Pandurra Formation (see Figures 3.3 and 8.1, as well as Figure 5.18 in Cowley, 1993), indicating that it must be younger than ~1420 Ma (see Chapter 8).

Measured magnetic susceptibilities of high strain rocks in all generations of shear zones in the western Gawler Craton are very low, and they are often characterised by abundant hydrous phases such as mica, amphibole and epidote; in contrast with the surrounding higher grade rocks which they transect. These observations are consistent with the low magnetic intensity aeromagnetic signature of the shear zones. Clearly an understanding of the magnetic petrology of the shear zones is vital here. Some important representative thin section to outcrop scale observations include:

- Fine grained, low magnetic intensity (~50-100 S.I.x10^{-5}) ultramylonite zones (associated with the Coorabie Shear Zone) crosscut high magnetic intensity amphibolites (~2000-4000 S.I.x10^{-5}) at Cape Adieu, in which early garnet, hornblende, plagioclase and magnetite have partially broken down to very fine grained biotite, K-feldspar, plagioclase and quartz. The partial breakdown of magnetite and the subsequent incorporation of Fe^{3+} into biotite explains the demagnetisation of high grade mafics in the Coorabie Shear Zone.
- Numerous boudins of moderate magnetic intensity (~500 S.I.x10^{-5}) mafic granulite in the Tallacootra Shear Zone have low magnetic intensity and highly deformed and reworked margins, in which early, pyroxene-magnetite bearing, anhydrous assemblages are breaking down to hydrous assemblages involving hornblende, cummingtonite and epidote. Early sphene is rimmed by ilmenite, indicating a decrease in fO_2. The breakdown of magnetite and the subsequent incorporation of Fe^{3+} into the hydrous phases (especially epidote) explains the demagnetisation of high grade mafics in the Tallacootra Shear Zone.
- High magnetic intensity Ifould Complex intrusives grade into low magnetic intensity mica schists in the Tallacootra Shear Zone. Early hornblende-magnetite-biotite bearing intrusives are retrogressed to biotite-epidote schists. The capacity of biotite and epidote to accommodate significant Fe^{3+} explains the increasing demagnetisation during retrograde deformation.
- Narrow, strike-slip, ultramylonite zones crosscutting moderate magnetic intensity (~1200 S.I.x10^{-5}), undeformed Hiltaba Suite granite in the Nuyts Subdomain exhibit zero magnetic susceptibility. The demagnetisation in the shear zones is explained by the retrogression of fine grained disseminated magnetite in the granite to elongate stringers of red, weathered hematite in the ultramylonites, suggesting the presence of oxidising fluids within the low grade shear zones. Similar observations have been made in the Coorabie Shear Zone in the Mulgathing area.

3.9.3 SZ_3 Karari Fault Zone

The Karari Fault Zone forms a significant, northeast-trending, linear magnetic high which extends over 700km from the Nullarbor coast in the southwest to the Torrens Hinge Zone in the northeast. It forms the southeastern margin of the Nawa and Coompana Subdomains, where it truncates both the northeastern and southwestern parts of the Coorabie and Tallacootra Shear Zones (see Figures 3.3 and 3.6). Magnetic susceptibility measurements of drill core from the Karari Fault Zone range from ~200-500 S.I.x10^{-5} in felsic mylonites to over 100000 S.I.x10^{-5} in magnetite-rich mylonites (the highest magnetic suscpetibility reading taken during this study). The very high magnetic intensity signature of the Karari Fault Zone is obviously caused by these magnetite rich lithologies, which are interpreted to be derived from magnetite rich gneisses in the southern Nawa Subdomain (i.e. the Moondrah Gneiss - see §3.4 and Chapter 4). Regional scale aeromagnetic interpretation suggests that the Karari Fault Zone must have a significant sinistral strike slip component (see Chapter 8).

3.10 Discussion

The observations presented in this chapter show that there is a remarkable correlation between surface geology and aeromagnetic data in the western Gawler Craton. Outcrop-scale observations; particularly rock magnetisation, contact relationships and structural orientations; can usually be extrapolated with a high degree of confidence to the regional-scale aeromagnetic data facilitating the construction of detailed interpretive geological maps of an area with less than 1% outcrop. Where possible, anomalies in unexposed areas have been correlated with similar, well constrained anomalies, although in some areas they can only be characterised by describing their magnetic geometry, intensity and texture, and as a result their interpretation is somewhat ambiguous.

An important feature of the geology of the western Gawler Craton which makes aeromagnetic interpretation a particularly powerful tool is the dominantly steep dips of structures and contacts. This contrasts markedly with terranes dominated by shallow structures and contacts which exhibit

very complex magnetic signatures which are very difficult to resolve due to overprinting of anomaly patterns (e.g. Gunn et al., 1997). As a result, the interpretive geological map presented in Figure I1 (at rear of thesis) is a powerful and accurate tool for understanding the geology of the western Gawler Craton, and the methods outlined in Chapter 2 for understanding poorly exposed terranes have been particularly relevant to the western Gawler Craton.

PART 2

THE TECTONOTHERMAL EVOLUTION

OF THE WESTERN GAWLER CRATON

Chapter 4
TECTONOTHERMAL EVOLUTION OF THE SOUTHERN NAWA SUBDOMAIN

4.1 Introduction

The recognition of potentially ultrahigh temperature, sapphirine-quartz granulites in rock chips from the ORP 1 drill hole near Ooldea by Purvis (1981) sparked great interest in the southern Nawa Subdomain. This is the only known locality of ultrahigh temperature (UHT) granulites (as defined by Harley, in press) in the Australian continent. Subsequently, Mines and Energy, South Australia (MESA) drilled several diamond drill holes in the Ooldea area in order to obtain a fully cored sample of the high grade gneiss. Previous work in the Nawa Subdomain has focussed on the Ooldea DDH2 drill core which provides the longest and best-preserved section of high grade gneiss, and includes the MESA well completion report (Daly, 1987), part of an honours thesis (Taylor, 1987) and brief work by Oliver & Purvis (1986) and Oliver et al. (1988). These workers largely focussed on the magnetite-rich lithologies, and several critical mineral assemblages were identified, including sapphirine-quartz, hypersthene-sillimanite-quartz and spinel-sillimanite-quartz, all of which indicate potentially ultrahigh temperature, granulite facies metamorphism. This study identified several previously unrecognised lithologies in the southern Nawa Subdomain, in particular garnet and hypersthene-sillimanite bearing, aluminous granulites. Daly et al. (1997) proposed the name *Moondrah Gneiss* to encompass all magnetite-bearing lithologies in the southern Nawa Subdomain.

This chapter focusses on the tectonothermal evolution of the southern Nawa Subdomain which is dominated by the Moondrah Gneiss (see Chapter 3). Section 4.2 summarises the petrological evolution of the Moondrah Gneiss. The metamorphic evolution of the Moondrah Gneiss is evaluated in Section 4.3, and the geochronology is discussed in Section 4.4. Section 4.5 contains a geological synthesis of the southern Nawa Subdomain. Section 4.6 discusses the tectonothermal evolution of the southern Nawa Subdomain, outlining relevant geodynamic problems posed by ultrahigh temperature metamorphism with various explanatory models.

4.2 Lithological and petrological summary

As outlined in Chapter 3, the southern Nawa Subdomain is dominated by two broad lithological associations; a heterogeneous sequence of layered, magnetite-bearing, mylonitic gneisses (the Moondrah Gneiss) which is interlayered with weakly magnetised, felsic gneiss and mylonite at scales ranging from a few centimetres to a few kilometres. All lithologies are clearly derived from coarse grained, granoblastic, migmatitic gneisses which have been variably overprinted by a fine grained, high strain fabric in which early, coarse grained phases are recognised as porphyroclasts. The Moondrah Gneiss includes a spectrum of

Figure 4.1 Typical physiography of the southern Nawa Subdomain - Ooldea Railway Siding on the edge of the Nullarbor Plain. Outcrop is non-existent!

lithologies ranging from aluminous granulites (probably derived from ferrugeneous pelites) through to ironstones (probably derived from banded iron formations). The petrography of the Moondrah Gneiss is summarised below. Most of the observations are taken from the Ooldea DDH2 drill core (see Figure 4.2). Representative mineral composition data can be found in Appendix 2.

In the Moondrah Gneiss early, coarse grained, granoblastic mineral assemblages have been variably overprinted by three stages of complex, fine grained reaction textures. The following early granoblastic assemblages are inferred:

• cordierite - osumilite - Fe^{3+}-rich spinel - perthite - quartz ± plagioclase ± hypersthene (in the aluminous lithologies);

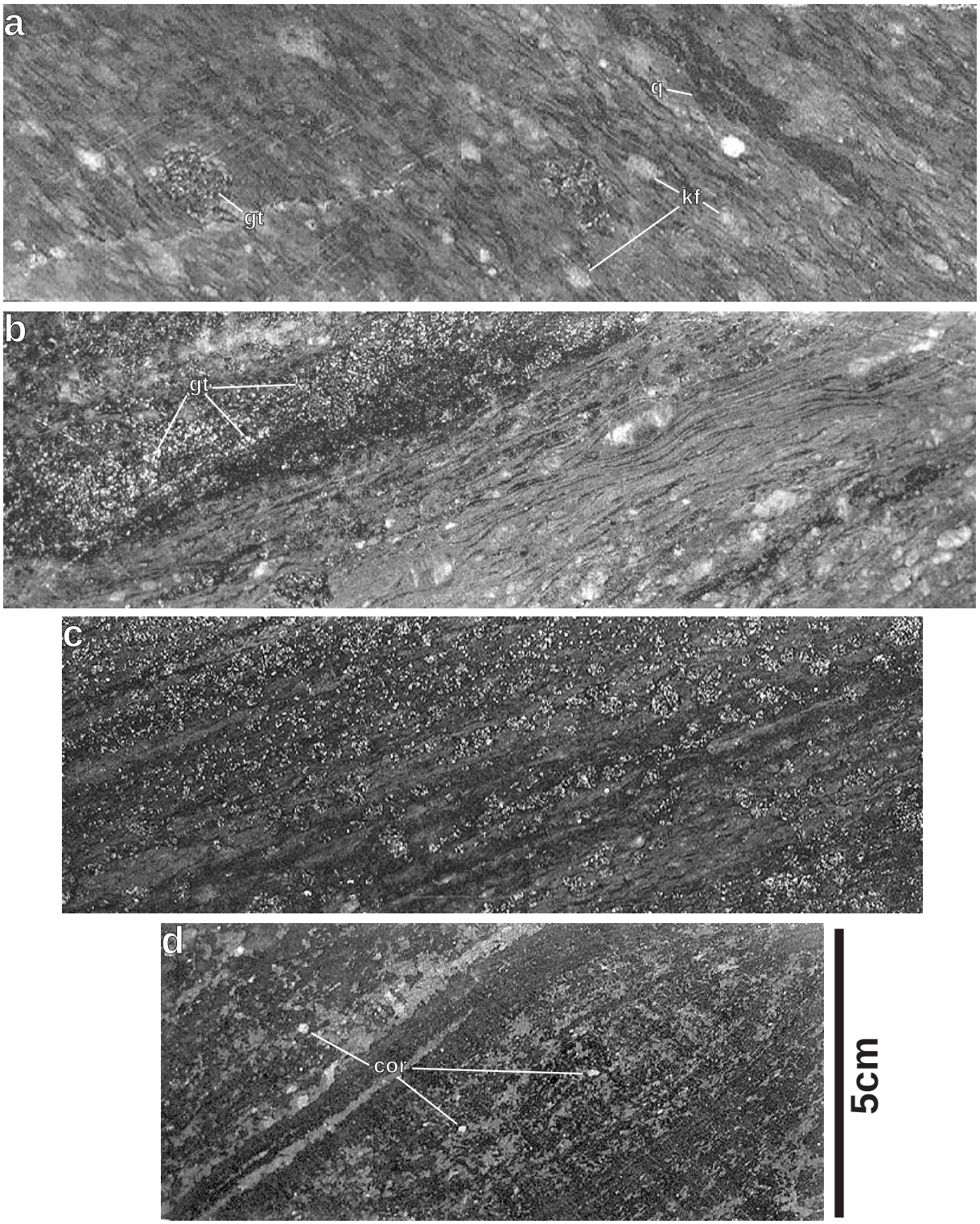

Figure 4.2a Strongly enhanced images of drill core from the southern Nawa Subdomain; (a) Ooldea DDH1 293.7m - felsic mylonitic gneiss with lobate garnet porphyroclasts; (b) Ooldea DDH2 139.5m - mylonitic garnet gneiss (LHS) and felsic gneiss (RHS); (c) Ooldea DDH2 138.3m - mylonitic garnet-sillimanite-cordierite-magnetite±sapphirine gneiss; (d) Ooldea DDH2 71.3m - magnetite-rich ironstone with corundum laths.

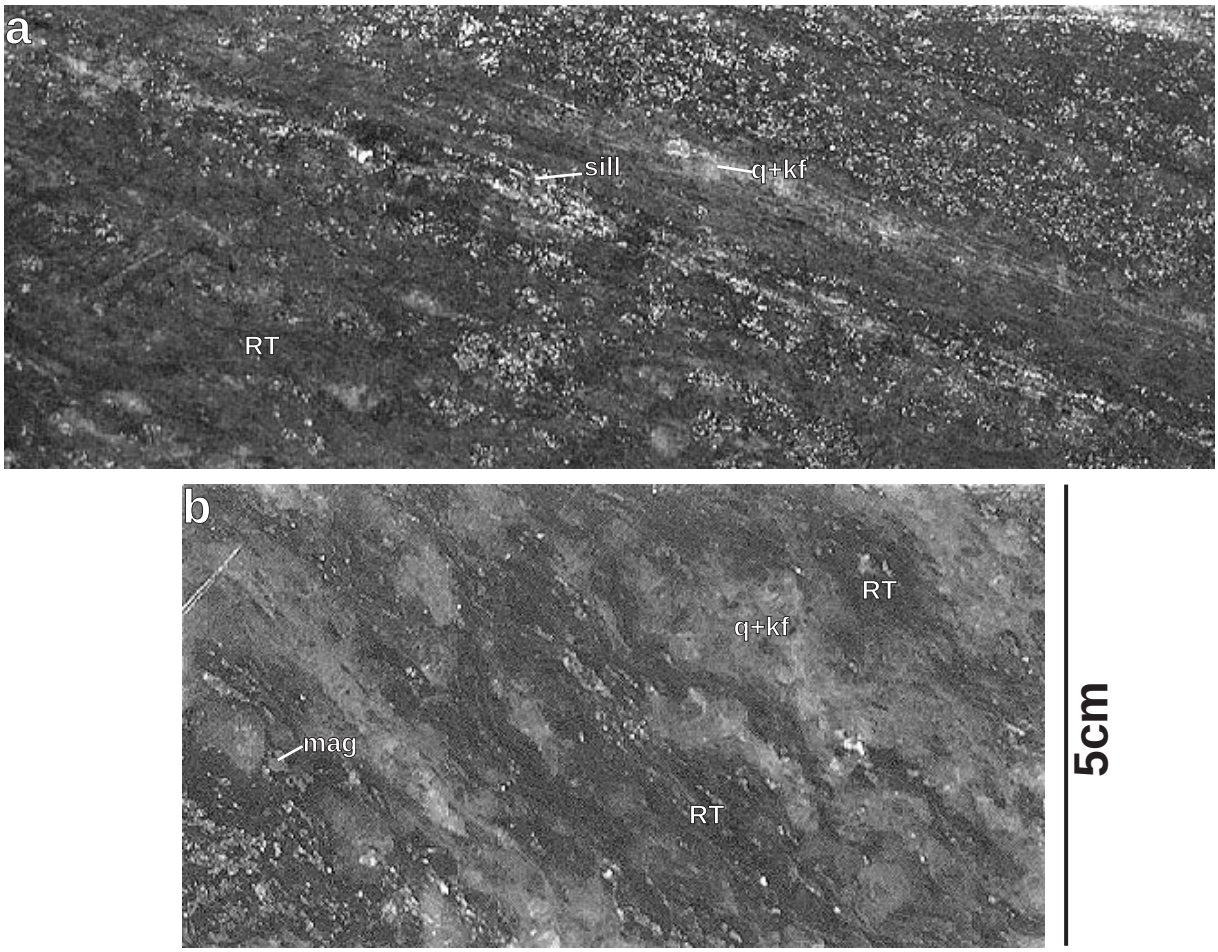

Figure 4.2b Strongly enhanced images of drill core from the southern Nawa Subdomain (cont'd); (a) Ooldea DDH2 74.5m - aluminous, hypersthene-sillimanite gneiss; (b) Ooldea DDH2 88.3m - aluminous, hypersthene-sillimanite gneiss (dark patches are very fine grained reaction textures [RT] involving hypersthene, sillimanite, sapphirine, cordierite and biotite after early, coarse grained cordierite and osumilite [see text for details]).

• Fe^{3+}-rich spinel - quartz ± perthite ± plagioclase ± magnetite ± ilmenohematite (in the sub-aluminous lithologies).

Subsequently, a three stage textural evolution is recognised:

Stage 1 involved the exsolution of magnetite and various silicates from an early, granoblastic, Fe^{3+}-rich phase. These breakdown textures are recognised as silicate coronas on magnetite, or silicate intergrowths with magnetite (see Figures 4.3 & 4.4). The metamorphic evolution of these textures is further discussed in §4.3.5. Examples include:

• pseudomorphic intergrowths of prismatic sillimanite and magnetite;

• pseudomorphic sapphirine coronas on magnetite;

• pseudomorphic corundum intergrowths with magnetite and quartz.

• hypersthene coronas on magnetite;

• garnet coronas on magnetite;

• spectacular garnet-magnetite symplectites;

Clearly the pseudomorphic reaction textures predate the coronitic reaction textures (see Figure 4.3). The intricate nature of these textures implies that they formed in a static environment (see §4.3.2).

Stage 2 involved replacement of early, coarse grained silicate phases by a variety of spectacular, fine grained reaction textures synchronous with the development of a fine grained, high strain fabric (see Figures 4.5 & 4.6). In low strain domains, reaction textures are often symplectic, reflecting relatively static conditions, whereas in higher strain domains the reaction textures form fine grained, granoblastic mosaics. Ongoing fabric development has clearly annealed many of the symplectic reaction textures. Reaction textures in the aluminous granulites (which contain the greatest diversity of mineral associations) include:

• the breakdown of early, coarse grained cordierite to fine grained symplectites and granoblastic mosaics of hypersthene, sillimanite and quartz via the reaction:

cd ▪ hy + sill (+q) (1)

• the breakdown of early, coarse grained osumilite to fine grained granoblastic mosaics of hypersthene, sapphirine, K-feldspar, plagioclase and quartz (with minor sillimanite) (see §4.3.4) via the reaction:

osm ▪ hy + sa + kf + plag (+q) (2)

• the breakdown of early, coarse grained hypersthene to symplectites of sapphirine and

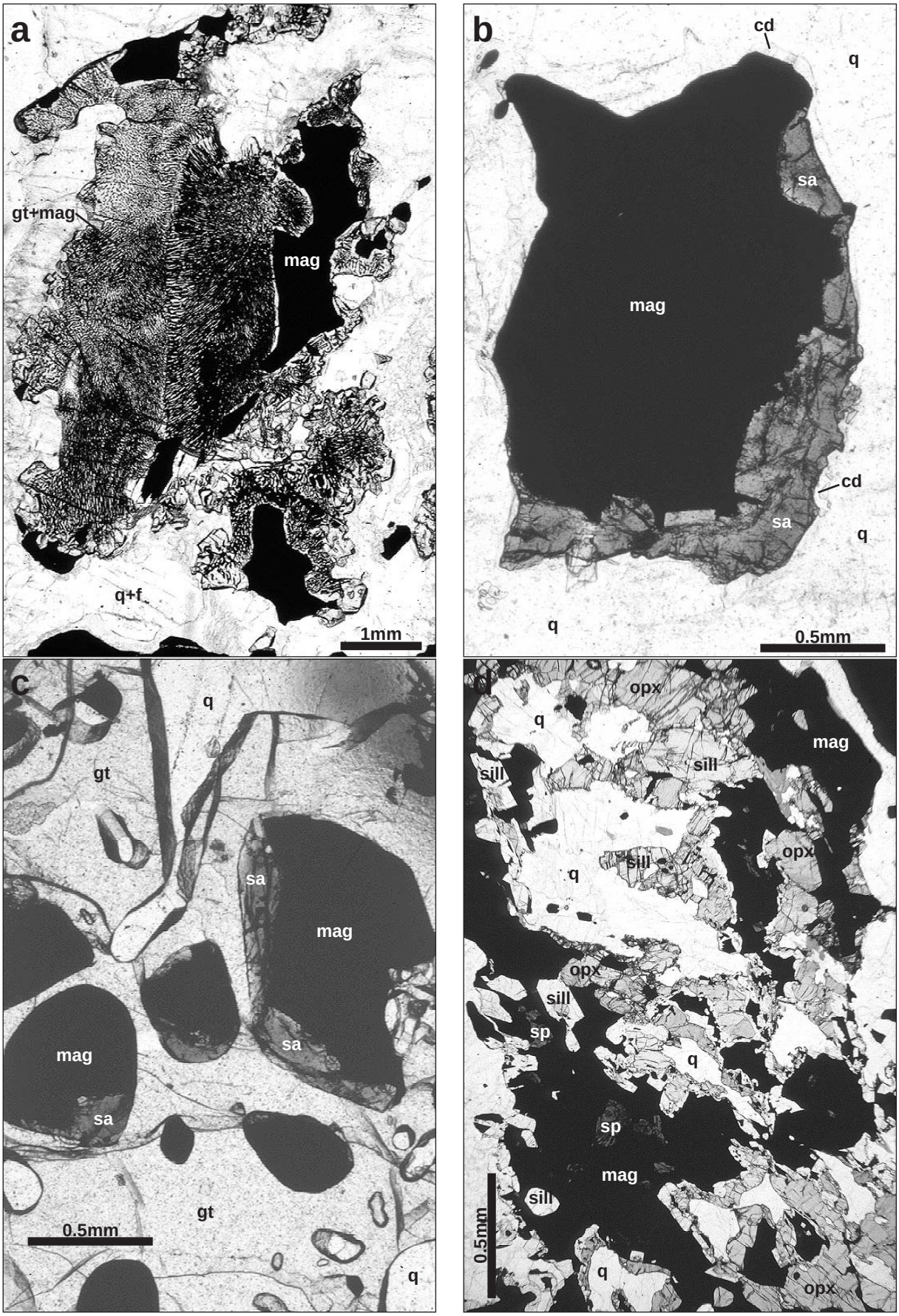

Figure 4.3 Photomicrographs of Stage 1 silicate-magnetite intergrowths from Ooldea DDH2; (a) 73.4-73.6m - garnet-magnetite symplectites after ?Fe^{3+}-rich spinel, surrounded by quartz, perthite and plagioclase; (b) 75.4-75.5m - pseudomorphic sapphirine-magnetite intergrowth after ?Fe^{3+}-rich spinel, surrounded by quartz and perthite (note late, retrograde rind of cordierite after sapphirine+quartz); (c) 73.6-73.7m - pseudomorphic blebs of sapphirine + magnetite after spinel, surrounded by garnet and quartz; (d) 116.0-116.1m - hypersthene-sillimanite-magnetite intergrowths after ?Fe^{3+}-rich spinel, surrounded by quartz (note late, retrograde spinel exsolution blebs in magnetite).

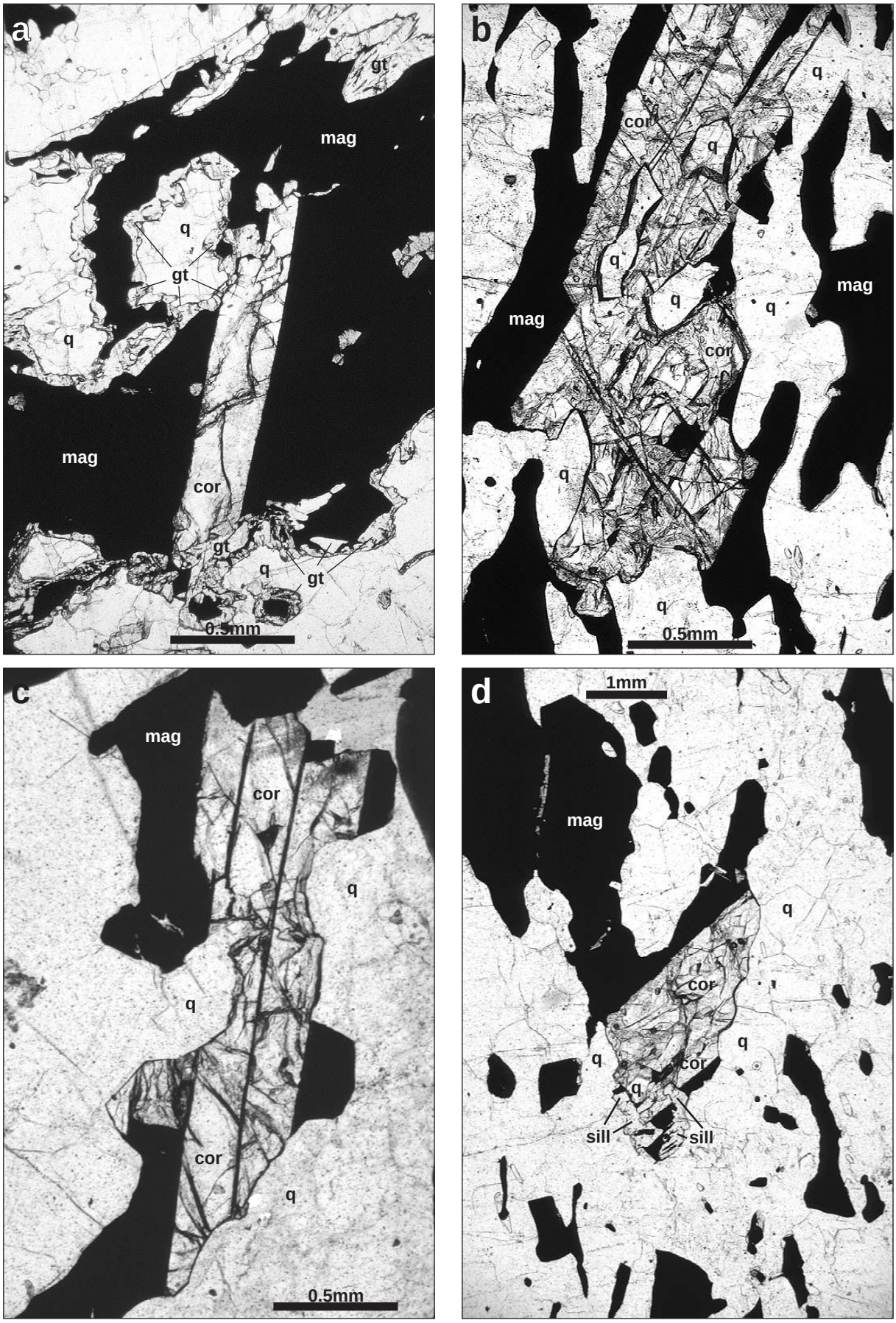

Figure 4.4 Four examples of corundum-magnetite-quartz intergrowths from Ooldea DDH2. (a) 101.3-101.4m - pseudomorphic corundum-magnetite intergrowth, surrounded by garnet and quartz. (b) 65.9-66.0m - note quartz inclusions in corundum in. (c) 43.2-43.3m. (d) 66.1-66.2m - note the stable intergrowth of sillimanite with corundum, magnetite and quartz.

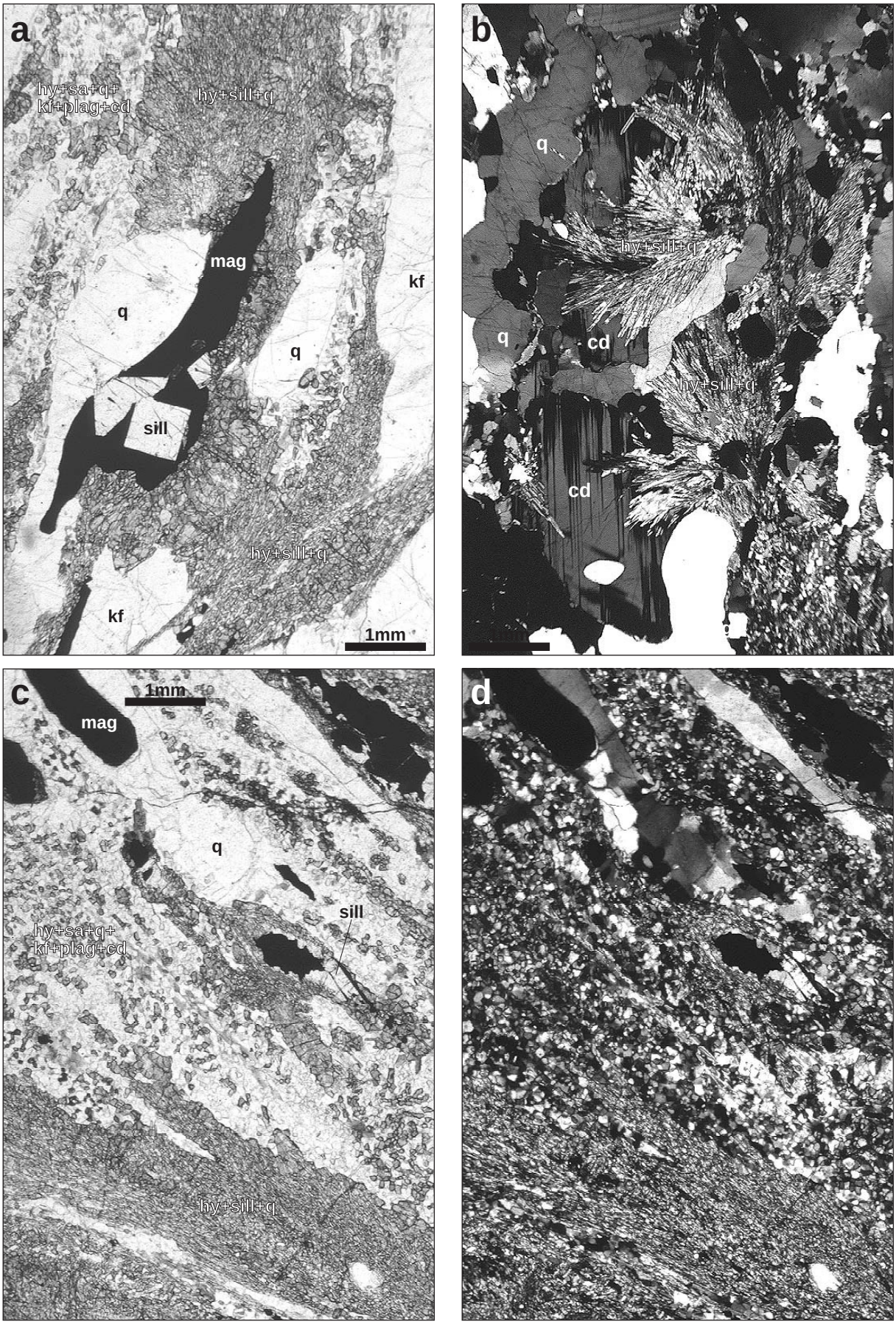

Figure 4.5 Overviews of Stage 2 fine grained, partially annealed reaction textures in the aluminous gneiss from Ooldea DDH2. Fibrous, hypersthene-sillimanite-quartz mats after early cordierite, and granular hypersthene-sapphirine-plagioclase-K-feldspar-quartz±sillimanite mosaics after early osumilite (see text for details). (a) 88.2-88.3m. (b) 74.5-75.0m (XPL). (c) & (d) 93.6-93.7m (PPL & XPL).

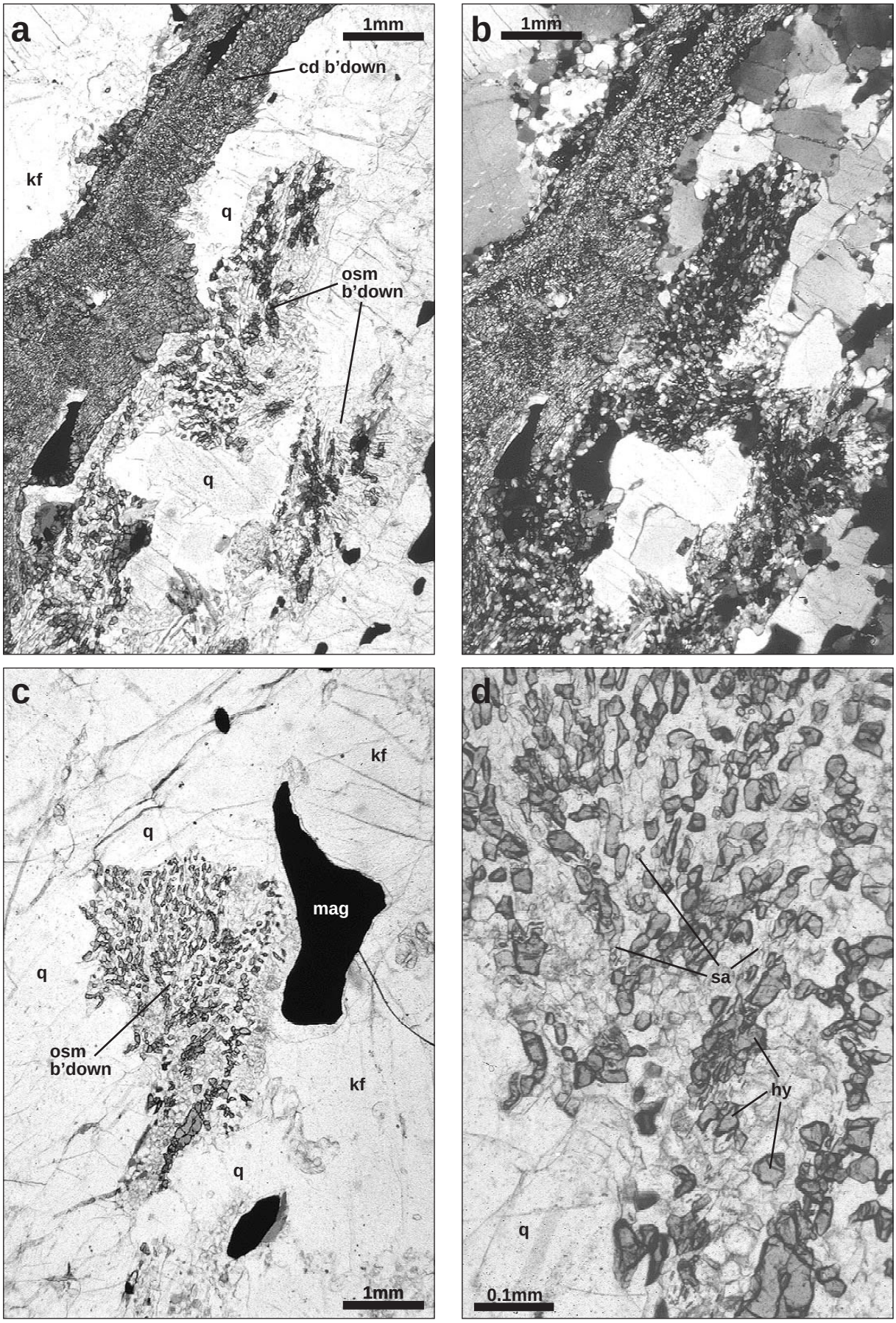

Figure 4.6 Interpreted Stage 2 osumilite breakdown textures from Ooldea DDH2 88.2-88.3m; (a) and (b) Overview of granular, hypersthene-sapphirine-plagioclase-K-feldspar-quartz±sillimanite±cordierite mosaics after osumilite, and fibrous hypersthene-sillimanite-quartz mats after cordierite; (c) Granular hypersthene-sapphirine-plagioclase-K-feldspar-quartz±cordierite mosaic after osumilite; (d) detail of (c).

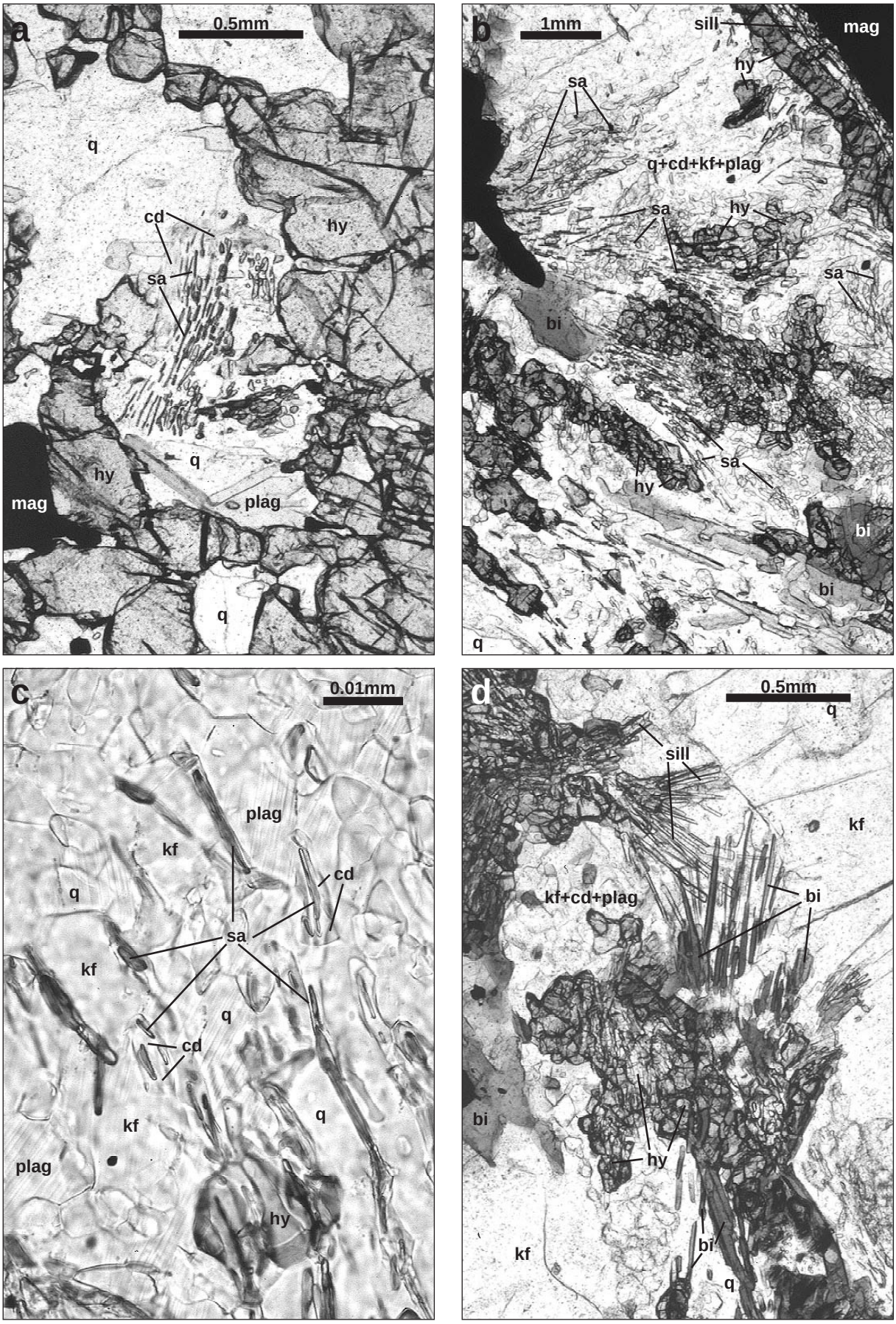

Figure 4.7 Miscellaneous photomicrographs from aluminous gneiss in Ooldea DDH2; (a) 75.4-75.5m - Stage 2 sapphirine-cordierite intergrowth after early hypersthene; (b) 73.0-73.1m - overview of complex, Stage 2 and Stage 3 sapphirine-rich reaction textures (probably after osumilite) with retrograde biotite after hypersthene and sapphirine; (c) 88.2-88.3m - Stage 3 cordierite coronas on sapphirine in the granular osumilite breakdown textures; (d) 93.6-93.7m - late, Stage 3 biotite after hypersthene.

cordierite.

- the growth of fine grained garnet with sillimanite and cordierite.

Stage 2 is also marked by the fine grained recrystallisation of quartz and feldspar into the high strain fabric, and the development of quartz ribbons.

Stage 3 involved the late to post-kinematic growth of retrograde biotite and cordierite after earlier anhydrous phases (see Figure 4.7). Reaction textures include:

- cordierite coronas on Stage 1 and Stage 2 sapphirine via the reaction:

  sa ▪ ▪cd (+q) (3)

- randomly oriented, fine grained biotite growing at the expense of earlier generations of sapphirine and hypersthene via the reaction:

  hy ± sa ▪ ▪bi (+q, kf) (4)

- exsolution of fine spinel blebs from magnetite.

4.3 Metamorphic evolution of the Moondrah Gneiss

4.3.1 Overview

The observed mineral assemblages and reaction textures in the Moondrah Gneiss suggest a complex metamorphic evolution accompanied in part by high strain deformation. The ubiquitous Stage 1 silicate-magnetite reaction textures are discussed in Section 4.3.2, and the extremely rare intergrowths of corundum, magnetite and quartz are discussed in Section 4.3.3. The evidence for early osumilite in the aluminous gneiss is discussed in Section 4.3.4. Aluminous lithologies contain relatively low variance mineral assemblages and reaction textures and provide the most compelling metamorphic information which is discussed in light of relevant petrogenetic grids in Section 4.3.5.

In order to constrain the pressure-temperature conditions experienced by the Moondrah Gneiss, it is important to recognise that conventional thermobarometry is unlikely to yield meaningful results in high grade granulites because the cation-exchange reactions on which such calculations are based will continue during retrogression, thus underestimating actual peak conditions (e.g. Harley, 1989, in press; Fitzsimons & Harley, 1994). The metamorphic interpretation of such rocks must therefore rely on the comparison of observed mineral assemblages and reaction textures with experimental and theoretical phase relationships using petrogenetic grids. Petrogenetic grids facilitate the qualitative and semi-quantitative analysis of changes in pressure and temperature implied by arrested reaction textures (Harley, in press). Low variance mineral assemblages are particularly particularly amenable to this type of analysis, and usually occur in Al-Mg rich, metapelitic rocks.

The abundance of magnetite, and the occurrence of the magnetite-ilmenohematite association in the Moondrah Gneiss indicates that metamorphism occurred at relatively high oxygen fugacity (fO_2), near that of the magnetite-hematite buffer (Lindsley, 1976). This is an important consideration, since most high grade pressure-temperature experiments and calculations were performed at low oxygen fugacity (e.g. Hensen & Green, 1971, 1972; Bertrand et al., 1991; Audibert et al., 1995; Carrington & Harley, 1995a). Several workers have recognised that oxygen fugacity can play a significant controlling role on the stability of Fe^{3+}-bearing phases in high grade metapelites, in particular spinel and sapphirine (e.g. Hensen, 1986; Sandiford et al., 1987; Powell & Sandiford, 1988). One consequence of this is that the stability fields of sapphirine and spinel will expand to lower temperatures and pressures, potentially effecting dramatic changes on the topology of relevant petrogenetic grids (see §4.3.5). Hence oxygen fugacity may have played an important stabilising role in the formation of the sapphirine-bearing assemblages in the Ooldea granulites, and the sapphirine-quartz paragenesis is likely to have formed at temperatures and pressures below those reported for reduced rocks by Hensen and Green (1971, 1972) and Harley (in press) (>1000°C, >8kb).

4.3.2 Stage 1 silicate-magnetite reaction textures

The Moondrah Gneiss invariably contains a silicate phase either rimming or intergrown with the magnetite (Stage 1 - see §4.2). Layers of different bulk composition and/or oxygen fugacity contain different magnetite-silicate intergrowths which are finely interleaved at small scales (0.1-1cm). No reaction textures are observed between the layers indicating that the metamorphic processes that caused the intergrowths operated with extremely small equilibration volumes, despite the extreme inferred metamorphic conditions. Although similar mineral textures are commonly observed in iron-rich, high fO_2 granulites, their paragenesis is not fully understood (S. Harley pers. comm., 1996). In the Moondrah Gneiss, the pseudomorpic and coronitic magnetite-silicate reaction textures grew relatively early in the metamorphic history, since they predate the Stage 2 and 3 reaction textures described above. Often the silicate-magnetite intergrowths share common grain boundaries, indicating that they pseudomorph an earlier, medium grained, Fe^{3+}-rich phase, probably Fe^{3+}-rich spinel (S. Harley pers. comm., 1996). Dasgupta et al. (1995) reported spinel-magnetite-Fe-Ti oxide mosaics rimmed by a silicate phase (garnet, sillimanite or sapphirine) and interpreted them as

granular exsolution from a homogeneous spinel solid solution which initially reacted with quartz to produce the silicate coronas. The silicate coronas in the Moondrah Gneiss possibly formed during the up-pressure breakdown of early Fe^{3+}-rich spinel via the reaction:

Fe^{3+}-rich spinel+quartz▪ silicate+magnetite
(S. Harley pers. comm., 1996)

This reaction implies that initally, the mineralogy of the Moondrah Gneiss may have been dominantly spinel+quartz. Inital spinel composition and oxygen fugacity probably governed which silicate phase formed during Stage 1 (since the ratio of Fe^{2+} to Fe^{3+} in a rock is governed by fO_2). Mg-poor spinels are likely to yield Mg-absent silicates such as sillimanite, and Mg-bearing spinels are likely to yield garnet, orthopyroxene or cordierite depending on fO_2 and Mg content. In highly oxidised samples, Mg-poor spinels yielded magnetite + corundum (see §4.3.3).

In the Moondrah Gneiss, magnetite generally contains green spinel exsolution blebs (see Figure 4.3d) which presumably formed from a magnetite-rich spinel solid solution cooling below the spinel-magnetite solvus at approximately 900°C (Nell & Wood, 1989). These features are clearly retrograde and can be considered a Stage 3 reaction texture.

4.3.3 The corundum conundrum

Some magnetite-rich ironstone gneisses from Ooldea DDH2 contain up to 5% medium grained, subhedral corundum which is often intergrown with quartz. The ironstones are fine grained, dark grey, finely layered, isoclinally folded, and contain 40-70% magnetite. Their basic mineralogy is magnetite-quartz-plagioclase±sillimanite with minor corundum, sapphirine, spinel, sillimanite, garnet, hypersthene and apatite. Where spinel is in contact with quartz, the spinel has at least partially reacted to form sapphirine, and the stable parageneses sapphirine+quartz and spinel+quartz both occur. Large, subhedral corundum grains (up to 3mm long) are commonly intergrown with quartz, and magnetite, and contain fine apatite inclusions (see Figure 4.4). Corundum contains signifiant Fe_2O_3 (between 0.9 and 2.8wt%), as does sillimanite (between 0.9 and 1.4 wt%, averaging about 1.0 wt%) (see Appendix 2). Often the corundum grains are almost entirely surrounded by quartz, and contain small, rounded quartz inclusions. In one sample, the apparently stable intergrowth of corundum, quartz and sillimanite was observed (see Figure 4.4d), with no apparent reaction textures between the three phases. The grain boundary continuity between corundum and magnetite suggests they pseudomorph an earlier phase, probably Fe^{3+}-rich spinel (see §4.3.2). The corundum-bearing layers are finely interleaved with slightly less magnetite-rich domains, which contain either sillimanite, garnet or hypersthene intergrown with or rimming magnetite. It is clear that the corundum-magnetite and sillimanite-magnetite intergrowths predate the ferromagnesian corona phases described in the preceding section.

The paragenesis of corundum + quartz in favour of sillimanite is extremely rare in the geological record, and only five other occurrences have been reported (Krogh, 1977; Tracy & McLellan, 1985; Bohlen, 1986; Motoyoshi et al., 1990; Guiraud et al., 1996), all from high grade terranes. The corundum + quartz paragenesis from Ooldea is the most spectacular and unambiguous example yet discovered. Conventional wisdom suggests that the corundum + quartz assemblage cannot exist even at extreme crustal pressure-temperature conditions, however the unambiguous coexistence of both naturally occurring and experimentally derived corundum + quartz demands explanation.

Three possible explanations for the coexistence of corundum and quartz have been postulated. Several workers have concluded that corundum + quartz is *metastable* with respect to sillimanite and kyanite at crustal pressure-temperature conditions (e.g. Shulters & Bohlen, 1989; Motoyoshi et al., 1990; Harlov & Newton, 1993). Others suggest that corundum + quartz is *unstable* but exists since corundum breakdown is inhibited by extremely sluggish reaction kinetics (e.g. Tracy & McLellan, 1985; Bohlen, 1986; S. Harley pers. comm., 1996). The possibility that corundum + quartz is a *stable* assemblage was suggested by Guiraud et al. (1996) for ironstones from In Ouzzal, Algeria. Guiraud et al. (1996) hypothesised that taking into account the uncertainties in relevant thermodynamic data, corundum + quartz may be stable at pressure-temperature conditions above 1100°C and 12kb.

Using the thermodynamic dataset of Powell & Holland (1988, 1994), a simple phase diagram for the components Fe_2O_3-Al_2O_3-SiO_2 was constructed for the phases corundum, sillimanite and kyanite with quartz in excess (see Figure 4.8). Using ideal (unit) activities for all phases, the corundum-sillimanite-kyanite (+ quartz) invariant point is located at 1104°C and 16kbar with relatively small calculated uncertainties (±36°C, ±0.9kb). In reality, however, these phases are unlikely to have ideal (unit) activities due to the measured Fe^{3+} impurities. Although the precise effects of Fe^{3+} impurities on mineral activities are not understood, small changes in the alumina activity of corundum can markedly expand the stability field of corundum + quartz to lower temperatures and pressures (see Figure 4.8). When combined with the large calculated thermodynamic uncertainties (up to ±5kb and ±300°C - independently calculated here and also

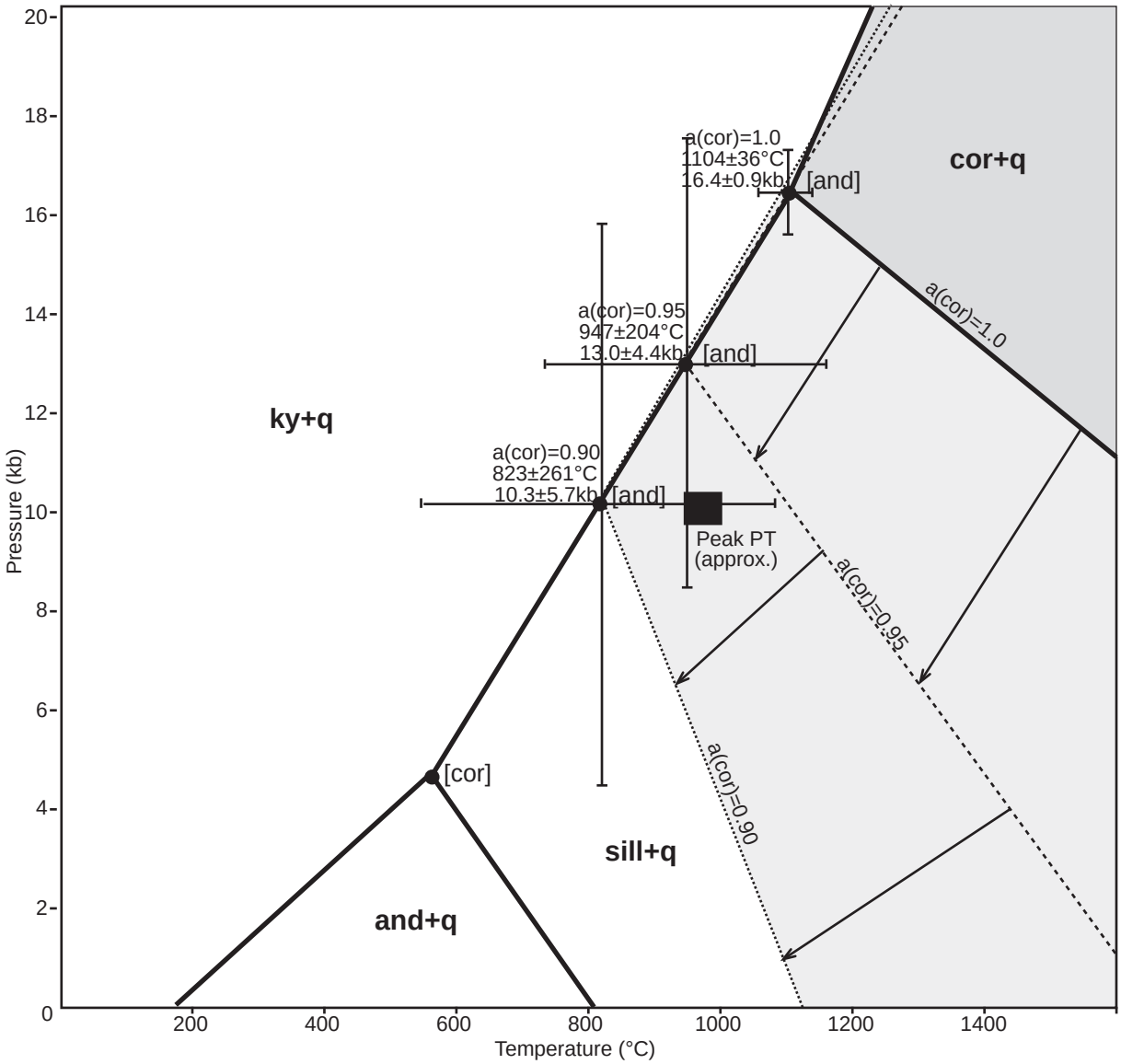

Figure 4.8 Theoretical phase diagram for the Al_2O_3-SiO_2 binary system for the aluminosilicates and corundum (with quartz in excess) calculated using the internally consistent dataset of Holland & Powell (1990, 1994). Slight reductions in corundum activity result in the significant expansion of the corundum+quartz stability field (shaded) to lower temperatures and pressures, with a concomittant increase in errors on the corundum-sillimanite-kyanite-quartz invariant. The peak PT conditions inferred for the Moondrah Gneiss are shown by the black box (>950°C, >10kb), indicating that taking into account the measured corundum impurities (ferric iron) and the large calculated errors it appears quite feasible to stabilise corundum+quartz at these conditions (see text for more details).

outlined by Guiraud et al., 1996), it appears quite feasible to stabilise corundum + quartz at the peak metamorphic conditions inferred for the Ooldea granulites (~950°C, ~10kb - see §4.3.5).

4.3.4 Evidence for osumilite

The Ooldea granulites preserve Stage 2 granular hypersthene - sapphirine - quartz - K-feldspar - plagioclase ± cordierite mosaics which clearly pseudomorph an earlier, coarse grained, polygonal phase (see Figure 4.6). This assemblage has been inferred to represent osumilite breakdown by several workers (e.g. Ellis et al., 1980; Grew, 1982; Sandiford et al., 1987) and has been confirmed experimentally by Carrington & Harley (1995a). Area scans of these granular mosaics using the Electron Dispersion Specrometer on the Cameca SX51 Microprobe at CEMMSA, University of Adelaide, indicate that these textures are chemically and stoichiometrically equivalent to naturally occurring osumilite, strongly implying that the hypersthene-sapphirine bearing, Stage 2 reaction textures replaced early granoblastic osumilite (see Table 4.1).

Osumilite is now recognised as an important potassic phase in high grade granulites (e.g. Carrington & Harley, 1995b). Recent experimental petrology suggests osumilite is stable above about 850°C at moderate pressures (Carrington & Harley, 1995a), however, naturally occurring osumilite is extremely rare in the geological record, and has only been observed in a few very high grade terranes (e.g. Berg & Wheeler, 1976; Maijer et al., 1977; Bogdanova et al., 1980; Ellis et al., 1980; Arima &

	1	2	3	4	5	6
SiO_2	60.03	61.57	61.73	62.18	60.37	60.86
TiO_2	0.09	0.00	0.00	0.12	0.22	0.14
Al_2O_3	22.71	24.10	23.75	21.58	22.95	23.88
MgO	7.75	7.16	8.50	7.46	7.02	8.31
CaO	1.47	0.01	0.00	0.06	0.00	0.12
MnO	0.49	0.00	0.00	0.07	0.13	0.01
FeO	3.27	2.81	1.25	3.97	3.95	2.07
Na_2O	1.32	0.03	0.32	0.22	0.59	0.42
K_2O	2.86	4.26	4.45	4.12	4.14	4.26
TOTAL	**100.00**	**99.93**	**100.00**	**100.06**	**99.37**	**100.31**
Si	10.02	10.18	10.16	10.36	10.13	10.06
Al [4]	1.98	1.82	1.84	1.64	1.87	1.94
Total [4]	12.00	12.00	12.00	12.00	12.00	12.00
Al [6]	2.49	2.87	2.77	2.60	2.67	2.71
Fe	0.46	0.39	0.17	0.55	0.55	0.29
Mg	1.93	1.76	2.08	1.85	1.77	2.05
Mn	0.07	0.00	0.00	0.01	0.02	0.00
Ti	0.01	0.00	0.00	0.02	0.03	0.02
Total [6]	4.95	5.02	5.02	5.03	5.04	5.06
Ca	0.26	0.00	0.00	0.01	0.00	0.02
Na	0.43	0.01	0.10	0.07	0.19	0.13
K	0.61	0.90	0.93	0.88	0.89	0.90
TOTAL	**18.25**	**17.93**	**18.05**	**17.99**	**18.12**	**18.12**
X_{Mg}	0.81	0.82	0.92	0.77	0.76	0.88

1 = Average EDS area scan for Stage 2 hy-sa-plag-Kf-q mosaics in the Moondrah Gneiss
2 = Experimental osumilite composition of Carrington & Harley (1995a)
3 = Osumilite from Enderby Land, Antarctica (Ellis et al., 1980)
4 = Osumilite from the contact aureole of the Nain Anorthosite Complex, Labrador, Canada (Berg & Wheeler, 1976)
5 = Osumilite from Rogalund, Norway (Maijer et al., 1977)
6 = Osumilite from Enderby Land, Antarctica (Grew, 1982a)

Table 4.1 Comparison of EDS area scans of hypersthene-sapphirine-plagioclase-K-feldspar-quartz±cordierite granular mosaics from the aluminous gneiss in Ooldea DDH2 with measured experimental and naturally occurring osumilite compositions.

& Gower, 1991). The scarcity of osumilite in the geological record is testament to its instability under retrograde conditions and at higher pressures, as evidenced in the aluminous granulites in the Moondrah Gneiss (see §4.3.5 below).

4.3.5 Petrogenetic evolution of the aluminous granulites

As detailed in Section 4.2, aluminous granulites in the Moondrah Gneiss underwent a complex, three stage textural evolution. Stage 1 breakdown of early, Fe^{3+}-rich spinel to sillimanite-magnetite and sapphirine-magnetite intergrowths are discussed in Section 4.3.2. Subsequent Stage 2 and 3 fine grained mineral parageneses can be described using the system K_2O-FeO-MgO-Al_2O_3-SiO_2-O_2 (KFMASHO) for the phases osumilite, cordierite, sapphirine, hypersthene, biotite, garnet, sillimanite, K-feldspar, quartz, magnetite and melt. As noted previously, it is clear that the Moondrah Gneiss is relatively oxidised. Although magnetite is present in varying quantities in the aluminous granulites (2-15wt%), it appears to be an inert phase and is not involved in any post-Stage 1 reaction textures. One effect of high fO_2 is to partition the bulk of the iron into magnetite (as Fe^{3+} and Fe^{2+}) leaving the effective silicate rock composition relatively magnesian. In low-fO_2 systems, it is recognised that relatively iron-rich bulk compositions do not "see" many KFMASH univariant equilibria, thus do not record changes in pressure and temperature (e.g. Carrington & Harley, 1995a), however the low variance mineral assemblages in the aluminous granulites in the Moondrah Gneiss demonstrate that at relatively high fO_2, iron-rich bulk compositions will "see" KFMASH equilibria since they have a magnesium-rich effective bulk composition. The compatibility diagram shown in Figure 4.9 indicates that the silicate component of the aluminous gneiss must have an effective silicate bulk composition of X_{Mg}~0.82-0.85 (see explanation below) even though the overall bulk composition approaches X_{Mg}<0.5. Compatibility relationships suggest that spinel and garnet-bearing assemblages are unlikely to form in systems of this effective bulk composition. Hence oxygen fugacity can play a dual role in stabilising very high grade mineral assemblages: (i) the presence of Fe^{3+} can expand the stability fields of diagnostic aluminous phases

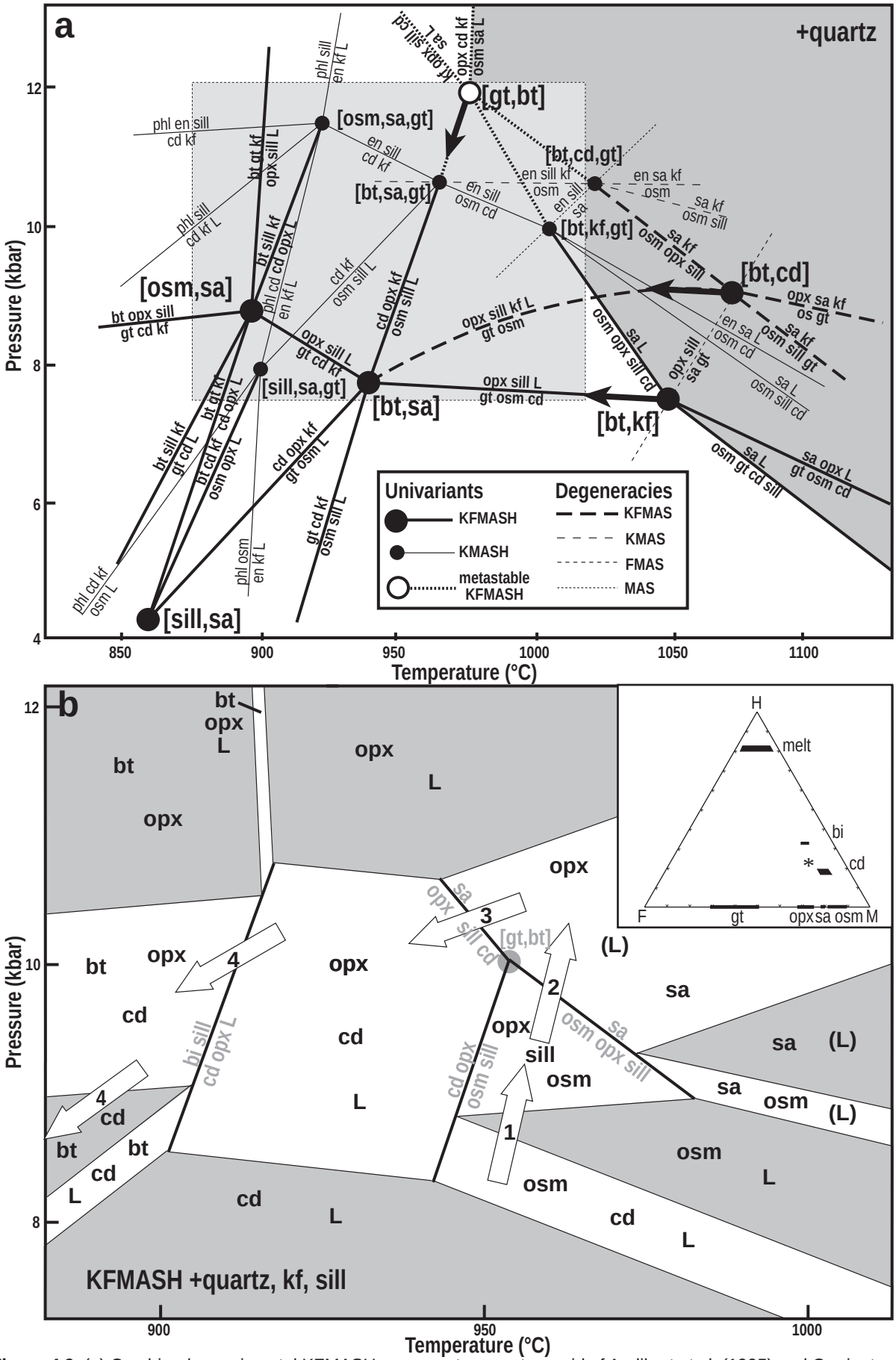

Figure 4.9 (a) Combined experimental KFMASH pressure-temperature grid of Audibert et al. (1995) and Carrington & Harley (1995a, 1995b) with quartz in excess. The sapphirine-quartz stability field (top RHS) is shaded. (b) Semi-quantitative pressure-temperature pseudosection constructed for the area represented by the shaded rectangle in (a). Pseudosection is constructed for a bulk composition of X_{Mg}~0.82-0.85 (* on HFM diagram) relevant to the aluminous hypersthene-sillimantie gneiss. Reactions 1 to 4 (see text) are represented by the arrows which combine to define an anticlockwise PT path.

such as sapphirine and spinel to lower PT conditions (as outlined above), and (ii) high fO_2 can modify the effective bulk composition of a system, potentially stabilising Mg-Al rich phases.

Recent experimental work by Audibert et al. (1995) and Carrington & Harley (1995a,b) defined a quantitative petrogenetic grid in the KFMASH system (and related sub-systems and degeneracies) for relatively low-fO_2 conditions involving the above phases over a pressure-temperature range of 4-12kb and 850-1100°C (see Figure 4.9a). In order to apply the higher fO_2 assemblages found in the aluminous granulites to this grid, the potential expansion of the sapphirine stability field must be taken into account. As a result, sapphirine-bearing invariant points are thought to move along the sapphirine-absent univariants towards sapphirine-absent invariant points (e.g. [osumilite, sapphirine] and [biotite, sapphirine] in Figure 4.9a). Hence the [garnet, biotite] invariant, which is metastable at low fO_2, will become stable when the fO_2 is sufficient to move it below the terminating KMASH [biotite, sapphirine, garnet] subsystem invariants. Ultimately, the sapphirine stability field may expand sufficiently to exclude the [biotite, sapphrine] and/or [osumilite, sapphirine] invariants, dramatically changing the topology of the grid. In the aluminous gneiss, the occurrence of the assemblage hypersthene-sillimanite-sapphirine-quartz-K-feldspar-(melt), and the subsequent replacement of sapphirine by cordierite can only be explained if the [garnet, biotite] invariant is stable (see Figure 4.9a). Hence the topology of the published grid is relevant to these assemblages, although the expansion of the sapphirine stability field and the resultant stability of the [garnet, biotite] invariant must be taken into account.

A common observation in high grade rocks is that mineral assemblages and reactions can rarely be described via univariant equilibria, thus the derivation of pressure-temperature information from univariant equilibria alone may lead to erroneous conclusions. Hence pressure-temperature grids which show higher variance equilibria (such as pseudosections which are constructed for a particular bulk composition) are far more likely to be relevant to naturally occurring mineral assemblages. In the aluminous gneiss, the inferred mineral assemblages and reactions are mainly divariant or trivariant, therefore are likely to be "seen" by a pseudosection drawn for the appropriate bulk composition. KFMASH phase relationships in the aluminous granulites can be qualitativley visualised using a triangular HFM (H_2O-FeO-MgO) projection from quartz, K-feldspar and sillimanite. The observed mineral assemblages constrain the effective silicate bulk composition of the aluminous granulites to X_{Mg} ~ 0.82-0.85. A qualitative pressure-temperature, KFMASH pseudosection (see Figure 4.9b) appropriate to the effective (i.e. magnetite absent, Mg-rich) bulk composition of the aluminous gneiss (X_{Mg} ~ 0.82-0.85) was constructed from the grid shown in Figure 4.9a, using an HFM compatibility diagram. Melt-absent, KFMAS degenerate equilibria are still relevant in this pseudosection, and still proceed in the presence of melt. The slopes of the divariant fields are estimated from the slopes of the subsystem (degenerate) univariants in the published petrogenetic grid. The widths of the divariant fields are qualitatively derived from the experimental data of Audibert et al. (1995) and Carrington & Harley (1995a). All inferred mineral reactions outlined in Section 4.2.1 are "seen" by this pseudosection: Stage 2 reaction textures are denoted by arrows 1 and 2 on the pseudosection, and indicate the up-pressure breakdown of the early, coarse grained cordierite and osumilite respectively, with a peak pressure above 10kb. The subsequent Stage 3 retrograde mineral reactions are denoted by arrows 3 and 4 on the pseudosection, indicating slightly decompressive cooling from Stage 2 peak conditions in excess of 950°C and 9.5kb. The early, granoblastic spinel-cordierite-quartz granulites probably equilibrated at temperatures in excess of 850°C at pressures less than 7kb (e.g. Waters, 1991). The subsequent breakdown of Fe^{3+}-rich spinel to magnetite + sillimanite is interpreted to be caused by the prograde pressure increase. These pressure-temperature vectors combine to define an *anticlockwise* pressure-temperature path involving near-isothermal compression from around 6-8kb to above 9.5kb, followed by cooling at slightly decreased pressures. The tectonic implications of this pressure-temperature path are discussed in Section 4.6.

4.3.6 Discussion

The pressure-temperature constraints inferred for the aluminous gneiss suggest peak metamorphic conditions in excess of 950°C and 9kb (see §4.3.2). Other lithologies from Ooldea also support this pressure-temperature data, such as: (i) the stability of the sapphirine-quartz and spinel-quartz parageneses, (ii) the presence of mesoperthite-antiperthite pairs in felsic gneiss, and (iii) the very high Al_2O_3 content in orthopyroxene (up to 10 weight percent) which is a key indicator of ultrahigh temperature metamorphism (Annersten & Seifert, 1981; Harley, in press). The coexistance of plagioclase with K-feldspar-rich perthite suggests that temperatures were probably below 1000°C, in contrast with other ultra-high temperature rocks which contained only one super-solvus feldspar, now mesoperthite (e.g. Sandiford & Powell, 1988). The presence of sapphirine inclusions in garnet indicates that the Ooldea granulites were at elevated

temperatures (within the high-fO_2 sapphirine-quartz stability field) prior to garnet growth. Since garnet growth occurred early in the metamorphic history of the Moondrah Gneiss, this indicates that the Ooldea granulites have undergone a prolonged ultrahigh temperature history. The peak PT conditions inferred for the aluminous gneiss are supported by average pressure calculations using Thermocalc (Powell & Holland, 1988, 1994) in conjunction with the internally consistent dataset of Holland & Powell (1990) for late, fine grained garnet-hypersthene-plagioclase-quartz intergrowths in the magnetite gneiss, which yield a pressure of 9.5±1.2kb at 950°C. Average temperature calculations yield unrealistically low results for the reasons described earlier in this section.

The preservation of fine grained, ultra-high temperature (UHT) mineral assemblages within the high strain fabric suggests that deformation occurred at extreme metamorphic conditions and that post-kinematic cooling must have been rapid. Presumably, slow cooling would have resulted in the annealing (i.e. coarsening) and retrogression of the UHT fabric, since such assemblages are highly sensitive to changes in pressure and temperature.

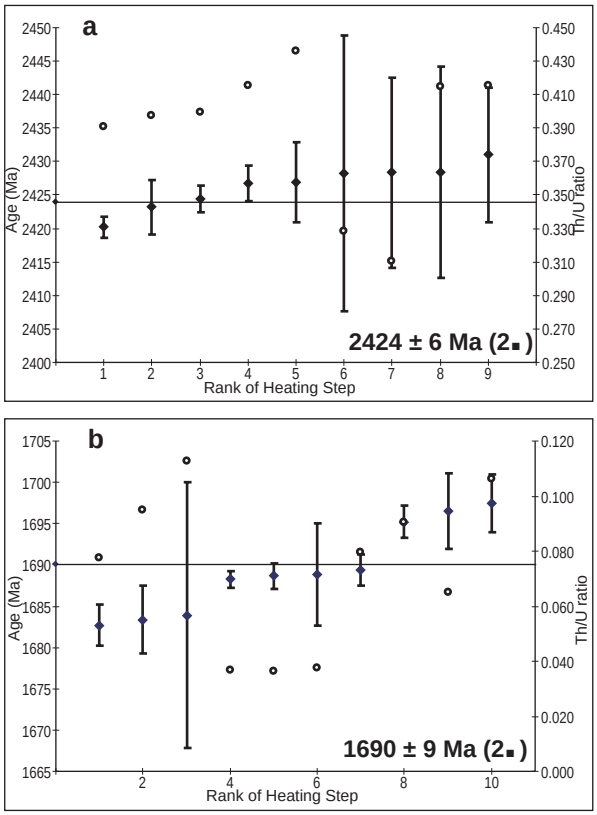

Figure 4.10 Pb-Pb zircon evaporation results for Ooldea DDH2 153-154m. Solid diamonds = $^{207}Pb/^{206}Pb$ age (with 1▪ error bars), open circles = model initial Th/U ratio. (a) Early Palaeoproterozoic inherited zircons, (b) Late Palaeoproterozoic metamorphic zircons (see Appendix 4 for more data).

4.4 Geochronology of the Moondrah Gneiss

Rb-Sr isotope data indicates that the Ooldea DDH2 drill core has a minimum metamorphic age of ~1700 Ma (Parker, 1993). Following the recognition of abundant zircons in several sections of the Ooldea DDH2 drill core, both U-Pb SHRIMP and Pb-Pb evaporation ages were obtained (see Appendix 4 for a summary of the techniques). Both sets of zircon data are derived from the same sample interval (153-154m). The zircon population is dominated by small (<0.1mm), ellipsoidal, rounded, presumed metamorphic zircons. Many of the zircons have nebulous, irregularly shaped, higher-U cores which constitute between 10-80vol% of the individual grains. This structural habit is indicative of recrystallisation of the zircons during high grade metamorphism (R. Pankhurst pers. comm., 1997). Some have very thin, low-U rims. The low Th/U ratios and the rounded morphologies of the this population support the notion that they have a metamorphic origin (e.g. Williams & Claesson, 1987; Söderlund, 1996). There is also a minor population of large (~0.2mm), ellipsoidal, faceted, structurally simple zircons, which are identical in morphology (and age - see below) to metamorphic zircons found in the Christie Gneiss (see Chapter 5).

Pb-Pb analysis using the Kober zircon evaporation technique (see §2.4.2.4) yielded precise ages of 1690±9 Ma for the rounded, metamorphic zircons, and 2424±6 Ma for the large, faceted zircons (see Figure 4.10). U-Pb SHRIMP analysis yielded a concordant age of 1653±8 Ma for the rounded metamorphic zircons, with inherited components (i.e. the nebulous cores) at ~1700 Ma (Daly et al., 1997). The Kober technique could not resolve the low-U parts of the younger population, and the 1690±9 Ma age is interpreted to represent inherited components. The relevance and significance of these ages is discussed in Section 4.5. Notably, the very thin, low-U rims present of some of the younger zircons have not yet been dated using the SHRIMP (M. Fanning pers. comm., 1997).

4.5 Geological synthesis

The information presented in this chapter shows that potentially widespread, ultrahigh temperature (UHT) metamorphism occurred in the southern Nawa Subdomain during the late Palaeoproterozoic (~1690-1650 Ma), and that the late stages of this metamorphism were accompanied by high strain, compressional deformation. Regional-scale geophysical data suggests that the strongly magnetised Moondrah Gneiss is part of a ~50km wide, ~northwest trending mobile belt which marks

the southern boundary of the Nawa Subdomain, and is defined by coincident magnetic and gravimetric anomalies (see Chapter 3). This mobile belt exhibits a markedly different geophysical signature (both in terms of geometry and intensity) to the rest of the Nawa Subdomain. Clearly future work must focus on more precisely defining the age and regional tectonic significance of this little-known mobile belt.

Geochronological data shows that UHT metamorphism in the Moondrah Gneiss resulted in initial zircon growth at ~1690 Ma, followed by recrystallisation of these zircons and new zircon growth at ~1653 Ma. The main zircon-forming "event" occurred at ~1690 Ma. A fundamental recognition in interpreting zircon ages in granulites is that zircon growth may not have occurred at peak metamorphic conditions (Roberts & Finger, 1997). Zircons are unlikely to grow or dissolve in a metamorphic rock unless a (partial) melt is present, since zirconium is usually partitioned into protolithic zircons which are insoluble at subsolidus conditions (Rubin et al., 1993; Roberts & Finger, 1997). Therefore metamorphism which is not accompanied by partial melting is unlikely to be recorded by zircon growth. Hence the major melt-producing metamorphism in the Moondrah Gneiss probably coincided with maximum zircon growth at ~1690 Ma. Partial melting in the Moondrah Gneiss is manifest in the early, coarse grained, granoblastic, migmatitic mineral associations. The subsequent fine grained textural development of the Moondrah Gneiss during high strain deformation (leading to the peak metamorphic conditions; >950°C, >9.5kb) is unlikely to be recorded by signficant zircon growth. The presence of younger, recrystallised rims, and a minor population of younger zircon (~1653 Ma) may well reflect the actual peak metamorphic conditions. The presence of late, retrograde, hydrous phases (in particular biotite and cordierite) indicates the presence of small amounts of melt in the rock, and that these fluids were probably sufficiently abundant to cause some zircon growth during peak metamorphism. However the question remains as to the geological significance of the apparent ~37 Ma time gap between zircon growth "events", and there are three possible explanations: (i) that there were two, unrelated metamorphic "events" ~37 Ma apart, (ii) that the thermal perturbation was long-lived and zircon growth occurred when partial melt was present, or (iii) that the bimodal age distribution is a statistical artefact of a broad spread of ages caused by dynamic zircon growth during the period ~1690-1650 Ma (alluded to by Fraser et al., 1997).

The peak metamorphic conditions inferred for the Moondrah Gneiss (>950°C, >10kb) represent the extremes of crustal metamorphism, and it is very likely that these rocks were metamorphosed in the lowermost parts of the crust in close proximity to the moho (UHT metamorphism is unlikely to occur in the mid-crust, since the lower crust is very unlikely to withstand even hotter temperatures without melting and/or flowing laterally). Cooling rates in the lower crust are likely to be slow (see below), therefore the possibility that the bimodal age population represents sporadic zircon growth during a long-lived thermal perturbation is favoured here.

4.6 Geodynamic considerations

The metamorphic conditions inferred for the Ooldea granulites are unique in the Australian geological record - they are the highest grade metamorphic rocks yet reported in the Australian continent. The documentation of such high grade terranes constitutes an important step towards understanding the tectonic processes which lead to ultrahigh temperature metamorphism, and the potential causes of the massive thermal events which punctuated the Proterozoic evolution of Australia. The extremes of crustal metamorphism have become increasingly recognised in the geological record, with both ultrahigh pressure (UHP) and ultrahigh temperature (UHT) metamorphism now generally accepted by most workers (Harley, in press). Harley (in press) defined ultrahigh temperature metamorphism as a subset of medium-pressure granulite facies metamorphism involving peak temperatures of 900-1100°C at pressures of 7-13kb. Well known ultrahigh temperature terranes include the Napier Complex, in Enderby Land, Antarctica (e.g. Sheraton et al., 1980; Ellis et al., 1980; Grew, 1980; Sandiford, 1985), Wilson Lake, in Labrador, Canada (e.g. Morse & Talley, 1971; Arima et al., 1986; Currie & Gittins, 1988), the Labwor Hills in northern Uganda (Nixon et al., 1973; Sandiford et al., 1987), the In Ouzzal Complex, Hoggar, southern Algeria (e.g. Kienast & Ouzegane, 1987; Bertrand et al., 1992; papers in Kienast et al., 1996), and the Eastern Ghats, southern India (Grew, 1982b; Lal et al., 1987; Dasgupta et al., 1995; Raith et al., 1997). Importantly, the age distribution and geological character of these terranes is diverse, indicating that UHT metamorphism is not confined to a particular time period or tectonic setting, therefore it is unlikely that UHT terranes share a common genesis (Harley, in press). Metamorphically, UHT terranes can be loosely grouped into those characterised by isobaric cooling (usually correlated with anticlockwise pressure-temperature paths), or those characterised by isothermal decompression (usually correlated with clockwise pressure-temperature paths) (Harley, 1989). The tectonic implications of these pressure-temperature paths have been broached by many

workers, and it is apparent that UHT metamorphism can occur in many different geological settings.

Tectonic constraints derived from pressure-temperature paths in granulite terranes usually focus on the retrograde evolution of the rocks since the signatures of prograde metamorphism are rarely preserved, largely due to fast reaction kinetics at such grades (e.g. Sandiford & Powell, 1986; Bohlen, 1987; Ellis, 1987; Harley, 1989; Fitzsimons & Harley, 1994; Dasgupta et al., 1995). However the nature of prograde metamorphism is critical to any pressure-temperature path and hence to any realistic tectonic syntheses in granulite terranes. The prograde reaction textures inferred in the Ooldea granulites provides rare constraints on the prograde pressure-temperature path, and insight into the tectonic processes which may lead to UHT metamorphism. The anticlockwise pressure-temperature path inferred for the Ooldea granulites implies that: (i) UHT metamorphism was accompanied by a significant pressure increase during high strain compressional deformation; (ii) cooling was near-isobaric and occurred at slightly decreased pressures during the latter stages of deformation; and (iii) there is no metamorphic record for the exhumation of the rocks. The preservation of the fine grained, high strain fabric and associated arrested reaction textures indicates that cooling occurred relatively rapidly after deformation ceased, and deformation occurred late during the UHT thermal perturbation.

Anticlockwise pressure-temperature paths have been inferred in many terranes where isobaric cooling has occurred (e.g. Harley, 1989), although in most documented terranes there is very little direct textural or thermobarometric evidence for compression prior to cooling. Indeed, anticlockwise pressure-temperature paths derived directly from reaction textures have only been inferred from a few terranes (e.g. Waters, 1986; Motoyoshi & Hensen, 1989; Warren & Hensen, 1989), and the Ooldea granulites are unique in the known UHT realm.

It is now widely recognised that collisional tectonic models involving conductive heating of a homogeneously thickened lithosphere are: (i) incapable of generating granulite facies temperatures in the crust at a regional scale (e.g. Harley, 1992), and (ii) cannot readily explain the the observation that many granulite terranes experienced heating prior to and during compressional deformation (e.g. Loosveld & Etheridge, 1989), hence cannot explain anticlockwise pressure-temperature paths (e.g. Harley, 1992). Models involving the decoupling of strain between the crust and the mantle lithosphere have been proposed by several workers to explain regional granulite facies metamorphism (e.g. Loosveld & Etheridge, 1989; Sandiford, 1989b; Sandiford & Powell, 1990; Sandiford & Powell, 1991; Platt & England, 1994). Such models generally favour the removal of part or all of the mantle lithosphere during crustal thickening, resulting in conductive heating of the crust and, in all likelihood, extensive mantle-derived magmatism resulting in advective heating (e.g. Sandiford, 1989b; Platt & England, 1994). Anticlockwise pressure-temperature paths characterised by near-isobaric cooling are a logical consequence of such models (e.g. Harley, 1992). The extensive, mantle-derived magmatism attendant with crustal thickening and mantle lithosphere thinning is expected to significantly weaken the crust, potentially causing greatly increased crustal thickening strains (Sandiford & Powell, 1991; Sandiford et al., 1991). This notion is supported by the Moondrah Gneiss, which experienced high strain compressional deformation late during a major thermal perturbation.

Exhumation of the Moondrah Gneiss is not recorded in the observed mineral assemblages, and was probably caused by a later, unrelated event. Several workers have argued that the scarcity of very high grade, lower crustal rocks in the geological record may be due to the unusual exhumation mechanisms required to expose them, rather than the rarity of tectonic events that caused them, and that many similar terranes may therefore remain in the lower crust until such time that they are fortuitously incorporated into an upper crustal allochton (Sandiford et al., 1987; Harley, 1989). The western Gawler Craton is dissected by numerous major, crustal scale shear zones (e.g. the Karari Fault Zone) which provide a plausible exhumation mechanism for lower crustal rocks, however the lack of accurate 3-dimensional structural data and geochronological information prevents any quantification of the exhumation of the Moondrah Gneiss.

Chapter 5
TECTONOTHERMAL EVOLUTION OF THE CHRISTIE SUBDOMAIN

5.1 Introduction

The Christie Subdomain forms a vast, northeast-trending, arcuate crustal block over 30,000km^2 in size, bound and dissected by major shear zones. Its geology is interpreted to be dominated by two lithological associations; the late Archaean to early Palaeoproterozoic *Mulgathing Complex*, and the late Palaeoproterozoic *Ifould Complex* (see Chapter 3). In the Christie Subdomain, the Mulgathing Complex is largely consists of the metasedimentary *Christie Gneiss*, which was deposited between ~2640 Ma and ~3000 Ma on an as-yet undiscovered, mid-Archaean basement (Daly & Fanning, 1993; Fanning, 1997). Deformation, granulite-facies metamorphism and minor mafic magmatism occurred during the early Palaeoproterozoic Sleafordian Orogeny (~2460-2420 Ma - Fanning et al., 1988; Daly et al., in press). The new term *Ifould Complex* has been defined in this study to describe voluminous, intermediate-felsic, I-type, ~1700-1670 Ma intrusive rocks in the Christie Subdomain. Subsequent reworking of the Mulgathing and Ifould Complexes by major Mesoproterozoic shear zones is discussed in detail in Chapter 8.

Prior to this study very little was known about the tectonothermal evolution of the Christie Subdomain. The metamorphic and structural evolution of the Mulgathing Complex was thought to be closely correlated with that of the temporally equivalent Sleaford Complex of southern Eyre Peninsula (e.g. Fanning et al., 1988; Daly & Fanning, 1993), however data generated during this study combined with that of Hand et al. (in prep.) suggests that tectonothermal activity in the Sleaford Complex was dominated by the 1.7-1.8 Ga Kimban Orogeny. Daly (1993) and Rankin et al. (1995) describe several key granulite facies mineral assemblages in the Christie Gneiss in the Mount Christie and Lake Ifould areas, however the spatial extent, nature and timing of metamorphism was not well constrained.

Prior to this study, all mapped granitoid intrusives in the Christie Subdomain were correlated with the ~1.85 Ga Lincoln Complex of the southeastern Gawler Craton, and subsequent deformation was attributed to the ~1.8-1.7 Ga Kimban Orogeny (e.g. Drexel et al., 1993; Rankin et al., 1995). The recognition that: (i) these intrusives are temporally and geologically distinct from the Lincoln Complex, and (ii) subsequent deformation and metamorphism occurred well after the Kimban Orogeny is of fundamental importance in understanding the tectonothermal evolution of the western and northern Gawler Craton.

This chapter outlines the tectonothermal evolution of the southern and central parts of the Christie Subdomain. Lithological and petrological observations are summarised in Section 5.2. Sections 5.3 and 5.4 outline its structural and metamorphic evolution. Section 5.5 contains an up-to-date summary of all geochronology in the Christie Subdomain. Section 5.6 details the regional geological significance and geodynamic problems posed by rocks in the Christie Subdomain.

Figure 5.1 Summit of Mount Christie, on which weathered banded iron formation of the Christie Gneiss outcrops.

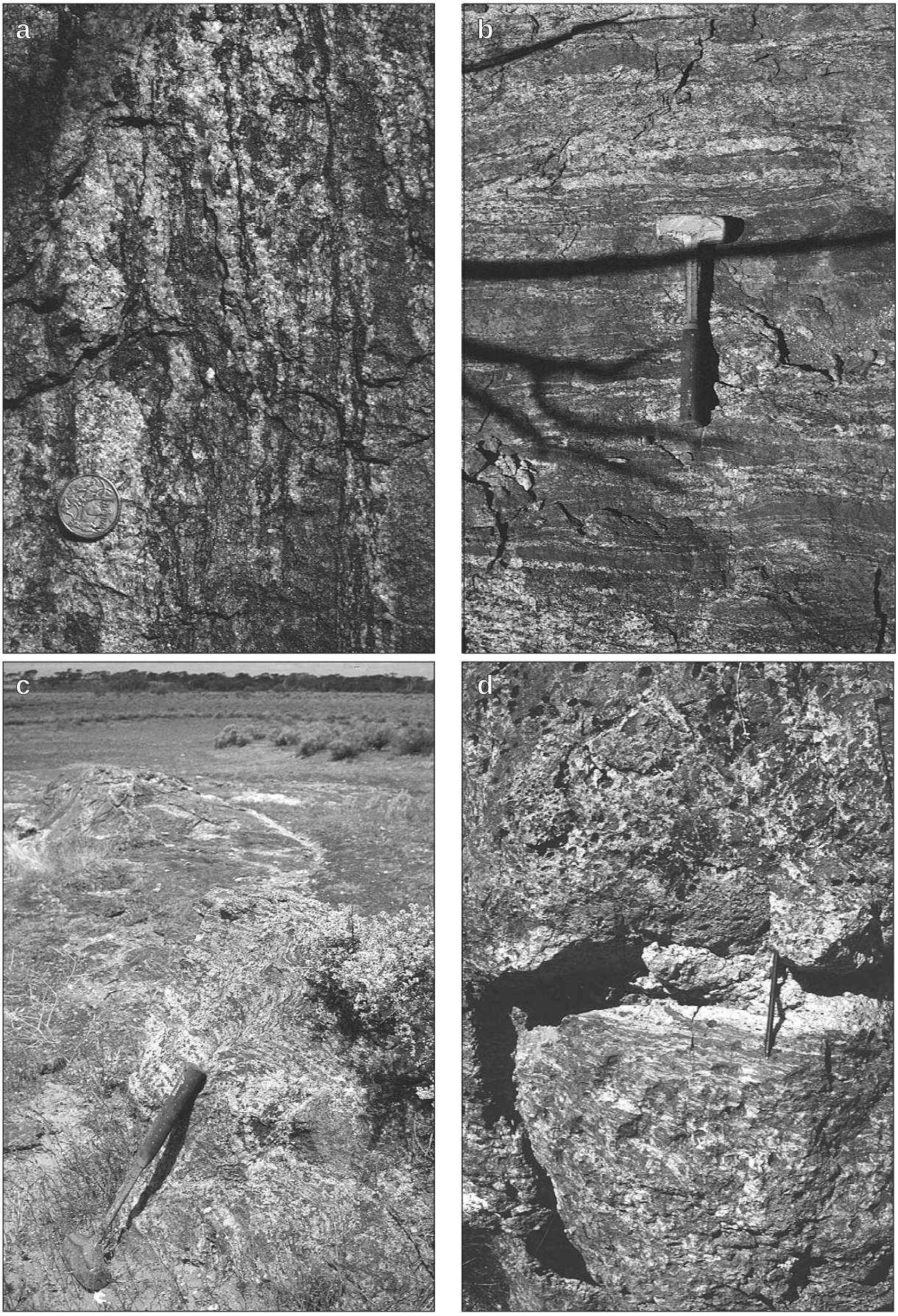

Figure 5.2 (a) Garnet-cordierite-biotite-sillimanite pelitic gneiss in the Mt Christie area. Note pre- and post-S_1 leucosomes. (b) Layered, semipelitic, garnet-biotite gneiss and 2-pyroxene-garnet±biotite mafic gneiss in the Mt Christie area. Note rootless, isoclinally folded, pre-S_1 leucosomes, and stromatic post-S_1 leucosomes. (c) Outcrop of migmatitic garnet-cordierite-sillimanite-biotite pelitic gneiss north of Lake Ifould, with coarse grained, late-kinematic pegmatites. (d) Detail of coarse grained, migmatitic, garnet-cordierite-sillimanite-biotite gneiss north of Lake Ifould. Note late shear zone and associated pegmatite (correlated with late, SZ_2 regional shear zones (see Chapter 8).

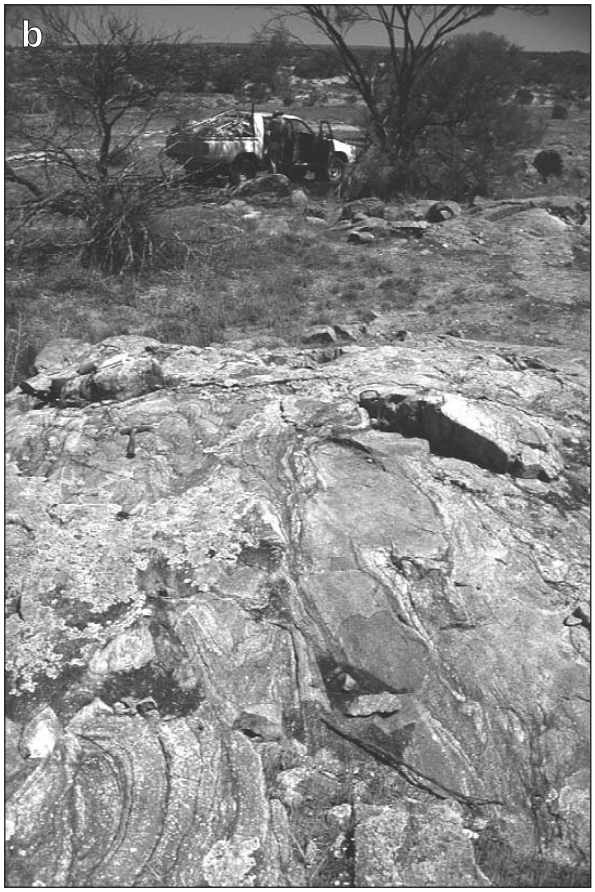

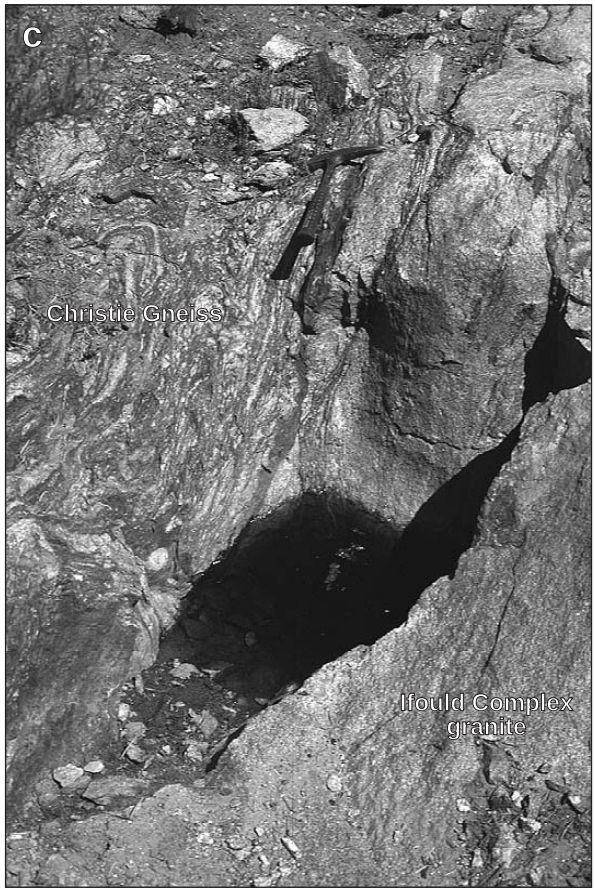

Figure 5.3 (a) Mulgathing Complex migmatitic garnet-cordierite-sillimanite-biotite pelitic gneiss + narrow layers of 2 pyroxene-garnet mafic gneiss near Mt Christie. Note pre- and post-S_1 garnetiferous leucosomes which grade into pegmatite. (b) Complexly deformed, presumed Mulgathing Complex paragneiss intruded by Ifould Complex leucogranite at an isolated rockhole south of Barton Railway Siding. (c) detail of(b). Both lithologies exhibit a NE-trending fabric parallel to that of the nearby Tallacootra Shear Zone.

Subsequent Mesoproterozoic reworking of the Christie Subdomain along major shear zones is discussed in Chapter 8. The relationship between the Christie Subdomain and other parts of the western Gawler Craton is discussed in Chapter 9.

5.2 Summary of lithological and petrological observations

5.2.1 Mulgathing Complex

The most dominant Archaean lithology in the Christie Subdomain is the Christie Gneiss, comprising a series of interlayered metasedimentary lithologies (see Figures 5.3 & 5.4). The Christie Gneiss appears to be remarkably uniform in character over a very broad region, and is dominated by migmatitic metapelites, which are interlayered with semipelitic gneiss, mafic gneiss, calc-silicate, felsic gneiss and localised banded iron formation. Lithological and petrological descriptions for the pelitic and mafic gneisses are summarised below:

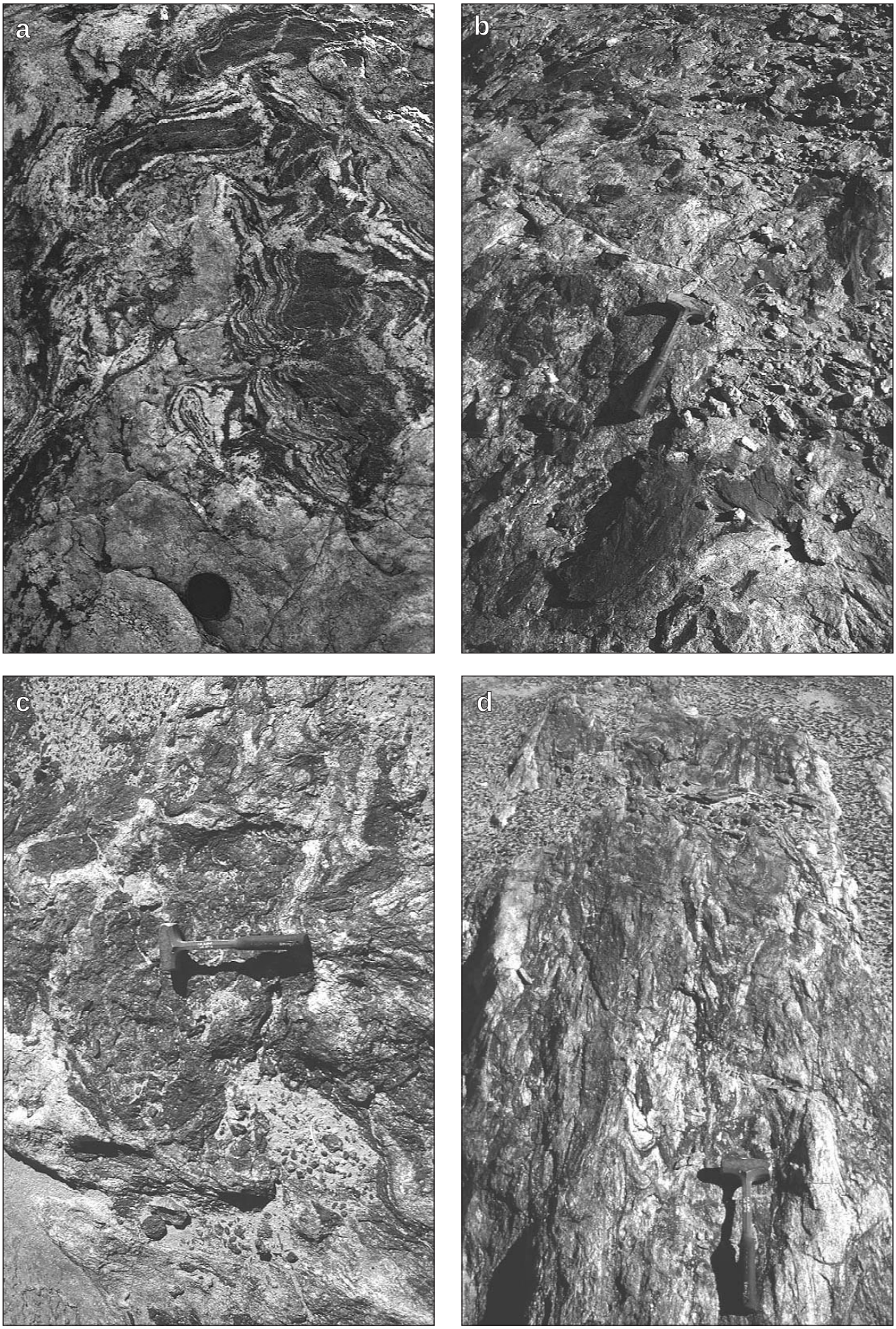

Figure 5.4 (a), (b) and (c) Partially resorbed, plastically deformed xenoliths of Christie Gneiss in Ifould Complex leucogranite, Lake Ifould south. (d) Deformed equivalent of (a) - (c) in which the Christie Gneiss is partially reworked into a orthoamphibole-staurolite-kyanite bearing schist (see Chapter 8).

Figure 5.5a Fine grained Ifould Complex agmatite, Lake Ifould south. Note angular rafts/enclaves of amphibolite in a leucocratic "matrix".

Figure 5.5b Medium grained, K-feldspar-plagioclase-quartz-biotite granite gneiss of the Ifould Complex near Pidinga Tanks, Lake Ifould (the *Lake Ifould Granite*). Geochronology sample site (see §5.5).

Pelitic gneiss

Pelitic gneisses in the Mulgathing Complex are typically medium-coarse grained, layered, weakly foliated, and migmatitic. They are dominated by coarse garnets (1-2cm), cordierite and biotite, and contain abundant garnetiferous leucosomes (and associated pegmatites) which comprise up to 60% of the rock volume (see Figures 5.2 & 5.3). The compositional layering (S_0) and layer-parallel foliation (SS_1) are isoclinally folded (SF_1), and locally overprinted by a weak-moderate SS_2 foliation which parallels the axial surface of SF_2 folds (see §5.3.1). Early, fine-medium grained garnetiferous leucosomes exhibit a penetrative SS_1 foliation and are isoclinally folded. Late, medium-coarse grained garnetiferous leucosomes crosscut the SS_1 foliation and are locally deformed by SS_2. A younger generation of very coarse grained pegmatites crosscut all Sleafordian structures and appear to be associated with retrograde features in the pelitic gneiss.

The early, coarse grained, granulite facies mineral assemblage in the pelitic gneiss is inferred to be cordierite-sillimanite-quartz-perthite ± biotite ± plagioclase ± spinel ± garnet with accessory zircon, monazite, ilmenite and rutile (see Figures 5.7 & 5.8). The S_1 fabric is defined by the alignment of peak sillimanite and biotite. Subsequent mineral parageneses involved the growth of sillimanite coronas on spinel, and the growth of large garnet porphyroblasts (see Figure 5.8), probably via the univariant reaction:

(1) spinel + cordierite ▪ garnet + sillimanite (+quartz, +K-feldspar, +melt)

The garnets generally contain both fine and coarse grained sillimanite and/or spinel inclusions (see Figure 5.7). The subsequent intergrowth of secondary, fine grained sillimanite and biotite around peak spinel-sillimanite intergrowths (see Figure 5.8) probably occurred via the reaction:

(2) garnet + cordierite ▪ sillimanite + biotite (+quartz, +K-feldspar, +melt)

Figure 5.6 Foliated, megacrystic K-felsdpar-plagioclase-quartz-biotite granite of the Ifould Complex at Wynbring Rocks. Geochronology sample site (see §5.5). Note partially resorbed mafic enclaves and compositional layering.

The generation of K-feldspar-garnet±quartz leucosomes is commonly observed in high grade metapelites, and is usually caused by the following partial melting reaction:

(3) biotite + sillimanite + quartz ▪ garnet + K-feldspar + melt

Late, fine grained, anhedral, secondary garnet growth appears to be associated with late, fine grained sillimanite and biotite, which defines the S_2 foliation (reaction 4).

In the pelitic gneisses, variable retrogression has occurred in areas which have undergone later reworking associated with major shear zones, where they grade into pelitic schists and mylonites (see Chapter 8). Minor reworking is manifest in several retrograde features in the pelitic granulites, including the partial breakdown of garnet to biotite±chlorite (along fractures), the partial breakdown of plagioclase and cordierite to very fine grained sillimanite and/or biotite, variable fine grained recrystallisation of felsic phases, and the myrmektic breakdown of early plagioclase and K-feldspar. All sampled granulites exhibit some or all of these retrograde features, indicating that retrogression is a pervasive feature in the Christie Gneiss.

Mafic gneiss

Mafic gneisses typically occur as narrow (1-20cm), structurally concordant layers within the Christie Gneiss, and are typically fine-medium grained and finely layered (see Figure 5.2). Their basic mineralogy is orthopyroxene-clinopyroxene-plagioclase-quartz ± biotite ± garnet (see Figure 5.8d). They contain narrow, layer-parallel, pre-SS_1 leucosomes, and late biotite defines a weak SS_1 foliation. The mafic gneisses do not exhibit post-SS_1 stromatic leuosomes (unlike the pelitic gneisses which underwent extensive post-SS_1 partial melting).

5.2.2 Ifould Complex

The *Ifould Complex* (new name) has been defined to describe all late Palaeoproterozoic (1700-1670 Ma), I-type intrusive rocks in the Christie Subdomain. The geophysical interpretation outlined in Chapter 3 suggests that they form large (5-30km), high magnetic intensity plutons which are deformed and truncated by regional shear zones. The geochronology of the Ifould Complex is outlined in Section 5.5.

The Ifould Complex contains two broad lithological associations: (i) a series of moderately deformed, layered orthogneisses of varying composition interpreted to be part of large, elongate, composite plutons (see Figures 5.5b & 5.6), and (ii) a complex, variably deformed, heterogeneous series of intrusives agmatites and migmatites interpreted to have formed at the pluton margins (see Figures 5.4 & 5.5a). Abundant leucosomes and pegmatite dykes intrude all lithologies. The contact relationships between the layered orthogneiss and the intrusive migmatites are gradational (see below).

The layered orthogneisses range compositionally from leucogranite to gabbro, including granite, tonalite, granodiorite, diorite and dolerite. In less deformed domains, the intrusives are migmatitic, and contain abundant distended mafic dykes, enclaves and pods. The intrusives are intermingled, and exhibit complex comagmatic contact relationships. In strongly foliated domains,lithological contacts within the orthogneiss sequence have been progressively transposed into the retrograde foliation.

The intrusive migmatites and agmatites consist of a highly complex, contorted mixture of fine grained mafics, diorite, granodiorite and

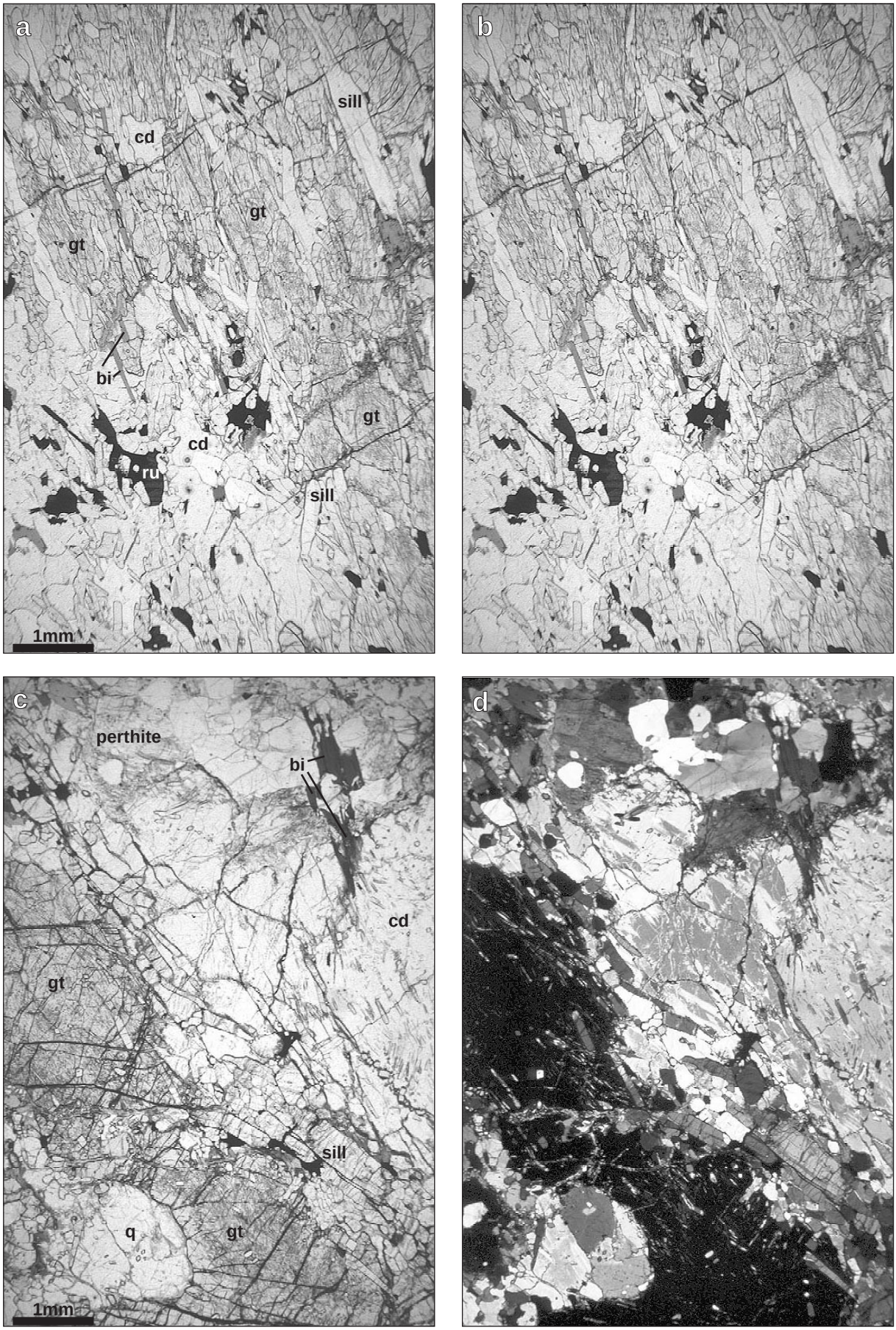

Figure 5.7 (a), (b) WGC55 garnet-sillimanite-cordierite-rutile granulite from the Christie Gneiss northwest of Lake Ifould. Note coarse, SS_1-defining, prismatic sillimanite laths surrounded by garnet. (c), (d) WGC52a garnet-cordierite-sillimanite-biotite granulite from the Christie Gneiss north of Lake Ifould. Note fine, SS_1-defining sillimanite inclusions in garnet and cordierite, and minor, late, SS_2-defining biotite laths.

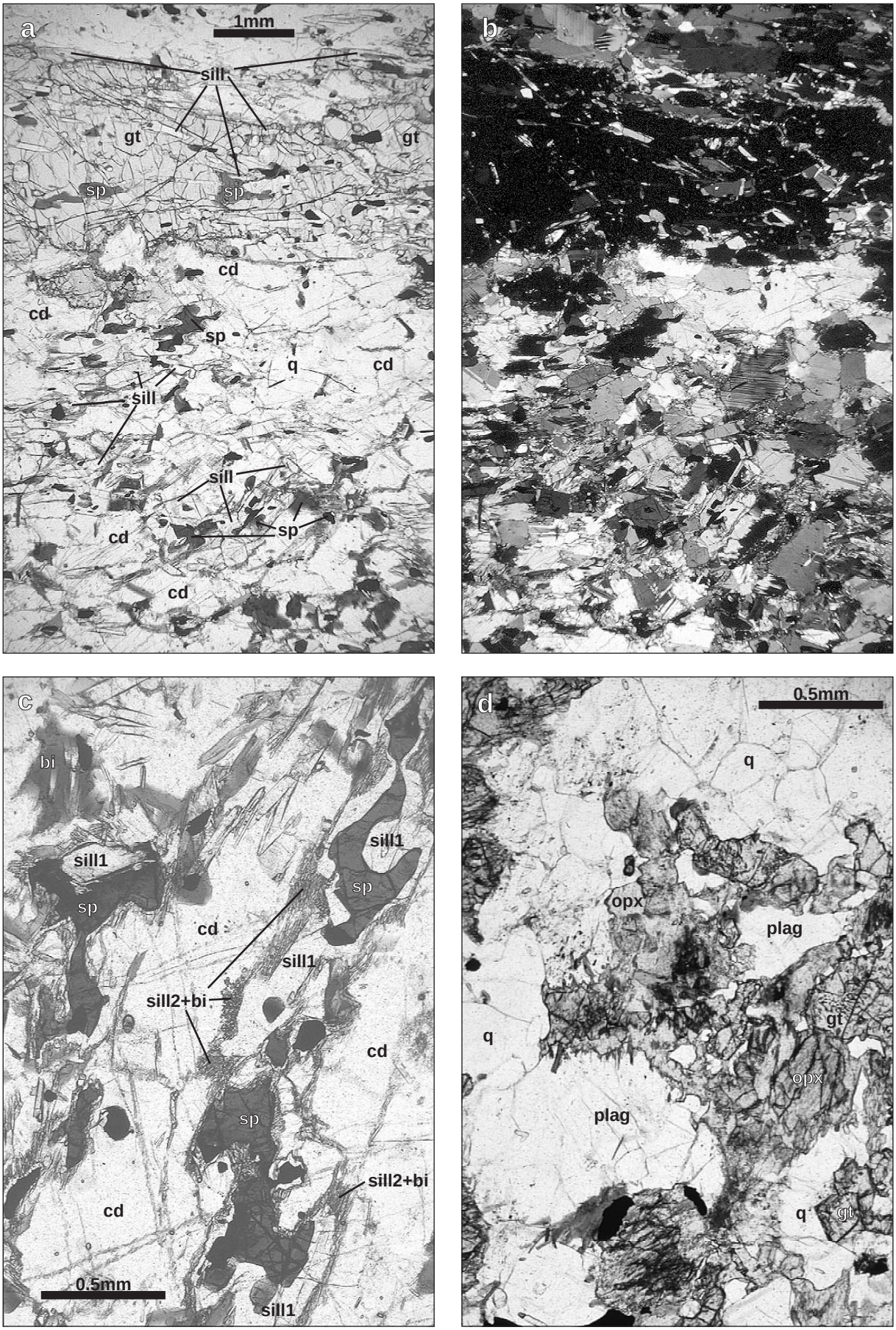

Figure 5.8 (a) and (b) Overview of WGC79 - Mulgathing Complex cordierite-garnet-sillimanite-spinel-biotite granulite from the Mt Christie area. (c) Two-stage reaction rims between early spinel and cordierite in WGC79: (i) coarse sillimanite, and (ii) fine sillimanite-biotite intergrowths. (d) WGC11 - Partially retrogressed, Mulgathing Complex, garnet-orthopyroxene mafic-intermediate granulite from the Mt Christie area. Orthopyroxene is partially repaced by cummingtonite and biotite.

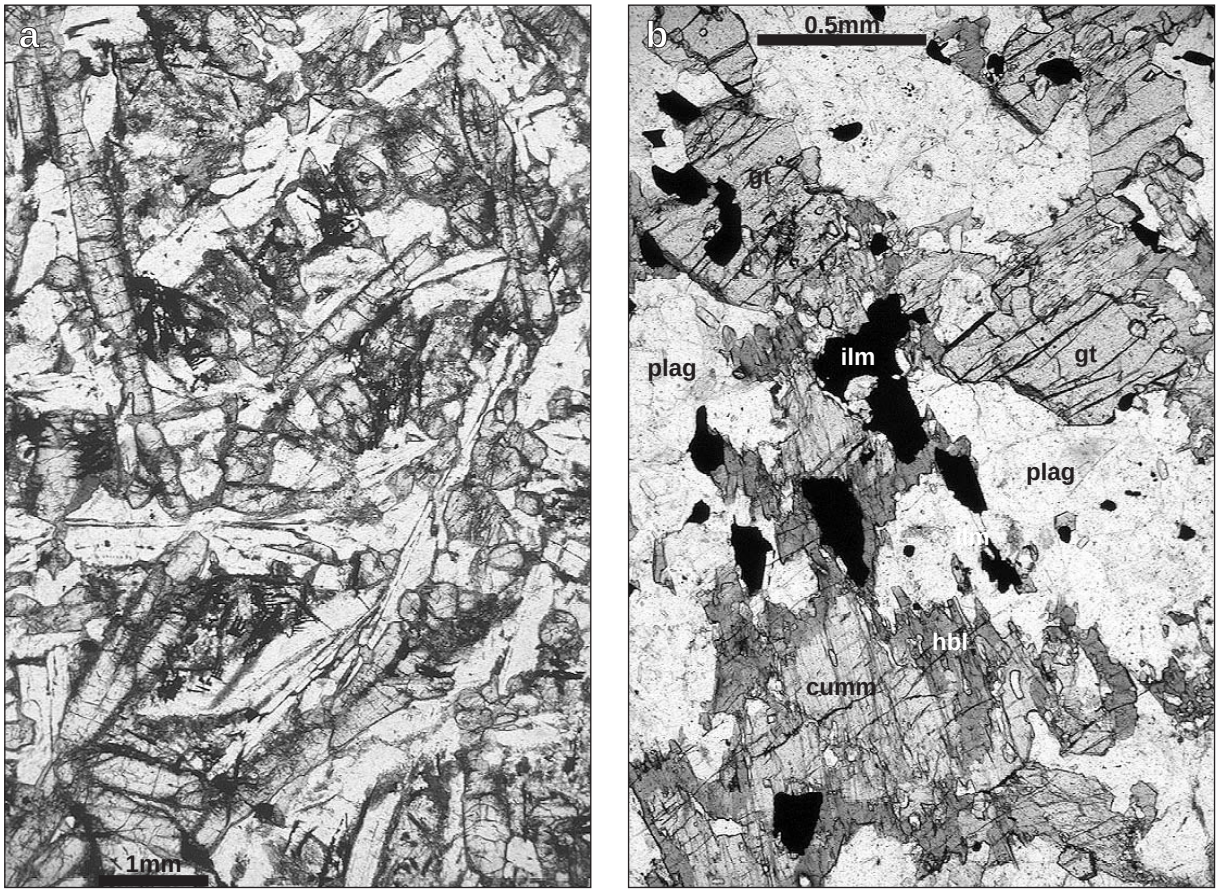

Figure 5.9 Mafic enclaves from Ifould Complex migmatites and agmatites, Lake Ifould: (a) Acicular dolerite with augite and plagioclase laths (WGC105). (b) Retrogressed mafic granulite (probably Mulgathing Complex), now a garnet-cummingtonite-hornblende gneiss (WGC182).

leucogranite (see Figures 5.4 & 5.5a). The intermediate lithologies appear to be derived from magmatic mixing and intermingling of mafic and felsic melt components. Widespread chlorite alteration in the migmatites appears to have been synchronous with the late stages of magmatism. Near contacts with the Christie Gneiss, the intrusives contain abundant partially resorbed xenoliths of metasedimentary granulite (see Figure 5.4). The agmatites consist of fine grained, biotite-hornblende rich mafic enclaves within a network of fine grained leucogranite or granodiorite (see Figure 5.5).

Abundant enclaves and xenoliths of mafic material occur in both the migmatites and the agmatites, including fine grained acicular dolerite, mafic granulites, garnet-hornblende-cummingtonite amphibolite and gabbros (see Figure 5.9). It is unclear whether they are derived from the Ifould Complex or the Mulgathing Complex.

The abundance of host rock material (presumed Christie Gneiss) within the migmatites, together with the complex nature of the igneous mixing relationships and the gradational nature of the boundary with the layered orthogneisses, suggests that the migmatites and agmatites represent the margin of the Lake Ifould composite pluton. Multiple melt injections from the evolving pluton into the country rock (i.e. the Christie Gneiss) caused complex mixing, resorption and alteration of both the country rock and earlier intrusive phases.

The intrusive migmatites and agmatites are highly deformed by the Lake Ifould shear zone, in which they form a series of heterogeneous, strongly layered, mylonitic orthoschists. With increasing strain, hornblende is progressively replaced by biotite suggesting that strain was associated with pervasive potassium metasomatism and calcium depletion (see Chapter 8).

5.3 Structural geology

The structural evolution of the Christie Subdomain occurred during two major episodes: (i) widespread ductile deformation synchronous with granulite facies metamorphism during the early Paleoproterozoic Sleafordian Orogeny, and (ii) extensive amphibolite-greenschist facies reworking of Archaean and Palaeoproterozoic protoliths during at least two phases of Mesoproterozoic deformation. The second episode is characterised by the development of extensive, regional shear zones which are discussed in Chapter 8.

5.3.1 Sleafordian Orogeny

The structural evolution of the Christie Gneiss is marked by two main phases of ductile deformation which are attributed to the Sleafordian Orogeny. SD_1 and SD_2 were associated with low-medium pressure, granulite-facies metamorphism (see §5.4.1). The first generation of structures recognised in the Christie Gneiss (SD_1) is a sub-horizontal, layer-parallel foliation (SS_1) which is axial planar to mesoscopic SF_1 isoclinal folds. SS_1 is defined by compositional layering and biotite-sillimanite alignment. During SD_1, compositional layering (S_0) within the Christie Gneiss was transposed into the SS_1 foliation. SF_1 isoclinal folds are recognised as rootless, intrafolial, folded leucosomes within the fine grained pelitic and mafic gneiss, and larger scale (0.2-1m) isoclines which fold the compositional layering. A weak SL_1 mineral elongation lineation is developed in some of the fine grained granulites.

The second generation of structures recognised in the Christie Gneiss (SD_2) is a set of open-tight, upright, doubly plunging SF_2 folds which occur over a wide range of scales, from ~0.1m to 10km. Short wavelength SF_2 folds are most spectacularly observed within outcrops of banded iron formation (e.g. Mount Christie summit), where the SS_1 foliation is folded about variably plunging, 0.1-0.3m scale tight SF_2 folds. In the pelitic gneiss, SF_2 is usually expressed as 10-100m open-tight folds which refold the SS_1 foliation and SF_1 isoclines. The intersection lineation between S_0/SS_1 compositional layering and the SS_2 foliation is well developed in SF_2 fold hinges, where a weak SS_2 foliation forms an axial planar fabric. Small scale (5-20cm), phaccolithic leucosomes occur in the thickened hinges of SF_2 folds in migmatitic lithologies, which have been dated to constrain the late stages of the Sleafordian deformation (see §5.5). Regional-scale, doubly plunging, upright folds, such as the Mulgathing Antiform (Daly, 1985; Daly & Fanning, 1993) are also interpreted to be SF_2 folds, since they parallel the shorter wavelength SF_2 folds. The variable plunge of SF_2 folds can either be attributed SD_2, or may have been caused by a later (probably unrelated) cross-folding event.

5.3.2 Later deformation

All Archaean to Palaeoproterozoic lithologies in the Christie Subdomain are variably overprinted by at least two generations of retrograde fabric. Overprinting ranges from minor but pervasive retrogression of Mulgathing Complex granulites to localised, high strain shear zones (see Chapter 8). At least two gnerations of retrograde fabric are recognised in the Christie Subdomain. Early retrograde fabrics are generally discordant with the late shear zones, and are particularly well developed in some Ifould Complex plutons (see Figure 5.6). Biotite from an early retrograde fabric in the Christie Gneiss has been dated via Rb-Sr geochronology (see §5.5.1). Later, relatively narrow, low grade shear zones crosscut and/or reactivate earlier, high grade structures.

In the Lake Ifould area, Mulgathing Complex granulites are variably overprinted by a northeast trending retrograde fabric. Effects range from very minor grain boundary recrystallisation and retrogression of granulite facies assemblage, through moderately reworked pelitic gneiss, to the incorporation of pelitic granulites into very high strain, amphibolite facies, regionally extensive shear zones. The Ifould Complex intrusives have also been variably effected by this fabric, and range from essentially undeformed intrusives (exhibiting well-defined, igneous contact relationships), through foliated gneiss (often augen gneiss), to intensely deformed mylonitic gneiss and schist. Abundant gneissic to protomylonitic Ifould Complex intrusives outcrop around the northern parts of Lake Ifould. The evolution of these shear zones is discussed in Chapter 8.

5.4 Metamorphic considerations

At least two episodes of regional metamorphism are inferred for the Christie Subdomain. The first occurred during the early Palaeoproterozoic Sleafordian Orogeny and caused widespread, low-moderate pressure, granulite facies metamorphism which was accompanied by complex ductile deformation and abundant partial melting. The second episode occurred during extensive reworking of both Archaean crust and late Palaeoproterozoic intrusives along major shear zones during the Mesoproterozoic (see Chapter 8).

5.4.1 Sleafordian Orogeny

5.4.1.1 Thermobarometry

The Christie Gneiss contains a variety of mafic and pelitic lithologies which are particularly suited to thermobarometry. Pressure-temperature estimates have been derived using two approaches; (i) cation-exchange thermobarometry and (ii) thermodynamic calculators (Thermocalc). The critical input in both approaches is the recognition of the equilibrium mineral assemblages, together with representative mineral composition measurements and appropriate activity expressions. A commonly recognised problem in obtaining peak pressure-temperature estimates in granulites is the determination of the "true" composition of the peak phases. The problem is twofold: (i) estimates of $a(H_2O)$ and $a(CO_2)$ are required for biotite and cordierite bearing

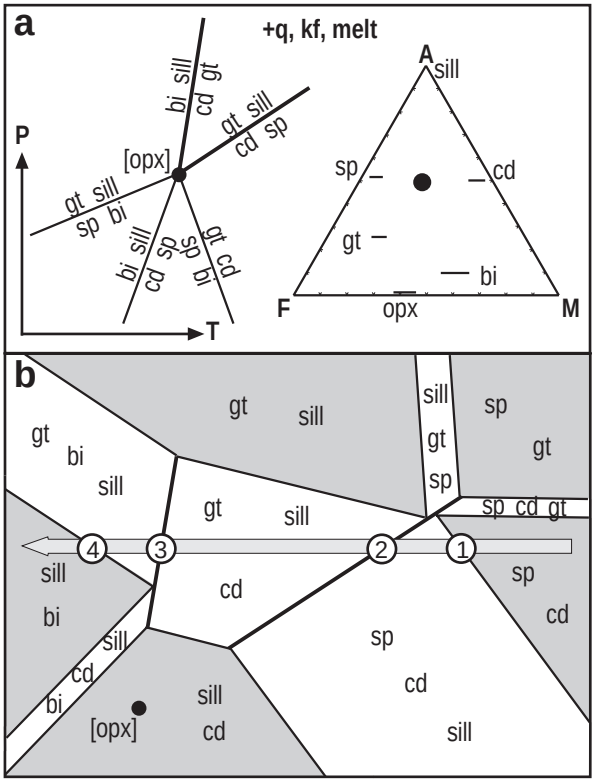

Figure 5.10 (a) [opx] Shreinemaker's bundle taken from the KFMASH PT grid of Clarke et al. (1989). AFM compatibility diagram shows measured mineral compositions in sample WGC79 (a metapelitic granulite from the Christie Gneiss) projected from quartz, K-feldspar and silicate melt. (b) Pressure-temperature pseudosection drawn for a bulk composition appropriate to sample WGC79 (black spot on AFM diagram) using the highlighted univariant equilibria in (a). The pressure-temperature path inferred from the observed mineral reactions (1-4 in text) indicates that isobaric cooling occurred in the Christie Gneiss (see text for details).

cordierite bearing assemblages, and (ii) retrograde re-equilibration of peak mineral assemblages can cause significant cation exchange between adjacent phases (which often results in significant underestimation of actual peak pressure-temperature conditions). In migmatitic metapelites such as the Christie Gneiss, it is generally recognised that a(H_2O) is relatively low (between ~0.1 and ~0.4), since silicate melts partition water (Phillips, 1980; Lamb & Valley, 1988; Young, 1989; Harley, 1992). Since calc-silicates are either volumetrically insignificant or non-existant within the Christie Gneiss, a(CO_2) is likely to be approximately zero. Garnet zoning profiles, together with the mild but pervasive retrogression of the Christie Gneiss during the Mesoproterozoic indicates that some compositional re-equilibration of peak granulite phases probably occurred, thus core mineral compositions were used in an attempt to negate these effects (notably rim compositions often produced spurious thermobarometric results). In samples containing perthite it was necessary to recalculate the peak feldspar composition based on modal proportions of K-feldspar and plagioclase in the perthite (approximately 60%:40% in most samples).

Results for geothermobarometry of peak Sleafordian granulite facies assemblages are summarised in Appendix 3. Pressure-temperature data were calculated using the average pressure-temperature approach of Powell & Holland (1988, 1994) and the internally consistent thermodynamic dataset of Holland & Powell (1990, 1994). A range of aH_2O values were tested (aH_2O=0.1, 0.3 and 0.5). Retrograde re-equilibration has clearly lead to the underestimation of peak temperatures in some samples (<600°C - clearly at odds with the observed granulite facies assemblages), however calculated pressures are remarkably consistent over the entire range of tested samples and/or mineral assemblages, occurring in the range 4.5 - 5.5kb. Of the more realistic results, temperatures of 750-800°C at pressures of 4.5-5.5kb (over a range of aH_2O) were obtained for a garnet-cordierite-sillimanite-perthite-biotite-quartz assemblage in sample WGC52A from the Lake Ifould area (see Appendix 3). In one silica-undersaturated sample from the Mount Christie area, average pressure-temperature calculations for the garnet-cordierite-spinel-sillimanite-plagioclase-corundum assemblage yielded results of 747±103°C and 4.6±0.7kb for aH_2O=0.3. Increasing aH_2O raises the calculated pressure-temperature conditions only slightly in most cases.

One mafic lithology (sample WGC11) from the Mount Christie area yielded good average pressure data with 5-6kb calculated (for a temperature range of 750-800°C) using both Thermocalc and conventional geothermobarometers for a garnet-hypersthene-plagioclase-quartz assemblage (see Appendix 3).

Hence the preferred peak pressure-temperature conditions calculated for the Christie Gneiss are 750-800°C and 4.5-5.5kb.

A late, SS_2-defining, garnet-biotite-cordierite-plagioclase-quartz assemblage from sample WGC79 yielded an average pressure of 4-5kb at around 700°C, indicating that SS_2 fabric development occurred at approximately the same pressures but possibly at lower temperatures than the peak granulite facies metamorphism. This data is consistent with the inferred pressure-temperature path for the Christie Gneiss (see §5.4.1.2 below).

5.4.1.2 Petrogenetic considerations

The mineral assemblages and reaction textures described in a pelitic gneiss (sample WGC79) from the Mount Christie area can be described using the system K_2O-FeO-MgO-Al_2O_3-SiO_2-H_2O (KFMASH) for the phases garnet, cordierite, sillimanite, spinel, biotite, K-feldspar, quartz and aqueous melt. A qualitative, KFMASH, pressure-temperature grid

relevant to low pressure, granulite facies metamorphism in pelitic rocks has been evaluated by Clarke et al. (1989) using the spinel-absent pressure-temperature grid of Grant (1985) and the biotite-absent grid of Hensen (1986) (see Figure 5.10). Since mineral assemblages and reactions in high grade metapelites can rarely be described via univariant equilibria alone, pressure-temperature grids which show higher variance phase equilibria (e.g. divariant and trivariant reactions) are likely to be far more relevant to "real" rocks. Pressure-temperature pseudosections, which are constructed for a particular bulk composition, are particularly useful tools for evaluating "real" mineral parageneses with respect to changing pressure and temperature, and provide a means for portraying higher variance phase equilibria. KFMASH phase relationships can be qualitatively visualised using the triangluar AFM (Al_2O_3-FeO-MgO) projection from quartz, K-feldspar and melt (see Figure 5.10). A qualitative pressure-temperature pseudosection relevant to the bulk composition of the Mount Christie metapelite (with quartz, K-feldspar and melt in excess) derived from the univariant grid of Clarke et al. (1989) is shown in Figure 5.8. Divariant field widths were estimated from the compatibility relationships and the measured natural variations in phase composition. Relative divariant field angles are estimated using calculated MASH and FASH subsystem equilibria, and the pseudosections of Hand et al. (1994).

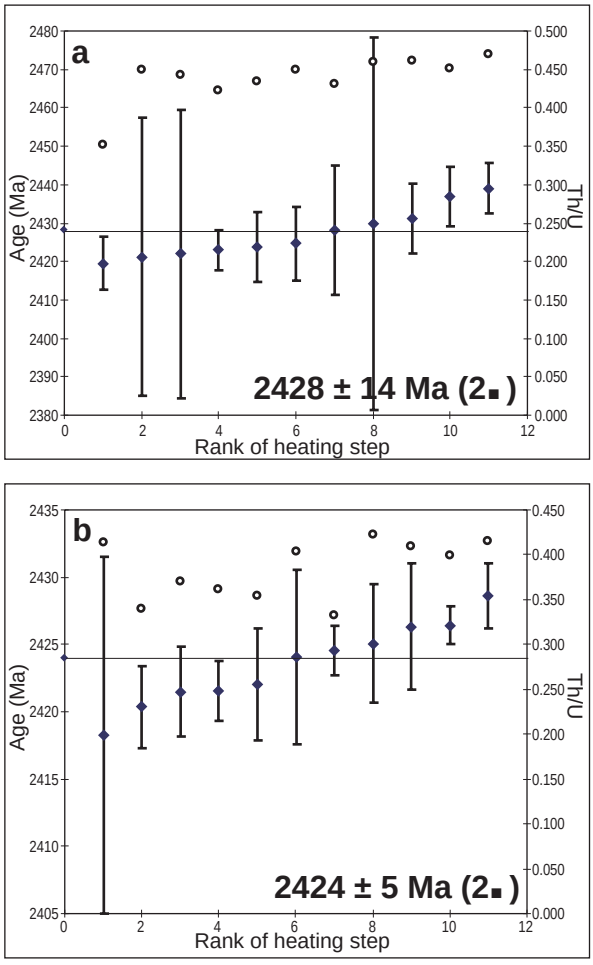

Figure 5.11 Pb/Pb zircon evaporation results for sample WGC54 - a late-kinematic pegmatite from the Christie Gneiss north of Lake Ifould. Solid diamonds = $^{207}Pb/^{206}Pb$ age (with 1▪ error bars), open circles = model initial Th/U ratio. (a) Small, prismatic zircons interpreted to have grown when the pegmatite crystallised. (b) Large, rounded, faceted "soccerball" zircons interpreted to be inherited metamorphic zircons from the surrounding granulites.

Using the pseudosection shown in Figure 5.10, the mineral assemblages and reaction textures in the Mount Christie metapelite can be used to constrain its retrograde pressure-temperature path. The early peak (trivariant) assemblage is interpreted to be cordierite-spinel-K-feldspar-quartz ±plagioclase (see §5.2.1). Subsequent reaction textures involve the growth of coarse sillimanite coronas between spinel and cordierite (reaction 1), the growth of coarse garnet porphyroblasts (which enclose the spinel-sillimanite reaction textures) (reaction 2), the intergrowth of fine grained sillimanite and biotite at the expense of cordierite (reaction 3), and the growth of medium-coarse grained, S_2 biotite at the expense of garnet (reaction 4). All four reactions can be accounted for using the grid shown in Figure 5.10, and they combine to define a pressure-temperature trajectory involving cooling at approximately constant pressure (i.e. isobaric cooling). This pressure-temperature path is supported by the thermobarometric calculations detailed in Section 5.4.1.1 above, whereby peak granulite facies assemblages, which equilibrated at ~800°C and 4.5-5.5kb, are overprinted by later, S_2-defining mineral assemblages which equilibrated at lower temperatures. The geodynamic implications of isobaric cooling in low-medium pressure granulites are discussed in Section 5.6.

5.5 Geochronology

5.5.1 Mulgathing Complex

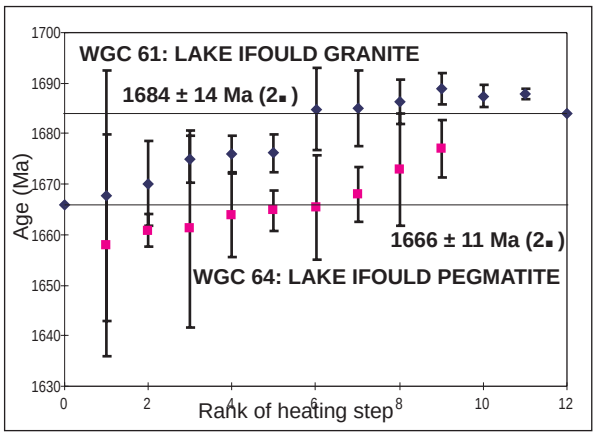

Figure 5.12 Pb/Pb zircon evaporation results for samples WGC61 (the Lake Ifould Granite) and WGC64 (a pegmatite which intrudes the Lake Ifould Granite).

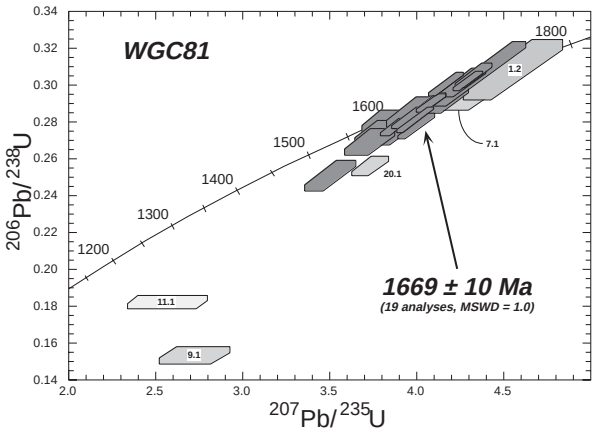

Figure 5.13 U-Pb concordia diagram showing SHRIMP zircon analyses for sample WGC81 - the Wynbring Rocks granite, plotted as 1▪ error polygons. Analyses used to calculate the weighted mean $^{207}Pb/^{206}Pb$ age are darkly shaded.

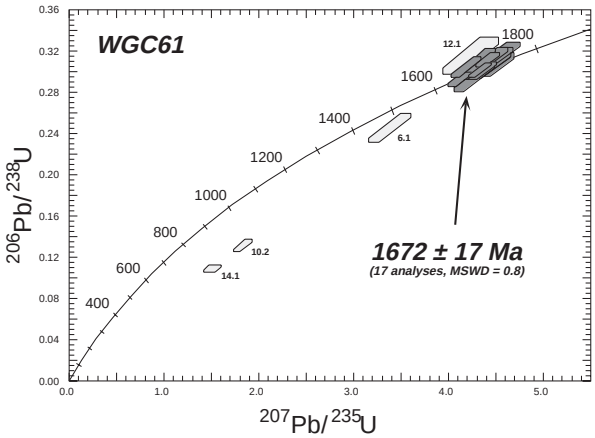

Figure 5.14 U-Pb concordia diagram showing SHRIMP zircon analyses for samples for sample WGC61 - the Lake Ifould granite, plotted as 1▪ error polygons. Analyses used to calculate the weighted mean $^{207}Pb/^{206}Pb$ age are darkly shaded.

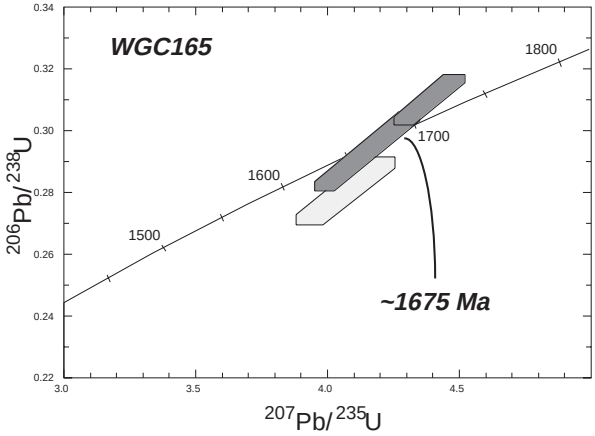

Figure 5.15 U-Pb concordia diagram showing SHRIMP zircon analyses for sample WGC165 - the Barton South granite, plotted as 1▪ error polygons.

The possibility that much of the northwestern Gawler Craton formed during the late Archaean was first postulated by Webb & Thomson (1977) who recorded an early Palaeoproterozoic Rb-Sr age of 2300±33 Ma for the post-orogenic Glenloth Granite in the Wilgena Subdomain, and Daly et al.

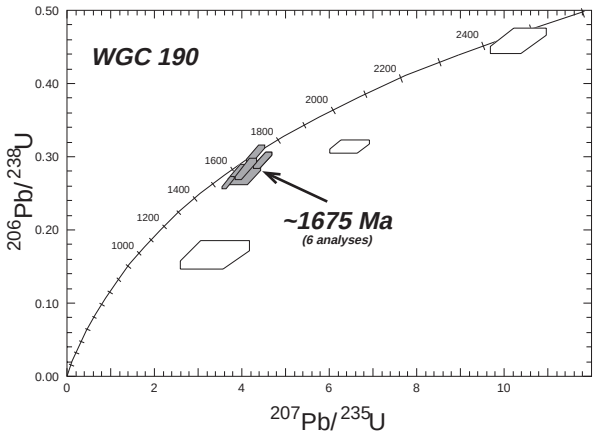

Figure 5.16 U-Pb concordia diagram showing SHRIMP zircon analyses for sample WGC190 - an unnamed rockhole at the western end of the Wynbring pluton, plotted as 1▪ error polygons.

(1978) who obtained latest Archaean - earliest Proterozoic minimum metamorphic ages of 2488±130 Ma and 2417±59 Ma for high grade gneisses from Earea Dam and Mount Christie. Subsequently many more late Archaean to earliest Proterozoic ages have been obtained via whole rock Rb-Sr, Sm-Nd and U-Pb zircon analyses (Daly & Fanning, 1993; Rankin et al., 1996; Daly et al., in press).

Granulite facies metamorphism and attendant ductile deformation and partial melting in the Mount Christie area occurred between ~2450-2420 Ma during the Sleafordian Orogeny (Daly & Fanning, 1993; Fanning, 1997; Daly et al., in press), as evidenced by numerous U-Pb zircon and Rb-Sr whole-rock ages. Metamorphic zircons from a pelitic granulite in Blackfellow Hill DDH1 gave a concordant U-Pb age of 2437±11 Ma (Fanning, 1997). Zircons from late leucosomes which segregated in the hinges of SF_2 folds (see §5.3.1) at Fingerpost Hill have been dated at ~2426 Ma (S. Daly & M. Fanning pers. comm., 1997).

Prior to this study the age of metamorphism in metapelitic granulites in the Lake Ifould area was unknown. Here, the Christie gneiss contains ubiquitous large (>0.2mm), perfectly faceted, spheroidal, internally flawless, jewel-like zircons which are interpreted to be metamorphic zircons based on their morphology and low model initial Th/U ratio (see Figure 5.11) (Williams & Claesson, 1987; Söderlund, 1996). These zircons have been extensively sampled by a series of late-kinematic pegmatites which are closely related to the post-S_1 leucosomes. The pegmatites also contain small, prismatic, igneous zircons which presumably crystallised from the pegmatite melt. Analysis of these zircons via the Kober zircon evaporation technique yielded Pb-Pb ages of 2424±5 Ma for inherited metamorphic zircons, and 2428±14 Ma for small, prismatic igneous zircons in sample WGC54 (see Figure 5.11 & Appendix 4). This

geochronological data supports the field observation that pegmatite intrusion accompanied peak metamorphism, and that the pegmatites were derived from the surrounding metapelites via partial melting (see §5.4.1). These ages confirm that granulite facies metamorphism in the southern Christie Subdomain was synchronous with that further north in the Mount Christie area.

Retrograde biotite in metapelitic granulites from Skuse Hill (near Mount Christie) gave a Rb-Sr age of 1650±10 Ma (Fanning, 1997). Retrograde biotite is common in the Christie Gneiss, and clearly overprints the granulite facies assemblages. Hence this age is interpreted to represent an episode of mild, late Palaeoproterozoic reworking of the Christie Gneiss and Ifould Complex.

5.5.2 Ifould Complex

Prior to this study, all intrusives in the Christie subdomain were correlated with the ~1.85 Ga Lincoln Complex of the southern Gawler Craton. This study revealed that they are significantly younger, and their ages cluster to define the Ifould Complex. Both Pb-Pb evaporation and U-Pb SHRIMP zircon ages have been obtained for several Ifould Complex intrusives, and are summarised as follows:

- Elongate, prismatic zircons from a foliated granite/augen gneiss near Pidinga Tank at Lake Ifould (sample WGC61) exhibit moderate to intense oscillatory zoning and are structurally simple. They yielded a Pb-Pb Kober zircon evaporation age of 1684±14 Ma (see Figure 5.12) and a concordant U-Pb SHRIMP age of 1672±17 Ma (see Figure 5.14), which is interpreted to be a magmatic crystallisation age. Although the two ages are within error of each other, the Kober Technique often cannot resolve inherited components in zircons and therefore may yield older mixing ages. The ~1672 Ma age is thought to be a representative intrusive age for the Lake Ifould pluton. Similar comagmatic intrusives occur throughout the Christie Subdomain.
- Small, prismatic zircons from a coarse grained pegmatite (sample WGC64) intruding this granite yielded a Pb-Pb Kober age of 1666±11 Ma (see Figure 5.12), interpreted to be a magmatic crystallisation age. This age is thought to represent late stage magmatism in the Lake Ifould pluton.
- U-Pb SHRIMP analysis of magmatic zircons from a weakly foliated, coarse grained granite at Wynbring Rocks (sample WGC81) yielded an age of 1669±10 Ma, with some inheritance at ~1720-1750 Ma and ~2100 Ma (see Figure 5.13). This age is interpreted to be the intrusive age of the Wynbring pluton.
- A weakly foliated granite from a remote rockhole on the western margin of the Wynbring pluton gave a preliminary U-Pb SHRIMP age of ~1675 Ma (see Figure 5.16), which is interpreted to be an intrusive age for the Wynbring Pluton (in good agreement with the age of the granite at Wynbring Rocks - see above).
- A weakly foliated, medium grained granite from the Barton South area (sample WGC165) yielded a U-Pb SHRIMP age of ~1675 Ma for the three grains analysed (see Figure 5.15). This age is interpreted to loosely constrain the intrusive age of the low magnetic intensity pluton south of Barton Railway Siding.

5.6 Discussion

In the Christie Subdomain, the Archaean Mulgathing Complex is dominated by a high grade, multiply deformed sequence of layered meta-sedimentary units known as the Christie Gneiss. Based on available data (which is admittedly limited by lack of outcrop) it appears that widespread granulite facies metamorphism and complex deformation occurred in the Christie Subdomain during the Sleafordian Orogeny between ~2460 and ~2420 Ma, over an area in excess of 25000km^2. In the Mount Christie and Nullarbor areas, peak pressure-temperature conditions in excess of 800°C and 4.5-5.5kb were followed by isobaric cooling (see §5.4.1). The apparent uniformity of metamorphic grade and structural style of the Christie Gneiss throughout the Christie Subdomain must be treated cautiously for two reasons: (i) the apparent unifomity is based on a very small sample set (due to the lack of outcrop), and (ii) the Christie Subdomain has been extensively reworked along major Mesoproterozoic transpressional shear zones which have caused further burial (to ~7kb), juxtaposition and/or exhumation of the granulites (see Chapter 8).

There is no obvious heat source for high grade Sleafordian metamorphism in the Christie Subdomain (i.e. negligible syn-tectonic igneous material), however temporally equivalent upper crustal mafic intrusives and extrusives (including komatiites) in the neighbouring Wilgena Subdomain indicate temporally equivalent, anomalous, mantle-derived thermal activity (see Chapter 7). The peak metamorphic constraints calculated for the Christie Gneiss clearly represent anomalously high temperatures at relatively low pressures; a significant departure from most stable continental geotherms (e.g. Harley, 1989, 1992; Sandiford & Powell, 1991). Similar pressure-temperature data has been evaluated for many regionally extensive, high grade Precambrian terranes, and are summarised by Harley (1989), however the explanation of such thermal regimes remains enigmatic. Isobaric cooling is commonly inferred in such high-temperature, low-pressure terranes,

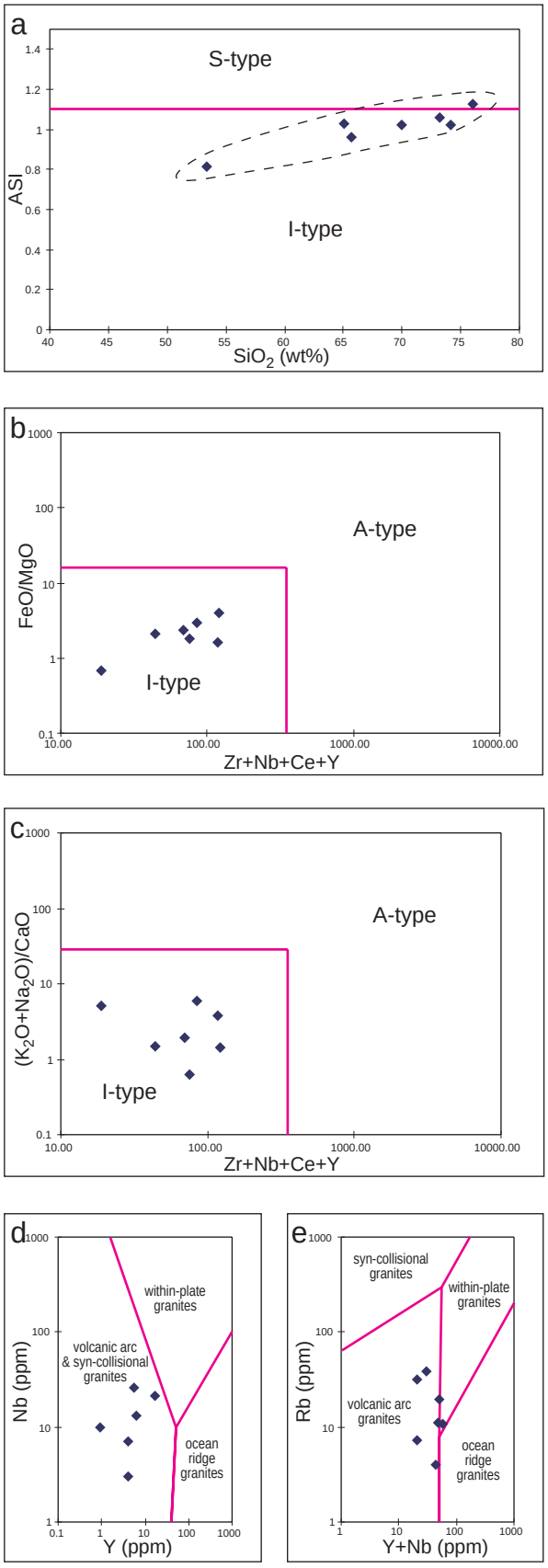

Figure 5.17 (a)-(c) I-S-A-type discrimination diagrams for the Ifould Complex granitoids from Lake Ifould (after Whalen et al., 1987, using the data of Taylor, 1987), showing distinctly I-type affinities, with notably no S- or A-type characteristics (ASI=aluminium saturation index). (d) & (e) Y-Nb-Rb tectonic discrimination diagrams for granitoids (after Pearce et al., 1984), indicating plate-margin, volcanic arc characteristics for the Ifould Complex.

and has usually been associated with metamorphism in an isostatically balanced crust, since isostatic disequilibrium in a cooling crust would lead to exhumation or possibly burial of the metamorphic pile resulting in pressure changes during cooling (e.g. Sandiford & Powell, 1986; Sandiford, 1989a, 1989b; Harley, 1989). Tectonic scenarios commonly invoked to explain low-pressure, high-temperature metamorphism followed by isobaric cooling include (i) magmatic accretion beneath stable crust (e.g. Bohlen, 1987), (ii) extension of normal-thickness crust (e.g. Sandiford & Powell, 1986; Sandiford, 1989a), and (iii) extensional collapse of overthickened crust due to mantle lithosphere thinning (e.g. England, 1987; Sandiford, 1989b; Sonder et al., 1987; Platt & England, 1994). The structural evolution of the Christie Gneiss was largely compressional, and therefore difficult to reconcile with extensional tectonic scenarios. Models involving removal of part or all of the mantle lithosphere ((ii) and (iii) above) are unlikely to result in mid-crustal granulite-facies conditions via conduction alone (Sandiford & Powell, 1991), and as a result heating via magmatic advection has been used to explain high-temperature, low-pressure metamorphism by many workers, implying that heating is transient (e.g. Loosveld & Etheridge, 1990; Sandiford & Powell, 1991). Problems with advection-based models for high-temperature, low-pressure metamorphism include the lack of evidence of significant syn-metamorphic intrusives (notable in the Christie Subdomain) and the long-lived nature of metamorphism observed in many such terranes (M.Hand pers. comm. 1997), as well as the the geologically absurd predicted moho temperatures (>1200°C - M. Sandiford pers. comm., 1997). A recent model by Sandiford et al. (in prep.) invokes a layer of high heat production granites in the upper crust (since eroded away in the Christie Subdomain) causing significant modification of the crustal geotherm to explain spatially extensive, high-temperature metamorphism in the mid-crust, while maintaining geologically plausible moho temperatures (<1000°C). Clearly more detailed geological information on the Christie Gneiss is required to make any realistic tectonic syntheses.

The term Ifould Complex has been defined here to describe a suite of variably deformed, late Palaeoproterozoic (~1700-1670 Ma), comagmatic, I-type granitoids and mafics in the Christie Subdomain (and possibly the Fowler Subdomain - see Chapter 5). Reinterpretation of very limited geochemical data generated by Taylor (1987) indicates distinctly I-type affinities for intrusives in the Lake Ifould area (see Figure 5.17), with no suggestion of anorogenic (A-type) affinities. The tectonic discrimination diagrams of Pearce et al. (1984) strongly suggest a volcanic arc/syn-collisional

collisional genesis for the Lake Ifould granitoids, and data plots well away from the within-plate fields (see Figure 5.17). Clearly more detailed investigations on the lithological, geochemical and isotopic nature of these granitoids is required to adequately characterise the Ifould Complex.

Chapter 6
TECTONOTHERMAL EVOLUTION OF THE FOWLER SUBDOMAIN

6.1 Introduction

The Fowler Subdomain (new name) forms a distinctive, northeast-trending, sinuous belt of strongly magnetic, metamorphic and igneous rocks which are dissected by numerous, anastomosing shear zones (see Chapter 3). Outcrop is extremely limited, and most of the data presented in this chapter is derived from drill core. Three drilling traverses by Mines and Energy, South Australia (MESA) and two mineral exploration traverses (North Exploration's BAC traverse and Afmeco's TAL traverse) provide reasonably continuous geological coverage over some areas, and a few isolated outcrops provide additional geological controls. Previous work is limited to various MESA reports (Daly et al., 1994; Morris et al., 1994) and conference abstracts (Daly et al., 1995; Daly, 1996), and prior to this study, nothing was known about the metamorphic and structural evolution of the Fowler Subdomain. The Fowler Subdomain has previously been termed the *Fowler Suture Zone* (e.g. Daly et al., 1995), and the *Fowler Orogenic Belt* (Daly et al, in press). Its intense magnetic signature has previously been ascribed to mafic and ultramafic lithologies similar to those found in several Proterozoic orogens in Canada (e.g. Drexel et al., 1993; Daly, 1996; Daly et al, in press). Although such lithologies clearly partially contribute to the magnetic signature, many intermediate-felsic igneous and metasedimentary lithologies from the Fowler Subdomain also exhibit high magnetic susceptibility (see Chapter 3).

This study has identified four major crustal blocks within the Fowler Subdomain (the Nundroo, Central, Colona and Barton Blocks), each bound by major shear zones (see Figure 6.2). Although the four blocks exhibit similar geophysical signatures, their geological characteristics (especially metamorphic grade) differ considerably. This chapter details the tectonothermal evolution of the Fowler Subdomain, and deals separately with the

Figure 6.1 Outcrops in the Fowler Subdomain. (a) Beach boulders of mafic and pelitic gneiss at Cape Adieu, Nundroo Block (cliffs are Tertiary Bridgewater Formation and Nullarbor Limestone). (b) Undeformed, equigranular, medium grained granite at White Gin Rockhole in the Great Victoria Desert, Central Block.

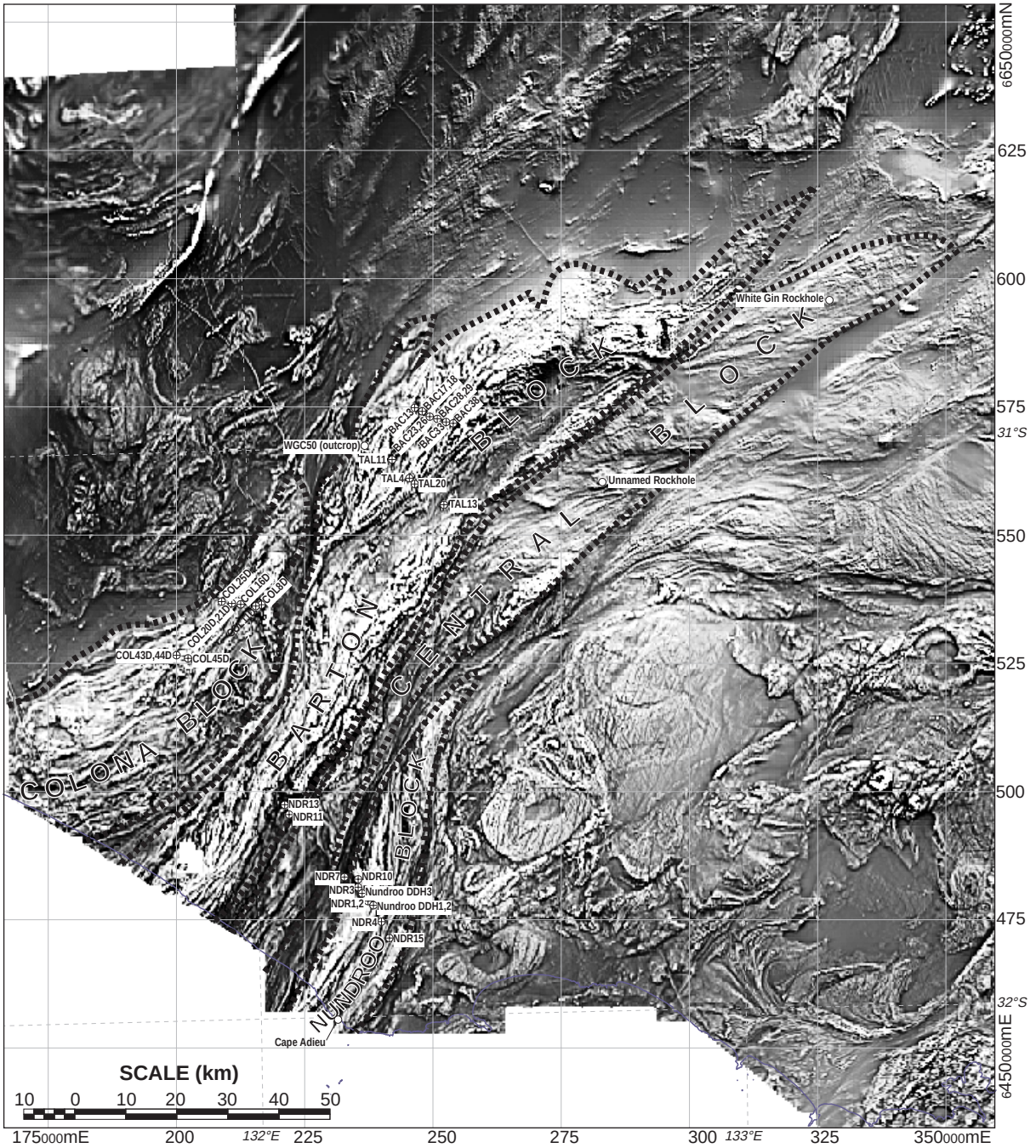

Figure 6.2 Greyscale first vertical derivative image of the study area in the western Gawler Craton highlighting the four blocks in the Fowler Subdomain, showing the location of drillholes and outcrops cited in this chapter.

geological evolution of the four blocks. The geological framework outlined in this chapter is based on the interpretive geological map discussed in Chapter 3 and shown in Figure I1 (at rear of thesis). Section 6.2 summarises the lithological and petrological diversity of the Fowler Subdomain . The structural and metamorphic evolution of the Fowler Subdomain are discussed in Sections 6.3 and 6.4. Section 6.5 summarises all available geochronology. The geochemistry of representative igneous and metamorphic rocks in Section 6.6. The tectonothermal evolution of the Fowler Subdomain is summarised and discussed in light of possible geodynamic scenarios in Section 6.7.

6.2 Lithological and petrological observations

6.2.1 Nundroo Block

The Nundroo Block forms a north-northeast trending, arcuate belt of strongly magnetic rocks approximately 15-20km wide and over 100km long. It is bound by two branches of the Coorabie Shear Zone, and the continental margin in the south (see Figure 6.2). The Nundroo Block was the focus of the 1987 MESA Nundroo Drilling Program, which drilled 15 rotary drill holes with ~1m of bottom-hole diamond coring (NDR1-15) and 3 diamond

Figure 6.3 Cape Adieu garnet-hornblende-plagioclase-quartz gneiss (interpreted as an M_2 amphibolite - see text).

Figure 6.4 Foliated, enclave-rich granite at an unnamed rockhole in a very remote part of the Central Block, Fowler Subdomain (geochronology sample).

drill holes (NUNDROO DDH1-3), targeted at magnetic and gravity anomalies delineated during the Nundroo Geophysical Traverses (Daly & Martin, work in prep.). In addition to the Nundroo drilling traverse, one small outcrop occurs beneath the limestone cliffs at Cape Adieu to which access is very difficult (see Figure 6.1). The Nundroo Block is the best-understood block in the Fowler Subdomain and is the main focus of this chapter. The observations presented in this section are related, where possible to the lithomagnetic associations defined in Chapter 3 and depicted on the interpretive geological map (see Figure I1 at rear of thesis).

The Nundroo Block is dominated by a range of intermediate to mafic lithologies interlayered with metapelitic gneiss, which are overprinted by localised, high strain, relatively low grade mylonite and ultramylonite zones. The mafic lithologies are clearly intrusive (see below) and are interpreted to form 1-200m thick sills within the metasedimentary lithologies. The mafic lithologies range from relatively undeformed, coarse grained diorites and gabbros (lithomagnetic Association 1 as defined in Chapter 3), through high grade mafic granulites (also part of Association 1), to well foliated hornblende and/or biotite rich amphibolites (lithomagnetic Association 2). This spectrum of mafic-intermediate lithologies is part of a lithological continuum whose petrography overlaps. All high grade lithologies are intruded by a series of very coarse grained pegmatites (which predate the mylonite zones).

Medium grained, well foliated and lineated garnet-sillimanite-biotite-K-feldspar-plagioclase-quartz-(magnetite) metapelitic gneiss (part of lithomagnetic Association 2) is interlayered with the mafic gneisses. They have undergone a two-stage petrogenetic evolution, whereby an early, coarse grained, granoblastic assemblage (garnet-sillimanite-plagioclase-K-feldspar-quartz) has been overprinted by a medium grained, foliation-defining assemblage (the above phases with biotite).

The mafic lithologies in the Nundroo Block are interpreted to be derived from a series of coarse grained, anhydrous, cumulus mafic intrusives, ranging compositionally from tonalite to gabbro (with minor anorthosite). These mafics preserve coarse grained, twinned pyroxenes and abundant sulfides and magnetite, which define presumably cumulate compositional layering. The mafic intrusives have subsequently undergone a three-stage metamorphic evolution, the effects of which are extremely heterogeneous and gradational. Initially the intrusives were overprinted by high grade, medium grained, granoblastic garnet - orthopyroxene - clinopyroxene - plagioclase - quartz

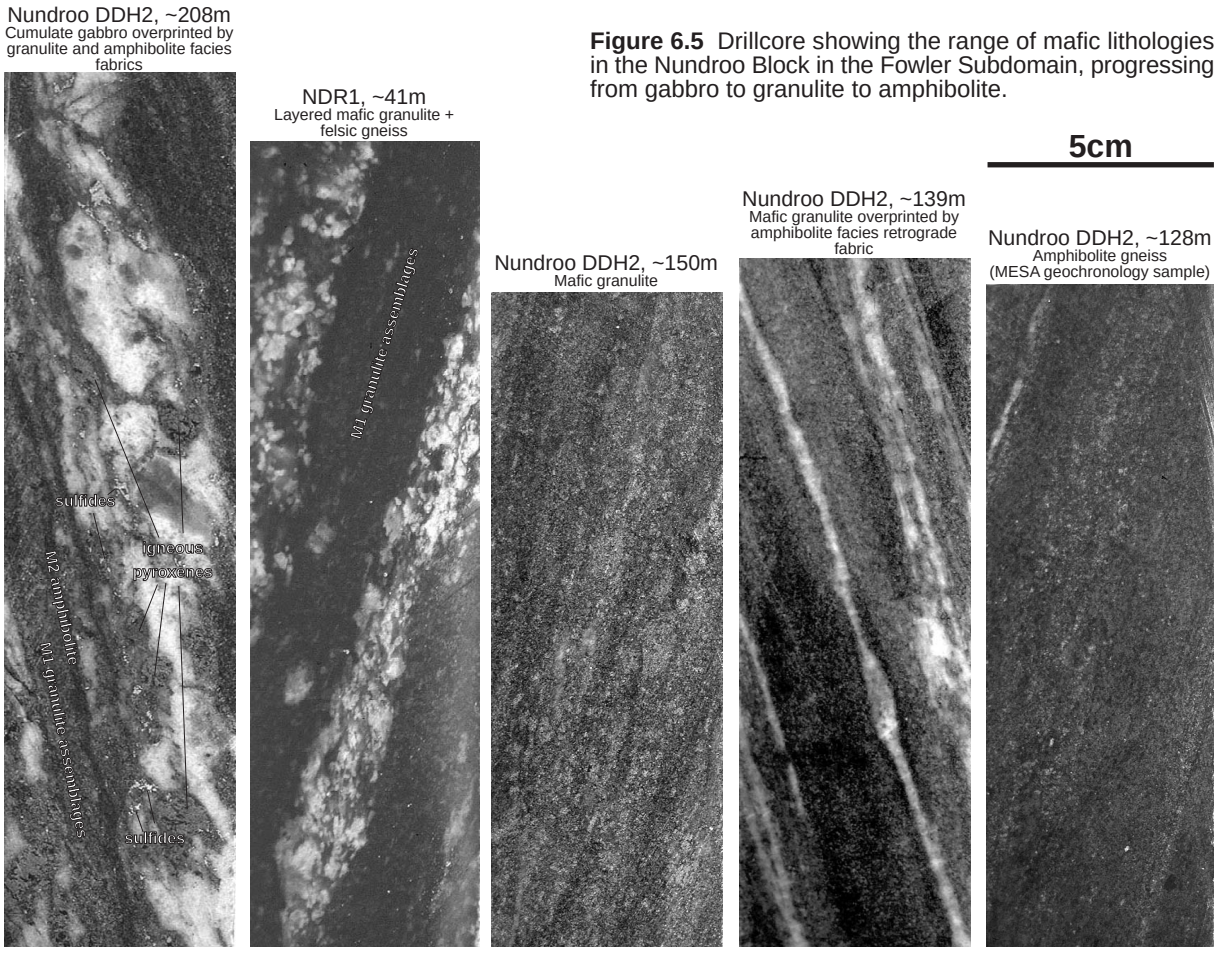

Figure 6.5 Drillcore showing the range of mafic lithologies in the Nundroo Block in the Fowler Subdomain, progressing from gabbro to granulite to amphibolite.

- magnetite ± scapolite, granulite facies assemblages which are associated with stromatic leucosomes (i.e. partial melts). Subsequently they have been heterogeneously retrogressed during amphibolite facies metamorphism, involving the breakdown of granulite facies assemblages to hydrous, biotite-hornblende±garnet bearing assemblages and the development of a well-defined fabric (i.e. lithomagnetic association 2). Finally they underwent localised retrogression associated with late shear zones, whereby all earlier mafic assemblages are overprinted by fine grained, biotite±epidote bearing schists and mylonites. Notably these mylonite zones crosscut the coarse grained pegmatites (see above). The replacement of hornblende and pyroxene by biotite is indicative of extensive potassium metasomatism and calcium depletion during hydration. Later, semi-brittle, cataclastic deformation is associated with moderate to intense, chlorite-sericite-hematite alteration.

A series of well foliated, garnet-biotite-plagioclase-quartz±hornblende, intermediate gneisses (Association 2) intersected by several drill holes in the Nundroo Block (notably Nundroo DDH3) could either represent reworked and potassium-enriched equivalents of the mafic intrusives or a separate, intermediate lithology. This ambiguity is resolved by geochemical data (see §6.6) which suggests that these gneisses are geochemically distinct from the reworked mafic intrusives, and that there are two distinct geochemical groupings of mafic-intermediate rocks in the Nundroo Block.

6.2.2 Central Block

The Central Block is dominated by felsic intrusive rocks and is interpreted to contain only minor amounts of mafic material, and as a result exhibits a lower average magnetic intensity than the other blocks in the Fowler Subdomain. It forms a linear belt approximately 10-20km wide and over 200km long, bound to the east and west by the Coorabie and Colona Shear Zones (see Figure 6.2). Both outcrop and drill core is extremely limited, however the uniform magnetic patterns of the Central Block indicates that the observed lithologies are likely to persist over most of the area. The observed lithologies are dominated by variably deformed granitoids, which have been divided into two suites loosely based on geochronological and geophysical evidence (see §6.5). An older suite (possibly a correlative of the Ifould Complex - see Chapter 5) comprises medium grained, equigranular, leucocratic granite and adamellite, such as that found at White Gin Rockhole (see Figure 6.1). These granitoids are variably deformed (grading into mylonites), and are intruded by a suite of younger granitoids. The younger granitoids (such as that found at the remote unnamed rockhole

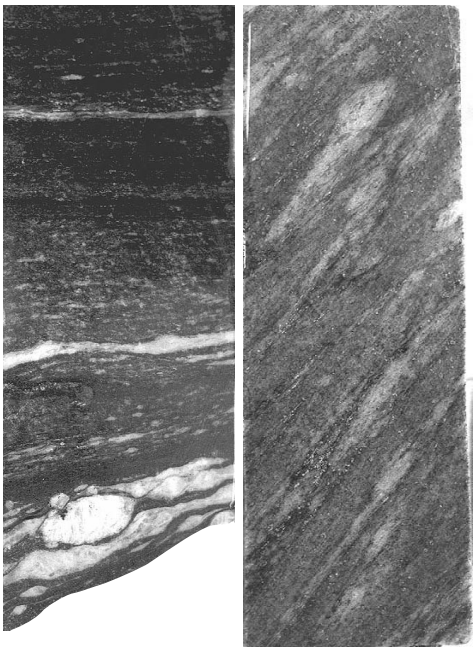

Figure 6.6 (a) Nundroo DDH2 ~130m - Late, ND_3, retrograde mylonite (strain partitioned by coarse grained pegmatite). (b) Nundroo DDH2 ~339m - Garnet-sillimanite-biotite gneiss (note isoclinally folded leucosomes).

in the central part of the Central Block - see Figure 6.3) are notably more biotite-rich than the older granitoids, usually contain variable amounts of mafic enclaves, and have a higher average magnetic susceptibility. Granitoids in the Central Block generally exhibit a steep, NNE to ENE-trending foliation which grades into mylonitic shear zones. No metamorphically useful mineral assemblages were found in the Central Block.

6.2.3 Barton Block

The Barton Block forms a striking magnetic and gravimetric high which dominates the Fowler Subdomain. It comprises a large, sigmoidal belt up to 30km wide and over 200km long, bound to the east and west by the Colona and Tallacootra Shear Zones and truncated in the southwest by the Karari Fault Zone (see Figure 6.2 & 8.1). Drill core and outcrop observations yield a wide variety of lithologies, which are broadly grouped into four lithological associations (as defined in Chapter 3), namely: mafics (Association 1), metasedimentary schists and gneisses (Association 2), granitoids (Association 3), and mylonites (Association 4). Due to the lack of outcrop and the sparse nature of the drill holes, the relationships between each lithological association are uncertain, and as a result, this study has focussed on regional-scale parameters such as metamorphic grade and structural style (see §6.3 and §6.4).

Many drillholes in the Barton Block intersected fine-medium grained, well foliated, compositionally layered, biotite±sillimanite±garnet-Kfeldspar-quartz-magnetite±plagioclase (semi)pelitic gneiss and schist. The pelitic lithologies invariably contain magnetite resulting in their high magnetic susceptibility (500-2000 S.I.x10^{-5}), and some samples contain abundant metamorphic monazite and zircon (see §6.5 - geochronology). One drill hole intersected fine grained, magnetite-rich banded iron formation (TAL1). Some samples have been overprinted by a later, lower grade, high strain fabric, in which sillimanite and biotite are still stable, but garnet has partially broken down to biotite.

A broad range of mafic and ultramafic rocks have been intersected by many drillholes in the Barton Block, including olivine-chromite bearing peridotites (Morris et al., 1994), through two-pyroxene metagabbros, to hornblende-garnet±biotite gneisses. Most mafic and ultramafic lithologies exhibit high to very high magnetic susceptibility (1000-10000 S.I.x10^{-5}) caused by magnetite, and some are interpreted to exhibit strong remenant magnetisation (see Chapter 3). They are interlayered with the metasedimentary gneiss, and are interpreted to be intrusive sills (as in the Nundroo Block - see §6.2.1).

Abundant felsic to intermediate, medium-coarse grained, variably deformed granitoids were intersected by drillholes in the Barton Block. They are interpreted to have intruded the metasediments described above, however their relationship with the mafics remains uncertain. They may be comagmatic with the mafics. Their basic mineralogy is quartz-plagioclase-biotite±Kfeldspar-zircon-magnetite±ilmenite. Some granitoids have been extensively deformed, and porphyroblastic, presumably metamorphic, euhedral epidote is commonly observed in the retrograde fabric.

A range of mylonitic lithologies exists in the Barton Block, which are associated with the complex system of anastamosing, low grade shear zones (see §6.3.5). Lithologies range from medium grained augen gneisses and protomylonites through to intensely strained, micaceous ultramylonites. Earlier pyroxene and hornblende bearing assemblages have been overprinted by biotite-epidote bearing assemblages, indicating that extensive potassium metasomatism accompanied deformation and rehydration.

6.2.4 Colona Block

The Colona Block forms an strongly magnetic, sigmoidal belt approximately 30km wide, narrowing to the north-northeast (see Figure 6.2). It is bound by two branches of the Tallacootra Shear Zone, and extends well to the west beyond the present coastline where it is truncated by the Karari Fault Zone. The Colona Block was the focus of the

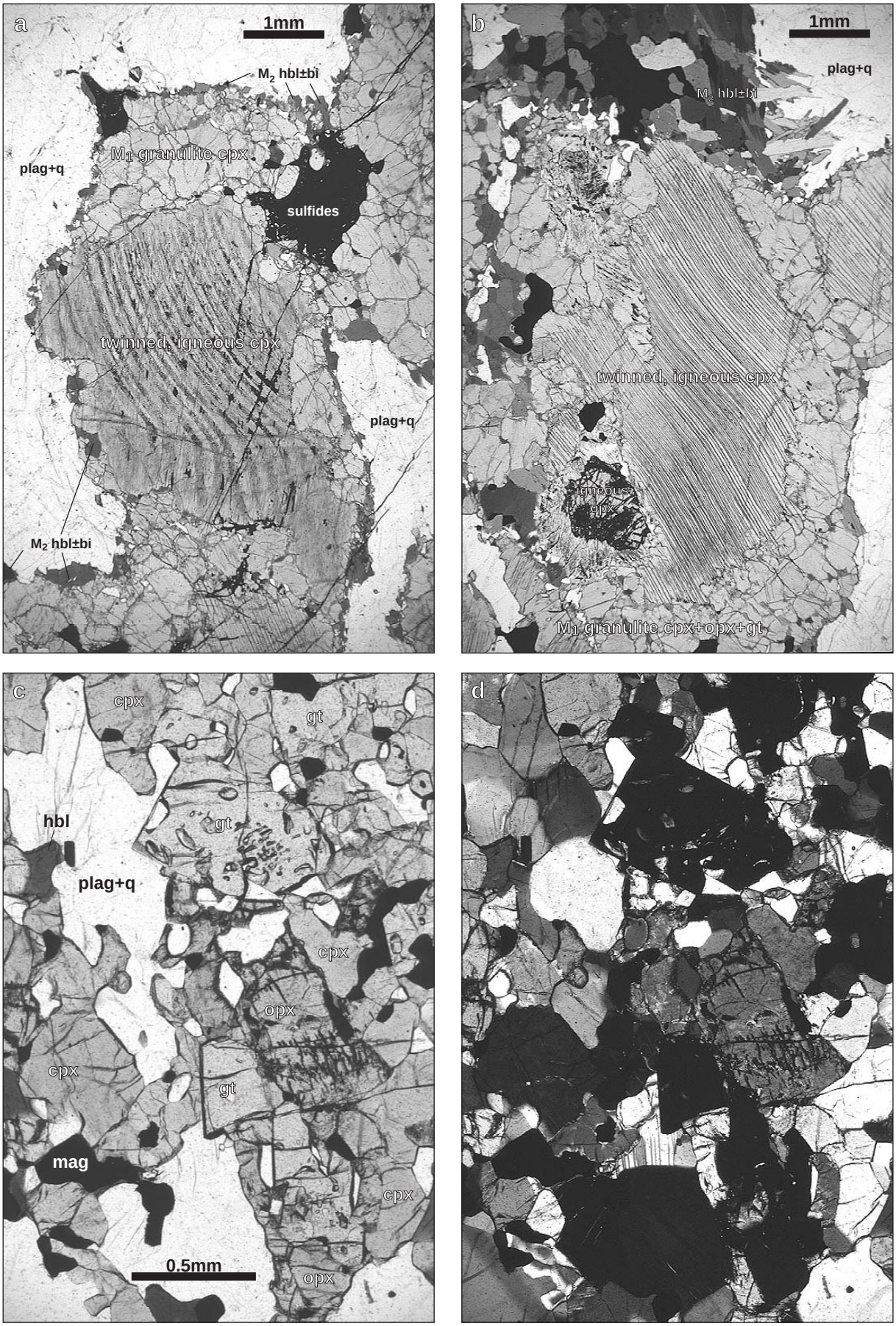

Figure 6.7 Photomicrographs of mafics from the Nundroo Block. (a) & (b) Nundroo DDH2 94.2m - Coarse grained gabbros , where early, twinned, presumed igneous pyroxenes are overprinted by NM_1, 2-pyroxene-garnet assemblages and NM_2, retrograde, hornblende±biotite assemblages. (c) & (d - XPL) Nundroo DDH2 160m - Detail of 2-pyroxene-garnet NM_1 granulite, with a very minor NM_2 retrograde hornblende.

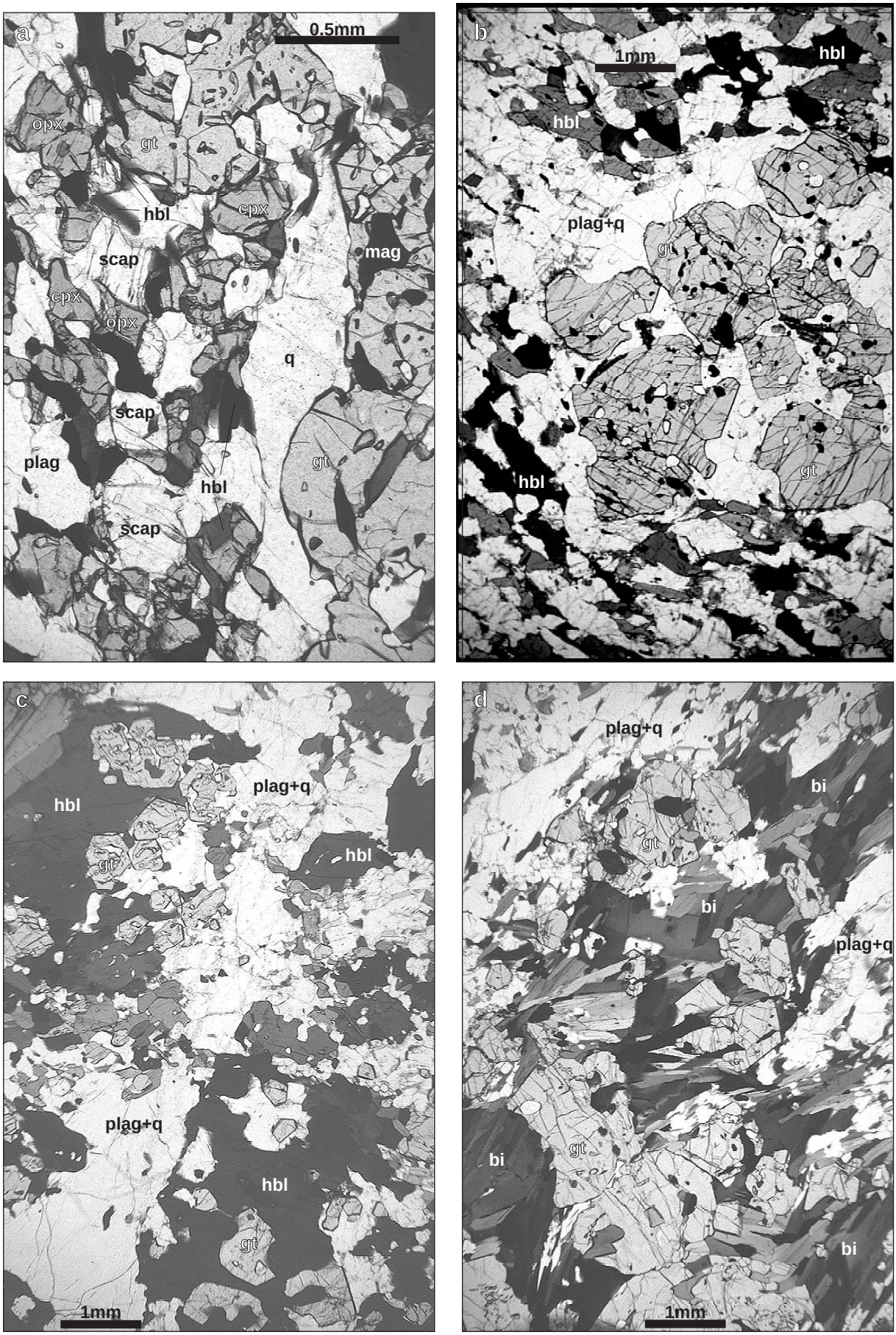

Figure 6.8 Photomicrographs of mafic lithologies from the Nundroo Block. (a) NDR1 41m - NM_1 garnet-2-pyroxene-scapolite granulite with a mild NM_2 hornblende overprint. (b) WGC20 (from Cape Adieu) - NM_2 garnet-hornblende amphibolite. (c) Nundroo DDH3 158.5m - NM_2 garnet-hornblende amphibolite. (d) Nundroo DDH3 164m - NM_2 garnet-biotite gneiss.

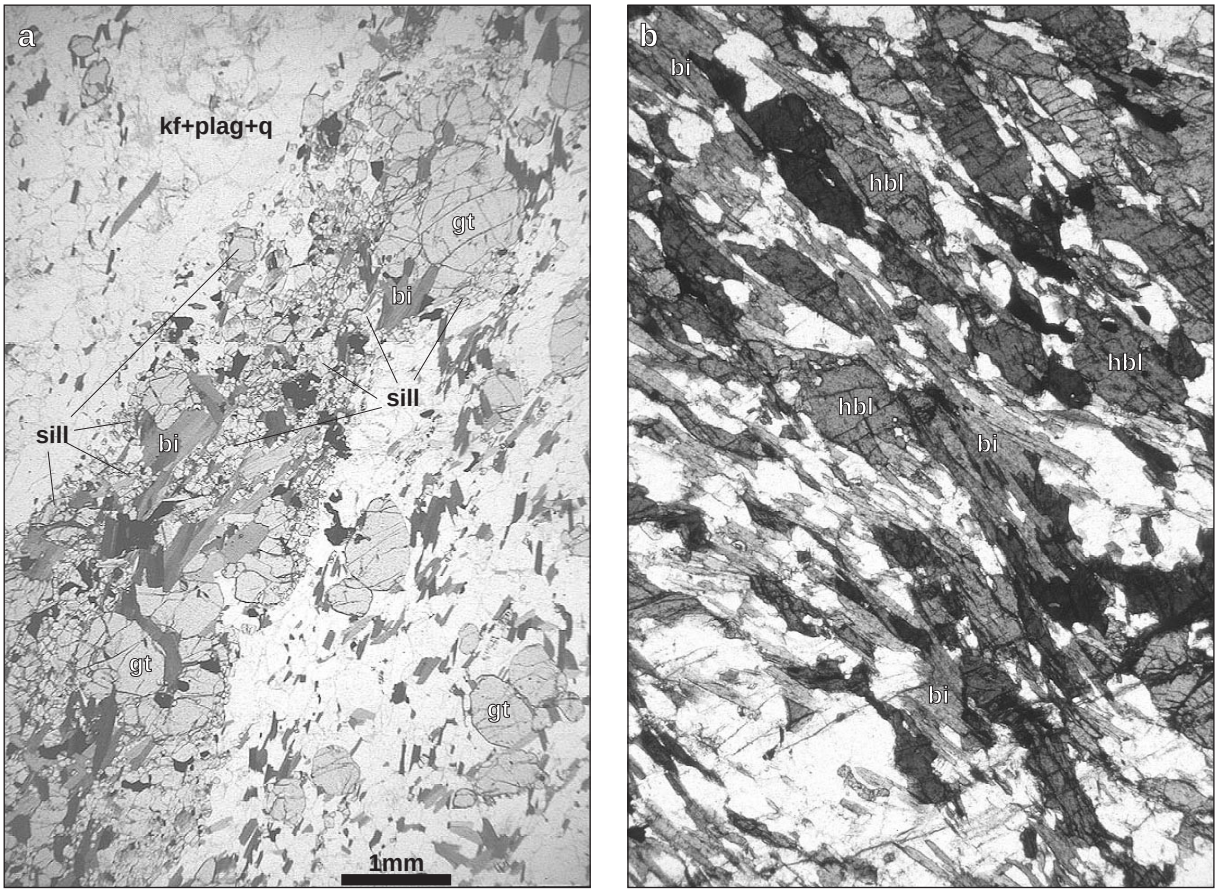

Figure 6.9 Photomicrographs of lithologies from the Nundroo Block. (a) Nundroo DDH2 320m - Garnet-sillimanite-biotite gneiss. (b) Nundroo DDH2 130m - ND_3 retrograde mylonite/schist, in which hornblende has partially broken down to biotite.

1993-4 MESA Colona Drilling Program which drilled 40 basement-intersecting holes, including 10 diamond drill holes, targeting magnetic and gravimetric anomalies delineated by two east-west trending, ground-based geophysical profiles (Morris et al., 1994). Thick Cainozoic cover on the southwestern parts of the Colona Block restricted the drilling program to its northeastern end, where basement is 20-100m below the surface.

The Colona Block comprises a series of variably deformed and metamorphosed, strongly magnetised, layered, intermediate-mafic intrusive igneous rocks. They range compositionally from biotite-rich tonalites and granodiorites through to hornblende gabbros. Numerous fine grained mafic enclaves, layers and/or dykes (dolerites) occur in the intrusives. Weakly deformed domains preserve coarse compositional layering which is interpreted to be cumulus. Coarse grained, sub-euhedral hornblende grains occur in most of the intrusives, and their poikilobastic habit, zoning patterns and textural character suggest that hornblende is a primary magmatic phase, not derived from clinopyroxene as interpreted by Daly et al. (1994). All lithologies contain variable amounts of magnetite (1-10%), and the mafics contain up to 5% pyrite. Complex intermingling and mixing textures between the range of intermediate to mafic lithologies indicate that they are comagmatic.

All lithologies in the Colona Block have been variably retrogressed. Early, coarse grained phases are variably recrystallised into a fine grained groundmass, and primary hornblende has broken down secondary hornblende, biotite and epidote. Early compositional, ?cumulus layering has been transposed into the retrograde fabric, in which early, coarse grained hornblende and plagioclase are porphyroclastic. The abundance of biotite in strongly retrogressed samples attests to significant potassium enrichment during hydration.

Late, fine-medium grained, equigranular, undeformed granite crosscuts the deformed intrusives described above (a potential geochronology target). Late, coarse grained, post-kinematic pegmatites crosscut all intrusives. Small-scale (1cm-1m), cataclastic shear zones/breccias crosscut all lithologies and are associated with minor chlorite-sericite alteration.

6.3 Structural geology

This section outlines a structural framework for the Fowler Subdomain by attempting to correlate aeromagnetic signatures (as outlined in Chapter 3)

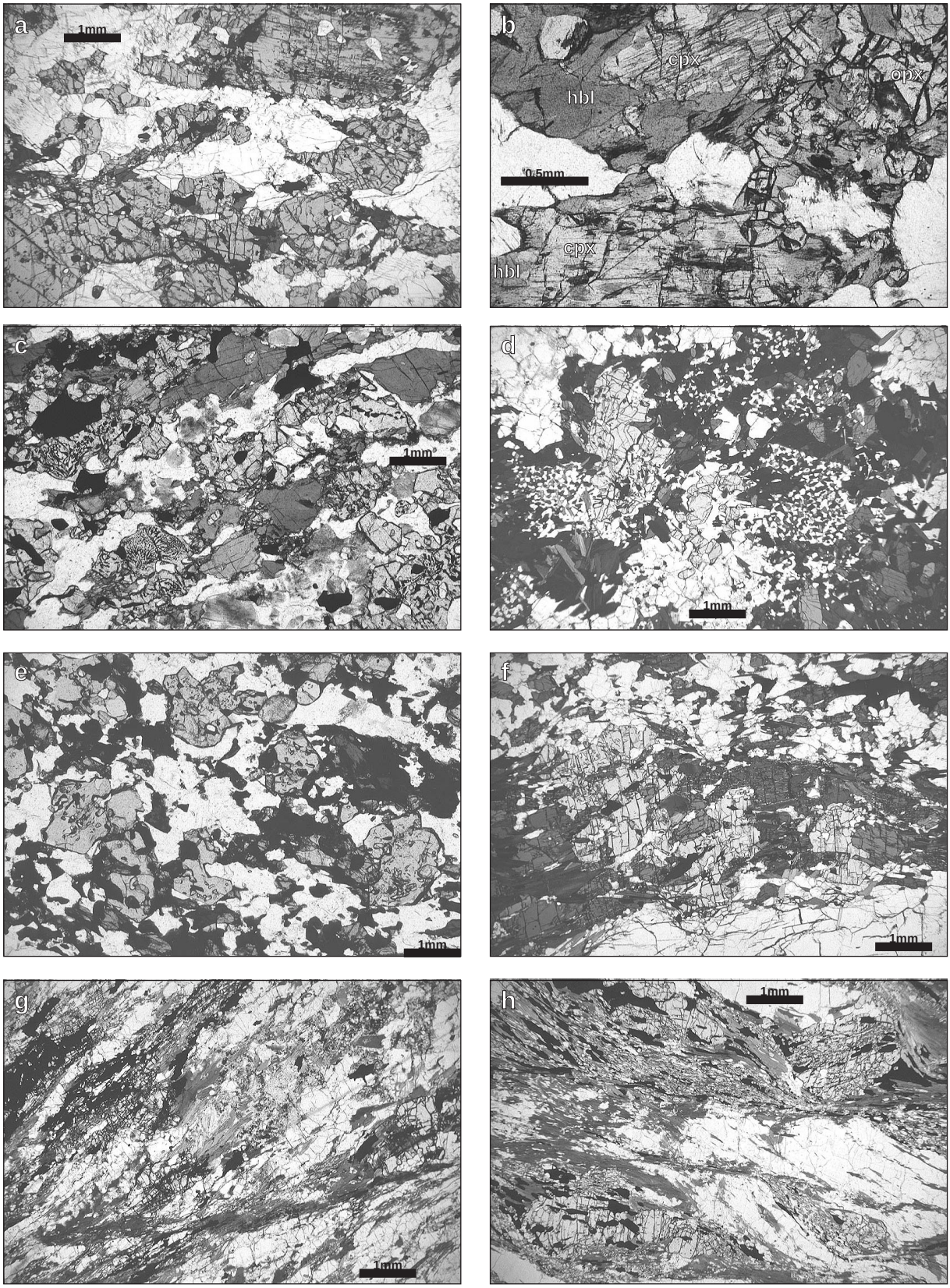

Figure 6.10 Photomicrographs of various lithologies from the Barton Block. (a) TAL11 - 2-pyroxene-plagioclase-quartz granulite (with some relict, twinned, ?igneous pyroxenes). (b) WGC50 (Tallacootra east outcrop) - retrogressed 2-pyroxene granulite (pyroxenes partially replaced by hornblende). (c) BAC17 - garnet-hornblende gneiss. (d) TAL13 - garnet-hornblende-biotite-plagioclase-quartz gneiss (fine hornblende-quartz mosaics possibly pseudomorph clinopyroxene). (e) BAC38 - garnet-clinopyroxene-hornblende gneiss. (f) BAC26 - garnet-hornblende gneiss. (g) BAC23 (monazite geochronology sample) - garnet-sillimanite-biotite-magnetite schist (monazite is part of biotite-sillimanite fabric). (h) BAC33 - porphyroblastic garnet-sillimanite-biotite schist.

with the different fabric elements observed in drill core and outcrop. Of particular note is the presence of a system of lower grade, narrow, anastomosing shear zones in all blocks which transect all high grade lithologies (see §6.3.5 below), but predate the major SZ_2 shear zones discussed in Chapter 8. Late, brittle deformation associated with low grade, cataclastic shear zones was accompanied by localised chlorite-sericite±hematite alteration in the mafic lithologies. Abbreviations used to describe structural elements in the Fowler Subdomain are of the form XY_Z, where X=block identifier (e.g. N=Nundroo Block), Y=fabric element (e.g. S=planar feature), and Z=order of structural element.

6.3.1 Nundroo Block

Variably defined compositional layering (NS_0), which is assumed to be of cumulus origin in the mafics and of sedimentary origin in the metapelites, is preserved in less reworked sections of the Nundroo DDH2 drill core. NS_0 is nebulous and variably oriented (10°-70° to the core axis). Subsequently, the Nundroo Block has been effected by two fabric-forming deformation events. ND_1 is characterised by a weak, NS_1 tectonic foliation which overprints NS_0, and is directly correlated with peak, NM_1 granulite facies metamorphism (see §6.4.1). NS_1 is defined by alignment of NM_1 biotite and hornblende, and the weak transposition of NS_0, however NM_1 stromatic leucosomes often disrupt NS_1. NS_1 is variably oriented with respect to the core axis - clearly reflecting both early folding, and disruption by NS_2. ND_2 is characterised by a moderate to intense, steep to sub-vertical, NS_2 retrograde fabric which overprints both NS_0 and NS_1, and is directly correlated with NM_2 retrograde, amphibolite facies metamorphism (see §6.4.1). NS_2 is defined by the strong alignment of hornblende and biotite in the mafics, and by biotite and sillimanite in the metapelites, which also define a moderate to intense NL_2 mineral lineation. NM_1 partial melts are transposed and intensely deformed by the NS_2 fabric, and often define isoclinal NF_2 folds. NS_2 is generally steeply dipping (65-90°) with respect to the core axis. Narrow, low grade, ND_3 shear zones crosscut all lithologies.

6.3.2 Central Block

The poor exposure and metamorphically unreactive nature of the observed rocks in the Central Block prevents any realistic characterisation of their structural evolution. The observed outcrop and drill core is variably effected by a steeply dipping foliation (CS_1) which generally parallels the magnetic trends (see Chapter 3). Based on geochronological evidence (see §6.5), this foliation is correlated with the NS_2 retrograde fabric in the Nundroo Block (see §6.3.1 above). CS_1 is overprinted by narrow (0.1-1m), low grade, ENE-trending mylonitic shear zones, in which biotite and chlorite are stable. These shear zones are correlated with the ND_3 shear zones in the Nundroo Block (see §6.2.2 above).

6.3.3 Barton Block

The Barton Block contains a diversity of variably deformed lithologies which are difficult to correlate, and as a result, it is difficult to develop a coherent structural framework. Compositional layering (BS_0) in the metasedimentary and mafic lithologies presumably reflects sedimentary and igneous (possibly cumulus) processes. BS_0 has been transposed into a steeply dipping, tectonic BS_1 fabric of varying intensity. In metasedimentary and felsic metaigneous lithologies, BS_1 is pervasive and is defined by biotite and/or sillimanite, contains high strain features such as quartz ribbons and shear bands, and is associated with a variably developed, BL_1 mineral elongation lineation. In mafic lithologies, BS_1 is defined by weak alignment of hornblende and/or biotite. BS_1 is associated with peak (BM_1) metamorphism in both the metasedimentary and metaigneous lithologies. A localised, retrograde, mylonitic BS_2 foliation crosscuts many of the observed lithologies in the Barton Block. BS_2 is associated with an intense BL_2 stretching lineation, and contains abundant quartz ribbons and shear bands. BM_1 phases are often porphyroclastic in the BS_2 fabric, and rheologically stronger lithologies (e.g. mafics) form boudins. Low grade, cataclastic, semi-brittle shear zones are observed in some drill holes.

6.3.4 Colona Block

Mafic-intermediate-felsic, comagmatic intrusives in the Colona Block exhibit CS_0 compositional layering (of cumulus origin). They have been variably overprinted by a CD_1 tectonic fabric, generally defined by retrograde biotite growth. Primary igneous phases are porphyroclastic in the CD_1 fabric. The CS_1 foliation is steeply dipping (60-90°).

6.3.5 Shear zones

All lithologies in the Fowler Subdomain are crosscut by narrow, demagnetised, 1-20km scale, anastamosing, retrograde shear zones (see Figure I1 at back of thesis). These shear zones form a signficant set of low magnetic intensity anomalies which are discussed in Chapter 3. Their kinematic evolution is not understood, however their anastamosing surface expression is characteristic of a transpressional fault system (see Chapter 8). Early mafic phases have broken down to fine grained biotite and chlorite which define a high

strain fabric.

6.4 Metamorphic considerations

Metamorphic and chronological constraints for the Fowler Subdomain suggest that each block has experienced a different metamorphic history. Metamorphic studies in the Fowler Subdomain are largely based on thermobarometry of metamorphosed mafic and pelitic lithologies. Both conventional, cation-exchange thermobarometers (as implemented by Kohn & Spear, 1996) and the average pressure-temperature approach implemented by Thermocalc (Powell & Holland, 1988, 1994) using the internally consistent dataset of Holland & Powell (1990, 1994) have been used to constrain peak pressure-temperature conditions in the Fowler Subdomain. The critical input for both thermobarometric approaches is the recognition of the true equilibrium mineral assemblages, together with precise, representative mineral composition measurements and appropriate activity expressions. A commonly recognised problem in obtaining peak pressure-temperature estimates in high grade rocks is the determination of the "true" composition of the peak phases, since mineral zoning can occur as a result of prograde growth patterns (especially in lower grade rocks), and as a result of reequilibration during cooling (especially in granulites). In some cases, peak pressure-temperature conditions cannot be realistically estimated using thermobarometry. For assemblages containing hydrous phases, it is vital to estimate water activity (aH_2O) in order to obtain realistic pressure-temperature estimates using Thermocalc. As a general rule, higher grade rocks have lower aH_2O (e.g. Phillips, 1980), however calculations for the transitional amphibolite-granulite facies assemblages described in the Fowler Subdomain are particularly sensitive to the chosen aH_2O value. In order to estimate the true aH_2O, Thermocalc results were matched to pressure-temperature estimates obtained from conventional thermobarometry (see below). Mineral activities were calculated (accounting for non-ideal site mixing) using the AX computer program (Holland, 1995). The following sections outline the metamorphic evolution of the Nundroo, Barton and Colona Blocks. No thermobarometrically useful mineral assemblages were found in the Central Block.

6.4.1 Nundroo Block

The Nundroo Block contains the highest grade, most diverse mineral associations yet found in the Fowler Subdomain, which appear to be temporally distinct from assemblages documented in the Barton and Colona Blocks (see §6.5). Peak metamorphism in the Nundroo Block is characterised by medium-high pressure, granulite facies assemblages in mafic and pelitic lithologies. Peak, often anhydrous granulite facies assemblages are variably overprinted by hydrous, medium pressure, amphibolite facies assemblages. Mafic lithologies preserve the most complete evidence for two-stage metamorphic overprinting of the intrusive tonalites, diorites and gabbros, whereby a continuum of assemblages grading from only slightly reworked igneous rocks to highly deformed, hornblende-biotite gneiss is recorded. Interlayered pelitic gneisses exhibit a well defined, layer-parallel foliation which parallels the retrograde foliation in the mafics. As a result, the late garnet-biotite-sillimanite assemblages in the pelitic gneiss are interpreted to reflect the later, NM_2/S_2 retrograde overprint (see §6.4.1.2).

6.4.1.1 Peak granulite metamorphism

Peak, granulite facies metamorphism in the Nundroo Block is characterised by medium grained, granular associations of garnet-orthopyroxene-clinopyroxene-plagioclase-quartz±scapolite with minor biotite and hornblende in mafic lithologies, and by medium-coarse grained, garnet-sillimanite-K-feldspar-plagioclase-quartz±biotite assemblages in metapelitic lithologies. These assemblages are associated with a weak NS_1 fabric defined by biotite and hornblende which parallels the S_0 compositional layering (which is related to cumulus layering in the igneous precursors). Garnets in both the mafic and pelitic gneiss contain aligned inclusions of biotite, and are intimately intergrown with the pyroxenes (see Figure 6.7). No reaction textures were observed between peak NM_1 phases. Stromatic, quartz-plagioclase leucosomes are often associated with peak assemblages in the mafic gneiss, and are interpreted to be partial melts.

Garnetiferous mafic assemblages are well recognised as being pressure sensitive (e.g. Schumacher et al., 1990), so the mafic assemblages in the Nundroo Block are particularly suited to thermobarometry using both conventional cation-exchange methods and Thermocalc (Powell & Holland (1988, 1994). Zoning in peak phases due to retrograde reequilibration (see §6.4.1.2 below) is evident in some phases, particularly garnet, and as a result core mineral compositions were used in all pressure-temperature calculations. Peak assemblages are thought to be essentially anhydrous, due to the relatively low abundance of hydrous phases, and the presence of partial melt. In any case, aH_2O is close to zero in such systems (e.g. Philips, 1980; Harley, 1989). Results of thermobarometric calculations for peak, granulite-facies assemblages are summarised in Appendix 3, and show a remarkable consistency across all samples and mineral assemblages. Peak pressure-

temperature conditions of 780-820°C and 8-9kb are recorded by a wide range of thermobarometers and by Thermocalc, although peak temperatures are often underestimated by some thermobarometers. The calculated peak, NM_1 pressure-temperature conditions are consitent with medium-high pressure granulite facies metamorphism (Harley, 1989).

6.4.1.2 Retrograde overprints

Gneisses in the Nundroo Block are variably overprinted by a retrograde, NS_2 fabric defined by hornblende and/or biotite (see §6.3.1). The retrograde fabric is characterised by medium grained, well foliated and layered hornblende and/or biotite-rich gneiss which overprint the mafic granulites. Pelitic gneisses exhibit a well-defined NS_2 fabric, and the late, biotite-rich assemblages which they contain are thought to reflect the retrograde, NM_2 metamorphic conditions. Retrograde hornblende and biotite has grown at the expense of peak pyroxenes and garnet. Stromatic leucosomes generated during peak metamorphism are transposed and deformed by NS_2 and form narrow, layer-parallel leucosomes which are isoclinally folded (see §6.3). Garnets are often associated with the deformed leucosomes, and contain aligned hornblende and/or biotite inclusions; hence are interpreted to have grown during NM_2 (see Figure 6.3).

Thermobarometry of retrograde, garnetiferous assemblages for mafic and pelitic assemblages in the Nundroo Block was performed using a combination of conventional thermobarometers and Thermocalc. The hydrous nature of the retrograde, amphibolite facies mineral assemblages suggests metamorphism occurred at higher aH_2O, than the granulite facies precursors, and PT results obtained using Thermocalc were matched with results from conventional thermobarometers in order to quantify aH_2O. Peak temperatures of ~700°C were obtained using a wide range of assemblages and thermometers. Pressure data shows a west-east pressure increase across the Nundroo Block, with results of ~6.5-7.5kb in the west (Nundroo DDH2 and DDH3), up to ~8.7-9kb in the east (Cape Adieu). Water activity in both the pelitic and mafic rocks was calculated to be ~0.5. The source of these hydrating fluids is ambiguous, since the precursor rocks were largely anhydrous. This problem is further discussed in Section 6.8.

6.4.2 Barton Block

Numerous thermobarometrically useful samples were found in the Barton Block, however their diversity and broad spacing makes it difficult to reconcile the observed assemblages with the relatively tightly constrained metamorphic history of the Nundroo Block. Geochronology suggests that metamorphism in the metapelitic lithologies predates granulite facies metamorphism in the Nundroo Block by approximately 150Ma (see §5.5), however much more geochronology is necessary to establish this as a fact.

Amphibolite facies, metapelitic, garnet-biotite-sillimanite gneisses and schists are relatively abundant in the Barton Block, and are particularly suited to thermobarometry. The estimation of fluid activity (aH_2O and aCO_2) is also of fundamental importance, since the chosen values can drastically alter the calculated pressure-temperature conditions. Water activity was estimated by matching Thermocalc results with those of conventional thermobarometers, and results indicate that aH_2O is likely to be between 0.1 and 0.2 for the metapelites. Results indicate that there is a slight grade increase from west to east across the Barton Block. Metapelites in the western Barton Block show peak preussure-temperature conditions of 625-650°C and 5.5-6.5kb, whereas those to the east equilibrated at 650-700°C and 6.5-7.0kb.

Garnetiferous amphibolites which are interlayered with the metapelites are also particularly suited to thermobarometry. Water activity (which is relevant in hornblende and/or biotite bearing mafics) was estimated using the method described in Section 6.4.1. Results indicate that garnetiferous mafic assemblages equilibrated at higher pressures than the metapelites. The west-east grade increase inferred from the metapelites is verified by the mafics. In the western Barton Block, peak pressure-temperature conditions of ~650°C and 5.5-6kb are recorded in BAC17 (note that Thermocalc gives spurious results here). Further to the east, peak pressure-temperature conditions in the range 700-750°C and 8-9kb were recorded by garnet-hornblende±clinopyroxene assemblages from two drillholes (BAC26 and BAC38).

The pressure discrepancy between the mafic and pelitic assemblages in the Barton Block may reflect either: (i) that the mafics genuinely record earlier, higher pressure metamorphism (i.e. they are boudins in the relatively intensely deformed pelites), or (ii) a problem with the thermobarometric calculations. Clearly this discrepancy can be resolved via more detailed geochronology of metamorphic assemblages in the relevant lithologies (see §6.5).

6.4.3 Colona Block

The Colona Block has only experienced minor retrogression associated with a retrograde fabric in the primary igneous rocks. No thermobarometrically useful assemblages were

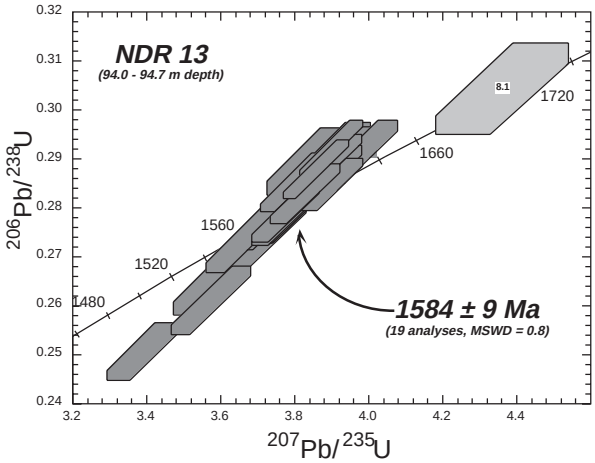

Figure 6.11 U-Pb concordia diagram showing SHRIMP zircon analyses for a weakly foliated granite intersected by NDR13 (Nundroo Block), plotted as 1▪ error polygons. Analyses used to calculate the weighted mean $^{207}Pb/^{206}Pb$ age are darkly shaded.

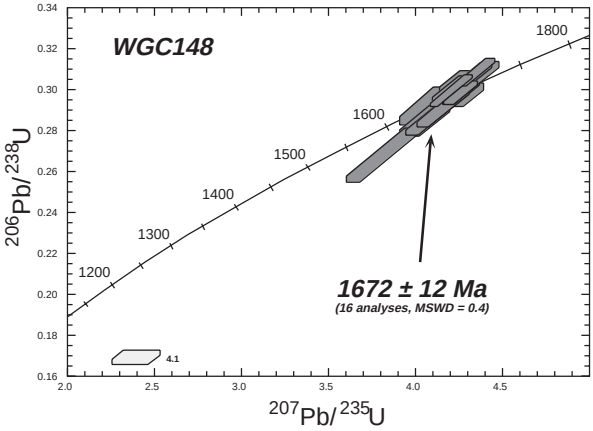

Figure 6.12 U-Pb concordia diagram showing SHRIMP zircon analyses for the weakly foliated granite from White Gin Rockhole (Central Block), plotted as 1▪ error polygons. Analyses used to calculate the weighted mean $^{207}Pb/^{206}Pb$ age are darkly shaded.

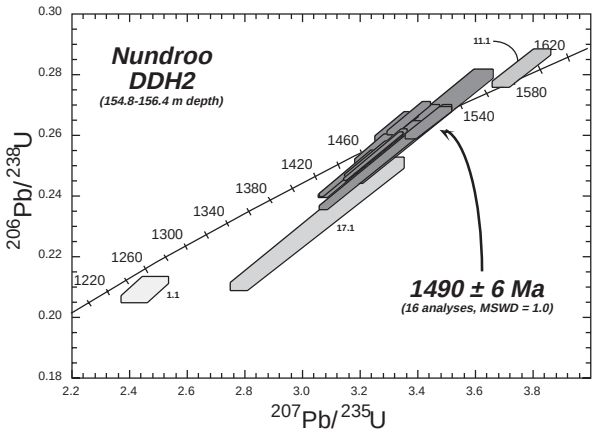

Figure 6.13 U-Pb concordia diagram showing SHRIMP zircon analyses for a late, discordant pegmatite from Nundroo DDH2 (Nundroo Block), plotted as 1▪ error polygons. Analyses used to calculate the weighted mean $^{207}Pb/^{206}Pb$ age are darkly shaded.

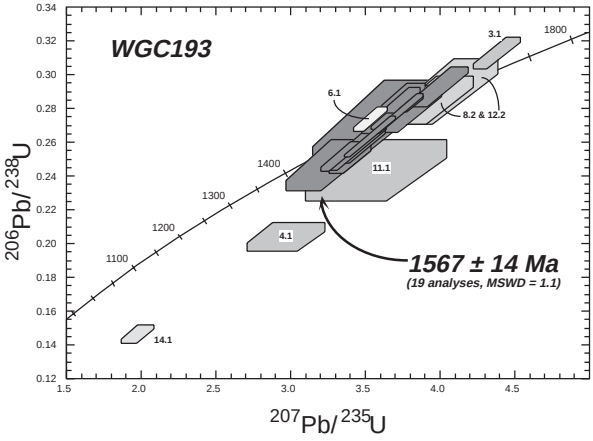

Figure 6.14 U-Pb concordia diagram showing SHRIMP zircon analyses for a foliated granite from an unnamed rockhole in the Central Block, plotted as 1▪ error polygons. Analyses used to calculate the weighted mean $^{207}Pb/^{206}Pb$ age are darkly shaded.

found. The retrograde biotite-epidote±hornblende fabric is interpreted to be lower amphibolite facies; distinctly lower grade than the Barton and Nundroo Blocks.

6.5 Geochronology

To date, geochronology in the Fowler Subdomain has focussed on U-Pb dating of zircon and monazite. Clearly a multi-technique approach involving other isotope systems is required to further define the complex tectonothermal evolution of the Fowler Subdomain. Results are as follows:

6.5.1 Nundroo Block

• Small, metamorphic zircons from mafic granulites in Nundroo DDH2 (interval 128-129m - see Figure 6.5) gave a U-Pb SHRIMP age of 1543±9 Ma (Daly et al, in press). This age is interpreted to represent peak granulite facies metamorphism in the Nundroo Block, since zircon growth appears closely associated with the peak mineral assemblages and the stromatic leucosomes. Notably, no zircons were observed in the early gabbroic, cumulus intrusives, possibly indicating that zirconium was partitioned into silicate phases (Fraser et al., 1997), which is supported by the absence of inheritence in the zircon population (M. Fanning pers. comm., 1997).

• Late, very coarse grained pegmatites which crosscut all lithologies in Nundroo DDH2 contain abundant, small, internally flawless, prismatic zircons with no internal structure or zoning. These zircons gave a concordant U-Pb SHRIMP age of 1490±6 Ma (see Figure 6.13), which is interpreted as an intrusive age. Importantly, the very coarse grained pegmatites are crosscut by lower grade, high strain, brittle-ductile shear zones.

• Hornblende growing in the NS_2 retrograde amphibolite facies fabric in Nundroo DDH2 (128-129m) yielded a K-Ar age of 1494±9 Ma (Daly & Fanning, 1993).

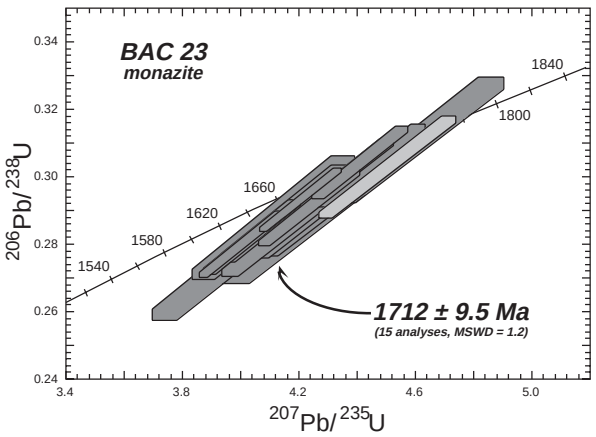

Figure 6.15 U-Pb concordia diagram showing SHRIMP monazite analyses for a pelitic schist intersected in BAC23 (Barton Block), plotted as 1▪ error polygons. Analyses used to calculate the weighted mean $^{207}Pb/^{206}Pb$ age are darkly shaded.

Thus thermal activity and deformation in the Nundroo Block spanned the time interval from ~1540 Ma to at least ~1490 Ma. The age of the metasediments and the magmatic age of the mafic intrusives are unknown at this time, although elsewhere in the Fowler Subdomain, mafic intrusives with similar geochemical affinities to the Nundroo mafics have been dated at ~1740 Ma (see §6.5.4), implying that the metasedimentary sequence may be older than ~1740 Ma.

6.5.2 Central Block

- Weakly deformed granite from White Gin Rockhole, in the northern part of the Central Block contains abundant, large, prismatic, zircons of presumed magmatic origin, which yielded a concordant U-Pb SHRIMP age of 1672±12 Ma (see Figure 6.12), and a Pb-Pb evaporation age of 1693±14 Ma (see Figure 6.16). This age is interpreted to be the crystallisation age of the granite. Although the SHRIMP and zircon evaporation ages are within error of each other, the slightly older evaporation age may be caused by an inherited component in

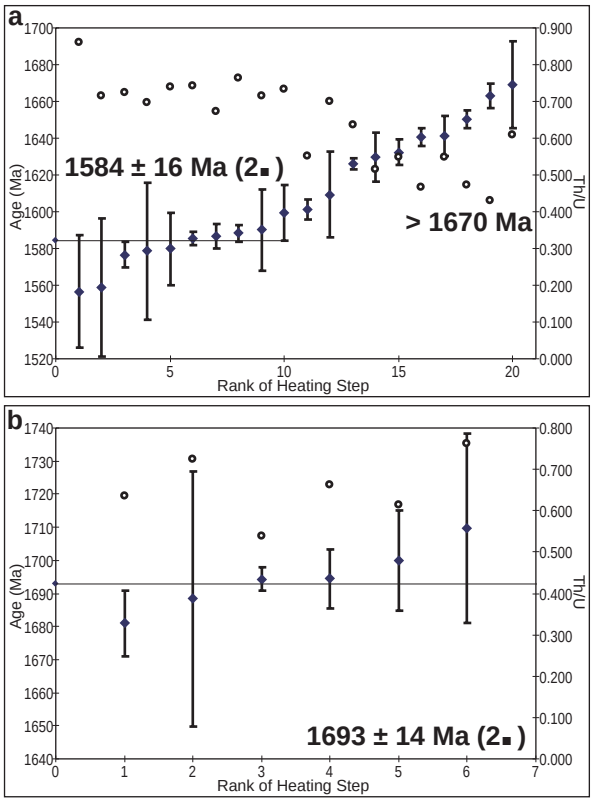

Figure 6.16 Pb-Pb zircon evaporation results for granites from the Central Block. Solid diamonds = $^{207}Pb/^{206}Pb$ age (with 1▪ error bars), open circles = model initial Th/U ratio. (a) Foliated granite from the unnamed rockhole. Note concomittant decrease in Th/U with increasing age. (b) weakly foliated granite from White Gin Rockhole.

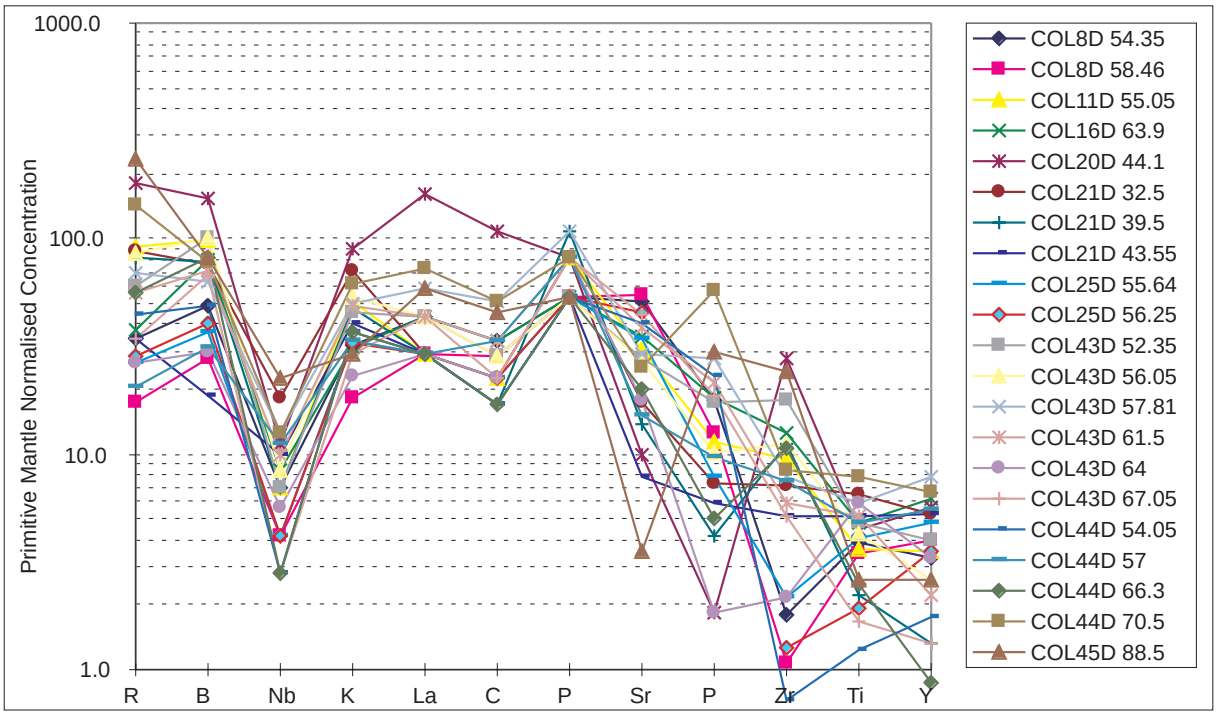

Figure 6.17 "Spidergram" geochemical plot for major and trace elements from intrusives in the Colona Block (MESA data), showing consistent Ba-Nb-K-La-Ce-Pb trends suggesting that they are probably comagmatic.

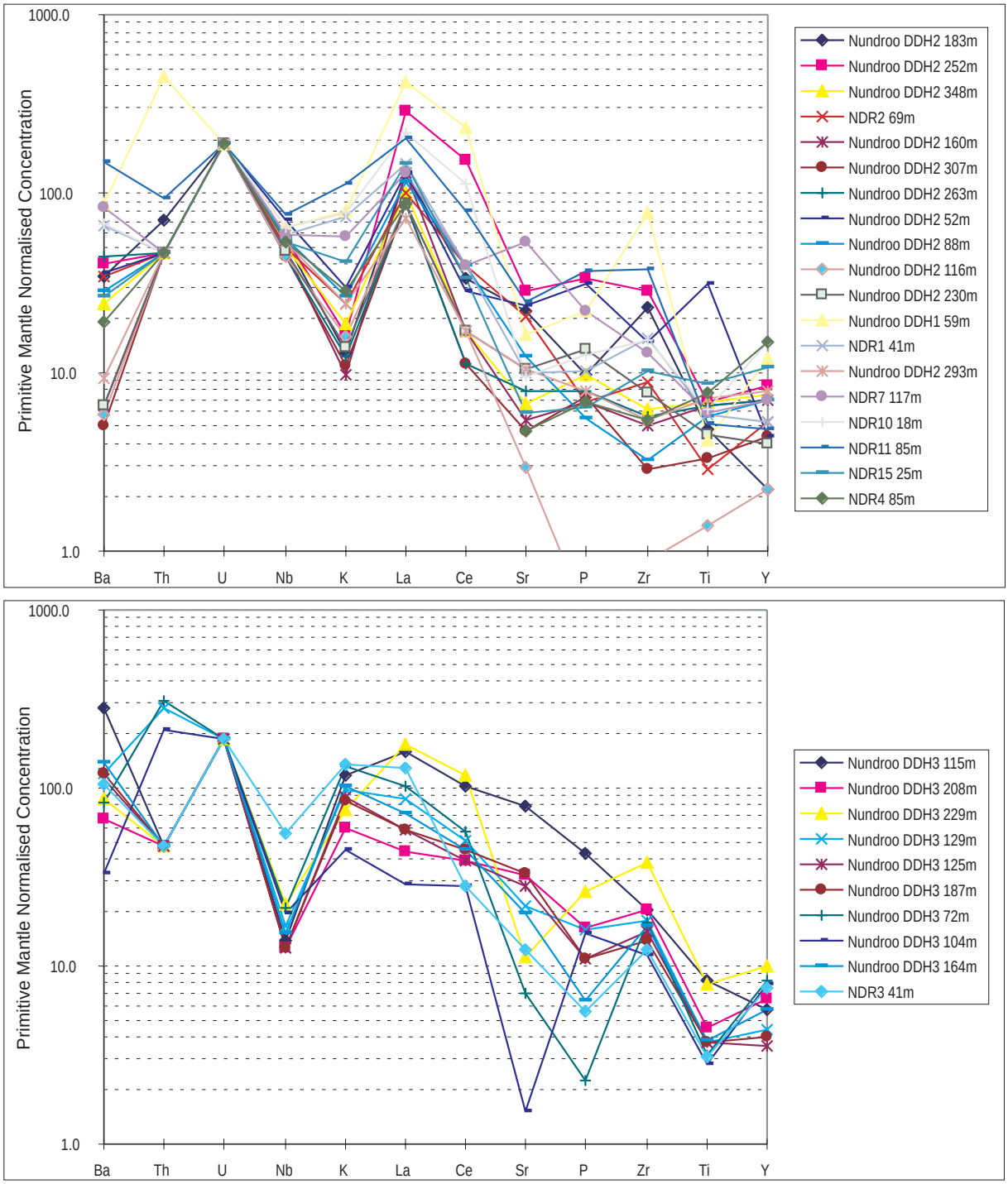

Figure 6.18 "Spidergrams" of geochemical data from mafic intrusives in the Nundroo Block (MESA data), showing two distinct geochemical groupings. (a) Mafic intrusives, granulites and amphibolites showing relatively high Ba-Nb-La and low K-Ce-Zr concentrations with repect to (b). (b) Biotite-bearing mafics and amphibolites. This data suggests that the biotite-bearing mafics are unlikely to be derived via rehydration/metasomatism from the coarse grained mafic intrusives.

the analysed zircons.

- A unnamed remote rockhole in the central part of the Central Block (see Figures 6.2 & 6.4) contains well foliated, relatively biotite-rich granite, with numerous mafic enclaves. The zircon population is dominated by relatively large, elongate, prismatic zircons, which often contain subhedral, inherited cores. U-Pb SHRIMP analysis of these zircons gave a magmatic crystallisation age of 1567±14 Ma, with inherited components at ~1630 ~1630 Ma and ~1730 Ma (see Figure 6.15). Pb-Pb zircon evaporation analysis yielded an age of 1584±16 Ma for this granite (see Figure 6.16), and although this age is within error of the SHRIMP ages, it may be a mixing age between the younger and older zircon components.

6.5.3 Barton Block

Metapelitic gneiss and schist from the Barton Block contain numerous monazites and zircons.

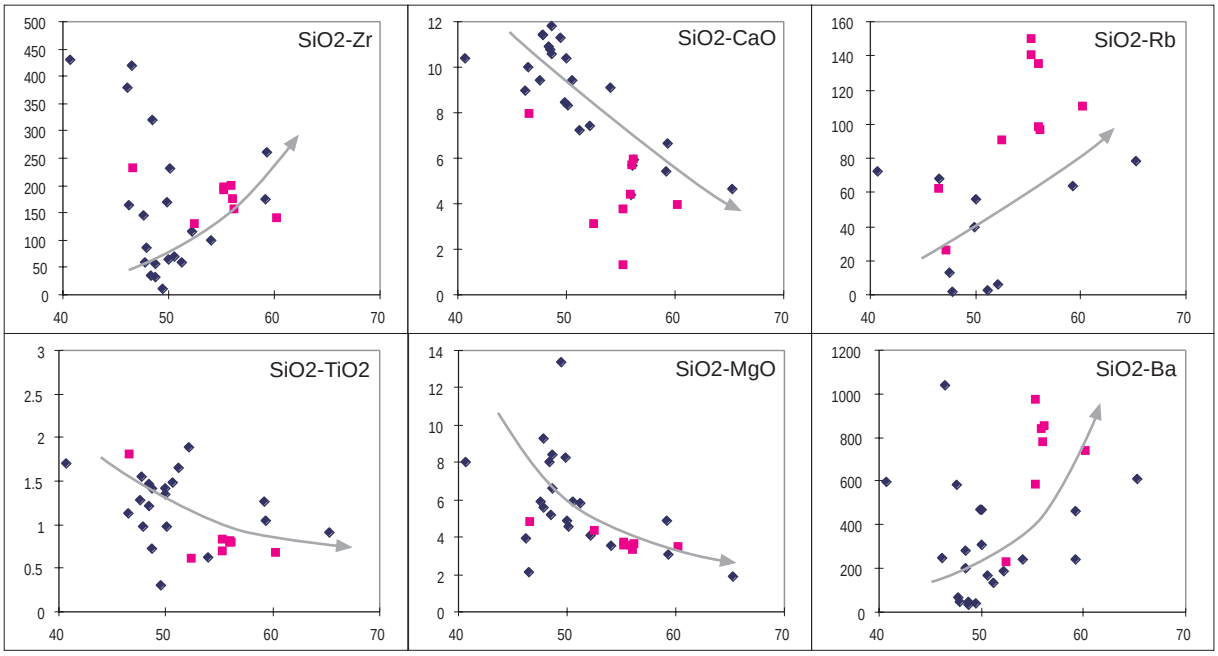

Figure 6.19 Bivariate "Harker" plots of silica against various major and trace elements for mafic to intermediate lithologies in the Nundroo Block, showing fractionation trends (grey arrows). Diamonds=Group 1 intrusives, squares=Group 2 intrusives (see text for details).

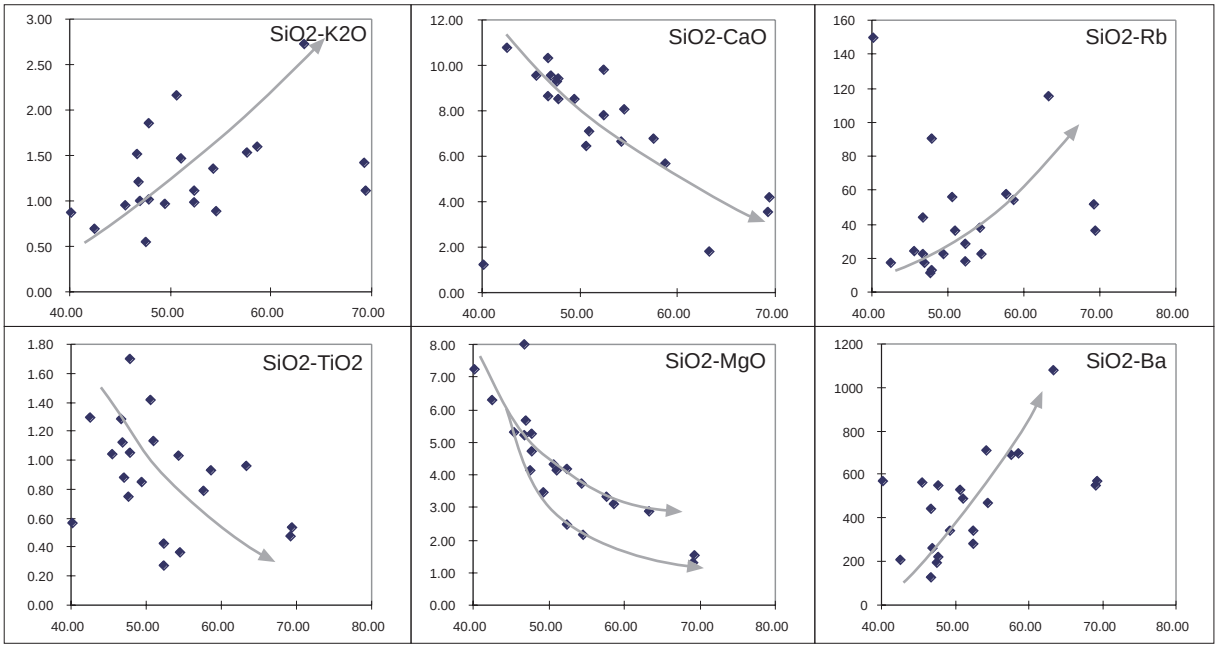

Figure 6.20 Bivariate "Harker" plots of silica against various major and trace elements for intermediate to felsic lithologies in the Colona Block, showing fractionation trends (grey arrows).

U-Pb SHRIMP analysis of metamorphic monazites in a well foliated, garnet-sillimanite-biotite gneiss from the BAC23 drill hole yielded a concordant age of 1712±9.5 Ma (see Figure 6.15). This age is interpreted to reflect peak, upper amphibolite facies metamorphism in the Barton Block.

6.5.4 Colona Block

A U-Pb SHRIMP emplacement age of 1730±10 Ma was obtained for zircons from a mildly deformed, coarse grained, layered hornblende gabbro from Colona DDH43 (Daly et al, in press). Other intermediate-felsic intrusives which comprise the bulk of the Colona Block are thought to be approximately the same age. The age of the retrograde foliation is unknown.

6.6 Geochemistry

Major and trace element, whole rock geochemistry has been obtained for the Nundroo and Colona drill holes by MESA. This data was compiled and analysed during this project in an attempt to: (i) categorise the variably reworked

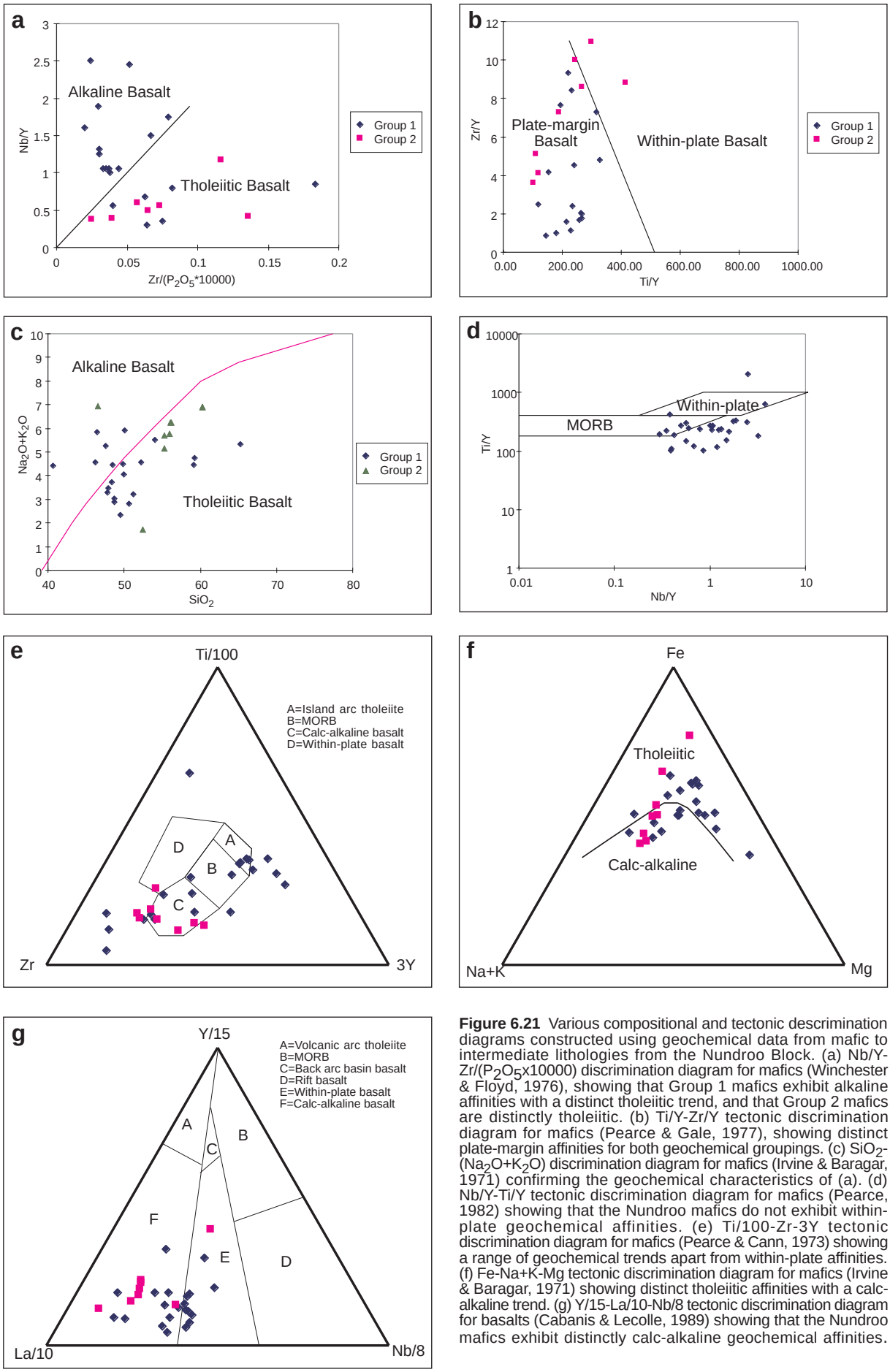

Figure 6.21 Various compositional and tectonic descrimination diagrams constructed using geochemical data from mafic to intermediate lithologies from the Nundroo Block. (a) Nb/Y-Zr/(P_2O_5x10000) discrimination diagram for mafics (Winchester & Floyd, 1976), showing that Group 1 mafics exhibit alkaline affinities with a distinct tholeiitic trend, and that Group 2 mafics are distinctly tholeiitic. (b) Ti/Y-Zr/Y tectonic discrimination diagram for mafics (Pearce & Gale, 1977), showing distinct plate-margin affinities for both geochemical groupings. (c) SiO_2-(Na_2O+K_2O) discrimination diagram for mafics (Irvine & Baragar, 1971) confirming the geochemical characteristics of (a). (d) Nb/Y-Ti/Y tectonic discrimination diagram for mafics (Pearce, 1982) showing that the Nundroo mafics do not exhibit within-plate geochemical affinities. (e) Ti/100-Zr-3Y tectonic discrimination diagram for mafics (Pearce & Cann, 1973) showing a range of geochemical trends apart from within-plate affinities. (f) Fe-Na+K-Mg tectonic discrimination diagram for mafics (Irvine & Baragar, 1971) showing distinct tholeiitic affinities with a calc-alkaline trend. (g) Y/15-La/10-Nb/8 tectonic discrimination diagram for basalts (Cabanis & Lecolle, 1989) showing that the Nundroo mafics exhibit distinctly calc-alkaline geochemical affinities.

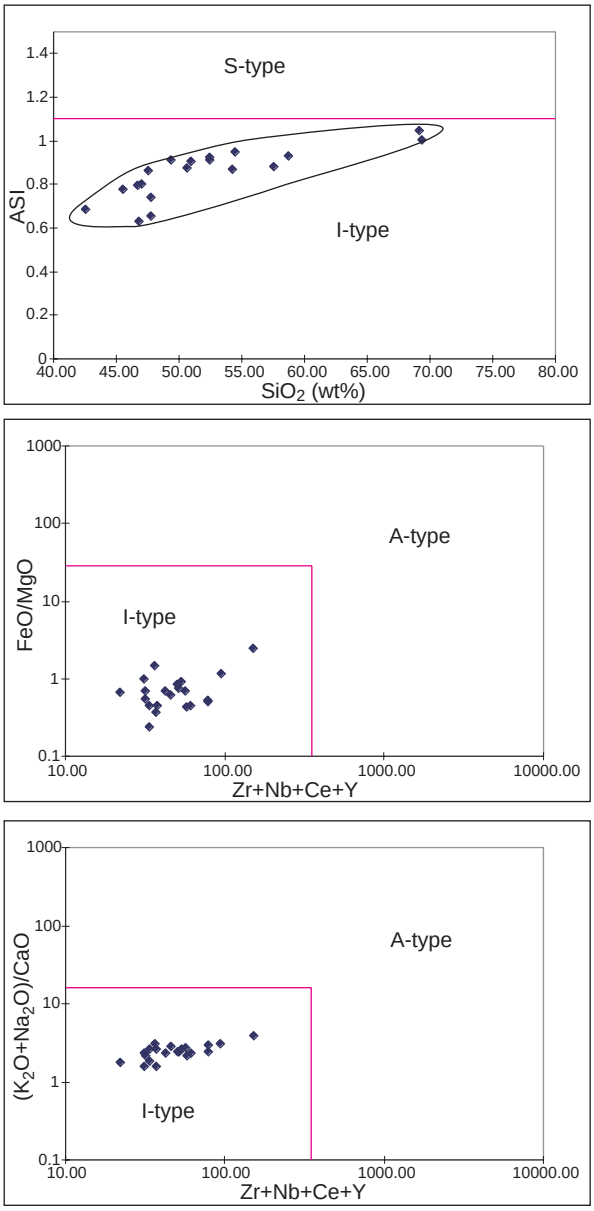

Figure 6.22 I-S-A-type discrimination diagrams for the Colona granitoids (after Whalen et al., 1987), showing distinctly I-type affinities, and notably no S- or A-type characteristics (ASI=aluminium saturation index).

mafic lithologies, (ii) determine if the more felsic units are related to the mafics via fractionation, and (iii) constrain the tectonic environment in which intrusion occurred.

Obviously it is difficult to classify the continuum of variably reworked mafic intrusives in the Fowler Subdomain based on petrological and metamorphic evidence alone, since it is unclear which anhydrous precursors the variably retrogressed lithologies are derived from, or if in fact many of the hydrous lithologies are unrelated to the gabbros and granulites with which they are interlayered. Whole rock geochemistry indicates two distinct geochemical groupings in the Nundroo Block. The "spidergrams" illustrated in Figure 6.18a show that most of the variably reworked Nundroo mafics (ranging from gabbro to granulite to amphibolite) are geochemically similar, with distinctive high Nb-La, low K-Ba values, and a broad spread of heavy trace elements (Group 1). The spidergram shown in Figure 6.18b indicates a suite of more potassic, geochemically distinct mafics (biotite-rich, K-feldspar bearing), with high K-Ba-Zr, low Nb-La values (Group 2). This is an important classification, since it shows that the biotite-bearing mafics are geochemically distinct and therefore unlikely to be derived from the pyroxene-hornblende bearing mafics. The geochemical similarities across the range of Group 1 variably reworked mafics shows that they are geochemically related, and probably derived from a suite of comagmatic mafic intrusives (i.e. the coarse grained gabbros, diorites and tonalites). The bivariate "Harker" diagrams shown in Figure 6.19 indicate trends characteristic of fractional crystallisation for the Nundroo Block.

The mafic-felsic intrusives in the Colona Block show broad geochemical similarities with the more potassic group in the Nundroo Block (Group 2), with uniformly high K-Ba, low Nb-La values (see Figure 6.17). Bivariate "Harker" plots for a variety of major and trace elements show trends characteristic of fractional crystallisation for the Colona Block intrusives (see Figure 6.20). Using the discrimination diagrams of Chappell & White (1974, 1992) and Whalen et al. (1987), they show distinctly I-type affinites and are definitely not A-type (see Figure 6.22).

Mafics from both the Nundroo and Colona Blocks are dominantly tholeiitic with some alkaline (quartz-undersaturated) members (see Figure 6.21a,c,f). Calc-alkaline tendencies occur in both the tholeiitic and alkaline groups. Various tectonic discrimination diagrams uniformly show that mafics in the Fowler Subdomain are supposedly associated with plate margins, and show no within-plate affinities (see Figure 6.21b,d,e,g).

6.7 Discussion

The Fowler Subdomain has had a complex geological history that can be divided into three tectonothermal episodes, the effects of which have varied in intensity and character across the four main crustal blocks in the Fowler Subdomain. This section summarises the main geological characteristics of the tectonothermal history and architecture of the Fowler Subdomain, and outlines possible tectonic scenarios for its evolution.

Episode 1: The first recognisable tectonic episode recognised in the Fowler Subdomain spanned the interval ~1740-1690 Ma. A sequence of sedimentary lithologies of unknown age was intruded by voluminous sheets, sills and plutons of strongly

magnetised, mafic-intermediate, I-type, layered intrusives at ~1740 Ma. These intrusives dominate the geology of the Fowler Subdomain, and exhibit plate-margin, tholeiitic to calc-alkaline geochemical affinities. Metamorphism accompanied heterogeneous compressional deformation at ~1710 Ma, and ranged from upper greenschist facies in the Colona Block to upper amphibolite facies in the eastern Barton Block. This tectonothermal episode concluded with the intrusion of voluminous, I-type granitoid sheets and plutons at ~1690 Ma.

Episode 2: The second tectonothermal episode recognised in the Fowler Subdomain spanned the interval ~1585-1490 Ma. Voluminous, heterogeneous, granitoid plutons and sheets intruded parts of the Fowler Subdomain between 1585-1560 Ma (especially in the Central Block). Subsequent metamorphism accompanied by compressional deformation affected the eastern parts of the Fowler Subdomain between ~1560-1540 Ma, ranging from minor amphibolite facies overprints in the Barton Block to high pressure granulite facies metamorphism in the Nundroo Block. Subsequent heterogeneous retrograde metamorphism, deformation and hydrous fluid flow occurred during the interval 1540-1490 Ma, and was followed by minor, post-kinematic, felsic magmatism at ~1490 Ma. Both peak and retrograde metamorphism was accompanied by compressional deformation which caused steep fabric development.

Episode 3: The third tectonothermal episode to effect the Fowler Subdomain involved major dissection, differential exhumation and reworking along at least two generations of major transpressional shear zones. The timing of deformation is poorly constrained, but is tentatively interpreted to have occurred in the interval 1200-1100 Ma. The nature, timing and significance of the late shear zones in the western Gawler Craton is discussed in Chapter 8.

The current architecture of the Fowler Subdomain is largely defined by Episode 3 structures. Sinuous magnetic and gravimetric highs generated during Episodes 1 and 2 are dissected by an array of early shear zones which anastomose at scales of 1-30km, and are bound and juxtaposed by a series of regional shear zones which anastomose at scales of ~100km. Two major, late shear zone systems transect the Fowler Subdomain - the Tallacootra and Coorabie Shear Zones, both of which are more fully discussed in Chapter 8. The contrasting metamorphic styles and chronology between and within the major crustal blocks in the Fowler Subdomain are probably testament to differential exhumation during Episode 3 transpressional deformation. A significant west to east palaeopressure increase is inferred from thermobarometric calculations (see §6.4), with pressures ranging from <5kb in the western Colona Block to ~10kb in the eastern Nundroo Block, corresponding to at least 16-20km of post-metamorphic structural relief. Hence the Fowler Subdomain forms an ~100km wide, west dipping, oblique crustal section, with the current surface levels representing exhumed crustal depths of ~16-20km in the west to over 35km in the east. The possibility that the present width of the Fowler Subdomain is caused by duplex-style stacking of thrust sheets must not be discounted.

The repeated magmatism, high pressure metamorphism, compressional structural style, geochemistry and architecture of the Fowler Subdomain are consistent with geological evolution at a convergent plate margin during the time interval ~1740-1490 Ma, and possibly as late as 1100 Ma (see Chapter 9). Hydration of essentially anhydrous, high grade metamorphic and igneous rocks in the eastern Fowler Subdomain during several phases of retrograde metamorphism and deformation demands an external hydrous fluid source, probably the upper mantle (Newton, 1989; Bucher-Nurminen, 1990; Frost & Bucher, 1994). The most plausible fluid source (which has been inferred in many modern orogens) is the dewatering of subducting lithosphere beneath the evolving orogen (e.g. Toft et al., 1993). The gross architecture of the Fowler Subdomain suggests that a southeast-dipping subduction zone may have operated during the Palaeo-Mesoproterozoic along the northwestern palaeomargin of the Gawler Craton. The geodynamic implications of the Episode 3 shear zones are further discussed in Chapters 8 and 9.

Chapter 7
TECTONOTHERMAL EVOLUTION OF THE WILGENA AND NUYTS SUBDOMAINS

7.1 Introduction

The Wilgena and Nuyts Subdomains contrast markedly with other subdomains discussed in this thesis in one fundamental way: *they have not undergone any significant burial since at least the late Palaeoproterozoic*. Both the Wilgena and Nuyts Subdomains have experienced quite similar Palaeo-Mesoproterozoic tectonothermal histories involving at least two phases of extensive felsic magmatism and volcanism, and deformation largely confined to narrow, relatively low grade shear zones and faults. They are separated by the east-west trending Yerda Shear Zone; a major sinistral strike slip fault system over 300km long (see Chapter 8). The main distinguishing feature of the Wilgena Subdomain is the presence of widespread, supracrustal Archaean rocks and numerous shallow, Palaeo-Mesoproterozoic sedimentary basins.

The geology of the Wilgena and Nuyts Subdomains has been peripheral to the main focus of this study (which concentrates on subdomains further to the west) and the information presented in this chapter is necessarily brief. However, much of the data presented here is vital to the development of a tectonothermal framework for the western Gawler Craton, and will be elaborated upon in Chapter 9. The Gawler Range Volcanics and Hiltaba Suite Granites are common to both the Wilgena and Nuyts Subdomains, and are outlined in Section 7.2. The geology of the Wilgena Subdomain is outlined in Section 7.3, and the Nuyts Subdomain in Section 7.4.

7.2 Gawler Range Volcanics and Hiltaba Suite magmatism

Massive, very high temperature, felsic igneous activity during the early Mesoproterozoic (~1590-1570 Ma) is marked by the voluminous Hiltaba Suite Granites and the Gawler Range Volcanics (GRV) which dominate the geology of the Wilgena and Nuyts Subdomains. The total area affected by this felsic magmatism in the Gawler Craton exceeds 100,000km^2, and resulted in the addition of at least 300,000km^3 to the crust (Stewart, 1997). The Gawler Range Volcanics form over 25,000km^2 of outcrop (Daly et. al, 1997), over 1000km^2 of which occurs in the Wilgena Subdomain. The GRV consists of rhyolites, dacites and minor basalts which form an undeformed, essentially flat-lying volcanic pile up to 3km thick (Drexel et. al, 1993). The Gawler Ranges are marked by a broad wavelength gravity high which is probably caused by a dense, mid-lower crustal mafic intrusive body (Stewart, 1994). The aeromagnetic signature of the GRV is characterised by short wavelength, rough-textured, moderate-high magnetic intensity anomalies which largely obscure the longer wavelength anomalies caused by the underlying crust. The contemporaneous Hiltaba Suite Granites form high level, elliptical plutons which dominate the magnetic signature of the Wilgena and Nuyts Subdomains. The Hiltaba Suite consists of medium to coarse grained, K-feldspar-rich granites which grade into rhyloite in some areas, attesting to their high-level nature. They generally form well-defined, elliptical, magnetically quiet anomalies, which coincide with distinct gravimetric lows (<-10mgal).

U-Pb zircon geochronology yields ages of ~1590 Ma for the Gawler Range Volcanics (Fanning et. al, 1988) and ~1580-1590 Ma for the Hiltaba Suite Granites (Flint, 1993; K. Stewart pers. comm., 1997). Geochemical and isotopic data indicates distinctly A-type (anorogenic), within-plate affinities for the GRV and the Hiltaba Suite, and show that they are comagmatic (Giles, 1988; Flint, 1993; Stewart, 1994, 1997). The felsic magmas probably evolved via assimilation fractional crystallisation (AFC) processes from an initially mantle-derived, mafic melt (Stewart, 1997). The Yerda Shear Zone, which marks the boundary of the Wilgena and Nuyts Subdomains forms a distinct geochemical discontinuity (B. Schaefer and K. Stewart pers. comm., 1997); to the north in the Wilgena Subdomain, the Hiltaba Suite and GRV show evidence for contamination by an Archaean crustal source (see §7.4.5). The massive volume, anorogenic setting and geochemical characteristics of the Hiltaba Suite and the GRV strongly suggest that magmatism was caused by a massive thermal perturbation in the mantle lithosphere, probably from a mantle plume; a notion supported by geophysical modelling which shows a large mid-crustal mafic intrusion beneath the GRV (Stewart, 1994, 1997). The circular-elliptical surface geometry of the Hiltaba Suite plutons suggests that they intruded into a relatively neutral stress regime (Emslie, 1980; Hoffman, 1989); an important consideration in light of Mesoproterozoic tectonic activity in subdomains to the north and west.

7.3 Wilgena Subdomain

7.3.1 Introduction

The Wilgena Subdomain forms a westward-narrowing wedge over 300km wide and 100km long, which is truncated to the north and west by the Coorabie Shear Zone, to the south by the Yerda Shear Zone, and to the east by the Stuart Shelf/Torrens Hinge Zone (see Figures 3.3 & 8.1). The geological framework of the Wilgena Subdomain is dominated by a complex Archaean basement (the ~3.0-2.4Ga Mulgathing Complex), intruded by Palaeoproterozoic granitoids (~1.7Ga - e.g. the Symon's Granite) and Mesoproterozoic granitoids and volcanics (the Hiltaba Suite/Gawler Range Volcanics event - see above). One of the most significant features of the Wilgena Subdomain is the widespread presence of low grade, clastic sediments deposited in several stages in localised basins during the Palaeo-Mesoproterozoic. Together with the presence of undeformed, fresh ~1.6Ga Gawler Range Volcanics, these sediments indicate that the Wilgena Subdomain has undergone very little burial since the Palaeoproterozoic; in marked contrast with the subdomains to the north and west. All units in the Wilgena Subdomain have been affected by at least two generations of narrow, low grade, strike slip shear zones which generally trend ENE, and have been instrumental in controlling basin development. Metamorphism appears to be low grade and locally reaches greenschist to lower-amphibolite facies. This section outlines the principal geological elements of the Wilgena Subdomain, and provides a brief discussion on its tectonic evolution.

7.3.2 Mulgathing Complex

The term Mulgathing Complex encompasses all late Archaean to early Palaeoproterozoic rocks in the northwestern Gawler Craton (Daly et. al, 1979). The Wilgena Subdomain contains a diversity of lithologies interpreted to be Mulgathing Complex which contrast with rocks of similar age in the Christie Subdomain (which experienced granulite facies metamorphism, partial melting and pervasive ductile deformation at this time - see Chapter 5). Archaean lithologies of the Mulgathing Complex have been subdivided into ten rock units (Daly & Fanning, 1993), all of which are found in the Wilgena Subdomain. The metasedimentary Christie Gneiss (which is the dominant Archaean lithology in the Christie Subdomain) is much lower grade (greenschist to amphibolite facies), less abundant and distinctly different in appearance in the Wilgena Subdomain, and is often interlayered with the felsic Kenella Gneiss and intruded by the high level, anorogenic, ~2500 Ma, Glenloth Granite. The presence of well-preserved Mulgathing Complex supracrustals, such as the Hopeful Hill Basalt (~2670Ma? tholeiitic pillow basalt - Daly & Fanning, 1990), very weakly deformed calc-alkaline volcanics in Esso-DP1 (2553±9 Ma - Fanning, 1997), and the Lake Harris Komatiite (serpentinised ultramafic with relict spinifex textures - Daly & Fanning, 1990, dated at 2499±11 Ma - Fanning, 1997) indicate that the Mulgathing Complex in the Wilgena Subdomain has not undergone significant deformation, metamorphism or burial during the Sleafordian Orogeny (2500-2300Ma - Fanning et. al, 1988), or during any subsequent tectonic activity.

7.3.3 Palaeoproterozoic sediments

In the Tarcoola-Kingoonya area, the Mulgathing Complex is unconformably overlain by the Wilgena Hill Jaspilite; a very fine grained, finely laminated, jaspilitic banded iron formation. The Wilgena Hill Jaspilite is openly folded, locally more deformed (near faults and shear zones) and is metamorphosed to upper-greenschist facies (as evidenced by narrow chloritic layers). Locally it reaches a maximum thickness of 700m (Daly et. al, 1997), and is overlain by the clastic Labyrinth Formation. Rhyolite interbedded with the Labyrinth Formation yields a U-Pb zircon age of 1723±10Ma (Daly et. al, 1997) which is a minimum age for the Wilgena Hill Jaspilite. The Labyrinth Formation is interpreted to have been deposited in a localised, shallow, fault-bound basin (Daly et. al, 1997). It exhibits a well-developed cleavage, but is essentially unmetamorphosed. In the Kingoonya area, the Eba Formation (which underlies the Labyrinth Formation) comprises a ~1200m thick sequence of quartzite with pebble conglomerate beds (Daly et. al, 1997). The Eba Formation contains pebbles of Wilgena Hill Jaspilite, hence postdates it (Daly et. al, 1997).

7.3.4 Palaeoproterozoic intrusives

The Wilgena Subdomain contains large tracts of granitic material which is locally well foliated. Lithologically, the granitoids comprise coarse grained, megacrystic, moderate-high magnetic susceptibility granitoids which grade into augen gneiss and medium-grained leucogranite. The Symon's Granite (near Mulgathing Homestead) has a U-Pb zircon age of 1690±10 Ma (Daly et. al, 1997). Little is known about the geochemical character and tectonic significance of these Palaeoproterozoic intrusives, which form a volumetrically significant part of the western Wilgena Subdomain (>1500km^2).

7.3.5 Tarcoola Formation

The Tarcoola Formation is a clastic, fluvial to marine sequence of sedimentary rocks deposited in shallow, elongate, east-west trending grabens and half grabens in the late Palaeoproterozoic (Daly, 1993; Daly et. al, 1997). Locally the Tarcoola Formation exceeds 2000m in thickness and is openly folded by a series of east-west trending, upright folds which exhibit a local axial planar cleavage (Daly et. al, 1997), and parallel regional-scale, ENE trending faults. It is essentially unmetamorphosed, with the exception of low grade contact metamorphism (up to lower greenschist facies, evidenced by randomly oriented chlorite in shales and mudstones) and alteration associated with the intrusive Hiltaba Suite Granites. It contains concordant tuff layers which have a U-Pb zircon age of 1656±7 Ma (Daly, 1993). The Tarcoola Formation contains significant hydrothermal gold mineralisation in areas where it is crosscut by later faults, and has been the focus of intense prospecting, mining and mineral exploration for the past century.

7.3.6 Pandurra Formation

The Pandurra Formation (of the Cariewerloo Basin) forms a thick (<950m) sequence of monotonous, flat-lying, unmetamorphosed, arenaceous redbed sediments (Cowley, 1993) which unconformably overlie older lithologies (including the Gawler Range Volcanics) in the eastern parts of the Wilgena Subdomain. Rb-Sr geochronology of interbedded siltstone and shale yield an isochron age of 1424±51 Ma interpreted to be a minimum depositional age (Fanning et. al, 1983). The Pandurra Formation is though to have been deposited in a braided stream/alluvial floodplain environment, in an elongate, northwest-trending graben (the Cariewerloo Basin), with a westerly provenance which included the Gawler Range Volcanics (Cowley, 1993). Importantly, a northern branch of the ?1100-1200 Ma Coorabie Shear Zone defines the northern margin of the Pandurra Formation (see Figure 8.1 and Chapter 8).

7.3.7 Discussion

Rocks in the Wilgena Subdomain record a >1500Ma Precambrian history of upper crustal tectonothermal processes spanning the late Archaean (?~3000Ma sediments and ~2600Ma volcanics) through to the Mesoproterozoic (~1400Ma Pandurra Formation). This contrasts significantly with subdomains to the west, which have undergone considerable Palaeo-Mesoproterozoic mid-lower crustal tectonism (see Chapters 4, 5 and 6). Importantly, metamorphism has been low grade (no more than lower amphibolite facies), and deformation is largely confined to narrow faults and shear zones ranging in age from early Palaeoproterozoic to Mesoproterozoic (see Chapter 8) and localised upright folding of the Tarcoola Formation prior to GRV/Hiltaba magmatism (which is also very proximal to the ENE-trending shear zones). Of particular note is the repeated development of small, relatively shallow sedimentary basins during the Palaeo-Mesoproterozoic and the associated clastic and chemical sediments (the Wilgena Hill Jaspilite, Eba Formation, Labyrinth Formation, Tarcoola Formation and Pandurra Formation).

7.4 Nuyts Subdomain

7.4.1 Introduction

The Nuyts Subdomain forms a large crustal block over 250km wide and 250km long, bound to the west by the Coorabie Shear Zone, to the north by the Yerda Shear Zone, to the east by the Gawler Range Volcanics and the Coulta Subdomain, and to the south by the coastline. The geological framework of the Nuyts Subdomain is dominated by a presumed Palaeoproterozoic basement (of unknown age and composition), a suite of late Palaeoproterozoic intrusives and extrusives (the ~1.63 Ga St Peter Suite), a suite of voluminous Mesoproterozoic intrusives (the ~1.59 Ga Hiltaba Suite - see §7.2 above), and a suite of late, S-type intrusives (the *Munjeela Suite - n*ew name). Importantly, the presence of ~1.63 Ga volcanic in the Nuyts Archipelago, undeformed Gawler Range Volcanics and high-level Hiltaba Suite plutons indicates that the Nuyts Subdomain has undergone no pervasive tectonism since at least the late Palaeoproterozoic. This contrasts markedly with the Fowler Subdomain immediately to the west, where lower crustal Mesoproterozoic granulites are exposed (see Chapter 6). The Nuyts Subdomain has been effected by a range of narrow, low grade, NE to EW-trending, narrow shear zones which are currently the focus of intensive mineral exploration, as they are known to have focussed gold mineralisation (e.g. the Yarlbrinda Shear Zone).

7.4.2 Undifferentiated basement

Presumed Palaeoproterozoic material forms the "basement" in the Nuyts Subdomain. Exposure of this older material is extremely limited, and its distribution is largely inferred from geophysical data. Well foliated, amphibolite facies, garnet-biotite-muscovite metasedimentary schist occurs as xenoliths in undeformed Munjeela Suite granite at Point Bell (see §7.4.4 below). The sharp nature of the xenolith margins suggests that they represent fragments of local country rock and that the layered magnetic anomalies which parallel the margins of the Munjeela Suite pluton are caused by similar lithologies. Complexly deformed metaigneous

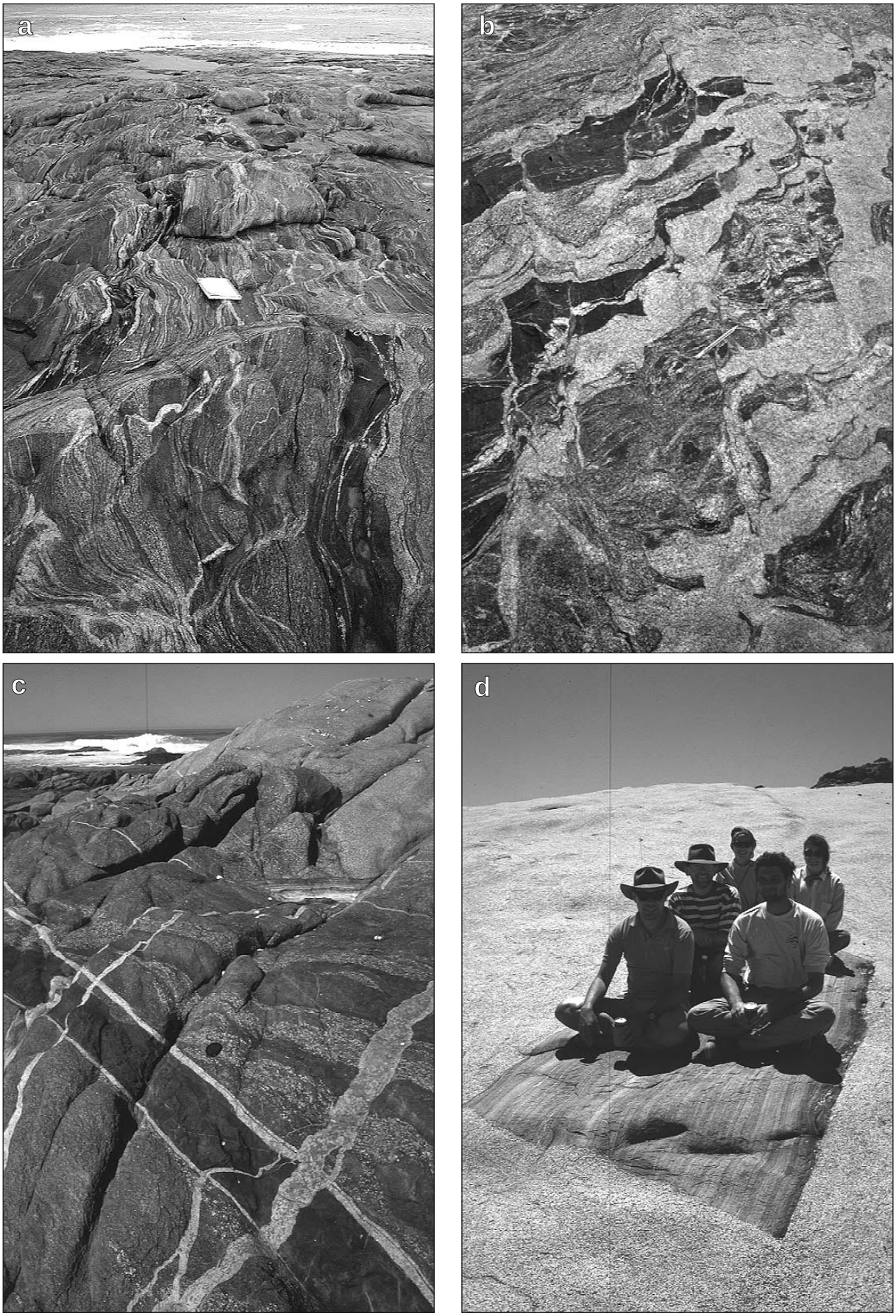

Figure 7.1 Photographs from coastal outcrops in the Nuyts Subdomain. (a) Complexly deformed, migmatitic "basement" orthogneisses of unknown age at Rocky Point. (b) Complexly deformed, dark-grey, "basement" orthogneisses at Rocky Point, intruded by St Peter Suite leucogranite and subsequently deformed by narrow, ductile shear zones. (c) Complex crosscutting igneous relationships in the St Peter Suite at Point Brown. (d) "Magic carpet" xenolith of fine grained, biotite-muscovite gneiss in an undeformed, Munjeela Suite, S-type granite at Point Sinclair. Note sharp xenolith margins, indicating a "proximal" source.

gneisses occur at several isolated outcrops in the Poondinga-Jellabinna area, as well as at Rocky Point, where an older, amphibolitic orthogneiss sequence is intruded and migmatised by St Peter Suite granitoids. No geochronological data exists for the older rocks in the Nuyts Subdomain, however isotopic data for the Mesoproterozoic granitoids unambiguously indicates that they have not been contaminated by Archaean crustal material; in contrast with temporally equivalent intrusives in the dominantly Archaean Wilgena and Coulta Subdomains (K. Stewart pers. comm., 1997). Therefore the age of undifferentiated basement in the Nuyts Subdomain is tentatively interpreted to span the time interval ~2000-1630 Ma.

7.4.3 St Peter Suite intrusives and Nuyts Volcanics

The St Peter Suite comprises a series of comagmatic intrusive rocks which outcrop in the Streaky Bay/Nuyts Archipelago area (Flint et. al, 1990). It consist of a series of intermingled, massive granitoids which contain varying amounts of comagmatic mafic material, and have A-type geochemical affinities (Flint et. al, 1990; Parker, 1993). Granitoids range from fine grained, equigranular leucogranite through to coarse grained, relatively mafic granodiorite. Mafic dykes and enclaves are dominated by hornblende and plagioclase. The contact relationships between different lithologies are often very complex, and exhibit spectacular igneous mixing textures (e.g. intermingling of mafic dykes and enclaves with granitoid melts). U-Pb zircon geochronology yields an age of 1620±4 Ma for the Point Brown granodiorite (Flint et. al, 1990). Knight (1997) obtained a Pb-Pb zircon evaporation age of 1608±10 Ma for a tonalite at Cape Beaufort west of Ceduna. The St Peter Suite is locally deformed by discrete, narrow, low grade, northeast trending, sinistral, strike-slip shear zones, and occasionally contains a weak, northeast trending tectonic foliation.

The Nuyts Volcanics comprise a series of porphyritic rhyolites to rhyodacites which are comagmatic with the St Peter Suite (Parker, 1993). U-Pb geochronology yields an age of 1627±2Ma for the Nuyts Volcanics (Rankin et. al, 1990). The Nuyts Volcanics both intrude, and are intruded by various St Peter Suite intrusives, indicating that the St Peter Suite pluton is relatively high level.

Aeromagnetic data suggests that the St Peter Suite forms a large, ~70km wide, moderate-high magnetic intensity, elliptical pluton which exhibits a complex, seemingly random magnetic fabric which probably reflects the complex lithological relationships described above. Narrow, northeast-trending demagnetised zones coincide with observed shear zones. St Peter Suite equivalents are interpreted over broad areas in the Nuyts Subdomain, although direct geochemical and/or geochronological evidence is not yet available to support this notion.

7.4.4 Munjeela Suite magmatism

Medium-grained, equigranular, garnet-muscovite-biotite bearing granites outcrop at Point Bell, Point Sinclair and Munjeela Rock Hole and combine to define the *Munjeela Suite* (new name). Aeromagnetic data indicates that these outcrops form part of a series regionally extensive, low magnetic intensity, irregularly shaped plutons up to 40km in diameter. The irregular boundary of the Munjeela pluton suggests that it stoped into the layered country rock, whose trend lines parallel the pluton margins (see Figure I1). The mineralogy and geochemistry of these granites suggest S-type affinities (K. Stewart pers. comm., 1997); at odds with the dominantly A-type St Peter and Hiltaba Suites. Granite from Munjeela Rock Hole has an Sm-Nd depleted mantle model age of ~2120 Ma (K. Stewart pers. comm., 1997) which places an upper bound on the age of the sedimentary material from which it is derived. This is very significant, since it shows no affinities with the Archaean Mulgathing/Sleaford Complexes, and suggests the widespread presence of unexposed Palaeoproterozoic metasedimentary rocks in the Nuyts Subdomain (see §7.4.2 above).

7.4.5 Discussion

The surface geology of the Nuyts Subdomain is dominated by Mesoproterozoic felsic intrusives of the St Peter, Hiltaba and Munjeela Suites which comprise over 75% of the interpreted surface geology. Geochemical and isotopic data for these intrusives indicates that they are not related to the Archaean Mulgathing/Sleaford Complex, in marked contrast with Mesoproterozoic intrusives in the dominantly Archaean Wilgena and Coulta Subdomains (K. Stewart pers. comm., 1997). In the context of the Gawler Craton, this period of massive crustal growth is largely focussed in the Nuyts Subdomain, with relatively minor synchronous magmatism in the now-adjacent Wilgena and Coulta Subdomains. Deformation and metamorphism in the Nuyts Subdomain has been low grade, and localised within narrow shear zones of varying age. The semi-brittle nature and abundant alteration present in these shear zones indicates major fluid flow which is known to have focussed significant gold mineralisation. Thus further geochronology aimed at constraining the age of these shear zones with respect to major intrusives is recommended.

Chapter 8
SHEAR ZONES IN THE WESTERN GAWLER CRATON

8.1 Introduction

Shear zones are an important key to unravelling the apparently disparate tectonic histories present within terranes such as the western Gawler Craton. The localisation of strain by shear zones at all scales fundamentally controls the crustal response to deformation, and as a result, shear zones are critical to the architecture of all orogenic belts. The geophysical interpretation of shear zones in the western Gawler Craton presented in Chapter 3 shows that it has been affected by at least three generations of major, craton scale shear zones which often juxtapose subdomains of significantly different geological character and have clearly been responsible for the exhumation of large tracts of lower crustal material. These shear zones comprise approximately 10% of the interpreted surface geology in the study area, and are termed "framework" shear zones in this chapter.

The three generations of late, "framework" shear zones that have been identified in the western Gawler Craton (see Chapter 3) are: (i) a set of early, east-west trending shear zones (SZ_1) which are responsible for some of the key subdomain juxtapositions in the western Gawler Craton (e.g. the Yerda Shear Zone which juxtaposes the Wilgena and Nuyts Subdomains), (ii) a set of major, northeast-trending shear zone systems (SZ_2) which dominate the geology of the western Gawler Craton (e.g. the Tallacootra and Coorabie Shear Zones, which juxtapose and transect the Nawa, Christie, Fowler, Wilgena and Nuyts Subdomains), and (iii) the Karari Fault Zone (SZ_3). These shear zones are illustrated in Figure 8.1. Numerous other, smaller scale shear zones which predate the above-mentioned systems occur throughout the western Gawler Craton. They range in age from early Palaeoproterozoic (Sleafordian) through to Mesoproterozoic, and are an important part of the intra-Subdomain structural evolution of the area. They have been discussed where relevant in the preceding chapters.

The relative timing of shear zones in the western Gawler Craton can be established from crosscutting relationships observed in the interpretive geological map. Important observations include:

- SZ_1 shear zones *postdate* the ~1580-1590 Ma Hiltaba Suite granites and Gawler Range Volcanics.
- SZ_1 shear zones *predate* the ~1424 Ma Pandurra Formation;
- SZ_2 shear zones *postdate*::
  - the ~1670 Ma Ifould Complex intrusives;
  - the ~1580 Ma Hiltaba Suite granites;
  - the SZ_1 east-west shear zones;
  - ~1550 Ma lower crustal granulites in the Coober Pedy Subdomain;
  - ~1540 Ma lower crustal granulites in the Fowler Subdomain;
  - ~1490 Ma retrograde amphibolites and pegmatites in the Fowler Subdomain;
  - ~1425 Ma Pandurra Formation in the Cariewerloo Basin.
- The SZ_3 Karari Fault Zone *postdates* the major, northeast trending, SZ_2 shear zones;
- Both SZ_2 and SZ_3 shear zones *predate* the ~800 Ma Gairdner Dyke Swarm.

This chapter summarises all available information about the composition, structure, kinematics, age and metamorphic grade of the late, "framework" shear zones in the western Gawler Craton. Section 8.2 contains information pertaining to the early, east-west trending SZ_1 shear zones, Section 8.3 describes the SZ_2 craton-scale, northeast trending shear zones, and Section 8.4 describes the Karari Fault Zone. Each section covers three areas of interest, outlining the lithological, structural and metamorphic aspects of the shear zones. The geochronology of the shear zones is discussed in Section 8.5, and a discussion of possible relevant geodynamic models for shear zones in the western Gawler Craton is presented in Section 8.6.

8.2 Early east-west trending shear zones (SZ_1)

The interpretive geological map discussed in Chapter 3 shows a set of major, east-west trending, anastomosing shear zones form the boundary between the Wilgena and Nuyts Subdomains (see Figure 8.1), and are collectively known as the Yerda Shear Zone (J. Parker pers. comm., 1997). Known outcrop of the Yerda Shear Zone is extremely limited and inaccessible, however highly strained felsic mylonites with shallow stretching lineations have been reported from a few remote outcrops (K. Stewart & G. Ferris pers. comm., 1997). Smaller scale offshoot shear zones to the north of the Yerda Shear Zone outcrop in the South Lake and Tarcoola areas, where felsic mylonites and ultramylonites

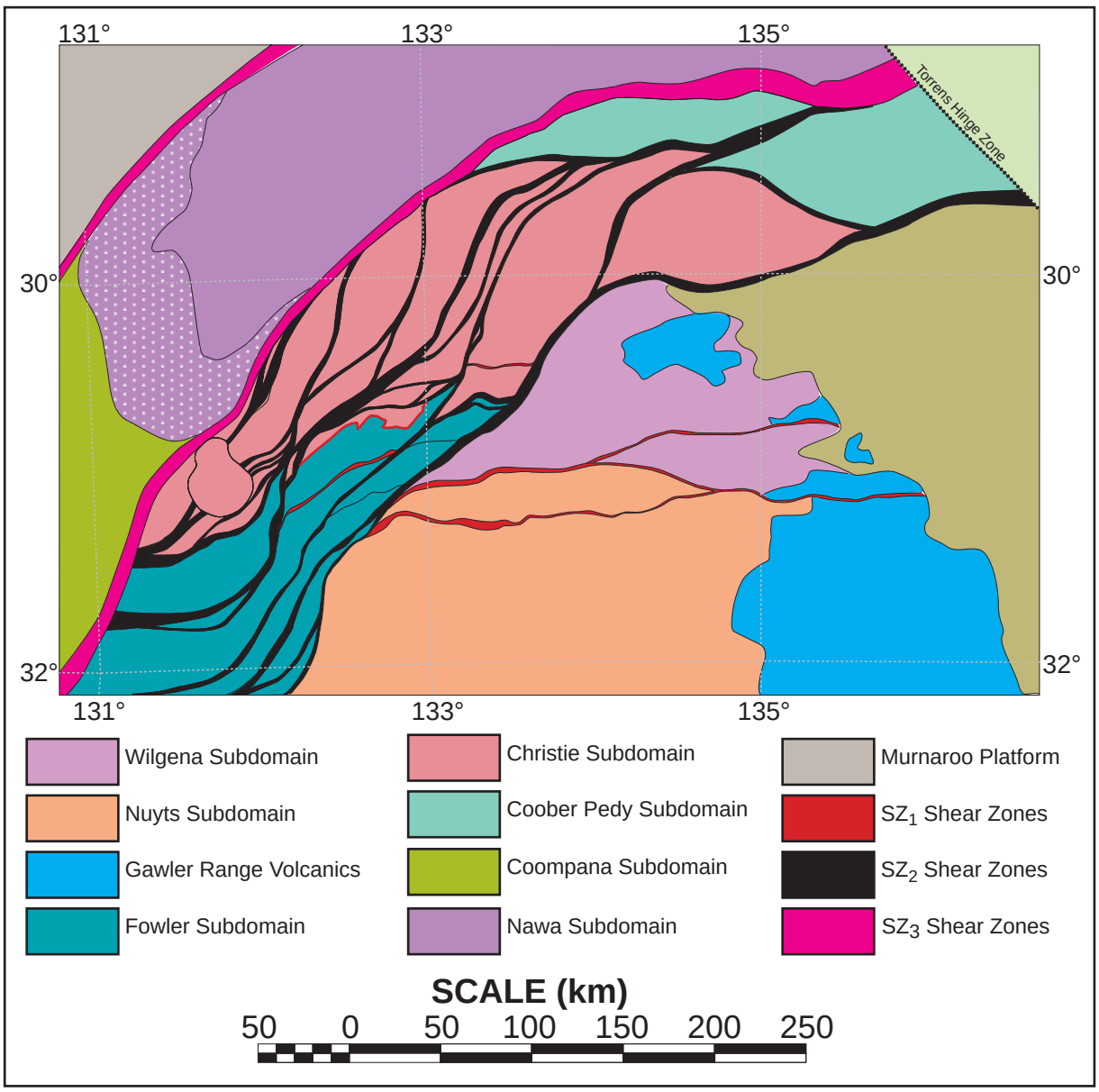

Figure 8.1a Subdomains and shear zones in the northwestern Gawler Craton. Stippled area is the Moondrah mobile belt which defines the southern boundary of the Nawa Subdomain (see Chapter 5).

exhibit a steep foliation and sub-horizontal stretching lineation. Kinematic indicators (asymmetric porphyroclasts and composite SC fabrics) suggest a sinistral, strike-slip shear sense. Some parts of these shear zones are only weakly foliated, with an intense stretching lineation (i.e. L-tectonites) defining sheath folds. In one outcrop south of South Lake, boudins of undeformed porphyritic rhyolite (presumed Gawler Range Volcanics) occur in a series of felsic ultramylonites.

Another set of poorly preserved, east-west trending shear zones are interpreted to form the original boundary between the Christie and Fowler Subdomains (see Chapter 3). These shear zones are correlated with the shear zone defining the northern margin of the Wynbring Pluton. Magnetic data suggests that they dip at moderate-shallow angles to the north. They are offset by a series of narrow, NNE-trending shear zones which are common in the Fowler Subdomain (see Chapter 6).

8.3 Late northeast-trending shear zones (SZ_2)

8.3.1 Introduction

Aeromagnetic images show that the geological framework of the western Gawler Craton is dominated by a system of northeast-trending, craton-scale, curvilinear, anastomosing, low magnetic intensity anomalies attributed to major shear zone systems; principally the Coorabie and Tallacootra Shear Zones. This network of shear zones forms a mobile belt which extends for over 800km at widths of 100-200km, and is responsible for the juxtaposition and exhumation of subdomains of distinctly different geological character (see Figure 8.1).

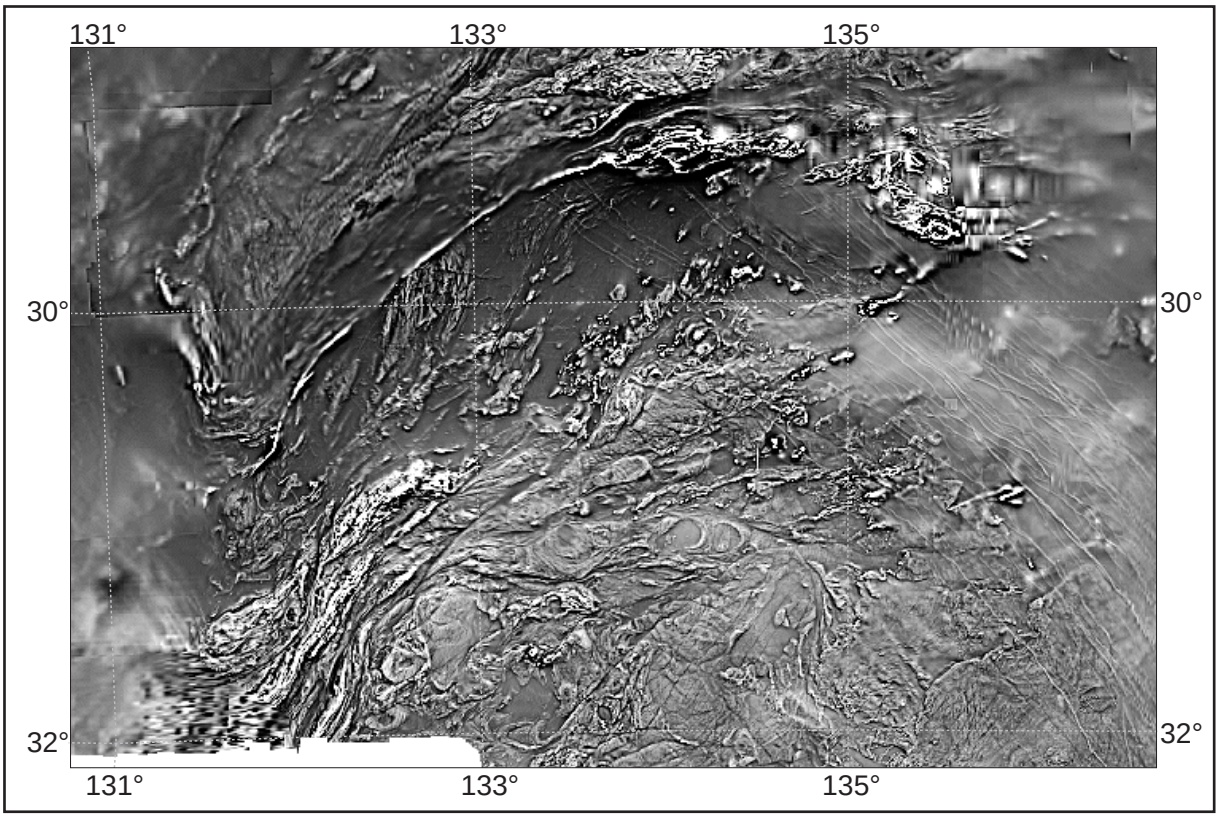

Figure 8.1b Greyscale first vertical derivative aeromagnetic image of the area covered by Figure 8.1a (MESA data).

8.3.2 Tallacootra Shear Zone

The Tallacootra Shear Zone (new name) forms one of the most significant geophysical boundaries in the western Gawler Craton. It can be traced for over 700km as a set of major, ~northeast trending, anastomosing, ductile structures extending from the Torrens Hinge Zone in the far northeastern Gawler Craton southwestward beyond the current coastline where it is truncated by the Karari Fault Zone. Two main exposures of the Tallacootra Shear Zone occur in the study area at Lake Tallacootra and Lake Ifould (see Figure 2.2) that preserve a diversity of high strain, high grade mylonitic lithologies which are detailed below.

8.3.2.1 Lithologies

Lake Tallacootra area

Outcrop at Lake Tallacootra straddles the main part of the Tallacootra Shear Zone, and extends sporadically over a 6km by 2km along-strike region (see Figure 2.2). Outcrop is confined to the topographic lows associated with a series of salt lakes which parallel the shear zone, and comprises platforms and stocks of intensely deformed, heterogeneous mylonites (see Figure 8.2). The dominant lithology is a fine grained, dark grey, quartz-plagioclase-biotite±garnet±epidote mylonite, interlayered with a heterogeneous series of mylonitic orthogneisses (see Figure 8.2), interpreted to be derived from Ifould Complex intrusives of the Christie Subdomain (see Chapter 5). Occasional narrow layers of pelitic, muscovite-biotite-quartz-Kfeldspar-plagioclase ± garnet ± kyanite ± staurolite mylonitic schist and abundant boudins of mafic and calc-silicate gneiss occur (see Figure 8.6). In the mafic boudins, early, pyroxene bearing, granulite facies assemblages have been variably overprinted (mainly at the boudin margins) by amphibolite facies assemblages involving hornblende, garnet, sphene and cummingtonite. Late epidote growth (at the expense of plagioclase and hornblende) is characteristic in all mafic and calc-silicate gneisses at Lake Tallacootra (see Figure 8.5d & 8.6). The most striking outcropping lithology are abundant, very coarse grained pegmatite boudins and dykes which are spectacularly elongated parallel to the steep stretching lineation in the mylonites, and flattened parallel to the foliation (forming "tombstone" outcrops - see Figure 8.2). A series of fine grained, quartz-feldspar-garnet-muscovite aplites intrude all lithologies at Lake Tallacootra (see Figure 8.4). Although they totally crosscut the high strain fabric, they are variably deformed by it (with the same foliation and lineation), therefore are interpreted to be syn-late kinematic. They are weakly folded on the ~10m scale.

Lake Ifould area

At Lake Ifould, the Tallacootra Shear Zone forms a zone of intensely deformed, heterogeneous schists and mylonites, which outcrops extensively along the western shores of Lake Ifould over a strike length of ~12km and projected width of ~2km (see Figure 8.3). The mylonites are layered on the 1cm-

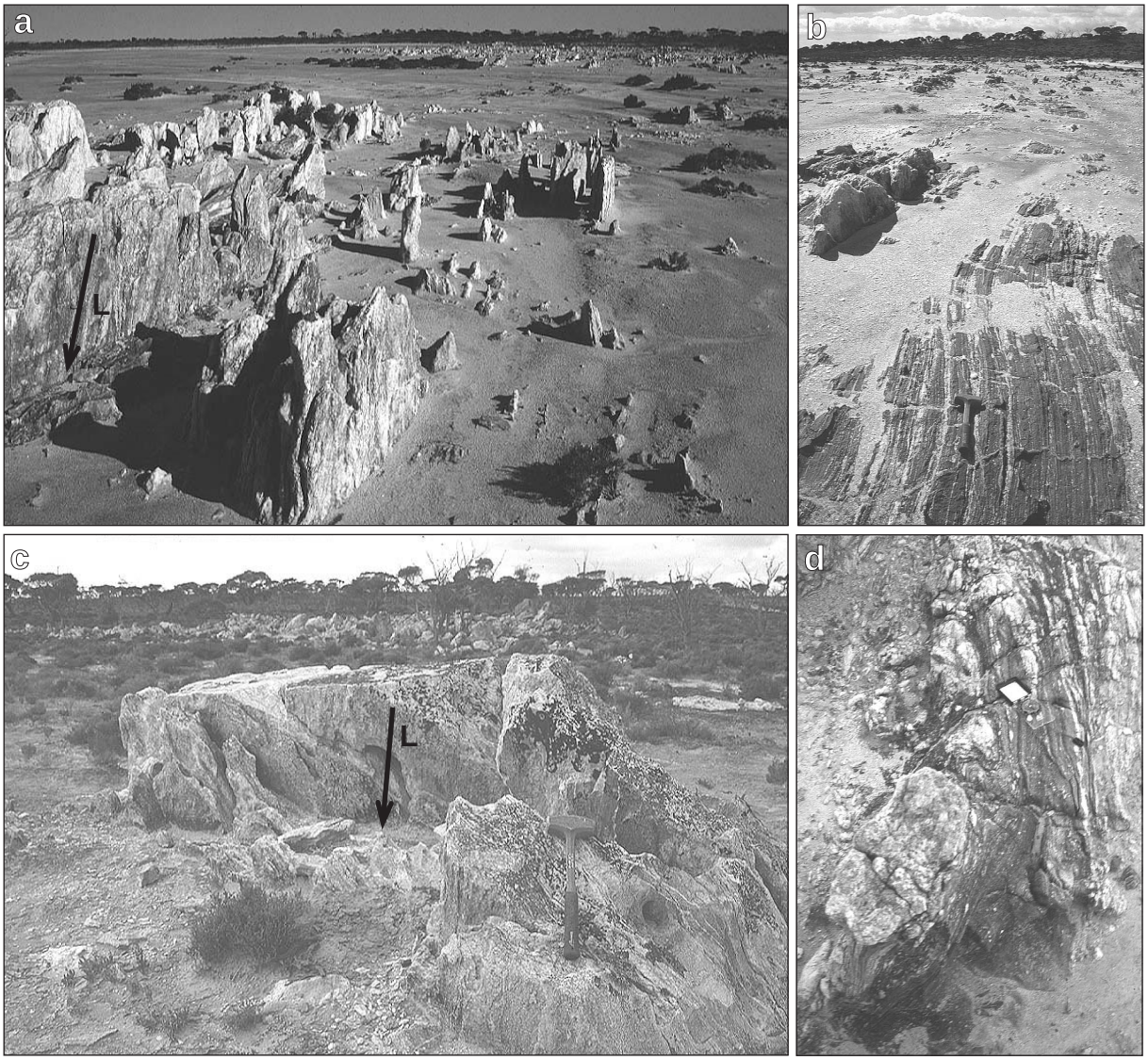

Figure 8.2 Photographs of outcrops in the Tallacootra Shear Zone at Lake Tallacootra. (a) & (b) "Tombstone" outcrops of coarse grained, mylonitised pegmatite boudins set in a matrix of dark grey, quartz-feldspar-biotite±garnet mylonites ("tombstones" are ~0.5-1m high). Note steep stretching lineation (denoted by arrow). (c) Mylonitised, presumed Ifould Complex granite. Note steep stretching lineation (denoted by arrow). (d) Dark grey mylonites folded around a pegmatite boudin (photo looks directly down the stretching lineation).

1m scale, and exhibit a sub-vertical foliation and steep lineation (see §8.3 & Figure 2.2). They contain abundant, narrow, deformed pegmatites and quartz veins, which are isoclinally and ptygmatically folded. Less deformed domains and boudins reveal that the mylonitic protoliths include both the Ifould Complex intrusives and the Christie Gneiss, therefore the mylonites comprise both metasedimentary and metaigneous lithologies (see Chapter 5). The Lake Ifould Shear Zone contains abundant mafic boudins of varying composition, which are related to both the Ifould and Mulgathing Complexes (see Chapter 5).

Lake Ifould area - mylonitic orthoschists

High strain rocks sourced from the Ifould Complex intrusives (principally the migmatites and agmatites) form a series of layered, heterogeneous, biotite-quartz-plagioclase±K-feldspar±epidote schistose mylonites, in which early, coarse, quartz and feldspar grains are porphyroclastic. Early hornblende has broken down to epidote and biotite. Epidote forms sub-euhedral, porphyroblastic laths in the high strain matrix. They are interlayered with a porphyroclastic felsic mylonite.

Lake Ifould area - reworked pelitic granulites

Partially reworked pelitic granulite outcrop extensively at the southern end of Lake Ifould in less strained domains on the margins of the shear zone (see Figures 8.3, 8.7 & 8.8). They form a heterogeneous sequence of moderately foliated, layered gneisses and schists with occasional mafic boudins. In low strain domains, complex, presumably Sleafordian fold patterns can be observed, as well as lithological associations commonly observed in outcrops of undisturbed Christie Gneiss (see Chapter 5). In higher strain domains, Sleafordian structures and are overprinted by the retrograde fabric, and outcrop grades into

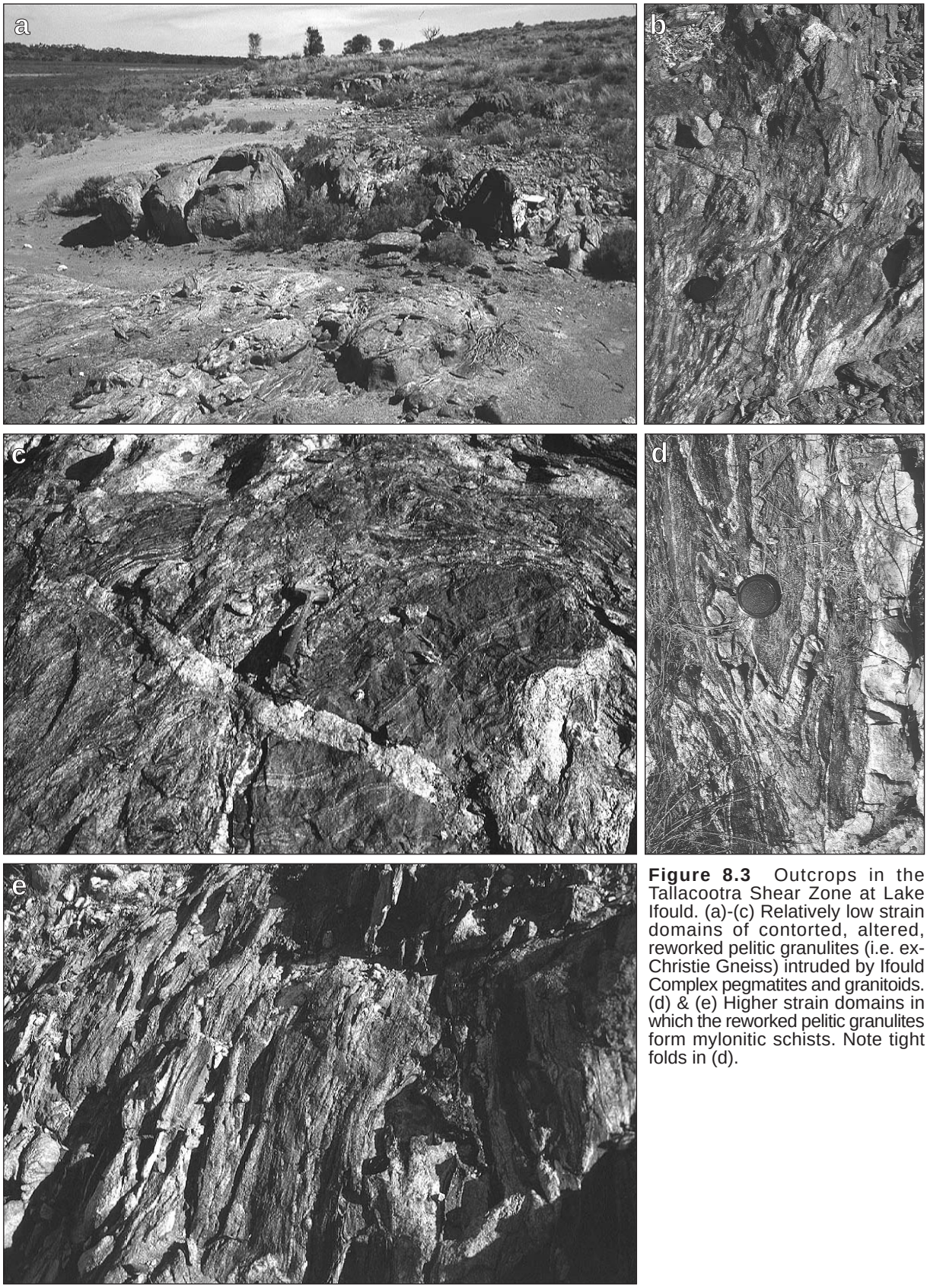

Figure 8.3 Outcrops in the Tallacootra Shear Zone at Lake Ifould. (a)-(c) Relatively low strain domains of contorted, altered, reworked pelitic granulites (i.e. ex-Christie Gneiss) intruded by Ifould Complex pegmatites and granitoids. (d) & (e) Higher strain domains in which the reworked pelitic granulites form mylonitic schists. Note tight folds in (d).

highly strained pelitic schists and mylonites. In thin section, the reworked granulites exhibit spectacular, very fine grained reaction and replacement textures overprinting an early, coarse grained, granulite facies assemblages. The early coarse grained assemblage is inferred to be garnet-cordierite-sillimanite-plagioclase-K-feldspar-quartz ±biotite ±spinel with accessory monazite, zircon and ilmenite (identical to the Mulgathing Complex pelitic granulites outcropping north of Lake Ifould - see Chapter 5). Subsequent reaction and replacement textures include:

- The spectacular breakdown of early cordierite±garnet to very complex, fine grained,

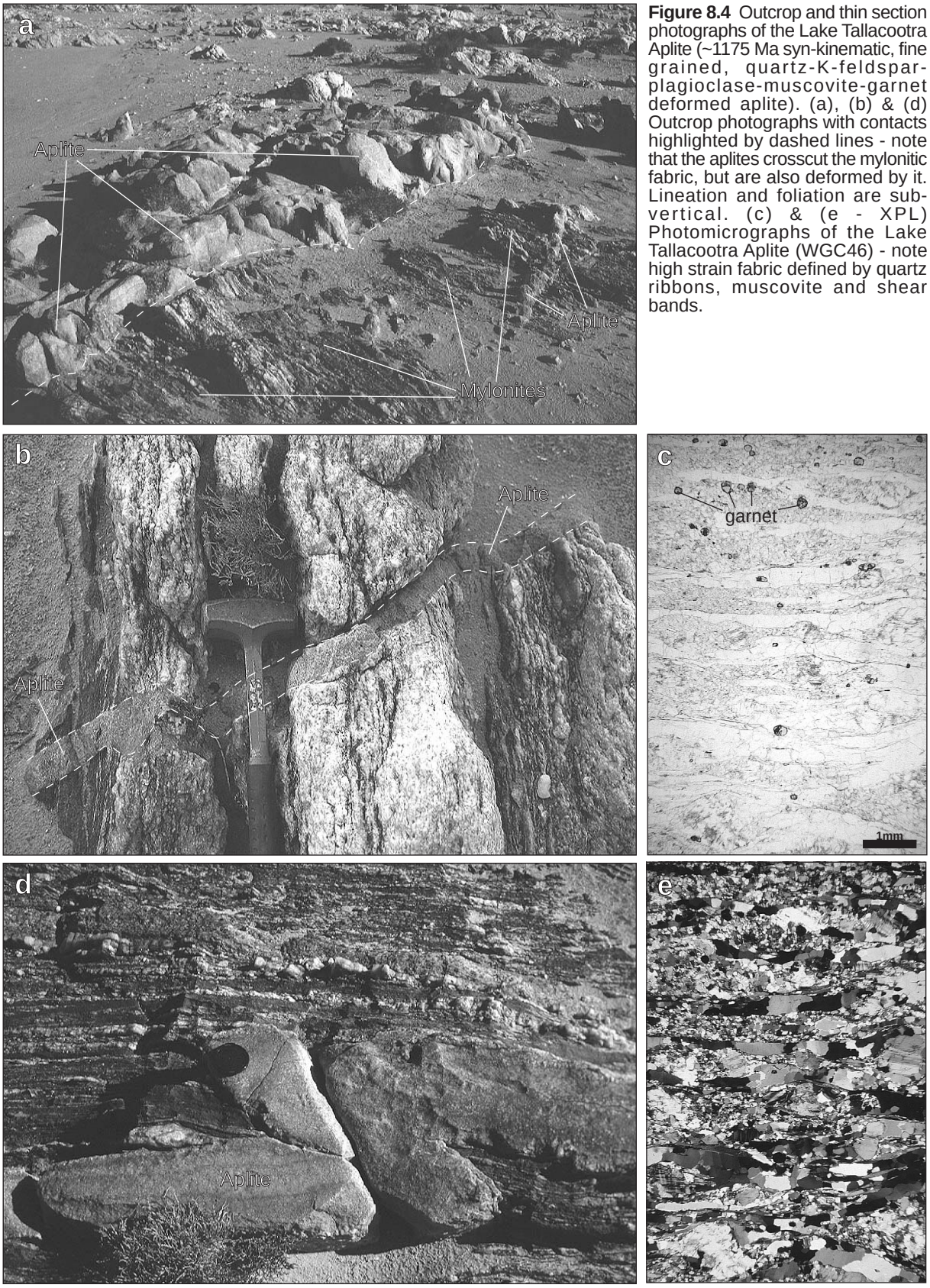

Figure 8.4 Outcrop and thin section photographs of the Lake Tallacootra Aplite (~1175 Ma syn-kinematic, fine grained, quartz-K-feldspar-plagioclase-muscovite-garnet deformed aplite). (a), (b) & (d) Outcrop photographs with contacts highlighted by dashed lines - note that the aplites crosscut the mylonitic fabric, but are also deformed by it. Lineation and foliation are sub-vertical. (c) & (e - XPL) Photomicrographs of the Lake Tallacootra Aplite (WGC46) - note high strain fabric defined by quartz ribbons, muscovite and shear bands.

vermicular intergrowths of staurolite, gedrite, kyanite and quartz. There are several types of reaction texture, which developed in the following order: (i) blocky, staurolite-gedrite intergrowths, (ii) acicular staurolite-quartz±gedrite intergrowths, (iii) very fine sillimanite-staurolite-gedrite-quartz symplectites, and (iv) ultra-fine ?kyanite-quartz symplectites. In general, these reaction textures surround relict cordierite cores and are associated with early garnet, although large, intra-cordierite monazites and zircons have nucleated type (iv) reaction textures (see Figure 8.8).

- The breakdown of early plagioclase to acicular mats of very fine sillimanite intergrown

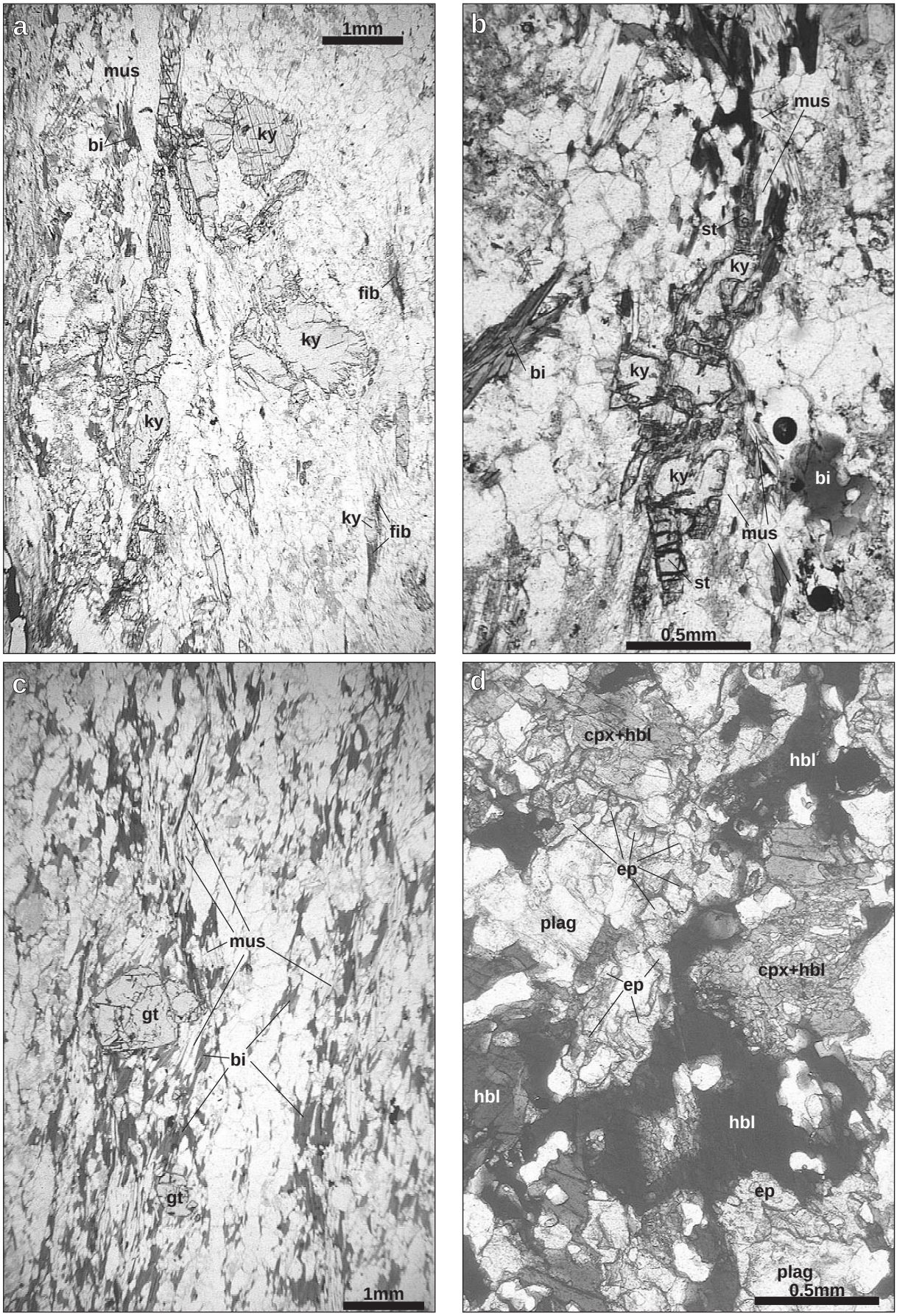

Figure 8.5 Photomicrographs of from the Tallacootra Shear Zone at Lake Tallacootra. (a) WGC39 - Weathered kyanite-biotite-muscovite-quartz-K-feldspar-plagioclase schist, with late fibrolite partially replacing kyanite. (b) WGC38 - Weathered kyanite-staurolite-muscovite-biotite-quartz-plagioclase-K-feldspar schist. (c) WGC98 - Garnet-biotite-muscovite-plagioclase-quartz mylonite. (d) WGC90 - Retrogressed mafic granulite - early clinopyroxene-plagioclase-quartz assemblage is partially replaced by hornblende and epidote, and subsequently the clinopyroxene has partially broken down to secondary hornblende.

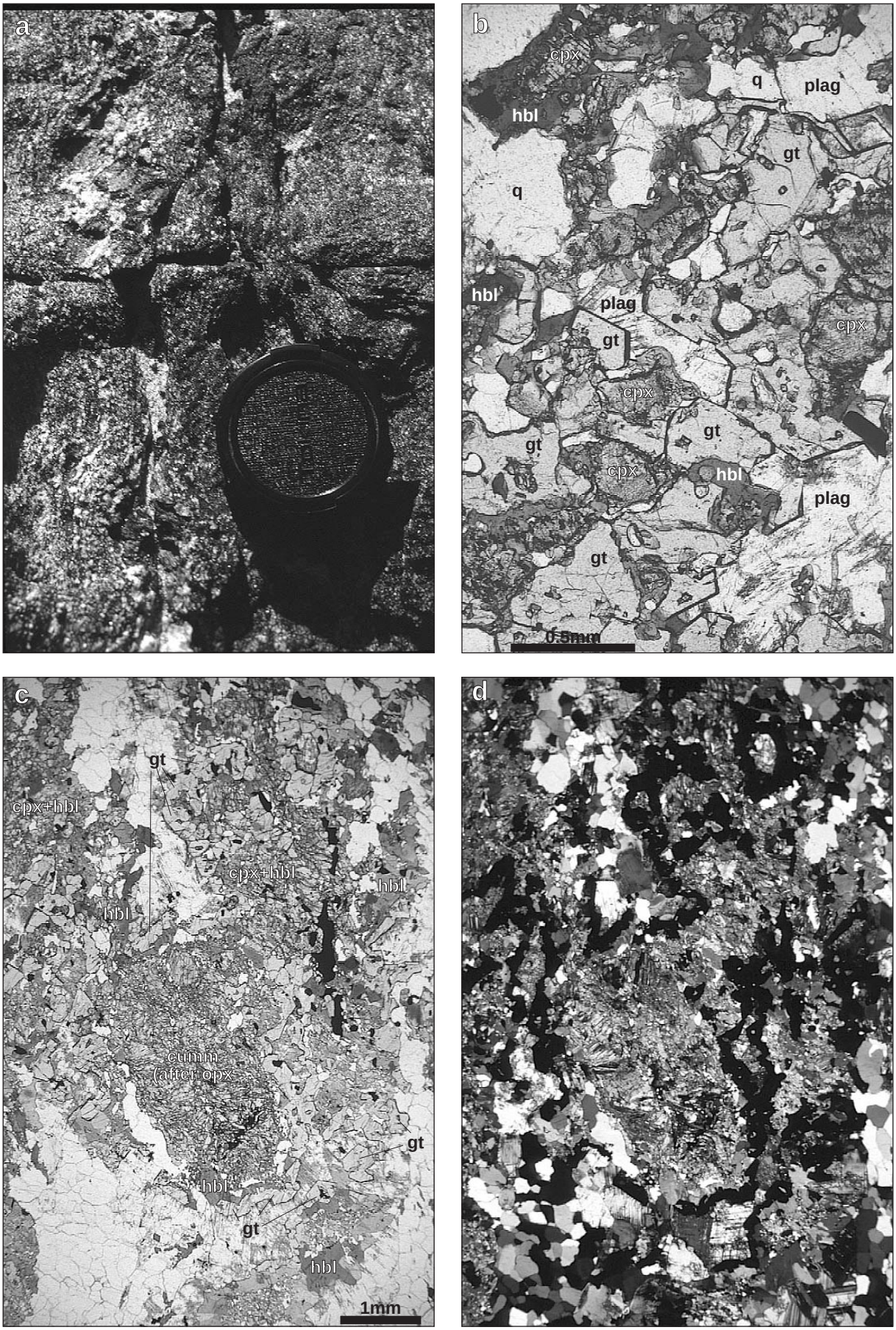

Figure 8.6 Retrogressed mafic granulites from the Tallacootra Shear Zone at Lake Tallacootra. (a) Outcrop photograph - note coarse pyroxenes in leucosomes. (b) WGC47c - Detail of garnet-hornblende intergrowths replacing early clinopyroxene (which has subsequently partially broken down to fine secondary hornblende). (c) & (d - XPL) WGC47c - Overview of retrogressed mafic granulite, showing large mats of cummingtonite (interpreted to isochemically replace orthopyroxene) and partially retrogressed clinopyroxene overprinted by garnet-hornblende intergrowths.

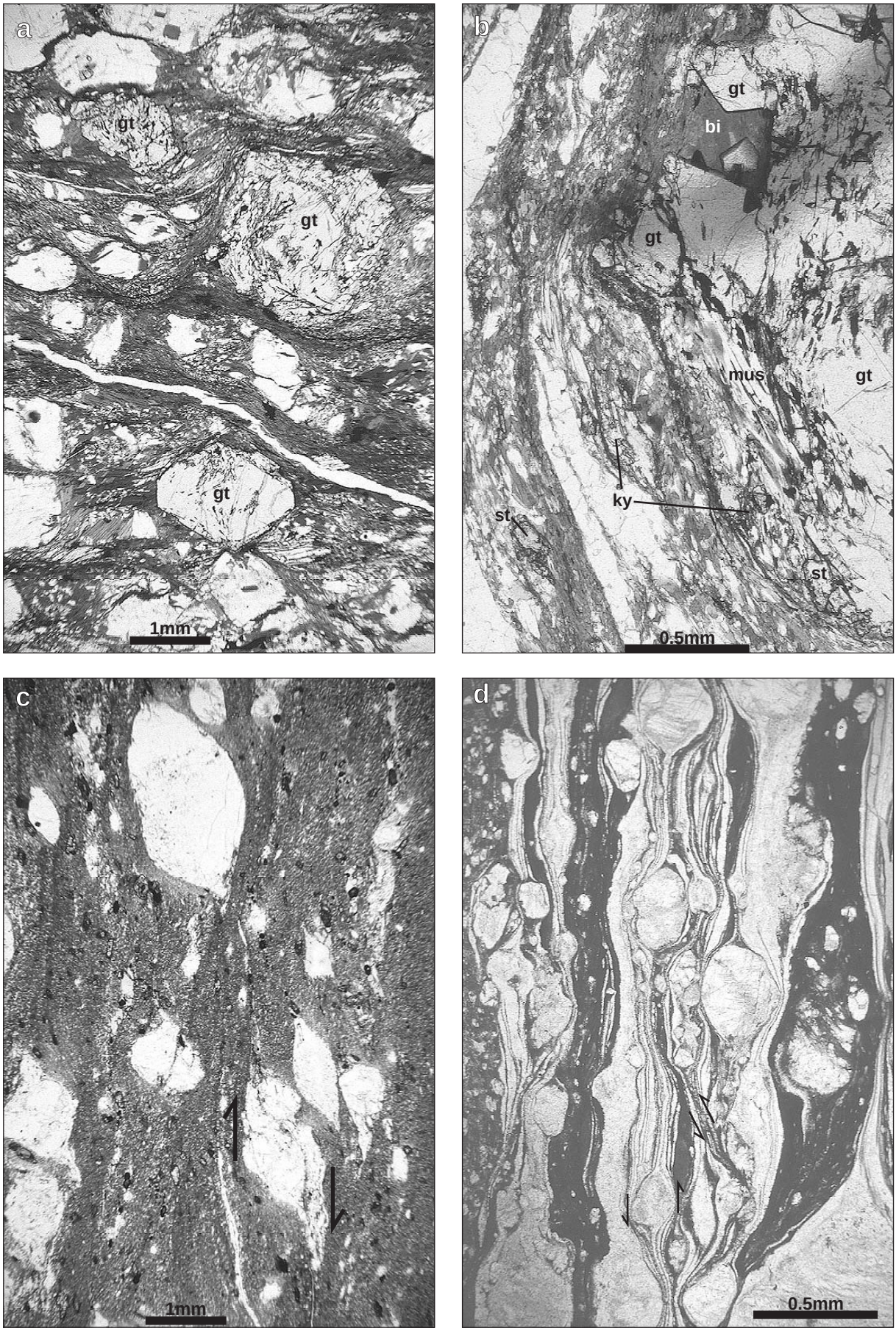

Figure 8.7 Photomicrographs of lithologies from the Tallacootra Shear Zone at Lake Ifould. (a) WGC66b - garnet-staurolite-kyanite-muscovite-biotite schist. Note rotated inclusion trails in garnet (comprising staurolite, mica and kyanite), and fine grained schistose matrix consisting of biotite, muscovite, staurolite, plagioclase, kyanite, K-feldspar and quartz. (b) Detail mineral assemblage in (a). (c) WGC174 - Biotite-rich mylonite with plagioclase and quartz porphyroclasts (east (left)-up kinematics). (d) WGC110 - Porphyroclastic mylonite (east (right)-up kinematics).

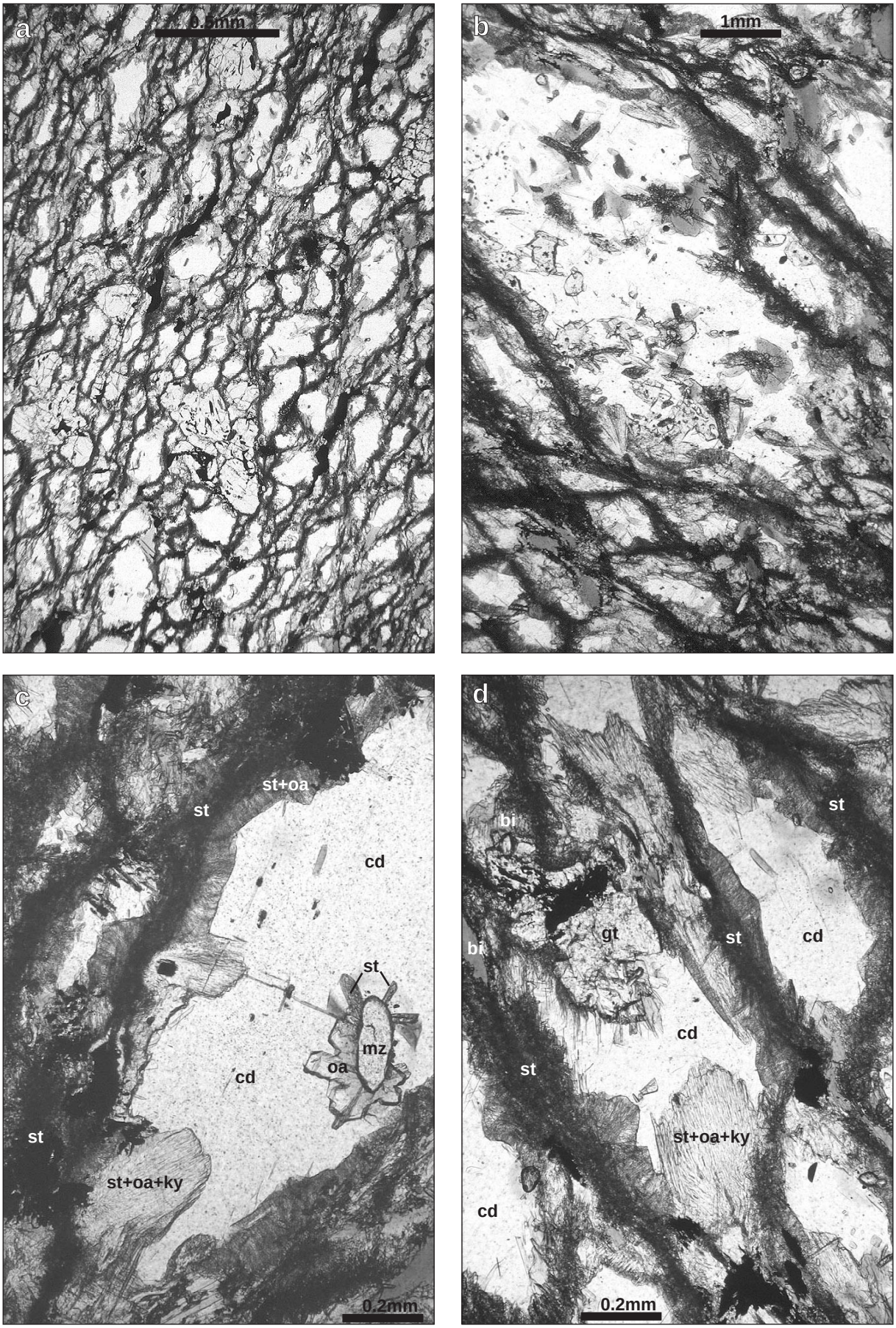

Figure 8.8 Photomicrographs of complex reaction textures in sample WGC101 - a partially retrogressed pelitic granulite from the Tallacootra Shear Zone at Lake Ifould. (a) & (b) Overview of very fine grained reaction textures replacing medium-coarse grained cordierite and plagioclase. (c) Detail of reaction textures. Note that intra-cordierite monazite grain has nucleated orthoamphibole and staurolite growth. (d) Detail of reaction textures, including secondary garnet intergrown with orthoamphibole and biotite.

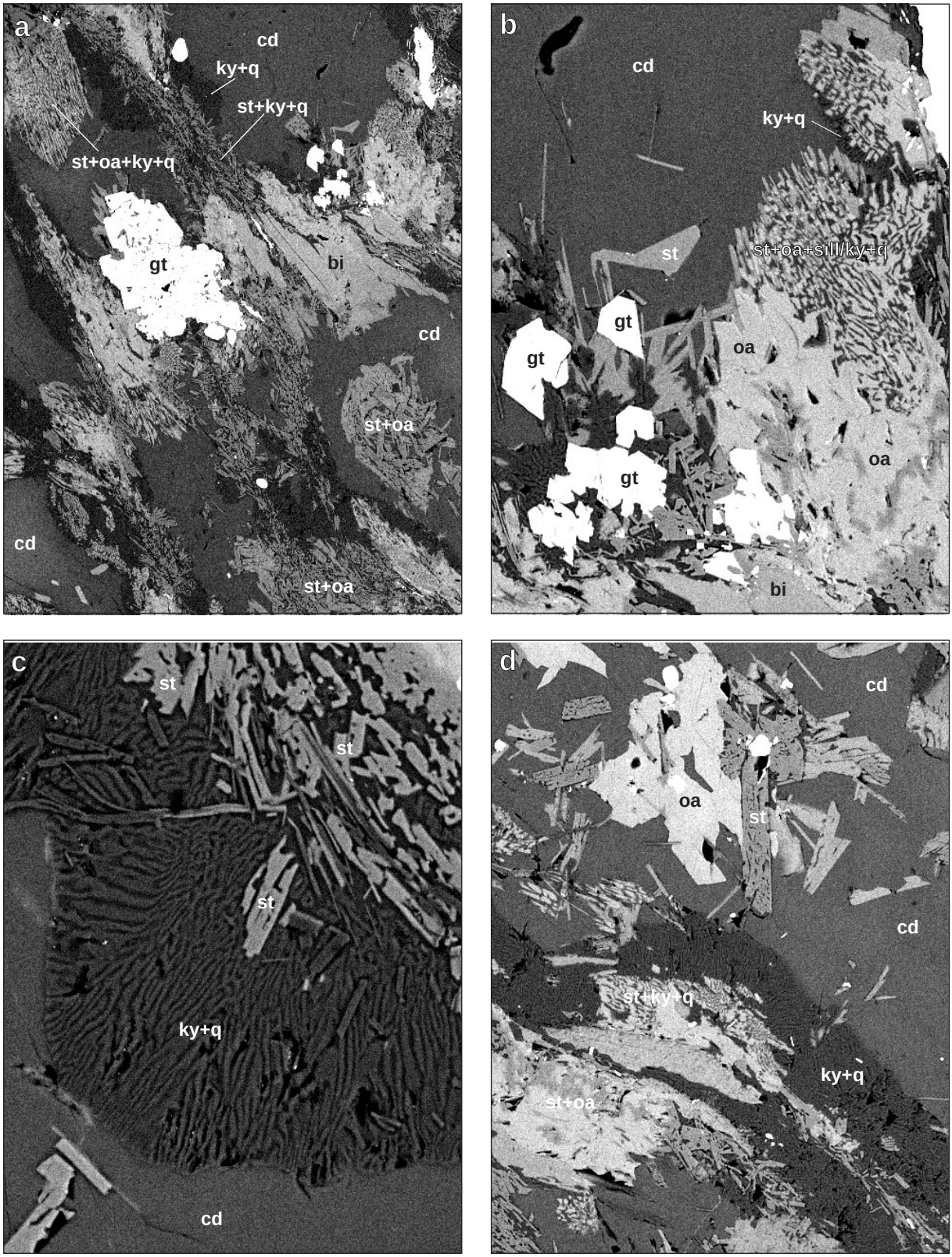

Figure 8.9 SEM images of the fine grained reaction textures in sample WGC101 - a partially reowrked pelitic granulite from the Tallacootra Shear Zone at Lake Ifould. (a) Overview of reaction textures, showing seqential development of (i) staurolite-quartz intergrowths, (ii) staurolite-orthoamphibole-quartz intergrowths, (iii) staurolite-orthoamphibole-sillimanite/kyanite-quartz intergrowths, and (iv) vermicular kyanite-quartz intergrowths, after early cordierite, garnet, K-feldspar, sillimanite and quartz. Note secondary, fine grained, subhedral garnet. (b) Detail of reaction textures, with fine, secondary garnet growth. (c) Detail of ultra-fine, kyanite-quartz intergrowths (presumed kyanite because of high optical relief and low birefringence). (d) Overview of sequential reaction textures, with intra-cordierite monazite and zircon nucleating coarser, subhedral, staurolite-orthoamphibole growth.

with quartz along plagioclase grain boundaries (see Figure 8.8).

- The breakdown of early, coarse grained garnet to fine grained secondary garnet, ilmenite and biotite. Secondary biotite is strongly zoned, and ranges from dark brown to colourless depending on Ti content.
- The breakdown of early, fine-medium grained, green spinel to complicated intergrowths of staurolite, gedrite, cordierite, kyanite and quartz. It is unclear whether the cordierite here is primary or secondary, or in fact if the spinel is breaking down at all. The staurolite-gedrite-kyanite reaction textures here may be derived from early cordierite which was intergrown with early spinel. Spinel is never in contact with quartz.
- The breakdown of early coarse biotite to very fine grained secondary biotite and ilmenite. The low Ti content in the secondary biotite is manifest in its pale colour and very weak pleochroism. This low-Ti biotite is often intergrown with the orthoamphibole-staurolite bearing reaction textures described above.
- The breakdown of early, coarse, prismatic sillimanite to fine grained sillimanite/fibrolite.
- The growth of secondary, fine grained, subhedral garnet which is often closely associated with the staurolite-orthoamphibole bearing reaction textures and the low-Ti secondary biotite.

Lake Ifould - pelitic schists

Several narrow (2-20cm) layers of schistose mylonites are interlayered with semipelitic schists and various orthoschists and mylonites. They are more deformed equivalents of the reworked granulites described above. They are fine grained, intensely foliated and lineated, strongly layered, and contain varying amounts of biotite, muscovite, garnet, staurolite, kyanite, sillimanite, plagioclase, K-feldspar and quartz, with accessory zircon, ilmenite and monazite (see Figures 8.8 & 8.9). The habit of the zircons is identical to those found in the nearby Christie Gneiss pelitic granulites (i.e. large, elliptical, brilliantly faceted, "soccerball" zircons). The pelitic schists are dominated by fine grained, foliation-defining biotite, muscovite, plagioclase, quartz, kyanite and/or staurolite, which wraps around syn-kinematic garnet porphyroblasts (with spectacular rotated, sigmoidal inclusion trails) and pre-kinematic quartz, biotite and feldspar porphyroclasts. In some samples, early, porphyroclastic garnet forms fine, inclusion-free euhedra which are often disrupted by antithetic microfaults.

8.3.2.2 Structural evolution

The structural evolution of the Tallacootra Shear Zone is characterised by high strain, ductile, TD_1 deformation about a steep TL_1 lineation and TS_1 foliation. Due to the sparse nature of outcrop in the Tallacootra Shear Zone, structural observations (especially kinematic information) must be treated cautiously when interpreting such shear zones, since it may not be representative of the entire shear zone (see §8.6).

Lake Tallacootra area

Outcrop in the Lake Tallacootra area is dominated by TD_1 mylonites which exhibit a pervasive, northeast-trending TS_1 foliation and intense, steeply plunging TL_1 stretching and mineral elongation lineation (see Figure 8.10a,b). Strain has been partitioned into the micaceous lithologies, which wrap around abundant pegmatite and mafic boudins that are generally strongly elongated parallel to the stretching lineation. TF_1 flow folding is commonly observed in boudin necks. More rigid felsic layers within the schistose mylonites are often tightly to isoclinally folded around the TL_1 stretching lineation (i.e. steep plunges). Narrow leucosomes often occur as rootless, isoclinal folds. A combination of kinematic indicators (shear bands defining composite SC fabrics, asymmetric porpyroclasts, fold vergence etc.) suggest east-block-up movement about the steep movement trajectory with a minor dextral, oblique strain component.

The intrusion of aplite dykes late during TD_1 fabric development provides a sound means for establishing the timing of TD_1 (see §8.5). These aplites exhibit a moderate-strong TL_1 stretching lineation and a weak TS_1 foliation, and totally crosscut all mylonitic lithologies (see Figure 8.4). They are unambiguously late syn-kinematic

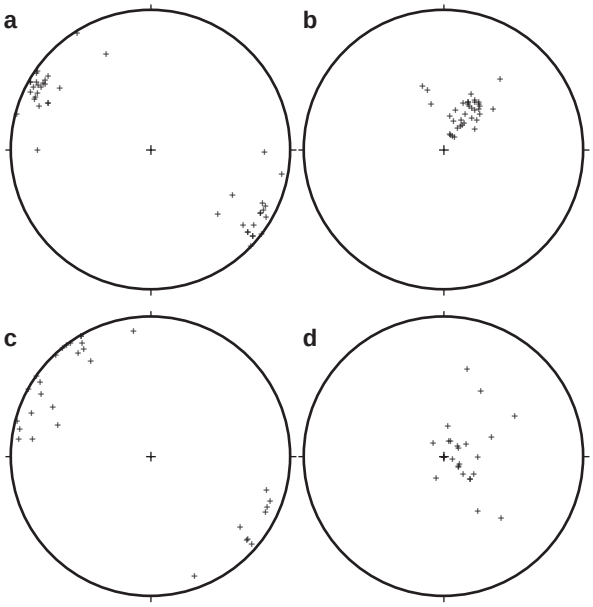

Figure 8.10 Stereoplots for structures in the Tallacootra Shear Zone. (a) Lake Tallacootra area, TS_1 foliation. (b) Lake Tallacootra area, TL_1 stretching lineation. (c) Lake Ifould area, TS_1 foliation. (d) Lake Ifould area, TL_1 stretching lineation.

intrusives, and are relatively abundant throughout the outcropping areas at Lake Tallacootra.

Lake Ifould area

In the Lake Ifould area, Mulgathing Complex granulites are variably overprinted by a northeast trending, TD_1 retrograde fabric associated with the Tallacootra Shear Zone. Effects range from very minor grain boundary recrystallisation and retrogression of granulite facies assemblages (see §5.2.1.2), through moderately reworked pelitic gneiss (in which the garnet is porphyroclastic and breaking down to TS_1 foliation-defining biotite, and other granulite phases are breaking down to muscovite-staurolite-kyanite assemblages - see §8.3.2.1), to high strain pelitic schists in TD_1 shear zones.

The Pidinga Complex intrusives have also been variably effected by the TD_1 fabric. Lithologies range from essentially undeformed intrusives (exhibiting well-defined, igneous contact relationships), through foliated gneiss (often augen gneiss), to intensely deformed mylonitic gneiss and schist in high strain zones. Abundant gneissic-protomylonitic Ifould Complex intrusives outcrop around the northern parts of Lake Ifould. They exhibit a pervasive TS_1 foliation (defined by biotite±hornblende alignment and gneissic layering), and TL_1 mineral and stretching lineation, both of which are steep to sub-vertical (see Figure 8.10b), and often contain small scale (1-20cm), rootless, isoclinally folded leucosomes. Igneous contacts have been transposed into the TS_1 foliation. Deformation was largely coaxial, since unambiguous kinematic indicators are rare, despite the propensity of such rocks (i.e. porphyroclastic augen gneiss and mylonite) to record kinematic information.

Ongoing, high strain deformation within TD_1 shear zones has resulted in the development of complex, ductile structures, especially in lower strain domains where pervasive, tight to isoclinal, TF_1 folds are preserved. The contrasting deformation styles within the Lake Ifould Shear Zone are testament to the marked rheological contrasts between lithologies. The high strain foliation wraps around lower strain domains (e.g. boudins), and often exhibits flow folding in their pressure shadows. Abundant very tight to isoclinal, TF_1 folds are evident in the mylonites; their fold axes parallel the stretching lineation. Ongoing ductile deformation has caused the hinges of these folds to be severely attenuated, and ultimately truncated by higher strain domains. West-up kinematic indicators are present, and have been observed in outcrop and thin section in porphyroclastic lithologies (asymmetric porphyroclasts, mica fish, composite SC fabrics). Tight TF_1 folds effect pre-kinematic, Pidinga Complex pegmatites. TF_1 fold axes parallel the TL_1 stretching lineation. Stereoplots of TS_1 and TL_1 are shown in Figure 8.10c-d.

8.3.2.3 Metamorphic evolution

Lake Tallacootra area

Mylonites at Lake Tallacootra contain several thermobarometrically useful lithologies, including a series of pelitic schists, intermediate garnet-biotite mylonites and mafic gneiss. Results of thermobarometry using a variety of techniques are detailed below:

Pelitic schists

Narrow pelitic layers in the Lake Tallacootra mylonites contain garnet-biotite-muscovite and kyanite-staurolite-biotite-muscovite assemblages which are generally too weathered to obtain precise, quantitative mineral analyses required for thermobarometry. However, petrogenetic grids and pseudosections by Xu et al. (1994, Figures 3(a) and 8(c)) indicate that the assemblage kyanite-staurolite-biotite (+muscovite, quartz and H_2O) is only stable in the pressure-temperature interval 5.5-8.6kb and 600-670°C. Poorly constrained Thermocalc (Powell & Holland, 1988, 1994) results for this assemblage suggest a preferred peak pressure-temperature range of 600-650°C and 6-9kb. The replacement of kyanite laths by fibrolite in some samples is consistent with ongoing fabric development at reduced pressures at temperatures in excess of ~600°C (constraints from Xu et al., 1994, Figure 8).

Intermediate mylonites

Fresh, garnet-biotite-plagioclase-quartz, intermediate mylonites give well constrained peak pressure-temperature conditions of 601±45°C and 6.3±1.4kb using the average pressure-temperature approach of Powell & Holland (1988, 1994).

Syn-kinematic aplites

The syn-kinematic aplites which have been dated to constrain the timing of movement along the Tallacootra Shear Zone give poorly constrained but consistent pressure-temperature estimates of ~5-7kb at ~600°C using a variety of garnet-muscovite-plagioclase-quartz thermometers as implemented by Kohn & Spear (1994). Since plagioclase has recrystallised in the high strain fabric, temperatures are constrained to be above ~550°C (M. Hand pers. omm., 1997).

Mafics

Boudins of layered mafic gneiss have been extensively reworked in the Tallacootra Shear Zone. Complex reaction textures involving the breakdown of early, presumed igneous pyroxenes to amphiboles and garnet occur in the retrograde fabric at the

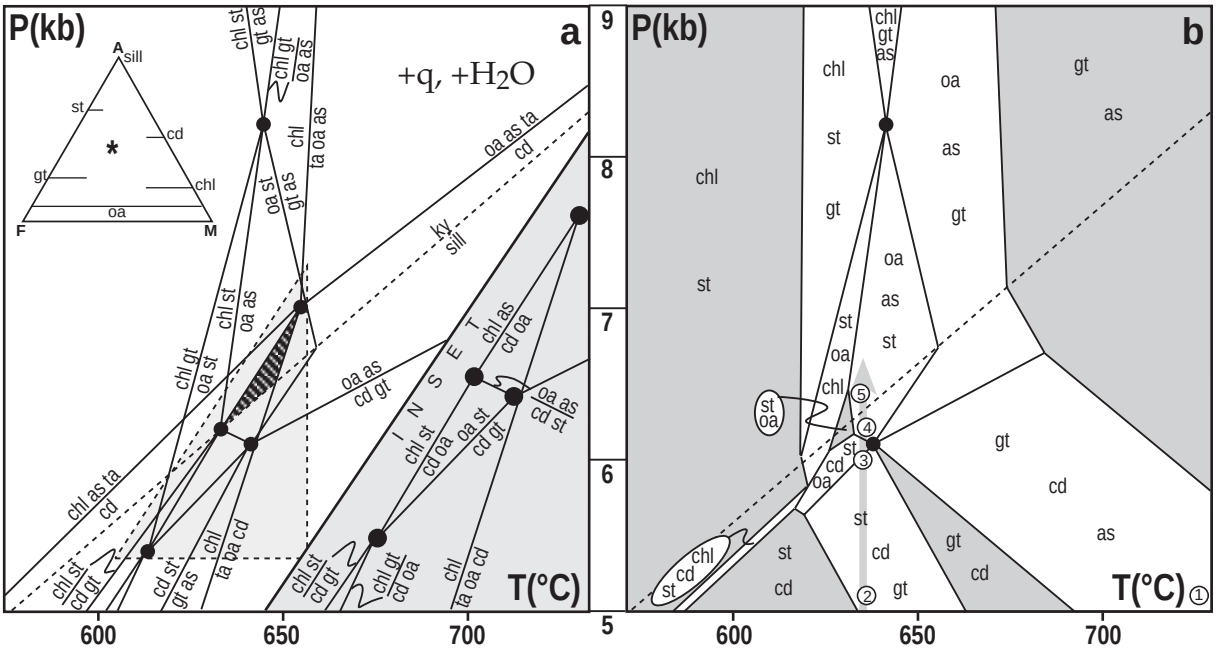

Figure 8.11 (a) Calculated FMASH univariant grid after Xu et. al (1994), with quartz and water in excess. Detail is shown in the triangular inset. The striped triangular area represents the peak FMASH mineral assemblage (orthoamphibole-kyanite-staurolite-quartz) found in the pelitic schists in the Tallacootra Shear Zone at Lake Ifould (6.1-6.7kb, 630-655°C). (b) Semi-quantitative pseudosection drawn for a bulk composition appropriate to the Lake Ifould reworked pelitic granulites (* on AFM compatibility diagram above). Critical mineral parageneses are numbered: 1 = early, peak, granulite-facies assemblage in the Christie Gneiss, 2 = onset of staurolite growth, 3 = onset of orthoamphibole growth, 4 = onset of sillimanite growth, 5 = onset of kyanite growth. Mineral reactions combine to define a PT path involving isothermal compression.

boudin margins. The early, anhydrous, ?igneous mineral assemblage is inferred to be twinned clinopyroxene, orthopyroxene, zoned plagioclase and quartz. The retrograde overprint is characterised by complex intergrowths of hornblende, cummingtonite (after orthopyroxene), garnet, secondary plagioclase and quartz. Complex and marked zoning patterns in the retrograde hornblende and garnet must be treated cautiously, and as a result, only rim compositions were used in thermobarometric calculations. Conventional thermobarometry for the assemblage garnet-hornblende-plagioclase-quartz yielded fairly consistent results of 600-650°C and 6.2-7.2kb, which are consistent with Thermocalc results for low water activity (aH_2O=0.1-0.3).

Lake Ifould area

Variably deformed metapelitic rocks in the Lake Ifould area record a range of metamorphic conditions reflecting the ongoing evolution of the Tallacootra Shear Zone. A continuum of progressively reworked metapelitic rocks indicates that they are all derived from the Christie Gneiss, which underwent granulite facies metamorphism (~750-800°C, 4.5-5.5kb) at ~2420Ma (see Chapter 5).

Spectacular, fine grained, orthoamphibole-staurolite bearing reaction textures overprint coarse grained, granulite facies assemblages in a series of moderately reworked pelitic granulites which outcrop at the southern end of Lake Ifould (see §8.3.3.1 and Figures 8.8 & 8.9 for detailed petrography). Orthoamphibole-bearing, pelitic mineral assemblages are known for their unusual bulk composition (e.g. Chinner & Fox, 1974), their complex reaction textures (e.g. Sharma and Macrae, 1981; Baker et al., 1987) and their sensitivity to changes in pressure and temperature (e.g. Harley, 1985). Critical mineral assemblages in the moderately reworked pelitic granulites at Lake Ifould can be described using the system FeO-MgO-Al_2O_3-SiO_2-H_2O (FMASH) for the phases cordierite, garnet, sillimanite, kyanite, staurolite, orthoamphibole (gedrite), quartz and hydrous fluid. The KFMASH phase diagram calculated by Xu et al. (1994) contains FMASH subsystem phase equilibria for the phases listed above. This phase diagram constrains the orthoamphibole-staurolite-sillimanite-quartz bearing reaction textures in the moderately reworked granulites to pressure-temperature conditions of 6.1-6.7kb at 630-655°C (see Figure 8.11a). In order to constrain the pressure-temperature path experienced by these rocks, a qualitative pseudosection based on the phase diagrams of Xu et al. (1996), incorporating some elements of the grids of Hudson and Harte (1985) and Arnold (1994) has been constructed (see Figure 8.11b). This pseudosection is relevant to bulk compositions with X_{Mg}~0.45-0.50 and X_{Al} above the garnet-cordierite tie-line (but below the staurolite-cordierite tie line) in the AFM compatibility diagram shown in Figure 8.12 (projected from quartz and water). The orientation and thickness of the divariant fields was evaluated

qualitatively using the above-mentioned compatibility diagram, the pseudosections of Xu (1993) and the subsystem (FASH and MASH) univariant equilibria of Hudson and Harte (1985). The complex mineral parageneses described above (§8.3.3.1) relate well to the pseudosection shown in Figure 8.11. The early, peak, granulite facies assemblage (garnet-cordierite-sillimanite-quartz-Kfeldspar±biotite, which equilibrated at ~4.5-5.5kb, 750-800°C), was partially overprinted by (i) fine grained staurolite, (ii) staurolite-orthoamphibole intergrowths, (iii) very fine, symplectic intergrowths of gedrite-staurolite-sillimanite-quartz, and (iv) extremely fine grained, symplectic, kyanite-quartz intergrowths. The mineral reactions inferred from these reaction textures combine to define a pressure-temperature path involving near-isothermal compression from ~4.5-5.5kb to >6.1kb at temperatures of 630-640°C, in good agreement with the peak thermobarometric calculations for the pelitic schists (see below).

The abundance of muscovite and biotite in the highly strained pelitic schists indicates that they are considerably more potassic than many of the granulite precursors. Although this may well be due to a differences in initial bulk composition (some of the pelitic granulites are quite potassic), it is clear that potassium metasomatism has effected many of the hornblende-bearing rocks in the Tallacootra Shear Zone, since hornblende and pyroxene is largely replaced by biotite in mafic-intermediate intrusive rocks. Potassium metasomatism has significant implications for the stability of orthoamphibole-bearing assemblages (e.g. Arnold & Sandiford, 1990; Xu, 1993). Although the orthoamphibole-bearing assemblages described here contain appreciable biotite (and hence some K_2O), it is impossible to grow orthoamphibole-bearing assemblages in potassic systems with $\blacksquare K_2O > -930$ at temperatures of 600-650°C (Figure 4.6 in Xu, 1993). This fact can be schematically represented on an A-K-FM mineral composition diagram (Arnold & Sandiford, 1990), which shows that only rocks with bulk compositions on the K_2O-poor side of the biotite-aluminosilicate tie line will "see" orthoamphibole-bearing assemblages. Orthoamphibole is absent in the high-$\blacksquare K_2O$ pelitic schists at Lake Ifould.

Highly strained, pelitic schists and mylonites at Lake Ifould are interpreted as more deformed equivalents of the moderately reworked metapelites described above. They contain a peak assemblage of garnet-staurolite-muscovite-biotite-kyanite-plagioclase-quartz which is particularly suited to thermobarometry using both conventional thermobarometers and Thermocalc (Powell & Holland, 1988, 1994). Average pressure-temperature calculations using Thermocalc yield results of 630±20°C at 6.9±0.8kb ($aH_2O=1.0$); in good agreement with the spread of data obtained using conventional thermobarometers. Lower than unit water activities (i.e. $aH_2O<1.0$) give rise to spurious results.

In summary, the pressure-temperature path implied by the moderately reworked granulites, combined with the peak conditions calculated for the highly strained pelitic schists indicate that ongoing strain in the Tallacootra Shear Zone at Lake Ifould was accompanied by a significant pressure increase from ~5kb to ~7kb at temperatures of 620-630°C. The "starting pressure" for this pressure-temperature path is the roughly same as that experienced during early Palaeoproterozoic, granulite facies metamorphism in the Christie Gneiss.

8.3.3 Coorabie Shear Zone

The Coorabie Shear Zone forms the easternmost system of SZ_2 shear zones in the western Gawler Craton, and defines the boundary between the Fowler/Christie Subdomains and the Wilgena/Nuyts Subdomains (see Figure 8.1). The Colona Fault (as defined by Drexel et al., 1993) forms the westernmost boundary of the Coorabie Shear Zone system. Outcrop and drillcore in the Coorabie Shear Zone is very sparse, probably because mylonites and schists are highly susceptible to weathering and erosion. The information presented here is derived from outcrop-subcrop in the Mount Christie/Mulgathing area, beach boulders at Cape Adieu, and isolated outcrops south of Barton Siding in the Great Victoria Desert.

8.3.3.1 Lithologies

Mulgathing area

Outcrop in the Coorabie Shear Zone in the Mulgathing area is dominated by felsic lithologies ranging from protomylonitic granite gneiss through to slaty ultramylonite (see Figure 8.12d). Ductile deformation is heterogeneous in the observed outcrops. Boudins of weakly foliated leucogranite are commonly observed. A few highly weathered mylonitic mafics occur. Many outcrops are weathered (saprolitic), although structural measurements are still possible. Mylonitic lithologies are often overprinted by low grade, brittle-cataclastic deformation which is associated with extensive hematite-chlorite-epidote alteration and quartz veining (with associated silicification).

In thin section the mylonites exhibit a fine to very fine grained, intensely recrystallised, quartzofeldspathic groundmass (containing variable amounts of mica and abundant quartz ribbons), which contains variable amounts of relict porphyroclastic material (see Figures 8.13 & 8.14).

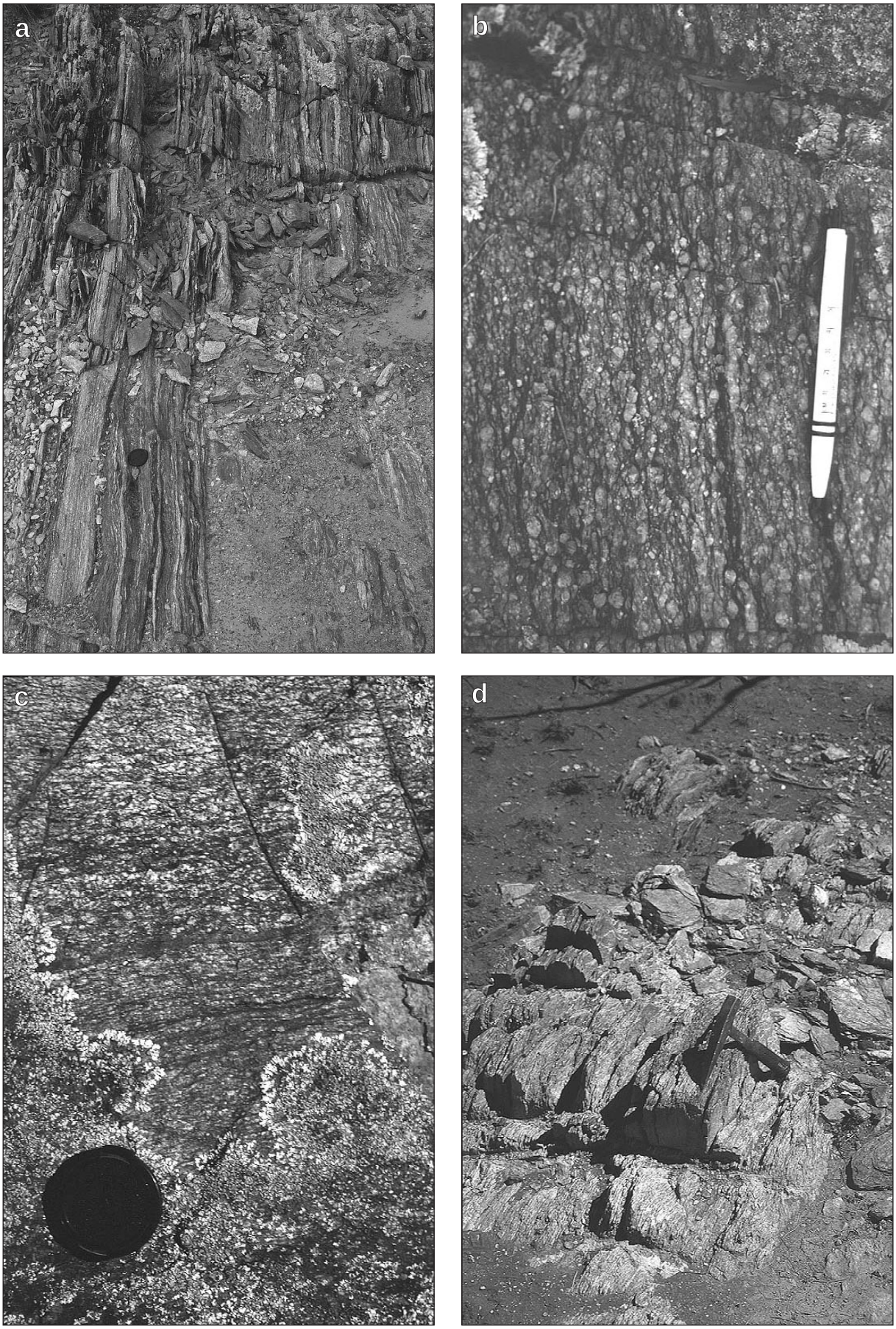

Figure 8.12 Photographs of outcrop in the Coorabie Shear Zone. (a) Mylonites on palaeohigh in the Colona Fault, south of Barton Siding. (b) Detail of outcrop shown in (a) - porphyroclastic mylonite. (c) narrow mylonite zones crosscutting a granite south of Barton Siding (geochronology site). (d) Ultramylonites in the Mt Christie area (hammer handle parallels lineation).

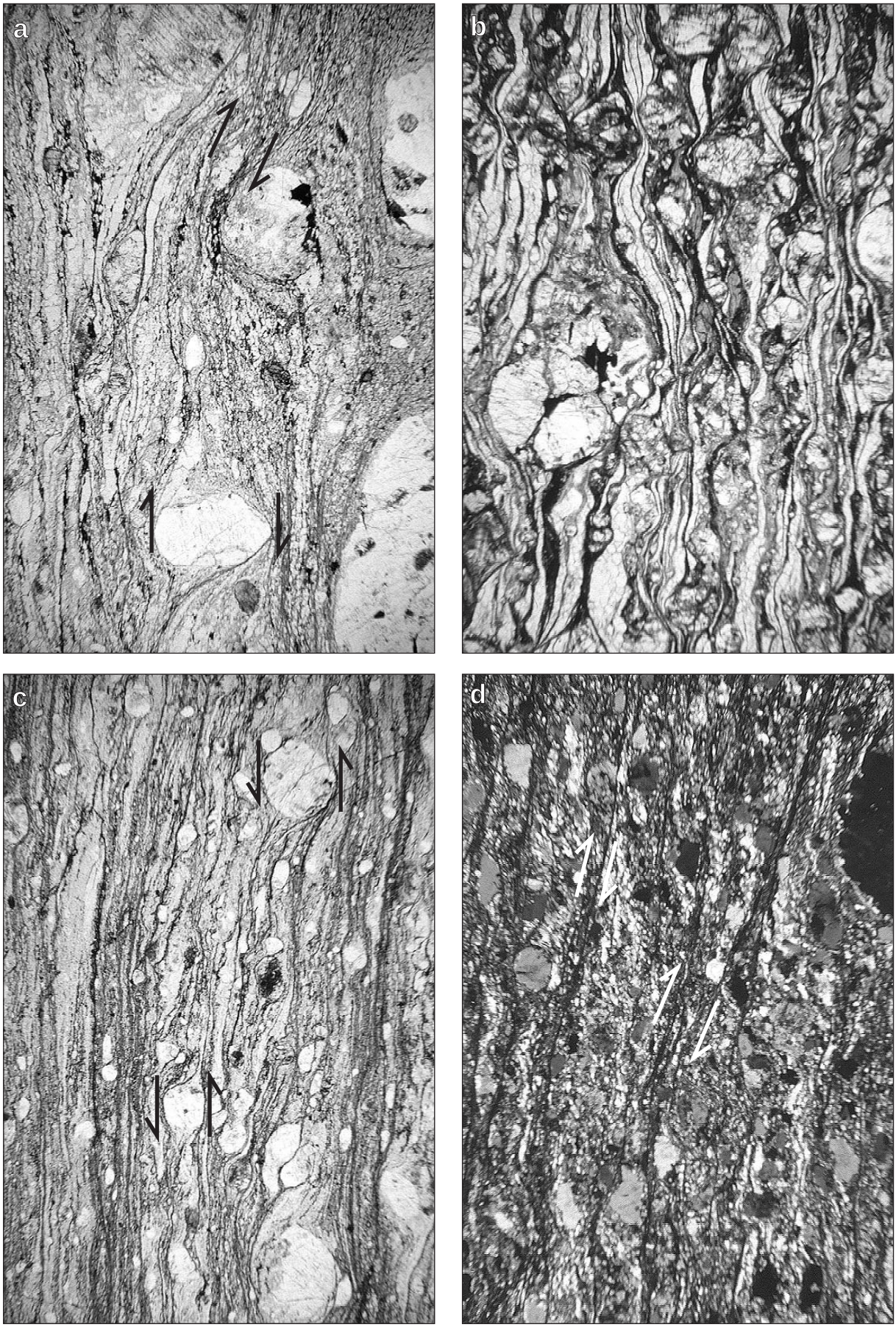

Figure 8.13 Photomicrographs of mylonites from the Coorabie Shear Zone, all of which exhibit west-up, dextral shear sense about an oblique movement direction. (a) WGC164 - mylonite from outcrop shown in Figure 8.13(c). (b) WGC163 - mylonite from outcrop shown in Figure 8.13(a). (c) WGC152 - mylonite from the Mt Christie area. (d) WGC205 (XPL) - Mylonite from outcrop showin in Figure 8.13(a). Note well-defined shear bands

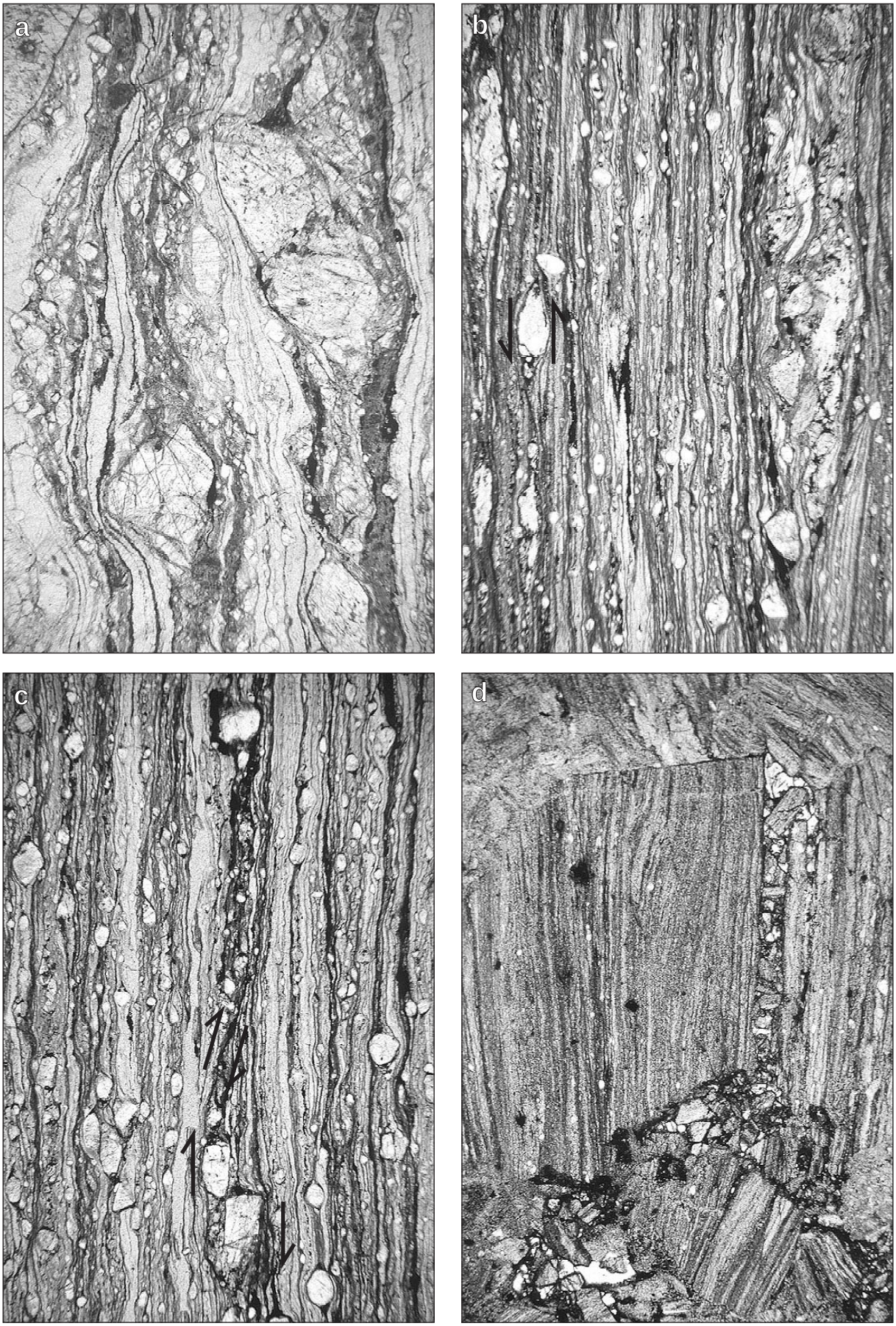

Figure 8.14 Photomicrographs of quartzofeldspathic mylonites from the Coorabie Shear Zone in the Mt Christie area, all of which indicate dextral, west-up shear sense about an oblique movement direction. (a) WGC122 - porphyroclastic mylonite. (b) WGC125 - ultramylonite. (c) WGC124 - mylonite. (d) WGC74 - brecciated and altered ultramylonite.

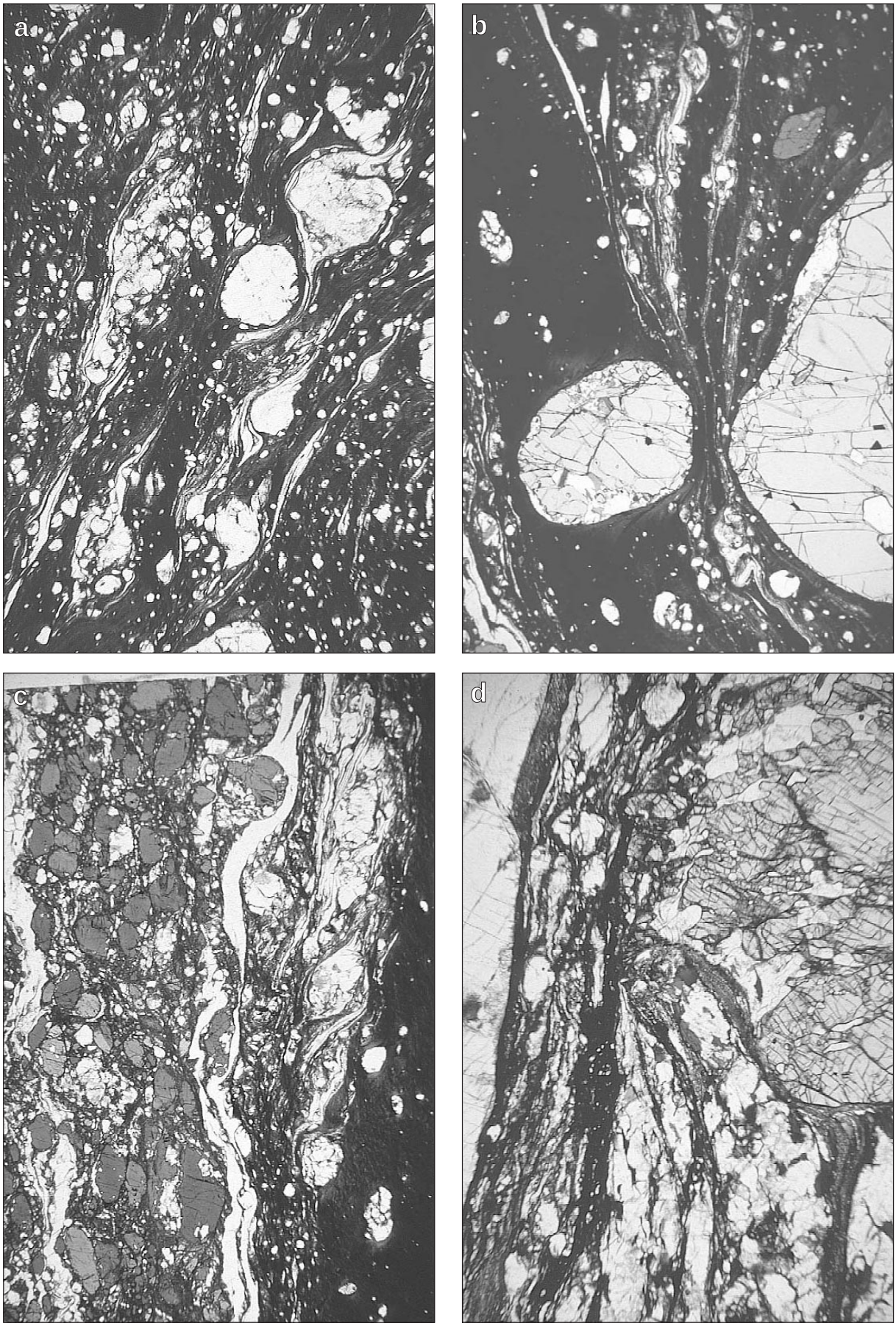

Figure 8.15 Photomicrographs of mylonites from the outcrop at Cape Adieu. Shear sense is unknown since beach boulders are not in place. (a), (b) & (c) WGC23 & WGC22 - Intensely mylonitised mafic gneiss (with garnet, hornblende, plagioclase and quartz porphyroclasts in a very fine grained, biotite-quartz-plagioclase matrix). (d) WGC24 - mylonitised pelitic gneiss (early garnet-sillimanite-biotite-K-feldspar-plagioclase-quartz assemblage is overprinted by a very fine grained, biotite-muscovite-plagioclase-K-feldspar-quartz mylonitic assemblage).

Porphyroclastic samples often exhibit well-defined micro-scale shear bands, and asymmetric porphyroclasts (see §8.3.4.2 below). Rocks are often heterogeneously deformed, with hematite-epidote-chlorite alteration localised in the high strain domains. Some samples show that static recrystallisation and annealment of the high strain fabric has occurred.

Barton South area

Several "new" outcrops in the Colona Fault (interpreted to be part of the Coorabie Shear Zone) were discovered during this project (see Figure 8.12). They consist of layered mylonite-ultramylonite, ranging in composition from felsic to relatively micaceous. In lower strain domains, it is clear that many of the mylonites are derived from granitoids. Although these mylonites exhibit an intense foliation, the stretching lineation is generally weak to invisible suggesting near-coaxial deformation. In thin section, samples are similar to mylonites from the Mulgathing area (see Figure 8.13).

Cape Adieu area

Mafic mylonites

Extremely fine grained, 0.1-5m wide mylonite-ultramylonite zones crosscut the high grade gneisses in the Nundroo Block of the Fowler Subdomain at the margins of the Coorabie Shear Zone at Cape Adieu. Medium-coarse grained, highly fractured garnet, hornblende and plagioclase porphyroclasts are enclosed by a very fine grained, high strain, biotite-quartz matrix (see Figure 8.15). These mylonites are obviously derived from the high pressure amphibolites documented in Chapter 7. Hornblende and garnet are partially replaced by very fine grained biotite in the high strain fabric. Spectacular "flow" folds occur in the porphyroclast pressure shadows.

Pelitic mylonites

Early, medium grained garnet-perthite-sillimanite-biotite-quartz assemblages are overprinted by a mylonitic fabric which has caused extensive recrystallisation and retrogression. Early sillimanite is retrogressed to muscovite, perthite to K-feldspar and plagioclase, and early garnet to biotite and/or chlorite in the high strain fabric. Early perthite exhibits coarse perthitic twinning which is indicative of very high temperature metamorphism. These pelitic units have clearly localised strain since they are often surrounded by unretrogressed, layered mafic gneiss (which has clearly escaped this lower grade reworking). The early, high grade assemblage is correlated with the high grade pelitic gneiss in Nundroo DDH2 (see Chapter 6), and the later, lower grade, mylonitic overprinting is correlated with the ultramylonites described above.

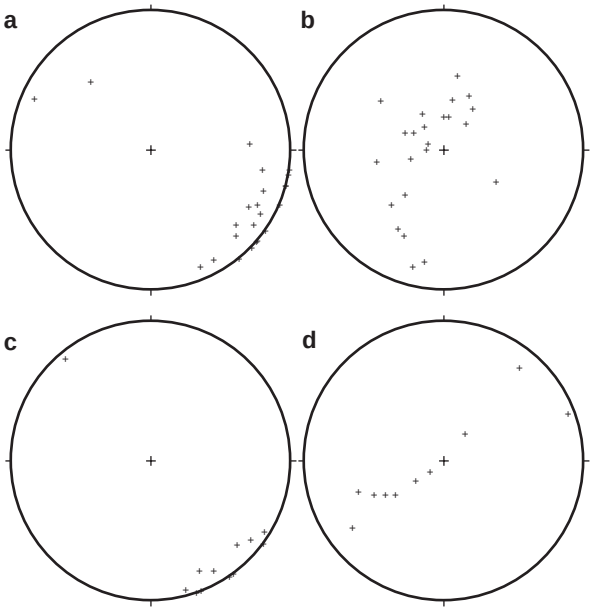

Figure 8.16 Equal area stereoplots for structures in the Coorabie Shear Zone. (a) poles to the CS_1 foliation in teh Mulgathing area. (b) CL_1 stretching lineations in the Mulgathing area (showing a broad spread of dip-slip to stike-slip orientations). (c) poles to the CS_1 foliation in the Barton South area. (d) CL_1 stretching lineation in the Barton South area.

8.3.3.2 Structural evolution

Available structural data in very poorly outcropping shear zones must be treated cautiously, since it may not be representative of the structural evolution of the entire shear zone (see §8.6). In the Mulgathing area, measured mylonitic foliations are generally steep, and stretching lineations are loosely grouped into two clusters; a steep, dip-slip set and a relatively shallow set (see Figure 8.16). Kinematic indicators (including shear bands, asymmetric porphyroclasts and antithetic microfaults in porphyroclasts) unambiguously suggest west-up/dextral vergence about a pervasive stretching lineation. In the Barton South area, mylonites in the Colona Fault exhibit variably plunging stretching lineations about a sub-vertical foliation. Kinematic indicators (shear bands and asymmetric porphyroclasts) imply west up/dextral vergence about the stretching lineation. Unfortunately the Cape Adieu mylonites are not in situ therefore it is impossible to quantify their structural evolution.

The Coorabie Shear Zone is interpreted to have undergone at least ~20-30km of west-over-east vertical displacement, as evidenced by the contrasting metamorphic grades between the Fowler and Nuyts, and the Christie and Wilgena Subdomains.

8.3.3.3 Metamorphic evolution

Metamorphic information in the Coorabie Shear Zone is very limited due to the lack of outcrop and metamorphically sensitive rocks. In the Mulgathing area, a few mafic mylonites are dominated by biotite

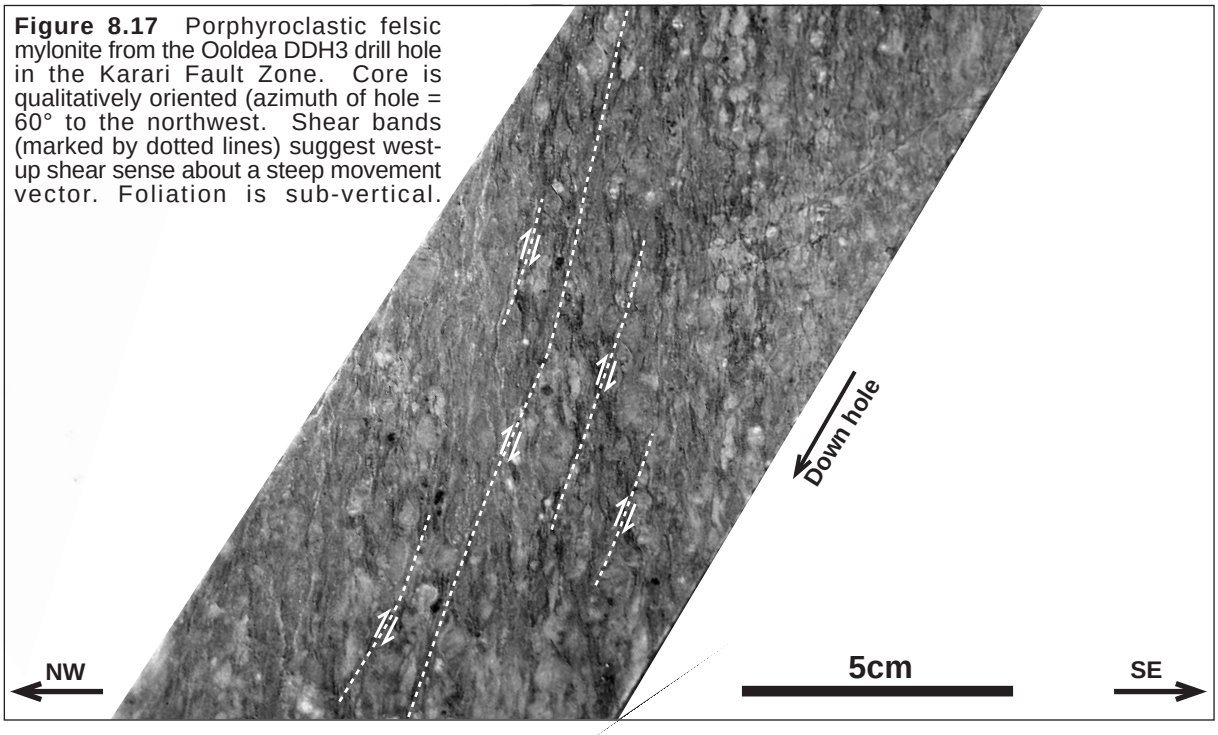

Figure 8.17 Porphyroclastic felsic mylonite from the Ooldea DDH3 drill hole in the Karari Fault Zone. Core is qualitatively oriented (azimuth of hole = 60° to the northwest. Shear bands (marked by dotted lines) suggest west-up shear sense about a steep movement vector. Foliation is sub-vertical.

which has grown at the expense of hornblende. At Cape Adieu, mafic mylonites also exhibit the breakdown of hornblende and garnet to biotite. Such metamorphism is characteristic of upper greenschist to lower amphibolite facies conditions at temperatures in excess of 500°C at relatively low pressures (<4kb). Clearly further work is required to quantify the thermobarometric evolution of the Coorabie Shear Zone (especially fluid inclusion studies)

8.4 SZ_3 - the Karari Fault Zone

The Karari Fault Zone forms a significant, northeast-trending, linear magnetic high which juxtaposes the Christie and Nawa Subdomains, (Rankin et al., 1989). It bifurcates around the Coober Pedy Ridge in the northeast where it anastomoses with the Tallacootra Shear Zone. The Karari Fault Zone does not outcrop, and only two drill holes (Ooldea DDH 3 and Watson Siding 1A) intersected it. Information about the composition, structural evolution and metamorphic grade of lithologies in the Karari Fault Zone are largely derived from the Ooldea DDH3 drill core combined with geophysical data. Rankin et al. (1989) provide a detailed description of Ooldea DDH3, although their kinematic interpretations are at odds with those presented here.

Ooldea DDH3 intersected ~280m of heterogeneous, intensely foliated mylonites. The dominant lithology is a fine grained, finely layered, dark grey, quartz -magnetite ±feldspar ±garnet ±sillimanite ±chlorite ±biotite mylonite, which is interlayered with medium grained, orange, felsic mylonite, fine grained amphibolite, and fine-medium grained, semipelitic, quartz-Kfeldspar-biotite±garnet mylonite. The mylonitic fabric is defined by the intense high strain layering, mineral elongation/alignment (which also defines a moderate stretching lineation) and quartz ribbons. In lower strain domains, the magnetite-rich gneiss strongly resembles those intersected by Ooldea DDH2 (see Chapter 2). In the very highest strain domains, the mylonites are dominated by chlorite, sericite and biotite which defines a distinctly lower grade assemblage than the less-deformed garnet-sillimanite mylonites. Early, foliation-defining prismatic sillimanite has been boudinaged within the later chlorite-biotite fabric. These observations suggest that the mylonites have experienced a complex structural evolution at progressively lower metamorphic grades.

Geophysical modelling of the southern part of the high magnetic intensity Karari Fault Zone indicates that the drilled anomaly is caused by a subvertical, northeast-trending, strongly magnetised body (Rankin et al., 1989). Ooldea DDH3 was drilled at an angle of 60° to the WNW. This data enables the qualitative orientation of the drill core (see Figure 8.17). Stretching/elongation lineations are mainly down-dip (i.e. sub-vertical), although in late, chloritic mylonites oblique lineations were observed (mainly with a moderate NNE plunge). Shear bands and asymmetric porphyroclasts unambiguously indicate NW-up/sinistral movement about the stretching lineation (see Figure 8.17). Over 30 consistent kinematic observations were made, mainly in the higher grade mylonites.

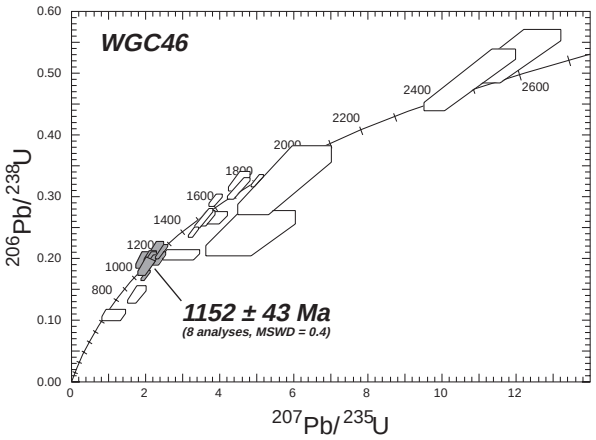

Figure 8.18 U-Pb concordia diagram showing SHRIMP zircon analyses for sample WGC46 - a syn-kinematic aplite from the Tallacootra Shear Zone at Lake Tallacootra, plotted as 1▪ error polygons. Analyses used to calculate the weighted mean $^{207}Pb/^{206}Pb$ age are shaded.

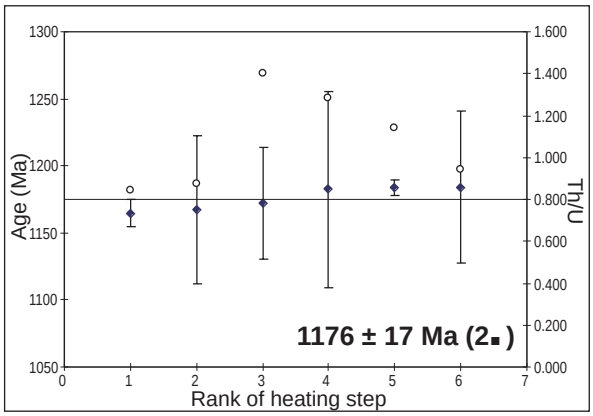

Figure 8.19 Pb/Pb zircon evaporation results for the youngest zircon population in sample WGC46 - a syn-kinematic aplite from the Tallacootra Shear Zone at Lake Tallacootra. Solid diamonds = $^{207}Pb/^{206}Pb$ age (with 1▪ error bars), open circles = model initial Th/U ratio.

This interpretation contrasts with that of Rankin et al. (1989), and the consistency and pervasiveness of clear kinematic indicators throughout the Ooldea 3 drill core renders their interpretation questionable.

The lithological, metamorphic and structural complexity of the Ooldea 3 mylonites indicates a prolonged high strain history at progressively lower metamorphic grades. Structural analysis suggests a major component of northwest-block-up movement about a steep stretching lineation. Clearly it is presumptuous to interpret the evolution of the entire Karari Fault Zone based on these observations alone. Regional scale aeromagnetic interpretation suggests that the Karari Fault Zone obaly underwent significant sinistral strike slip movement, and that the high-magnetic intensity Moondrah Gneiss may once have been contiguous with the high magnetic intensity Coober Pedy Ridge (see Chapter 3). The southern parts of the Karari Fault Zone are interpreted to have undergone west-over-east, vertical displacement of at least 18-22km (and possibly up to 35km); consistent with the contrasting metamorphic grades between the southern Nawa and Christie Subdomains.

8.5 Geochronology of shear zones in the western Gawler Craton

Due to the lack of outcrop of shear zones in the western Gawler Craton, it is difficult to find samples likely to yield meaningful absolute deformation ages via U-Pb and Pb-Pb zircon dating. The use of other techniques (e.g. K-Ar dating of micas, Sm-Nd isochron dating of mineral separates) has not been attempted during this project and clearly future work must focus on such techniques. One sample from the Lake Tallacootra Shear Zone (a demonstrably syn-kinematic aplite) has been dated via Kober and SHRIMP zircon analysis (see below). Relative timing constraints for the shear zones can be obtained from crosscutting relationships observed in the interpretive geological map and outlined in Section 8.1.

A series of late-kinematic aplites from Lake Tallacootra contain very minor amounts of zircon which have been analysed via both the Kober zircon evaporation technique and the SHRIMP. The zircon

Shear Zone	Scale	Age	Strike-slip shear sense	Dip-slip shear sense	Metamorphic grade
Yerda Shear Zone (SZ_1)	~300kmx2-20km system	~1580-1427Ma	sinistral	negligible	low grade, ductile
Coorabie Shear Zone (SZ_2)	>800kmx~50km anastomosing system	~1100-1200Ma?	dextral	west-up (up to 30km)	greenschist facies (gt, sill unstable, bi, mus stable)
Tallacootra Shear Zone (SZ_2)	>800kmx50km anastomosing system	~1150-1200Ma	dextral	east up (up to 15km)	amphibolite facies (~600-650°C, 6-8kb)
Karari Fault Zone (SZ_3)	>800kmx1-5km curvilinear	<1175Ma	?sinistral	west-up (up to 20km?)	variable (greenschist to amphibolite facies)

Table 8.1 Summary of the main characteristics of the key “framework” shear zones in the western Gawler Craton.

population is dominated by small (~0.1mm), subhedral, simple, unstructured zircons which yield a Kober Pb-Pb age of 1175±17 Ma (see Figure 8.19) and a concordant SHRIMP U-Pb age of ~1180 Ma (see Figure 8.18). Larger, older zircons and zircon fragments give ages of ~1550-1600 Ma, ~1810 Ma, ~2100 Ma and ~2440 Ma which are interpreted to be inherited components. The composition of the aplites is typically S-type (since they are dominated by K-feldspar, garnet and muscovite) and such rocks usually contain significant amounts of inherited zircon derived from a presumably metasedimentary precursor. The inherited ages a representative of nearby metasediments in the Fowler and Christie Subdomains (see Chapters 5 and 6). Both the zircons and garnets in the Lake Tallacootra Aplite exhibit variably pitted/frosted surfaces which are tentatively attributed to corrosion caused by late- to post-kinematic, presumably alkaline fluids in the rock. The possibility that such surface features are due to mechanical abrasion in a sedimentary environment are discounted since the corrosion must have occurred after the rock crystallised (hence after the high strain deformation - see Figure 8.3).

This interpretation implies that a significant part of the high strain deformation in the Tallacootra Shear Zone occurred after ~1175 Ma at relatively high metamorphic grades (>550°C, >5kb).

8.6 Discussion

Shear zones played a fundamental role in the Mesoproterozoic tectonic evolution of the Gawler Craton and no doubt hold the key to understanding the differential exhumation, juxtaposition and amalgamation of the contrasting subdomains discussed in the preceding chapters. The western Gawler Craton is dominated by at least three generations of major shear zones (SZ_{1-3}), reflecting a protracted history of transpressional deformation during the Mesoproterozoic. Their main features are summarised in Table 8.1.

SZ_2 shear zones are generally steeply dipping, and anastomose at scales of 20-100km. Since outcrop in the shear zones is very limited, it is unreasonable to assume that the observed movement directions are likely reflect the overall evolution of the shear zones. A common observation in high grade transpressional shear zones is that deformation is partitioned into broad dip-slip and narrow strike-slip domains (e.g. Jones & Tanner, 1995; Kirkwood, 1995). The anastomosing, imbricate surface expression of SZ_2 shear zones in the western Gawler Craton signifies that they probably evolved during a predominantly strike-slip deformation regime, since their asymmetric, anastomosing pattern is analogous to a cross-sections through a dip-slip duplex (Woodcock & Fischer, 1986). However, the abundance of steep observed lineations in shear zones in the western Gawler Craton signifies a significant component of near-vertical, ductile, dip-slip deformation occurred. The dip-slip deformation is demonstrably kinematically consistent with the differential exhumation implied by the regional metamorphic grade distribution (which provides an independent test of shear zone vergence). However, the scale of SZ_2 shear zones (up to 800km long) far exceeds the scale of differential exhumation (<25-30km), suggesting that dip-slip movement was minimal relative to strike-slip movement. As a result, SZ_2 shear zones in the western Gawler Craton are interpreted to be transpressional, and collectively form a large (>800km by 100-200km), dextral, transpressional mobile belt active at various stages during the Mesoproterozoic. This mobile belt was subsequently truncated to the west by the SZ_3 Karari Fault Zone.

Petrological comparisons between the country rocks and their sheared equivalents attests to large scale metasomatic activity in shear zones in the western Gawler Craton, principally involving aqueous fluids. Anhydrous country rocks have been extensively rehydrated in the shear zones, generally forming micaceous schists after early pyroxene and/or amphibole bearing assemblages. Mylonitic lithologies are commonly enriched in potassium, as evidenced by the abundant growth of biotite (and minor K-feldspar) after early, potassium-absent phases such as pyroxenes, amphiboles and plagioclase, indicating that significant potassium metasomatism accompanied rehydration and deformation. The anhydrous nature of most of the country rocks implies that the hydrating fluids must have originated from an external source. Shear zones have long been recognised as effective fluid conduits in the crust (e.g. Kerrich et al., 1984; Newton, 1989; Oliver, 1996), however the fluid source is often ambiguous, especially in the mid to lower crust. The most common source for mid-lower crustal fluids in evolving orogens where no magmatism is occurring is from underlying dehydrating rock masses, and the most plausible way of achieving this is to via tectonic underthrusting of hydrous material. The largest scale examples of this phenomenon are subduction zones, where a dewatering slab can cause rehydration of the overlying rocks.

The late "framework" shear zones have significantly reworked, juxtaposed and/or reactivated the subdomains in the western Gawler Craton, and appear to be unrelated to tectonothermal events recorded in the surrounding country rocks. The localisation of strain along shear zones in the western Gawler Craton during the

Mesoproterozoic indicates that by this time it had a rigidity in contrast with its prior evolution which involved widespread, relatively penetrative, ductile deformation during several major tectonothermal events in the Nawa, Christie and Fowler Subdomains. Shearing has not been accompanied by significant magmatism or penetrative metamorphism, however the up-pressure metamorphic evolution implied for the Tallacootra Shear Zone indicates that deformation was accompanied by significant crustal thickening (at least in the Christie Subdomain). Elsewhere, notably in the Fowler Subdomain, SZ_2 deformation involved down-pressure retrograde metamorphism most probably associated with exhumation. The close spatial association and geometric relationships between SZ_2 shear zones across the Christie and Fowler Subdomains indicates that they probably formed synchronously, and the contrasting baric evolution of SZ_2 shear zones may attest to an allochton/autochton relationship between the Fowler and Christie Subdomains. In this scenario, the Christie Subdomain may have underwent autochtonous burial at the same time that the Fowler Subdomain was being allochtonously exhumed. This notion is supported by the palaeopressure differences between the two subdomains.

Based on the above discussion, any explanatory model for the evolution of SZ_2 (and SZ_3?) shear zones in the western Gawler Craton must take into account the fact that: (i) shearing was largely transpressional with an overall dextral shear sense, (ii) presumably synchronous crustal thickening (i.e. burial) and exhumation occurred in different subdomains during deformation, and (iii) shearing was accompanied by significant movement of potassic, aqueous fluids. Such models are further discussed in the next chapter.

Chapter 9

DISCUSSION

9.1 The tectonothermal evolution of the western Gawler Craton

The observations and interpretations made during this study indicate that the western Gawler Craton underwent a complex and varied tectonothermal evolution spanning almost 2000 Ma from the late Archaean to the late Mesoproterozoic. The broad range of geology present in the five studied subdomains reflects a diversity of tectonothermal environments, the geodynamic significance of which has been discussed in the preceding chapters. The tectonothermal evolution of the western Gawler Craton is summarised in Table 9.1, which illustrates the heterogeneous history of crustal growth, metamorphism and deformation experienced by the studied subdomains. Five major cycles of tectonothermal development have been identified:

CYCLE 1: ~3000-2400 Ma - deposition of sediments and volcanics of the Mulgathing Complex during the late Archaean onto an as-yet undiscovered, presumed mid-Archaean basement (Daly et. al, in press), followed by complex deformation, metamorphism (up to granulite facies), high level felsic plutonism and minor mafic magmatism during the ~2500-2400 Ma Sleafordian Orogeny. Importantly, although the Mulgathing Complex is undoubtedly derived from Archaean protoliths, its main tectonic features are early Palaeoproterozoic in age. The Archaean components of the Mulgathing Complex differ considerably from the classic granite-greenstone architecture of many Archaean terranes, in particular that of the Yilgarn Craton in western Australia (e.g. Ayers et. al, 1985; Myers, 1993; Choukroune et. al, 1997).

CYCLE 2: ~1740-1655 Ma - periods of voluminous, I-type, mafic to felsic plutonism (e.g. the Ifould Complex) associated with heterogeneous compressional deformation, (ultra)high grade metamorphism (e.g. the Moondrah Gneiss) and minor sedimentation (e.g. the Tarcoola Formation). This cycle of tectonothermal activity is also manifested in the southeastern Gawler Craton via magmatism in the Cleve and Moonta Subdomains and tectonism during the Kimban Orogeny. Elsewhere in Australia this time period is largely marked by presumed intracratonic tectonic processes involving extensional rifting, sedimentation and associated magmatism, followed by compressional deformation (Myers et. al, 1996), particularly in the Mount Isa and Broken Hill Blocks. This intracratonic tectonism contrasts with the largely compressional tectonic regimes of the Gawler Craton, which show active plate margin characteristics, including voluminous, mafic to intermediate calc-alkaline magmatism, high pressure metamorphism and extensive hydrous fluid flow.

CYCLE 3: ~1630-1560 Ma - voluminous, anorogenic felsic magmatism, including the St Peter Suite and the comagmatic Hiltaba Suite and Gawler Range Volcanics, interpreted by Stewart (1994, 1997) to have been caused by a mantle plume. Notably this magmatism only occurred southeast of the Coorabie Shear Zone, as well as the Mount Painter Inlier, the Olary Block and the Broken Hill Block (Flint, 1993). This voluminous magmatism is recorded on a global scale (most notably in the North American cratons), and is attributed to large-scale mantle upwelling, termed a mantle "superswell" (Hoffman, 1989). Such superswells are thought to be generated due to thermal instabilities in the lithosphere cuased by the thermal blanketing effects of large, stationary continental masses (Hoffman, 1989).

CYCLE 4: ~1540-1490 Ma - felsic plutonism, high grade metamorphism and heterogeneous compressional deformation, largely restricted to the Fowler Subdomain. These geological processes may have operated at an active plate margin. Notably, this cycle of tectonism coicides with the supposedly intracratonic Isan Orogeny in the Mount Isa Inlier (e.g. Connors & Page, 1995).

CYCLE 5: ~1200-1100 Ma - reworking and crustal thickening along craton-scale shear zones during a major transpressional orogeny (see below).

Of fundamental importance is the recognition that the five orogenic cycles outlined above are not "seen" by every subdomain, and this notion is illustrated by Table 9.1 which emphasises that each of the studied subdomains has undergone a significantly different tectonothermal evolution. Cycles 2, 4 and 5 were unrecognised prior to this study, and are a significant departure from previously published tectonic syntheses on the Gawler Craton (e.g. Fanning et. al, 1988; Drexel et. al, 1993; Daly et. al, 1997). They indicate that the western Gawler Craton underwent significant tectonism during the Mesoproterozoic, and that this activity was temporally and geologically distinct

from tectonism in the southeastern Gawler Craton. The apparent quiescence of tectonothermal activity between ~2400 Ma and ~1740 Ma in the western Gawler Craton contrasts with that of the southeastern Gawler Craton (and many other Australian Proterozoic terranes) which experienced extensive magmatism (e.g. the ~1.85 Ga Lincoln Complex) and tectonism (e.g. the Kimban Orogeny) during this time interval.

The present configuration of the collage of subdomains in the western Gawler Craton is interpreted to reflect significant juxtaposition, differential exhumation and amalgamation achieved during Cycle 5. Cycle 5 shear zones define a ~50-100km wide, >700km long, northeast-trending mobile belt, the significance and nature of which is discussed in Chapter 8. The scale of Cycle 5 shear zones (>800km long - possibly up to many thousands of kilometres into Antarctica) indicates that the magnitude of differential strike-slip movement between the subdomains may have been considerable. As a result, any temporal and geological correlations between the studied subdomains must be treated very cautiously, and the palaeo-configurations of the subdomains are essentially unknown. However, the dextral transpressional vergence of Cycle 5 shear zones suggests that the Christie and Fowler Subdomains would have originally resided further to the southwest with respect to the relatively intact Wilgena and Nuyts Subdomains. The interpreted sinistral transpressional vergence of the Karari Fault Zone which operated late during Cycle 5 suggests that the Nawa Subdomain may have originally resided northeast of the Christie, Fowler, Wilgena and Nuyts Subdomains. The observed metamorphic field gradients in the western Gawler Craton show a markedly heterogeneous distribution of metamorphic grade with respect to space and time, which can largely be attributed to differential exhumation by various generations of Cycle 5 shear zones. In the western Gawler Craton, these structures clearly postdate, and bear no relevance to the processes that lead to burial and high grade metamorphism in the studied subdomains; a common observation in many high grade terranes (e.g. Clarke, 1995a).

The Gawler Craton has previously been defined as "that region of crystalline basement that has not been substantially deformed or remobilised, except by minor epeirogenic movements, since about 1450 Ma" (Parker, 1993a), and its northwestern boundary was drawn to define the approximate extent of near-surface basement. The recognition that significant tectonism occurred during Cycle 5 which clearly postdates the ~1450 Ma "cratonisation" is of fundamental importance to the definition and recognition of the Gawler "Craton". In light of this

	Age (Ma)	Nawa Subdomain
CYCLE 1	~3500-3000?	
	~3000-2500?	Deposition of sediments?
	~2500-2400?	Low pressure, granulite facies metamorphism?
CYCLE 2	~2000?	
	~1740-1730	
	~1730-1700	
	~1690	Ultrahigh temperature, high pressure, granulite facies metamorphism (>950°C, >10kb) and late, high strain, compressional deformation
	~1680-1670	
	~1670-1655	
CYCLE 3	~1630-1610	
	~1590-1580	
	~1570-1540	
CYCLE 4	~1540-1530	
	~1530-1490	
	~1580-1420	
	~1425	
CYCLE 5	~1200-1150	Minor plutonism?
	~1150-1100?	Juxtaposition and exhumation of the Nawa and Christie Subdomains by the trans-pressional Karari Fault Zone.
	~800	Gairdner Dyke Swarm.

Table 9.1 Summary of the tectonothermal evolution of the western Gawler Craton, derived from the data presented in the preceding chapters (continued overleaf). The reader is encouraged to use the interpretive geological map (at rear of thesis) and various maps and geophysical images presented in Chapters 3 and 8 in conjunction with this table.

<table>
<tr><th>Christie Subdomain</th><th>Fowler Subdomain</th><th>Wilgena Subdomain</th><th>Nuyts Subdomain</th></tr>
<tr><td>Development of an as-yet undiscovered basement.</td><td></td><td>Development of an as-yet undiscovered basement.</td><td rowspan="3"></td></tr>
<tr><td>Deposition of the sedimentary precursors to the Christie Gneiss (pelites, BIF, carbonate, psammite) and minor mafic volcanism.</td><td rowspan="2">Deposition of sediments?</td><td>Extensive felsic and mafic volcanism (e.g. ~2670Ma unnamed calc-alkaline volcanics, Lake Harris Komatiite, Hopeful Hill Pillow Basalt), minor sedimentation and plutonism.</td></tr>
<tr><td>Sleafordian Orogeny: Widespread, low-medium pressure, granulite facies metamorphism (~750-800°C, ~5kb) and complex ductile deformation (forming the Christie Gneiss). Minor mafic and felsic intrusives (e.g. Aristarchus Peridotite).</td><td>Sleafordian Orogeny: Localised deformation and greenschist to lower amphibolite facies metamorphism (<550°C, <3kb). Voluminous felsic magmatism (e.g. Glenloth Granite, Kenella Gneiss).</td></tr>
<tr><td rowspan="4"></td><td></td><td></td><td rowspan="4">Development of complex, undifferentiated, variably deformed basement material, comprising granitoids, mafics and minor metasediments.</td></tr>
<tr><td>Voluminous, I-type, layered, mafic-intermediate intrusive plutons and sheets.</td><td rowspan="2">Deposition of the Wilgena Hill Jaspilite, clastic Eba Formation and the ~1723Ma clastic Labyrinth Formation in shallow, localised sedimentary basins and graben.</td></tr>
<tr><td>Upper amphibolite facies, high pressure metamorphism (~650-700°C, ~5-8kb) and variable, ductile, compressional deformation.</td></tr>
<tr><td></td><td>A-type plutonism (e.g. the Symon's Granite</td></tr>
<tr><td>Extensive, I-type plutonism (the Ifould Complex).</td><td>Felsic plutonism (e.g. White Gin granite).</td><td></td><td></td></tr>
<tr><td>Localised, retrograde, ductile deformation of the Christie Gneiss and Ifould Complex.</td><td rowspan="5"></td><td colspan="2">Deposition of clastic sediments in localised graben (~1655Ma Tarcoola Formation). Minor volcanism. Localised, low grade, ductile deformation.</td></tr>
<tr><td rowspan="5"></td><td></td><td>Voluminous, A-type, intermediate to felsic plutonism and volcanism (St Peter Suite).</td></tr>
<tr><td>Minor, I-type, felsic plutonism</td><td colspan="2">Massive, voluminous, very high temperature, A-type, felsic magmatism including the Gawler Range Volcanics and high-level Hiltaba Suite Granites.</td></tr>
<tr><td>I-type, felsic plutonism.</td><td rowspan="3"></td><td rowspan="2"></td></tr>
<tr><td>High pressure, granulite facies metamorphism (~750-800°C, 8-10kb) accompanied by minor ductile deformation.</td></tr>
<tr><td>Retrograde, amphibolite facies metamorphism and widespread compressional deformation, accompanied by extensive rehydration. Minor felsic magmatism.</td><td>Voluminous, S-type, high level plutonism (Munjeela Suite). Deformation along minor, strike slip shear zones.</td></tr>
<tr><td colspan="4">SZ_1 - Juxtaposition of subdomains along major, east-west trending, strike-slip shear zones (e.g. the Yerda Shear Zone).</td></tr>
<tr><td></td><td></td><td>Deposition of arenaceous redbed of the Pandurra Formation.</td><td></td></tr>
<tr><td colspan="2">SZ2 - Extensive reworking and differential exhumation at relatively high pressures (up to 7-8kb at ~620°C) along major, transpressional, northeast-trending shear zones (principally the Tallacootra and Coorabie Shear Zones).</td><td colspan="2">SZ2 - Juxtaposition of the Wilgena/Nuyts Subdomains and the Christie/Fowler Subdomains by the transpressional Coorabie Shear Zone.</td></tr>
<tr><td>Granitoid plutonism.</td><td colspan="3">Minor brittle reactivation of major shear zones.</td></tr>
<tr><td colspan="4">Gairdner Dyke Swarm.</td></tr>
</table>

recognition, there are two possible new definitions for the Gawler Craton:

(i) that the MESA definition holds, which implies that the Gawler Craton is significantly smaller than previously thought, and is bound to the northwest by the Coorabie Shear Zone; or,

(ii) that the Gawler Craton was "cratonised" at ~1100 Ma.

In the case of (i) above, terranes northwest of the Coorabie Shear Zone would be part of a later orogenic belt, the significance of which is discussed below. In the case of (ii) above, it is important to realise that no definite northwestern boundary of the Gawler "Craton" exists, and intact, continuous

basement is interpreted to extend as far north as the Musgrave Block and as far west as the Albany-Fraser Province. Hence the Gawler "Craton" would encompass all basement terranes south of the Musgrave Block and east of the Yilgarn Craton. Clearly the notion that the Gawler is a "craton" is somewhat flawed!

9.2 The western Gawler Craton in a regional context

The dominant, northeast-trending structural grain of the northwestern Gawler Craton parallels those interpreted in basement rocks beneath the Officer Basin, as well as that of the Albany Fraser Province further to the west. This structural grain is largely attributed to Cycle 5 shear zones which are interpreted to have operated in the time interval ~1200-1100 Ma; synchronous with major tectonism in the Albany-Fraser Province (Myers, 1990, 1993; Nelson et. al, 1995) and the Musgrave Block (Maboko et. al, 1991; Camacho & Fanning, 1995; Clarke et. al, 1995b). This geometric and temporal link between the Gawler Craton and adjacent terranes was previously unrecognised, and have wide-ranging implications for Australian Proterozoic geology. Previously the Gawler Craton was thought to be totally unrelated to these younger terranes. Myers et. al (1996) and Daly et. al (in press) proposed that the Gawler Craton was part of a larger "South Australian Craton" which had formed by ~1530 Ma and extended west to the Albany-Fraser Province and east to what is now the Broken Hill Block. Myers et. al (1996) hypothesised that the South Australian Craton collided with the western and northern Australian cratons during the ~1300-1100 Ma time interval resulting in the development of a continuous, narrow orogenic belt now recognised in the Albany-Fraser Province and the Musgrave Block. Fanning et. al (1995, 1996) propose that this "South Australian Craton" was part of a larger continent (the Mawson Continent) that extended well into what is now Antarctica, and along with Daly et. al (1997) attributed the northeast-trending structural grain in the western Gawler Craton to earlier, poorly constrained tectonic activity, collectively termed the Kararan Orogeny.

Linear gravimetric anomalies northeast of the Gawler Craton show that Cycle 5 shear zones continue in basement beneath the Adelaide Fold Belt and Cooper-Eromanga Basin. These anomalies extend to define the southern margin of the Mount Isa Inlier (see Figure 9.1). The current whereabouts of the southern extension of the Mount Isa Inlier has been the focus of recent debate in Australian earth science (e.g. Connors & Page, 1995; O'Dea et. al, 1997). The possibility that this truncation occurred synchronously with Cycle 5 tectonism in the Gawler Craton has significant implications for the Proterozoic geological framework of Australia. In the western Gawler Craton, these shear zones largely exhibit dextral vergence, suggesting that the southern continuation of the Mount Isa Inlier may now reside to the southwest, possibly beneath the Cooper-Eromanga Basin and the Adelaide Fold Belt. The fact that the Ewen and Kalkadoon Batholiths and mafic volcanics of the Mount Isa Inlier are geochemically and temporally indistinguishable from the Lincoln Batholith and Tournefort Dyke Swarm of the southeastern Gawler Craton (Schaefer, 1998) may indicate a spatial relationship between the two terranes.

9.3 The western Gawler Craton in a global context

The recognition that the global distribution of ~1300-1000 Ma orogenic belts were instrumental in the assembly of a Neoproterozoic supercontinent named Rodinia has tantalising implications for global Precambrian geology. The supercontinent reconstructions of Moores (1991), Dalziel (1991, 1992) and Hoffman (1991) have initiated numerous subsequent studies which have recently culminated in the publication of an up-to-date reconstructive map of Rodinia and Gondwana (Unrug et. al, 1997; Unrug, 1997) (see Figure 9.1). This reconstruction implies that (i) the ~1300-1000 Ma orogenic belts once linked to form an interconnected, global orogenic system known as the *Grenvillian Orogen*, after its type province in eastern Canada (Davidson, 1995), and (ii) that Rodinia comprised a collage of continental fragments including what is now Australia, East Antarctica, India, Laurentia (i.e. North America), Amazonia and Baltica (see Figure 9.1) which amalgamated along the network of ~1300-1000 Ma Grenvillian mobile belts. A mobile belt of Grenvillian age extended from north America (i.e. Laurentia) around what is now the east Antarctic and Indian coastlines into the Albany Fraser Province and Musgrave Block in Australia (see Figure 9.2). The observation that in most Rodinia reconstructions, this Grenvillian orogenic belt became considerably narrower as it entered Australia compared with its Indo-Antarctic and American extension (changing from ~600km to less than 200km wide) has only been pointed out by Davidson (1995) as being geometrically problematic. Davidson (1995) suggested that in all likelihood, the Grenvillian orogen in Australia must extend east to the margins of the Gawler Craton in order to account for its projected width further to the southwest. The recognition in this study that significant Grenvillian tectonism occurred in the western Gawler Craton suggests that a Grenvillian orogen extended west from the Albany-Fraser Province into the Gawler "Craton", forming a ~500-

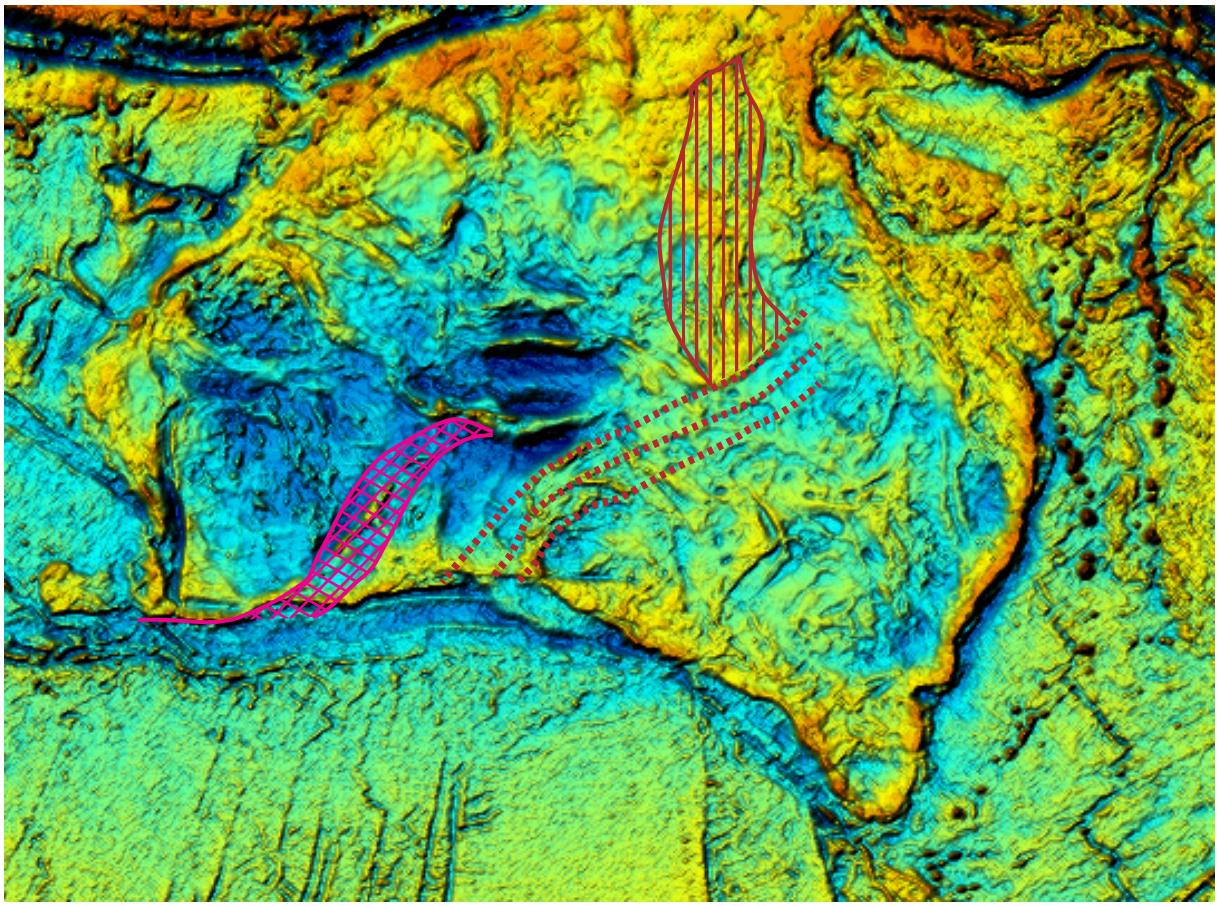

Figure 9.1 Bouger gravimetric image of the Australian continent (AGSO data), showing the Albany Fraser Orogen (in pink), and the linear anomalies caused by Cycle 5 shear zones in the western Gawler Craton, which extend northeast beneath the Adelaide Fold Belt and the Cooper-Eromanga basin to define the southern boundary of the Mount Isa Inlier (in red).

600km wide, northeast trending orogenic belt. This scenario provides a far more credible reconstructive geometry for this part of Rodinia (see Figure 9.2), and implies that the "Grenville Front" (i.e. the shear zone marking the structural limit of Grenvillian tectonism - Green et. al, 1988) may be represented by the Coorabie Shear Zone, which forms the eastern limit of supposedly Grenvillian tectonism in the Gawler Craton and is a fundamental geological discontinuity (see Chapter 8).

The structural framework of this orogenic belt delineated elsewhere in Antarctica and North America is dominated by parallel belts comprising: (i) a "foreland" or parautochthonous belt in which older crust (up to Archaean in age) was variably reworked during Grenvillian tectonism usually associated with a network of anastomosing shear zones, and (ii) a belt of "inboard", or allochthonous terranes in which extensive Grenvillian magmatism, high grade metamorphism and pervasive ductile deformation occurred (e.g. Rivers et. al, 1989, 1993; Dalziel, 1992; Davidson, 1995). The Albany-Fraser Province, Musgrave Block and many East Antarctic terranes all underwent extensive magmatism, high grade metamorphism (mainly granulite facies) and pervasive ductile deformation during the Grenvillian, in marked contrast with the western Gawler Craton, which underwent extensive reworking along major shear zones at this time. This observation suggests that the western Gawler Craton may be considered analagous to the parautochthonous belt of the Grenvillian orogens of North America and Antarctica.

The amalgamation of Rodinia along Grenvillian mobile belts has traditionally been interpreted in terms of modern-day, plate-margin, collisional processes, whereby numerous continental fragments amalgamated along Grenville-age sutures, presumably associated with subduction zones (e.g. Moores, 1991; Dalziel, 1991, 1992; Hoffman, 1991; Davidson, 1995; Myers et. al, 1996; Sadowski & Bettencourt, 1996). While this scenario is indisputable for many Grenville-age orogens, as evidenced by extensive obducted oceanic relics and calc-alkaline intrusives, the possibility that some orogens were intracratonic (especially those in Australia) was first postulated by Li et. al (1995, 1996) who noted the absense of Grenville-age oceanic relics in the Albany-Fraser Province and the Musgrave Block. Such oceanic relics are clearly absent from Cycle 5 tectonism in the western Gawler Craton.

Given the complexity and extent of the inferred

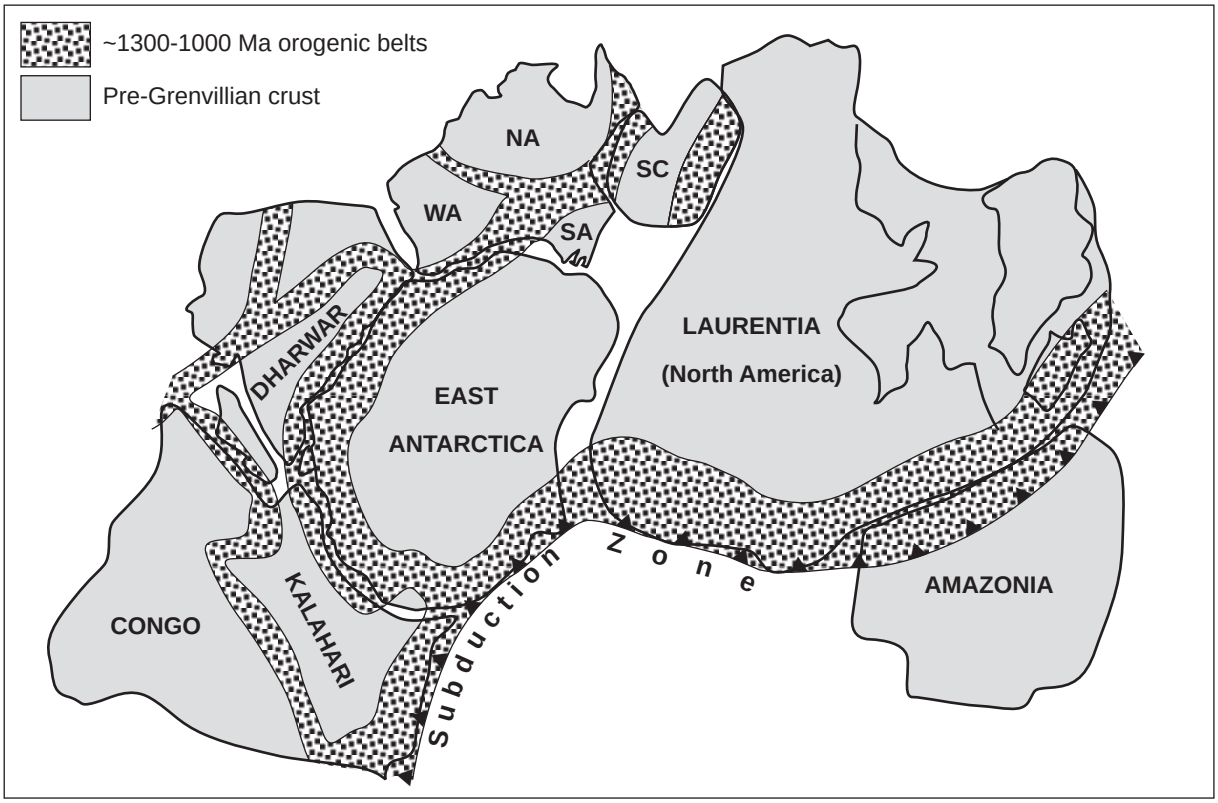

Figure 9.2 Up-to-date reconstructive map of the Rodinia supercontinent at ~1000-700 Ma, adapted from Unrug (1997) and Unrug et. al (1997). The network of ~1300-1000 Ma "Grenvillian" orogenic belts along which Rodinia amalgamated are shown, taking into account the inferred Grenvillian orogenic belt in the western Gawler Craton. The resultant width of this Grenvillian mobile belt in Australia provides a far more plausible reconstructive geometry for this part of Rodinia. NA=Northern Australian "craton", WA=Western Australian "craton", SA=South Australian "craton", SC=South China "cratons" (after Li et. al, 1995, 1996).

network of Grenvillian orogens in Rodinia, it is geometrically improbable that each was associated with a subduction zone. A modern-day analogue for the "assembly" of Rodinia may be the collision of the Indo-Australian and Asian plates, where the Himalayan Orogen has formed as a direct response to plate-margin collisional processes. However deformation associated with this collision is occurring away from the plate margins which is demonstrably intracontinental. In fact, spatially over 80% of the deformation associated with the Himalayan collision can be considered intracratonic, and is manifest in a complexity of major mobile belts up to 4000km north of the plate margin. Clearly the in-plane stresses which drive the Himalayan Orogen are sufficient to drive continent-scale deformation well away from the plate margins. Such driving forces can clearly reactivate zones of fundamental crustal weakness anywhere within the continents, and are likely to be independent of the distance from the plate margins. If the orogenic system associated with the Himalayan collision is at all representative of tectonism in the past, then it is reasonable to assume that many mobile belts associated with older collisional episodes (e.g. the Grenvillian and the Pan-African) are also likely to be intracratonic, even though the driving forces responsible for deformation are directly related to plate-margin processes. If this scenario holds for the Grenvillian then it is reasonable to expect both plate-margin and intracratonic mobile belts to have developed synchronously. Therefore the notion that "supercontinents" resulted from the synchronous amalgamation of numerous continental fragments may be somewhat flawed, and the possibility that they may have resulted in the collision and intracratonic reworking of several larger continents must not be discounted.

REFERENCES

Annersten, H. & Seifert, F., 1981, Stability of the assemblage orthopyroxene-sillimanite-quartz in the system MgO - FeO - Fe_2O_3 - Al_2O_3 - SiO_2 - H_2O. *Contributions to Mineralogy and Petrology*, 77:158-165.

Arima, M., Kerrich, R. & Thomas, A., 1986, Sapphirine-bearing paragneiss from the northern Grenville Province in Labrador, Canada: protolith composition and metamorphic PT conditions. *Geology*, 14, p844-847.

Arima, M., & Gower, C.F., 1991, Osumilite-bearing granulites in the eastern Grenville Province, Eastern Labrador, Canada: mineral parageneses and metamorphic conditions. *Journal of Petrology*, 32:29-61.

Arnold, J. & Sandiford, M., 1990, Petrogenesis of cordierite-orthoamphibole assemblages from the Springton region, South Australia. *Contributions to Mineralogy and Petrology*, 106, p100-109.

Arnold, J.L., 1994, Staurolite-kyanite-amphibolites: Calculated phase relations with application to amphibolites from the Harts Range, central Australia and the Zillertaler Alpen, Austria. *Unpublished PhD Thesis*, University of Adelaide.

Audibert, N., Hensen, B.J. & Bertrand, P., 1995, Experimental study of phase relations involving osumilite in the system K_2O-FeO-MgO-Al_2O_3-SiO_2-H_2O at high pressure and temperature. *Journal of Metamorphic Geology*, 13:331-344.

Ayers, L.D., Thurston, P.C., Card, K.D. & Weber, W., 1985, *Evolution of Archaean Supracrustal Sequences*, Geological Society of Canada Special Paper 28.

Baker, J., Powell, R., Sandiford, M. & Muhling, J., 1987, Corona textures between kyanite, garnet and gedrite in gneisses from Errabiddy, Western Australia. *Journal of Metamorphic Geology*, 5(3), p357-370.

Bartlett, J.M., Dougherty-Page, J.S., Harris, B.W., Hawkesworth, C.J. & Santosh, M., in press, The application of zircon evaporation and model Nd ages to the interpretation of polymetamorphic terranes: An example from the Proterozoic mobile belt of south India. *Contributions to Mineralogy and Petrology*.

Berg, J.J. & Wheeler, E.P., 1976, Osumilite of deep-seated origin in the contact aureole of the anorthositic Nain complex, Labrador. *American Mineralogist*, 61:29-37.

Bertrand, P., Ellis, D.J. & Green, D.H., 1991, The stability of sapphirine-quartz and hypersthene-sillimanite-quartz assemblages: an experimental investigation in the system FeO-MgO-Al_2O_3-SiO_2 under H_2O and CO_2 conditions. *Contributions to Mineralogy and Petrology*, 108(1-2), p55-71.

Bertrand, P., Ouzegane, K. & Kienast, J.R., 1992, P-T-X relationships in the Precambrian Al-Mg-rich granulites from In Ouzzal, Hoggar, Algeria. *Journal of Petrology*, 32, p629-656.

Bhattacharya, A., Krishnakumar, K.R., Raith, M. & Sen, S.K., 1991, An improved set of a-X parameters for Fe-Mg-Ca garnets and refinements of the orthopyroxene-garnet thermometer and the orthopyroxene - garnet - plagioclase - quartz barometer. *Journal of Petrology*, 32(3), p629-656.

Blissett, A.H. & Vitols, V., 1973, Helicopter geological survey of the Gawler Block, 1973. *South Australian Department of Mines Report*, 74/144.

Blissett, A.H., 1986, Subdivision of the Gawler Range Volcanics in the Gawler Ranges. *South Australian Geological Survey. Quarterly Geological Notes*, 97, p2-11.

Blissett, A.H. (Compiler), 1987, Geological setting of the Gawler Range Volcanics. *South Australian Geological Survey. 1:500,000 Special Map.*

Bogdanova, N.G., Trovena, N.V., Zaborovskaya, N.B., Sukhanov, M.K. & Berkhin, S.I., 1980, The first find of metamorphic osumilite in the U.S.S.R. *Dok. Akad. Nauk. Uzb. SSR.* 250:690-693.

Bohlen, S. R., Wall, V. J. & Boettcher, A. L., 1983a, Experimental investigation and application of garnet granulite equilibria. *Contributions to Mineralogy and Petrology*, 83, p52-61.

Bohlen, S.R., 1986, Instability of the assemblage corundum + quartz. *EOS, Transactions, American Geophysical Union*, 67(44):1280.

Bohlen, S.R., 1987, Pressure-temperature-time paths and a tectonic model for the evolution of granulites. *Journal of Geology*, 95:617-632.

Bohlen, S.R. & Metzger, K., 1989, Origin of granulite terranes and the formation of the lowermost continental crust. *Science*, 244:326-329.

Bohlen, S.R., 1991, On the formation of granulites. *Journal of Metamorphic Geology*, 9:223-229.

Brown, H.Y.L., 1885, Report on the geological character of country passed over from Port Augusta to Eucla. *South Australian Parliamentary Papers*, 145.

Brown, H.Y.L., 1897, Government Geologist's Report on Explorations in the Western Part of South Australia. *South Australian Parliamentary Papers*, 46.

Brown, H.Y.L., 1905, Geological explorations in the west and northwest of South Australia. *South Australian Parliamentary Papers*, 71.

Bucher-Nurminen, K., 1990, Transfer of mantle fluids to the lower continental crust: Constraints from mantle mineralogy and Moho temperature. *Chemical Geology*, 83, p249-261.

Cabanis, B. & Lecolle, M., 1989, Le diagramme La/10-Y/15/-Nb/8: un outil pour la discrimination des series volcaniques et la mise en evidence des processus de melange et/ou de contamination crustale. *C.R. Acad. Sci. Ser. II*, 309, p2023-2029.

Camacho, A. & Fanning, C.M., 1995, Some isotopic constraints on the evolution of the granulite and upper amphibolite facies terranes in the eastern Musgrave Block, central Australia. *Precambrian Research*, 71, p155-181.

Carrington, D.P. & Harley, S.L., 1995a, Partial melting and phase relations in high-grade metapelites: an experimental petrogenetic grid in the KFMASH system. *Contributions to Mineralogy and Petrology,* 120:270-291.

Carrington, D.P. & Harley, S.L., 1995b, The stability of osumilite in metapelitic granulites. *Journal of Metamorphic Geology,* 13:613-625.

Chappell, B.W. & White, A.J.R., 1974, Two contrasting granite types. *Pacific Geology*, 8, p173-174.

Chappell, B.W. & White, A.J.R., 1992, I- and S-type granites in the Lachlan Fold Belt. *Transactions of the Royal Society of Edinburgh: Earth Sciences*, 83, p1-26.

Chinner, G.A. & Fox, J.S., 1974, The origin of cordierite-anthophyllite rocks in the Land's End aureole. *Geological Magazine*, 111, p397-408.

Choukroune, P., Ludden, J.N., Chardon, D., Calvert, A.J. & Bouhallier, H., 1997, Archaean crustal growth and tectonic processes: a comparison of the Superior Province, Canada and the Dharwar Craton, India. In Burg, J.P. & Ford, M. (eds.), *Orogeny Through Time*, Geological Society Special Publication No. 121, p63-98.

Clark, D.A., 1997, Magnetic petrophysics and magnetic petrology: aids to geological interpretation of magnetic surveys. *AGSO Journal of Australian Geology and Geophysics*, 17(2), p83-103.

Clarke, G.L., Powell, R. & Guiraud, M., 1989, Low-pressure granulite facies metapelitic assemblages and corona textures from MacRobertson Land, east Antarctica: the importance of Fe_2O_3 and TiO_2 in accounting for spinel-bearing assemblages. *Journal of Metamorphic Geology*, 7, p323-335.

Clarke, G.L., Sun, S.-S & White, R.W., 1995a, Grenville-age belts and associated older terranes in Australia and Antarctica. *AGSO Journal of Australian Geology & Geophysics*, 16(1/2), p25-39.

Clarke, G.L., Buick, I.S., Glikson, A.Y. & Stewart, A.J., 1995, Timing of Giles Complex intrusion and multiple high-P events in the western Musgrave Block, central Australia. *AGSO Journal of Australian Geology & Geophysics*, 16(1/2).

Compston, W., Williams, I.S. & Meyer, C., 1984, U-Pb geochronology of zircons from lunar breccia 73217 using a sensitive high mass-resolution ion microprobe. *Journal of Geophysical Research (suppl.)*, 89, pB525-B534.

Connors, K.A & Page, R.W., 1995, Relationships between magmatism, metamorphism and deformation in the western Mount Isa Inlier, Australia. *Precambrian Research*, 71, p131-153.

Cowley, W.M., 1993, Cariewerloo Basin. In Drexel, J.F., Preiss, W.V. & Parker, A.J., 1993, The geology of South Australia. Vol. 1. The Precambrian. *South Australian Geological Survey Bulletin,* 54.

Crawford, A.R., 1957, Iron ore near Mount Christie. With notes on other outcrops in the Wynbring-Tarcoola district. *Mining Review, Adelaide,* 104, p5-14.

Cunningham, W.D., Windley, B.F., Dorjnamjaa, D., Badamgarov, J. & Saandar, M., 1996, Late Cenozoic transpression in southwestern Mongolia and the Gobi Altai-Tien Shan connection. *Earth and Planetary Science Letters*, 140, p67-81.

Currie, K.L. & Gittins, J., 1988, Contrasting sapphirine parageneses from Wilson Lake, Labrador and their tectonic implications. *Journal of Metamorphic Geology*, 6, p603-622.

Daly, S.J., Webb, A.W. & Whitehead, S.G., 1978, Archean to early Proterozoic banded iron formation in the Tarcoola region, South Australia. *Transactions of the Royal Society of South Australia*, 102(5), p141-149.

Daly, S.J., Benbow, M.C. & Blissett, A.H., 1979, Archaean to early Proterozoic geology of the northwestern Gawler Craton. In Parker, A.J. (Compiler), *Symposium on the Gawler Craton, Adelaide, 1979. Extended Abstracts*. Geological Society of South Australia (SA Division), p16-19.

Daly, S.J., 1981, The stratigraphy of the TARCOOLA 1:250,000 map sheet area. *South Australian Department of Mines and Energy, Report Book,* 81/5.

Daly, S.J., 1985, TARCOOLA map sheet. *South Australia. Geological Survey. Geological Atlas 1:250,000 series*, sheet SH53-10.

Daly, S.J., 1986, The Mulgathing Complex. *South Australian Department of Mines and Energy. Report Book,* 86/48.

Daly, S.J., 1987, Ooldea 2 - Well Completion Report. *Mines and Energy, South Australia. Report Book,* 87/48.

Daly, S.J. & Fanning, C.M., 1990, Archaean geology of the Gawler Craton, South Australia. In Glover, J.E. & Ho, S.E. (Compilers), *3rd Internation Archaean Symposium, Perth, 1990. Extended Abstracts,* p91-92.

Daly, S.J. & Fanning, C.M., 1993, Chapter 3: Archaean. In Drexel, J.F., Preiss, W.V. & Parker, A.J., 1993, The geology of South Australia. Vol. 1. The Precambrian. *South Australian Geological Survey Bulletin,* 54.

Daly, S.J., 1993, Tarcoola Formation. In Drexel, J.F., Preiss, W.V. & Parker, A.J., 1993, The geology of South Australia. Vol. 1. The Precambrian. *South Australian Geological Survey Bulletin,* 54.

Daly, S.J., Tonkin, D.G., Purvis, A.C. & Shi, Z., 1994, Colona drilling program. *Mines & Energy, South Australia Open File Envelope 8768.*

Daly, S.J., Fairclough, M.C., Fanning, C.M. & Rankin, L.R., 1995, Tectonic evolution of the western Gawler Craton: a Palaeoproterozoic collision zone and likely plate margin. *Geological Society of Australia, Abstracts,* 40, p35-36.

Daly, S.J., 1996, The Thompson Nickel Belt and other new exploration models for the west Gawler Craton. *Resources '96 Convention - Conference Abstracts*, Mines & Energy, South Australia.

Daly, S.J., Fanning, C.M. & Fairclough, M.C., in press, Tectonic evolution and exploration potential of the Gawler Craton. *AGSO Journal of Geology & Geophysics*, in press.

Dalziel, I.W.D., 1991, Pacific margins of Laurentia and East Antarctica - Australia as a conjugate rift pair: Evidence and implications for an Eocambrian supercontinent. *Geology*, 19, p598-601.

Dalziel, I.W.D., 1992, Antarctica; a tale of two supercontinents? *Annual Reviews of Earth and Planetary Sciences*, 20, p501-526.

Dasgupta, S., Sengupta, P., Ehl, J., Raith, M. & Bardhan, S., 1995, Reaction textures in a suite of spinel granulites from the easter Ghats Belt, India: Evidence for polymetamorphism, a partial petrogenetic grid in the system KFMASH and the roles of ZnO and Fe_2O_3. *Journal of Petrology,* 36(2):435-461.

Davidson, A., 1995, A review of the Grenville Orogen in its North American type area. *AGSO Journal of Australian Geology & Geophysics*, 16(1/2), p3-24.

Denham, D., 1997, Airborne geophysics in Australia: the government contribution. *AGSO Journal of Australian Geology and Geophysics*, 17(2), p3-9.

Dougherty-Page, J.S. & Foden, J., 1996, Pb-Pb zircon evaporation date for the Charleston Granite, South Australia: comparisons with other zircon geochronology techniques. *Australian Journal of Earth Sciences*, 43, p133-137.

Drexel, J.F., Preiss, W.V. & Parker, A.J., 1993, The geology of South Australia. Vol. 1. The Precambrian. *South Australian Geological Survey Bulletin,* 54.

Ellis, D.J., 1987, Origin and evolution of granulites in normal and thickened crust. *Geology*, 15:167-170.

Ellis, D.J., Sheraton, J.W., England, R.N. & Dallwitz, W.B., 1980, Osumilite-sapphirine-quartz granulites from Enderby Land, Antarctica: mineral assemblages and reactions. *Contributions to Mineralogy and Petrology,* 72:123-143.

Emslie, R.F., 1980, Geology and petrology of the Harp Lake Complex, central Labrador: An example of Elsonian magmatism. *Geological Survey of Canada Bulletin*, 293, 136p.

England, P.C., 1987, Diffuse continental deformation: length scales, rates and metamorphic evolution. *Philosphical Transactions of the Royal Society of London*, A321, p3-22.

Fanning, C.M., Flint, R.B. & Preiss, W.V., 1983, Geochronology of the Pandurra Formation. *South Australian Geolgical Survey. Quarterly Geological Notes*, 88, p11-16.

Fanning, C.M., Flint, R.B., Parker, A.J., Ludwig, K.R. & Blissett, A.H., 1988, Refined Proterozoic evolution of the Gawler Craton, South Australia, through U/Pb zircon geochronology. *Precambrian Research*, 40/41, p363-386.

Fanning, C.M., Daly, S.J., Bennett, V.C., Menot, R.P., Peucat, J.J. and Oliver, R.L., 1995, The 'Mawson Block': once contiguous Archaean to Proterozoic crust in the East Antarctic Shield and Gawler Craton, Australia. *7th International Symposium on Antarctic Earth Sciences, Siena, 1995. Extended abstracts.*

Fanning, C.M., Moore, D.H., Bennett, V.C. and Daly, S.J., 1996, The 'Mawson Continent': Archaean to Proterozoic crust in the East Antarctic Shield and Gawler Craton, Australia. A cornerstone in Rhodinia and Gondwanaland. *Geological Society of Australia. Abstracts*, 41, p135.

Fanning, C.M., 1997, Geochronological Synthesis of South Australia. Part II: The Gawler Craton. *Unpublished PRISE report*, Research School of Earth Sciences, Australian National University.

Firman, J.B. (compiler), 1975, FOWLER map sheet and explanatory notes, South Australia, Geological Survey, *Geological Atlas 1:250,000 series*, sheet SH/53-13.

Fitzsimons, I.C.W. & Harley, S.L., 1994, The influence of retrograde cation exchange on granulite PT estimates and a convergence technique for the recovery of peak metamorphic conditions. *Journal of Petrology*, 35, p543-576.

Flint, R.B., 1987, NUYTS map sheet and explanatory notes, South Australia, Geological Survey, *Geological Atlas 1:250,000 series*, sheet SI/53-1.

Flint, R.B., Rankin, L.R. & Fanning, C.M., 1990, Definition - The Palaeoproterozoic St Peter Suite of the western Gawler Craton. *South Australian Geological Survey. Quarterly Geological Notes*, 114, p2.

Flint, R.B., 1993, Chapter 5: Mesoproterozoic. In Drexel, J.F., Preiss, W.V. & Parker, A.J., 1993, The geology of South Australia. Vol. 1. The Precambrian. *South Australian Geological Survey Bulletin,* 54.

Flint, R.B. & Daly, S.J., 1993, Coompana Block. In Drexel, J.F., Preiss, W.V. & Parker, A.J., 1993, The geology of South Australia. Vol. 1. The Precambrian. *South Australian Geological Survey Bulletin,* 54.

Forbes, B.G., 1970, Geology of COOK, OOLDEA and BARTON 1:250,000 sheet areas. *South Australian Department of Mines Report*, 70/42 (unpublished).

Fraser, G., Ellis, D. & Eggins, S., 1997, Zirconium abundance in granulite-facies minerals, with implications for zircon geochronology in high-grade rocks. *Geology*, 25(7), p607.

Frost, B.R. & Bucher, K., 1994, Is water responsible for geophysical anomalies in the deep continental crust? A petrological perspective. *Tectonophysics*, 231, p293-309.

Ganguly, J. & Saxena, S. K., 1984, Mixing properties of aluminosilicate garnets: constraints from natural and experimental data, and applications to geothermo-barometry. *American Mineralogist*, 69, p88-97.

Gasparini, P., Mantovani, M.S.M., Corrado, G. & Rapolla, A., 1979, Depth of Curie Temperature in continental shields: a compositional boundary? *Nature*, 278, p845-846.

George, F.R., 1905, Report of Mr F.R. George on his Prospecting Expedition North of the Nullarbor Plains. *South Australian Parliamentary Paper*.

Giles, C.W., 1988, Petrogenesis of the Proterozoic Gawler Ranges Volcanics, South Australia. *Precambrian Research*, 40/41, p407-427.

Giles, E., 1889, *Australia Twice Traversed*. Sampson Low, Marston, Searle & Rivington, London.

Graham, C. M. & Powell, R., 1984, A garnet-hornblende geothermometer: calibration, testing, and application to the Pelona Schist, Southern California. *Journal of Metamorphic Geology*, 2, p13-21.

Grant, F.S., 1985a, Aeromagnetics, geology and ore environments, I. Magnetite in igneous, sedimentary and metamorphic rocks: and overview. *Geoexploration*, 23, p303-333.

Grant, F.S., 1985b, Aeromagnetics, geology and ore environments, II. Magnetite and ore environments. *Geoexploration*, 23, p335-362.

Grant, J.A., 1985, Phase equilibria in partial melting of pelitic rocks. In Ashworth, J. (ed.),*Migmatites*, Blackie, London, p86-144.

Green, A.G., Milkereit, B., Davidson, A., Spencer, C., Hutchinsom, D.R., Cannon, W.F., Lee, M.W., Agena, W.F., Behrendt, J.C. & Hinze, W.J., 1988, Crustal structure of the Grenville Front and adjacent terranes. *Geology*, 16, p788-792.

Grew, E.S., 1980, Sapphirine + quartz association from Archaean rocks in Enderby Land, Antarctica. *American Mineralogist*, 65, p821-836.

Grew, E.S., 1982a, Osumilite in the sapphirine-quart terrane of Enderby Land, Antarctica: implications for osumilite petrogenesis in the granulite facies. *American Mineralogist*, 67:762-787.

Grew, E.S., 1982b, Sapphirine, kornerupine and sillimanite orthopyroxene in the charnockitic region of south India. *Journal of the Geological Society of India*, 23, p469-505.

Guiraud, M., Kienast, J.-R. & Ouzegane, K., 1996, Corundum-quartz bearing assemblage in the Ihouhaouene area (In Ouzzal, Algeria), *Journal of Metamorphic Geology*, 14:755-761.

Gunn, P.J., Maidment, D. & Milligan, P.R., 1997, Interpreting aeromagnetic data in areas of limited outcrop. *AGSO Journal of Australian Geology and Geophysics*, 17(2), p175-185.

Haggerty, S.E., 1978, Mineralogical constraints on Curie Isotherms in deep crustal magnetic anomalies. *Geophysical Research Letters*, 5(2), p105-108.

Hall, D.H., 1968, Regional magnetic anomalies, magnetic units, and crustal structure in the Kenora District of Ontario. *Canadian Journal of Earth Sciences*, 5, p1277-1296.

Hand, M., Scrimgeour, I., Powell, R., Stuwe, K. & Wilson, C.J.L, 1994, Metapelitic granulites from Jetty Pensinsula, East Antarctica; formation during a single event or by polymetamorphism? *Journal of Metamorphic Geology*, 12(4), p557-573.

Harley, S. L., 1984, An experimental study of the partitioning of Fe and Mg between garnet and orthopyroxene. *Contributions to Mineralogy and Petrology*, 86, p359-373.

Harley, S.L., 1985, Paragenetic and mineral-chemical relationships in ortho-amphibole-bearing gneisses from Enderby Land, East Antarctica; a record of Proterozoic uplift. *Journal of Metamorphic Geology*, 3(2), p179-200.

Harley, S.L., 1989, The origins of granulites: a metamorphic perspective. *Geological Magazine*, 126:215-247.

Harley, S.L., 1992, Proterozoic granulite terranes. Chapter 8 in Condie, K. (ed.), *Proterozoic Crustal Evolution*. Elsevier, Amsterdam, p301-359.

Harley, S.L., in press, On the occurrence and characterisation of ultrahigh-temperature (UHT) crustal metamorphism. *Journal of the Geological Society of London*.

Harlov, D.E. & Newton, R.C., 1993, Reversal of the metastable kyanite + corundum + quartz and andalusite + corundum + quartz equilibria and the enthalpy of formation of kyanite and andalusite. *American Mineralogist*, 78:594-600.

Henkel, H., 1991a, Petrophysical properties (density and magnetisation) of rocks from the northern part of the Baltic Shield. *Tectonophysics*, 192, p1-19.

Henkel, H., 1991b, Magnetic crustal structures in northern Fennoscandia. *Tectonophysics*, 192, p57-79.

Hensen, B.J. & Green, D.H., 1971, Experimental study of the stability of cordierite and garnet in pelitic

compositions at high pressures and temperatures I. Compositions with excess alumino-silicate. *Contributions to Mineralogy and Petrology,* 33:309-330.

Hensen, B.J. & Green, D.H., 1972, Experimental studies of cordierite and garnet in pelitic compositions at high pressures and temperatures II. Compositions without excess alumino-silicate. *Contributions to Mineralogy and Petrology,* 35:331-354.

Hensen, B.J., 1986, Theoretical phase relations involving cordierite and garnet revisited: the influence of oxygen fugacity on the stability of sapphirine and spinel in the system Mg-Fe-Al-Si-O. *Contributions to Mineralogy and Petrology,* 92:362-367.

Hinze, W.J. & Hood, P.J., 1989, The magnetic anomaly map of North America; a new tool for regional geologic mapping. In Bally, A.W. & Palmer, A.R. (eds.), *The Geology of North America - An Overview*. Boulder, Colorado, Geological Society of America, The Geology of North America, Volume A.

Hinze, W.J. & Zietz, I., 1985, The composite magnetic anomaly map of the conterminous United States. In Hinze, W.J. (ed.), 1985, *The Utility of Regional Gravity and Magnetic Anomaly Maps*. Society of Exploration Geophysicists, Tulsa, Oklahoma.

Hinze, W.J. (ed.), 1985, *The Utility of Regional Gravity and Magnetic Anomaly Maps*. Society of Exploration Geophysicists, Tulsa, Oklahoma.

Hoffman, P.F., 1989, Speculations on Laurentia's first gigayear (2.0 to 1.0 Ga). *Geology*, 17, p135-138.

Hoffman, P.F., 1991, Did the breakout of Laurentia turn Gondwanaland inside out? *Science*, 252, p1409-1412.

Holland, T.J.B. & Powell, R., 1990, An enlarged and updated internally consistent thermodynamic dataset with uncertainties and correlations: the system K_2O-Na_2O-CaO-MgO-MnO-FeO-Fe_2O_3-Al_2O_3-TiO_2-SiO_2-C-H_2-O_2. *Journal of Metamorphic Geology*, 8, p89-124.

Holland, T.J.B., 1995, AX (Activity-Composition calculator). Computer Program.

Hone, I.G., Milligan, P.R., Mitchell, J.N. & Horsfall, K.R., 1997, Australian national airborne geophysical databases. *AGSO Journal of Australian Geology and Geophysics*, 17(2), p11-21.

Horsfall, K.R., 1997, Airborne magnetic and gamma-ray data aquisition. *AGSO Journal of Australian Geology and Geophysics*, 17(2), p23-30.

Hudson, N.F.C. & Harte, B., 1985, K_2O-poor, aluminous assemblages from the Buchan Dalradian, and the variety of orthoamphibole assemblages in aluminous bulk compositions in the amphibolite facies. *American Journal of Science*, 285, p224-266.

Irvine, T.N. & Baragar, W.R.A., 1971, A guide to the chemical classification of the common volcanic rocks. *Canadian Journal of Earth Science*, 8, p523-548.

Ishihara, S., 1977, The magnetite-series and ilmenite-series granitic rocks. *Mining Geology*, 27, p293-305.

Isles, D., Valenta, R. & Cooke, A., 1995, *Interpretation of Airborne Magnetic Data*. World Geoscience and VIEPS software package.

Jaques, A.L., Wellman, P., Whitaker, A. & Wyborn, D., 1997, High-resolution geophysics in modern geological mapping. *AGSO Journal of Australian Geology and Geophysics*, 17(2), p159-173.

Jones, R.R. & Tanner, P.W.G., 1995, Strain partitioning in transpression zones. *Journal of Structural Geology*, 17(6), p793-802.

Jorgensen, G., Kisabeth, J., Krasny, L, Kwan, K., Liu, G.D., Macrab, R., Morris, P., Qu, G.S., Roest, W., Verba, V., Verhoef, J., Wu, C.Z., Xu, Z.G. & Zhao, S.Q., 1995, Magnetic anomalies and tectonic elements of northeast Eurasia. *Geological Survey of Canada Open File*, 2574 (image on the Canadian Geological Survey web site).

Kerrich, R., La Tour, T.E. & Willmore, L., 1984, Fluid participation in deep fault zones: evidence from geological, geochemical and $^{18}O/^{16}O$ relations. *Journal of Geophysical Research*, 89(B6), p4331-4343.

Kienast, J.R. & Ouzegane, K., 1987, Polymetamorphic Al-Mg rich parageneses in Archaean rocks from Hoggar, Algeria. *Geological Journal*, 22, p57-79.

Kienast, J.R., Fourcade, S., Guiraud, M., Hensen, B.J. & Ouzegane, K. (eds.), 1996, Special issue on the In Ouzzal Granulite Unit, Hoggar, Algeria. *Journal of Metamorphic Geology*, 14.

King, D., 1950, *A geological investigation along the eastern margin of the Nullarbor Plain*. Unpublished Master's Thesis, University of Adelaide.

King, D., 1951, Geology of the Pidinga Area. *Transactions of the Royal Society of South Australia*, 74(1), p25-43.

Kirkwood, D., 1995, Strain partitioning and progressive deformation history in a transpressive belt, northern Appalachians. *Tectonophysics*, 241, p15-34.

Knight, J., 1997, Geochemistry and geochronology of the St Peter Suite west of Ceduna. *Unpublished Honours Thesis*, University of Adelaide.

Kober, B., 1986, Whole grain evaporation for $^{207}Pb/^{206}Pb$ age investigations using a double-filament ion source. *Contributions to Mineralogy and Petrology*, 93, p482-490.

Kober, B., 1987, Single zircon evaporation combined with Pb^+ emitter bedding for $^{207}Pb/^{206}Pb$ age investigations using thermal ionisation mass spectroscopy, and implications for zirconology. *Contributions to Mineralogy and Petrology*, 96, p63-71.

Kohn, M. J. & Spear, F. S., 1990, Two new barometers for garnet amphibolites with applications to

eastern Vermont. *American Mineralogist*, 75, p89-96.

Kohn, M.J. & Spear, F.S., 1996, *Program THERMOBAROMETRY*, v2.0.

Krogh, E.J., 1977, Origin and metamorphism of iron formations and associated rocks, Lofoten-Vesteralaen, N. Norway. I. The Vestpolltind Fe-Mn deposit. *Lithos*, 10:243-255.

Lal, R.K., Ackermand, D. & Upadhyay, H., 1987, P-T-X relationships deduced from corona textures in sapphirine-spinel-quartz assemblages from Paderu, southern India. *Journal of Petrology*, 28, p1139-1168.

Lamb, W.M. & Valley, J.W., 1984, Metamorphism of reduced granulites in low-CO_2, vapour-free environments. *Nature*, 321, p56-58.

Lee, H.Y. & Ganguly, J., 1988, Equilibrium compositions of co-existing garnet and orthopyroxene; experimental determinations in the system FeO-MgO-Al_2O_3 -SiO_2 , and applications. *Journal of Petrology*, 29(1), p93-113.

Li, Z-X., Zhang, L. & Powell, C.McA., 1995, South China in Rodinia: Part of the missing link between Australia-East Antarctica and Laurentia? *Geology*, 23, p405-410.

Li, Z-X., Zhang, L. & Powell, C.McA., 1996, Positions of the East Asian cratons in the Neoproterozoic supercontinent Rodinia. *Australian Journal of Earth Sciences*, 43, p593-604.

Lidiak, E.G., 1974, Magnetic characteristics of some Precambrian basement rocks. *Journal of Geophysics*, 40, p549-564.

Lindsley, D.H., 1976, Experimental studies on oxide minerals. In Rumble, D. (ed.), *Oxide Minerals. Mineralogical Society of America - Short Course Notes*: 101-130.

Loosveld, R.J.H. & Etheridge, M.A., 1989, A model for low-pressure facies metamorphism during crustal thickening. *Journal of Metamorphic Geology*, 8, p257-267.

Luyendyk, A.P.J., 1997, Processing of airborne magnetic data. *AGSO Journal of Australian Geology and Geophysics*, 17(2), p31-38.

Maboko, M.A.H., Williams, I.S. & Compston, W., 1991, Zircon U-Pb chronometry of the pressure and temperature history of granulites in the Musgrave Ranges, central Australia. *Journal of Geology*, 99, p675-697.

Maijer, C., Jansen, J.B.H., Wevers, J. & Poorter, R.P.E., 1977, Osumilite, a new mineral to Norway. *Norsk Geologisk Tidsskrift*, 57:187-188.

Martin, A.R., Rankin, L.R., Benbow, M.C. & Daly, S.J., 1989, Helicopter Survey of the geology of the BARTON and TARCOOLA 1:250,000 map sheets. *South Australian Department of Mines and Energy Report*, 89/59.

McIntyre, J.I., 1980, Geological significance of magnetic patterns related to magnetite in sediments and metasediments - a review. *Bulletin of the Australian Society of Exploration Geophysicists*, 11, p19-33.

Milligan, P.R. & Gunn, P.J., 1997, Enhancement and presentation of airborne geophysical data. *AGSO Journal of Australian Geology and Geophysics*, 17(2), p63-75.

Moecher D. P., Essene, E. J. & Anovitz, L. M., 1988, Calculation and application of clinopyroxene - garnet - plagioclase - quartz geobarometers. *Contributions to Mineralogy and Petrology*, 100, p92-106.

Moores, E.M., 1991, Southwest U.S. - East Antarctic (SWEAT) connection: A hypothesis. *Geology*, 19, p425-428.

Morris, B.J., Hill, P.W. & Ferris, G.M., 1994, Barton bedrock drilling project. *Mines & Energy, South Australia. Report Book,* 163/92.

Morse, S.A. & Talley, J.H., 1971, Sapphirine reactions in deep seated granulites near Wilson Lake, Central Labrador, Canada. *Earth and Planetary Science Letters*, 10, p325-328.

Motoyoshi, Y. & Hensen, B.J., 1989, Sapphirine-quartz-orthopyroxene symplectites after cordierite in the Archaean Napier Complex, Antarctica: evidence for a counterclockwise P-T path? *European Journal of Mineralogy,* 1:467-471.

Motoyoshi, Y., Hensen, B.J. & Matsueda, H., 1990, Metastable growth of corundum adjacent to quartz in a spinel-bearing quartzite from the Archaean Napier Complex, Antarctica, *Journal of Metamorphic Geology*, 8:125-130.

Myers, J.S., 1990, Precambrian tectonic evolution of part of Gondwana, southwestern Australia. *Geology*, 18, p537-540.

Myers, J.S., 1993, Precambrian tectonic evolution of the West Australian Craton and adjacent orogens. *Annual Review of Earth and Planetary Sciences*, 21, p453-485.

Myers, J.S., Shaw, R.D. & Tyler, I.M., 1996, Tectonic evolution of Proterozoic Australia. *Tectonics*, 15(6), p1431-1446.

Nell, J. & Wood, B.J., 1989, Thermodynamic properties in a multicomponent solid solution involving cation disorder: Fe_2O_3-$MgFe_2O_4$-$FeAl_2O_4$-$MgAl_2O_4$ spinels. *American Mineralogist*, 74, p1000-1015.

Nelson, D.R., Myers, J.S. & Nutman, A.P., 1995, Chronology and evolution of the Middle Proterozoic Albany-Fraser Orogen, Western Australia. *Australian Journal of Earth Sciences*, 42, p481-495.

Newton, R. C. & Perkins, D. III, 1982, Thermodynamic calibration of geobarometers based on the assemblages garnet - plagioclase - orthopyroxene (clinopyroxene) - quartz. *American Mineralogist*, 67, p203-222.

Newton, R.C., 1989, Metamorphic fluids in the deep crust. *Annual Reviews of Earth and Planetary Science*, 17, p385-412.

Nixon, P.H., Reedman, A.J. & Burns, L.K., 1973, Sapphirine-bearing granulites from Labwor, Uganda. *Mineralogical Magazine*, 39, p420-428.

O'Dea, M.G., Lister, G.S., MacCready, T., Betts, P.G., Oliver, N.H.S., Pound, K.S., Huang, W. & Valenta, R.K., 1997, Geodynamic evolution of the Proterozoic Mount Isa terrain. In Burg, J.-P. & Ford, M. (eds.), *Orogeny Through Time*, Geological Society Special Publication No. 121, p99-122.

Olesen, O., Henkel, H., Kaada, K. & Tveten, E., 1991, Petrophysical properties of a prograde amphibolite-granulite facies transition zone at Sigerfjord, Vesterålen, northern Norway. *Tectonophysics*, 192, p33-39.

Oliver, N.H.S., 1996, Review and classification of structural controls on fluid flow during regional metamorphism. *Journal of Metamorphic Geology*, 14, p477-492.

Oliver, R.L. & Purvis, A.C., 1986, High pressure, high temperature metamorphism, northern Eyre Peninsula. *Geological Society of Australia, Abstracts*, 15:151-152.

Oliver, R.L., Purvis, A.J. & Taylor, M.J., 1988, Extra high grade (?) metamorphism in the northwest Gawler Craton, South Australia. *Geological Society of Australia, Abstracts*, 21:302.

Osborne, E.F., 1962, Reaction series for subalkaline igneous rocks based on different oxygen pressure conditions. *American Mineralogist*, 57, p211-226.

Pain, A.M. & Morris, B.J., 1981, Railway ballast survey - Wynbring to Immarna. *Mineral Resources Review, South Australia*, 153, p53-61.

Parker, A.J., 1978, Structural, stratigraphic and metamorphic geology of Lower Proterozoic rocks in the Cowell/Cleve district, eastern Eyre Peninsula. *University of Adelaide, PhD Thesis* (unpublished).

Parker, A.J. & Lemon, N.M., 1982, Reconstruction fo the Early Proterozoic stratigraphy of the Gawler Craton, South Australia. *Geological Society of Australia, Journal*, 29, p221-238.

Parker, A.J., 1990a, Precambrian provinces of South Australia - tectonic setting. In Hughes, F.E. (ed.). *Geology of the Mineral Deposits of Australia and Papua New Guinea*, Australian Institute of Mining and Metallurgy, Melbourne, p985-990.

Parker, A.J., 1990b, Gawler Craton and Stuart Shelf - regional geology and mineralisation. In Hughes, F.E. (ed.),*Geology of the Mineral Deposits of Australia and Papua New Guinea.* Australian Institute of Mining and Metallurgy, Melbourne, p999-1008.

Parker, A.J., 1993a, Chapter 2: Geological Framework. In Drexel, J.F., Preiss, W.V. & Parker, A.J., 1993, The geology of South Australia. Vol. 1. The Precambrian. *South Australian Geological Survey Bulletin*, 54.

Parker, A.J., 1993b, Chapter 4: Palaeoproterozoic. In Drexel, J.F., Preiss, W.V. & Parker, A.J., 1993, The geology of South Australia. Vol. 1. The Precambrian. *South Australian Geological Survey Bulletin*, 54.

Parkinson, W.D., 1983, *Introduction to Geomagnetism*. Scottish Academic Press, Edinburgh.

Pearce, J.A. & Cann, J.R., 1973, Tectonic setting of basic volcanic rocks determined using trace element analyses. *Earth and Planetary Science Letters*, 19, p290-300.

Pearce, J.A. & Gale, G.A., 1977, Identification of ore-deposition environment from trace element geochemistry of associated igneous host rocks. *Geological Society Special Publication*, 7, p14-24.

Pearce, J.A., 1982, Trace element characteristics of lavas from destructive plate boundaries. In Thorpe, R.S. (ed.), *Andesites*. Wiley, Chichester, p525-548.

Pearce, J.A, Harris, N.B.W. & Tindle, A.G., 1984, Trace element discrimination diagrams for the tectonic interpretation of granitic rocks. *Journal of Petrology*, 25, p956-983.

Pelton, C., 1987, A computer program for hill-shading digital topographic datasets. *Computers and Geosciences*, 13, p545-548.

Perchuk, L. L. & Lavrent'eva, I. V., 1981, Experimental investigation of exchange equilibria in the system cordierite-garnet-biotite. In Saxena, S. K. (ed.), *Kinetics and Equilibrium in Mineral Reactions*. Springer Verlag, p199-240.

Perkins D. III & Chipera S. J., 1985, Garnet - orthopyroxene - plagioclase - quartz barometry: refinement and application to the English River subprovince and the Minnesota River valley. *Contributions to Mineralogy and Petrology*, 89, p69-80.

Phillips, G.N., 1980, Water activity changes across an amphibolite-granulite facies transition, Broken Hill, Australia. *Contributions to Mineralogy and Petrology*, 75, p377-386.

Platt, J.P. & England, P.C., 1994, Convective removal of lithosphere beneath mountain belts; thermal and mechanical consequences. *American Journal of Science*, 294(3), p307-336.

Powell, R. & Holland, T.J.B., 1988, An internally consistent thermodynamic dataset with uncertainties and correlations: 3. Applications to geobarometry, worked examples and a computer program. *Journal of Metamorphic Geology*, 6, p173-204.

Powell, R. & Holland, T.J.B., 1994, Optimal geothermometry and geobarometry. *American Mineralogist*, 79, p120-133.

Powell, R. & Sandiford, M., 1988, Sapphirine and spinel phase relationships in the system FeO-MgO-Al_2O_3-SiO_2-TiO_2-O_2 in the presence of quartz and hypersthene. *Contributions to Mineralogy and Petrology,* 98:64-71.

Preiss, W.V., 1993, Chapter 6: Neoproterozoic. In Drexel, J.F., Preiss, W.V. & Parker, A.J., 1993, The geology of South Australia. Vol. 1. The Precambrian. *South Australian Geological Survey Bulletin,* 54.

Purvis, A.C., 1981, Pontifex & Associates: Mineralogical Report No. 3343. In Miller, G., Report on EL 616. *South Australian Department of Mines and Energy Open File Envelope, 3855,* unpublished.

Radke, F. & Fanning, M., 1986, Amdel Report G 6647/86. In Daly, S.J., 1987, Ooldea 2 - Well Completion Report, *Mines and Energy, South Australia. Report Book,* 87/48.

Raith, M., Karmakar, S. & Brown, M., 1997, Ultra-high temperature metamorphism and multistage decompressional evolution of sapphirine granulites from the Parm Hill ranges, southern India. *Journal of Metamorphic Geology*, 15(3), p379 - 400.

Rankin, L.R., Martin, A.R. & Parker, A.J., 1989, Early Proterozoic history of the Karari Fault Zone, northwest Gawler Craton, South Australia. *Australian Journal of Earth Sciences*, 36:123-133.

Rankin, L.R., Flint, R.B. & Fanning, C.M., 1990, Early Proterozoic Nuyts Volcanics of the western Gawler Craton. *South Australian Department of Mines and Energy. Report Book*, 90/60.

Rankin, L.R., Crooks, A.F., Benbow, M.C., Martin, A.R. & Fairclough, M.C., 1996, BARTON map sheet and explanatory notes, South Australia, Geological Survey, *Geological Atlas 1:250,000 series*, sheet SH/53-9.

Rivers, T., Martignole, J., Gower, C.F. & Davidson, A., 1989, New tectonic divisions of the Grenville Province, southeast Canadian Shield. *Tectonics*, 8(1), p63-84.

Rivers, T., van Gool, J.A.M. & Connely, J.N., 1993, Contrasting tectonic styles in the northern Grenville province: Implications for the dynamics of orogenic fronts. *Geology*, 21, p1127-1130.

Roberts, M.P. & Finger, F., 1997, Do U-Pb zircon ages from granulites reflect peak metamorphic conditions? *Geology*, 25(5), p319-322.

Rubin, J.F., Henry, C.D. & Price, J.G., 1993, The mobility of zirconium and other "immobile" elements during hydrothermal alteration. *Chemical Geology*, 110, p29-47.

Sadowski, G.R. & Bettencourt, J.S., 1996, Mesoproterozoic tectonic correlations between eastern Laurentia and the western border of the Amazon Craton. *Precambrian Research*, 76, p213-227.

Sandiford, M.A., 1985, The metamorphic evolution of granulites at Fyfe Hills: implications for Archaean crustal thickness in Enderby Land, Antarctica. *Journal of Metamorphic Geology*, 3, p155-178.

Sandiford, M. & Powell, R., 1986, Deep crustal metamorphism during continental extension: ancient and modern examples. *Earth and Planetary Science Letters,* 79:151-158.

Sandiford, M.A., Neill, F.B. & Powell, R., 1987, Metamorphic evolution of aluminous granulites from Labwor Hills, Uganda. *Contributions to Mineralogy and Petrology,* 95:217-225.

Sandiford, M.A. & Powell, R.P., 1988, Pyroxene exsolution in granulites from Fyfe Hills, Enderby Land, Antarctica: Evidence for 1000°C metamorphic temperatures in Archaean continental crust - Reply, *American Mineralogist*, 73:434-438.

Sandiford, M.A., 1989a, Horizontal structures in granulite terrains: A record of mountian building or mountain collapse? *Geology*, 17, p449-452.

Sandiford, M.A., 1989b, Secular trends in the thermal evolution of metamorphic terrains. *Earth and Planetary Science Letters*, 95(1-2), p85-96.

Sandiford, M.A. & Powell, R., 1990, Some isostatic and thermal consequences of the vertical strain geometry in convergent orogens. *Earth and Planetary Science Letters*, 98, p154-165.

Sandiford, M.A. & Powell. R., 1991, Some remarks on high-temperature--low-pressure metamorphism in convergent orogens. *Journal of Metamorphic Geology*, 9, p333-340.

Sandiford, M.A., Martin, N., Zhou, S. & Fraser, G., 1991, Mechanical consequences of granite emplacement during high-T, low-P metamrophism and the origin of "anticlockwise" PT paths. *Earth and Planetary Science Letters*, 107, p164-172.

Schaefer, B.F., 1998, Insights into Proterozoic tectonics from the Lincoln Batholith, South Australia. *Unpublished PhD Thesis*, University of Adelaide.

Schlinger, C.M., 1985, Magnetisation of lower crust and interpretation of regional magnetic anomalies: example from Lofoten adn Versterålen, Norway. *Journal of Geophysical Research*, 90(813), p11484-11504.

Schumacher, R., Schenk, V., Raase, P. & Vitanage, P.W., 1990, Granulite facies metamorphism of metabasic and intermediate rocks in the highland series of Sri Lanka. In Ashworth, J.R. & Brown, M., *High Temperature Metamorphism and Crustal Anatexis*, Unwin Hyman, London, p235-271.

Sharma, R.S. & Macrae, N.D., 1981, Paragenetic relations in gedrite-cordierite-staurolite-biotite-sillimanite-kyanite gneisses at Ajitpura, Rajasthan, India. *Contributions to Mineralogy and Petrology*, 78(1), p48-60.

Shaw, R.D., Wellman, P., Gunn, P., Whitaker, A.J. & Palfreyman, W.D., 1995, *Australian crustal elements*

based on distribution of geophysical domains; 1:5,000,000 scale map. Australian Geological Survey Organisation, Canberra.

Sheraton, J.W., Offe, L.A., Tingey, R.J. & Ellis, D.J., 1980, Enderby Land, Antarctica; an unusual Precambrian high-grade metamorphic terrane. *Journal of the Geological Society of Australia*, 27, p1-18.

Shulters, J.C. & Bohlen, S.R., 1989, The stability of hercynite and hercynite-gahnite spinels in corundum- or quartz-bearing assemblages, *Journal of Petrology*, 30:1017-1031.

Skilbrei, J.R., Skyseth, T. & Olesen, O., 1991, Petrophysical data and opaque mineralogy of high-grade and retrogressed lithologies: implications for the interpretation of aeromagnetic anomalies in Northern Verstranden, Central Norway. *Tectonophysics*, 192, p21-31.

Söderlund, U., 1996, Conventional U-Pb dating versus single-grain Pb evaporation dating of complex zircons from a pegmatite in the high grade gneisses of southwestern Sweden. *Lithos*, 38, p93-105.

Sonder, L.J., England, P.C., Wernicke, B.P. & Christiansen, R.L., 1987, A physical model for Cenozoic extension of western North America. In Coward, M.P., Dewey, J.F. & Hancock, P.L., *Continental Extension Tectonics*, Geological Society of London Special Publication 28, p187-201.

Spector, A., 1968, Spectral analysis of aeromagnetic data. *Unpublished PhD Thesis*, University of Toronto, Canada.

Spector, A. & Grant, F.S., 1970, Statistical methods for interpreting aeromagnetic data. *Geophysics*, 35, p293-302.

Spector, A. & Grant, F.S., 1975, Comments on "Two-dimensional power spectral analysis of aeromagnetic fields". *Geophysical Prospecting*, 23, p391.

Spector, A., 1985, Comment on "Statistical models for interpreting aeromagnetic data by A. Spector and F.S. Grant". *Geophysics*, 50, p2278.

Stewart, K.P., 1994, High temperature felsic volcanism and the role of mantle magmas in Proterozoic crustal growth: The Gawler Range Volcanic Province. *Unpublished PhD Thesis*, University of Adelaide.

Stewart, K.P., 1997, A large, mantle-derived igneous province dominated by felsic magmatic rocks. In *Seventh Annual V.M. Goldschmidt Conference Abstracts*, p197, L.P.I. Contribution No. 921, Lunar & Planetary Institute, Houston.

Tarlowski, C., Gunn, P.J. & Mackey, T., 1997, Enhancements of the magnetic map of Australia. *AGSO Journal of Australian Geology and Geophysics*, 17(2), p77-82.

Tate, R., 1879, The natural history of the country around the Head of the Great Australian Bight. *Philosophical Society of South Australia. Transactions*, 2, p94-128.

Taylor, M.J., 1987, *The metamorphism, petrology and geochemistry of the Ooldea 2 drill core and the Lake Ifould area*. Unpublished Honours Thesis, University of Adelaide.

Teskey, D.J. & Hood, P.J., 1991, The Canadian aeromagnetic database: Evolution and applications to the definition of major crustal boundaries. *Tectonophysics*, 192, p41-51.

Thomson, B.P., 1980, Geological map of South Australia. *South Australian Geological Survey. Maps of South Australia Series, 1:1,000,000.*

Toft, P.B., Scowen, P.A.H., Arkani-Hamed, J. & Francis, D., 1993, Demagnetisation by hydration in deep-crustal rocks in the Grenville Province of Quebec, Canada: Implications for magnetic anomalies of continental collision zones. *Geology*, 21, p999-1002.

Tracy, R.J. & McLellan, E.L., 1985, A natural example of the kinetic controls of compositional and textural equilibration. In Thompson, A.B. & Rubie, D.C. (eds.), *Metamorphic Reactions: Kinetics, Textures and Deformation*, Springer, New York.

Unrug, R. and 67 others, 1997, *The Geodynamic Map of Gondwana Supercontinent Assembly*, 1:10 million map, Bureau de Recherches Geologiques et Minieres, Orleans.

Unrug, R., 1997, Rodinia to Gondwana: The geodynamic map of Gondwana supercontinent assembly. *GSA Today*, 7(1), p1-6.

Urquhart, W.E.S., 1989, Field examples of controls on magnetite content. *Exploration Geophysics*, 20, p93-97.

Veevers, J.J., 1986, Breakup of Australia and Antarctica estimated as mid-Cretaceous (95±5 Ma) from magnetic and siesmic data at the continental margin. *Earth and Planetary Science Letters*, 77, p91-99.

Veevers, J.J. & Eittreim, S.L., 1988, Reconstruction of Antarctica and Australia at breakup (95±5 Ma) and before rifting (160 Ma). *Australian Journal of Earth Sciences*, 35, p355-362.

Walter, M.R., Veevers, J.J., Calver, C.R. & Grey, K., 1995, Neoproterozoic stratigraphy of the Centralian Superbasin, Australia. *Precambrian Research*, 73, p173-195.

Warren, R.G. & Hensen, B.J., 1989, The PT evolution of the Proterozoic Arunta Block, central Australia, and implications for tectonic evolution. In Daly, J.S., Cliff, R.A. & Yardley, B.W.D., The evolution of metamorphic belts. *Geological Society Special Publication*, 43, p349-355.

Wasilewski, P. & Warner, R.D., 1988, Magnetic petrology of deep crustla rocks - Ivrea Zone, Italy. *Earth and Planetary Science Letters*, 87, p347-361.

Waters, D.J., 1991, Hercynite-quartz granulites: phase relations, and implications for crustal processes. *European Journal of Mineralogy*, 3, p367-386.

Watson, E.B. & Harrison, T.M., 1983, Zircon saturation revisited: temperature and compositional effects in a variety of crustal magma types. *Earth and Planetary Science Letters*, 26, p207-221.

Webb, A.W. & Thomson, B.P., 1977, Archaean basement rocks in the Gawler Craton, South Australia. *Search*, 8, p34-36.

Webb, A.W., Thomson, B.P., Blissett, A.H., Daly, S.J., Flint, R.B. & Parker, A.J., 1986, Geochronology of the Gawler Craton, South Australia, *Australian Journal of Earth Sciences*, 33:119-143.

Wellman, P., 1988, Development of the Australian Proterozoic crust as inferred from gravity and magnetic anomalies. *Precambrian Research*, 40/41, p89-100.

Whalen, J.B., Currie, K.L. & Chappell, B.W., 1987, A-type granites: geochemical characteristics, discrimination and petrogenesis. *Contributions to Mineralogy and Petrology*, 95, p407-419.

Whitten, G.F., 1960, Report on geological reconnaissance of the TARCOOLA four-mile sheet and eleven adjoining one-mile sheets. *South Australia, Department of Mines Report Book,* 50/162.

Willcox, J.B. & Stagg, H.M.J., 1990, Australia's southern margin: a product of oblique extension. *Tectonophysics*, 173, p269-281.

Williams, I.S. & Claesson, S., 1987, Isotopic evidence for the Precambrian provenance and Caledonian metamorphism of high grade paragneisses from the Seve Nappes, Scandinavian Caledonides; 2, Ion microprobe zircon U-Th-Pb. *Contributions to Mineralogy and Petrology*, 97, p205-217.

Winchester, J.A. & Floyd, P.A., 1976, Geochemical magma type discrimination; application to altered and metamorphosed basic igneous rocks. *Earth and Planetary Science Letters*, 28, p459-469.

Woodcock, N.H. & Fischer, M., 1986, Strike-slip duplexes. *Journal of Structural Geology*, 8(7), p725-735.

Xu, G., 1993, Phase relationships in metapelitic rocks with applications to the metamorphism in the contact aureole of the Stawell Granite, western Victoria, Australia. *Unpublished PhD Thesis*, University of Melbourne.

Xu, G., Will, T.M. & Powell, R., 1994, A calculated petrogenetic grid for the system K_2O-FeO-MgO-Al_2O_3-SiO_2-H_2O, with particular reference to contact-metamorphosed pelites. *Journal of Metamorphic Geology*, 12, p99-119.

Young, E.D., 1989, Petrology of biotite-cordierite-garnet gneiss of the McCullough Tange, Nevada, II. P-T-a(H_2O) path and growth of cordierite during late stages of low-P granulite-grade metamorphism. *Journal of Petrology*, 30, p61-78.

Zang, W., 1995, Early Neoproterozoic seqence stratigraphy and acritarch biostratigraphy, eastern Officer Basin, South Australia. *Precambrian Research*, 74, p119-175.

Zietz, I., 1980, Exploration of the continental crust using aeromagnetic data. In *Continental Tectonics*, Studies in Geophysics, National Academy of Sciences, Washington D.C.

Appendix 1

LIST OF SAMPLES

Table A1.1 List of field samples with brief sample descriptions.

#	Easting	Northing	Locality	Subdomain/SZ	Rock type	Mineralogy	Age	Work Done	Mag.Sus	K'matics
1	499926	6585911	South Lake	Wilgena	Layered gneiss, spectacularly folded	?opx-cd-bi-q-f	?mid-Archaean basement		20	
2	499926	6585911	South Lake	Wilgena	Felsic migmatite	?gt-cd-bi-q-f	?mid-Archaean basement		0	
3	499926	6585911	South Lake	Wilgena	Sheared amphibolite (large dyke)		?Sleafordian		400	
4	499926	6585911	South Lake	Wilgena	Sheared amphibolite (small dyke)		?Sleafordian		350*	
5	495922	6577773	S of South Lake	Wilgena	Felsic mylonite (slaty)		1585Ma?		20*	
6	495922	6577773	S of South Lake	Wilgena	Felsic mylonite with porphyroclasts		1585Ma?		0	
7	495922	6577773	S of South Lake	Wilgena	Undeformedporphyritic rhyolite		1585Ma GRV		1300*	
8	495922	6577773	S of South Lake	Wilgena	Sheared amphibolite		?		150*	
9	390993	6651040	Mulgathing	Coorabie SZ	Mylonite		Pal. Prot?		200	
10	356781	6644743	2km S of Mt Christie	Christie	Mafic gneiss	?gt-opx-plag-q	Archaean		80*	
11	356781	6644743	2km S of Mt Christie	Christie	Mafic gneiss	gt-opx-plag-q	Archaean	Petrology, P/T work	50*	
12	356781	6644743	2km S of Mt Christie	Christie	Mafic gneiss	?gt-opx-plag-q	Archaean		20*	
13	356781	6644743	2km S of Mt Christie	Christie	Intermediate gneiss	?opx-bi	Archaean		70*	
14	365102	6630650	Mulgathing	Coorabie SZ	D1 mylonite		?		0	
15	365102	6630650	Mulgathing	Coorabie SZ	?D1 sheared mafic		?		80*	
16	365102	6630650	Mulgathing	Coorabie SZ	D2 mylonite, strongly lineated		?		0	
17	231612	6455793	Cape Adieu	Fowler	Amphibolite + semipelitic gneiss	gt-hbl-plag-q, gt-sill-plag-kf-q	1540-1490Ma	Petrology, P/T work	800*	
18	231612	6455793	Cape Adieu	Fowler	mylonite	hbl-gt-plag-q-bi	1540-1490Ma	Petrology, P/T work	1300	
19	231612	6455793	Cape Adieu	Fowler	Amphibolite	gt-hbl-plag-q	1540-1490Ma	Petrology, P/T work	2800	
20	231612	6455793	Cape Adieu	Fowler	Amphibolite	gt-hbl-plag-q	1540-1490Ma	Petrology, P/T work	2800	
21	231612	6455793	Cape Adieu	Fowler	Amphibolite	gt-hbl-plag-q	1540-1490Ma	Petrology, P/T work	950	
22	231612	6455793	Cape Adieu	Coorabie SZ	Ultramylonite	bi-gt-hbl-plag-q	?1100-1200Ma	Petrology, P/T work	2300	
23	231612	6455793	Cape Adieu	Coorabie SZ	Ultramylonite	bi-gt-hbl-plag-q	?1100-1200Ma	Petrology, P/T work	100*	
24	231612	6455793	Cape Adieu	Coorabie SZ	Mylonitised pelitic gneiss	gt-sill-bi-mus-plag-kf-q	?1100-1200Ma	Petrology, P/T work	80	
25	276547	6519787	Chundie Swamp	Nuyts	c gr ?Hiltaba granite		1580Ma?		2500	
26	276168	6521825	Chundie Swamp	Nuyts	m gr ?Hiltaba granite		1580Ma?		20	
27	229910	6562120	Lake Tallacootra	Tallacootra SZ	Mylonitised mafic		?1100-1200Ma		30*	
28	229910	6562120	Lake Tallacootra	Tallacootra SZ	Mylonitic gneiss	q-f-bi	?1100-1200Ma	Petrology, kinematics	5	East up
29	229910	6562120	Lake Tallacootra	Tallacootra SZ	Calc-silicate	?gt-cpx	?Archaean		27*	
30	230052	6562452	Lake Tallacootra	Tallacootra SZ	Mylonitised mafic		?1100-1200Ma	Kinematics	30*	East up
31	230052	6562452	Lake Tallacootra	Tallacootra SZ	?calc-silicate		?1100-1200Ma		5	
32	229906	6563076	Lake Tallacootra	Tallacootra SZ	Mafic gneiss, ?opx bearing		?1100-1200Ma		35	
33	230300	6563650	Lake Tallacootra	Tallacootra SZ	Mafic gneiss		?1100-1200Ma		40*	
34	230300	6563650	Lake Tallacootra	Tallacootra SZ	Mafic gneiss		?1100-1200Ma		60*	
35	230300	6563650	Lake Tallacootra	Tallacootra SZ	Mafic gneiss		?1100-1200Ma		40*	
36	230300	6563650	Lake Tallacootra	Tallacootra SZ	Felsic mylonite from hinge of fold		?1100-1200Ma	Kinematics	0	East up
37	230300	6563650	Lake Tallacootra	Tallacootra SZ	Amphibolite	cpx-hbl-plag-q-ep-sphene	?1100-1200Ma	Petrology, kinematics	35*	East up

38	230342	6563773	Lake Tallacootra	Tallacootra SZ	Mylonitic schist	gt-bi-mus + ky-st-mus-bi schist	?1100-1200Ma	Petrology, P/T work	25	
39	230342	6563773	Lake Tallacootra	Tallacootra SZ	Mylonitic schist	gt-bi-mus + ky-st-mus-bi schist	?1100-1200Ma	Petrology, P/T work	15	
40	231474	6564772	Lake Tallacootra	Tallacootra SZ	Felsic mylonite		?1100-1200Ma		5	
41	231474	6564772	Lake Tallacootra	Tallacootra SZ	Mylonitic gneiss	q-f-bi	?1100-1200Ma	Petrology, kinematics	<5	East up
42	231474	6564772	Lake Tallacootra	Tallacootra SZ	Mylonitic gneiss	q-f-bi-gt	?1100-1200Ma	Petrology, kinematics	12	East up
43	231474	6564772	Lake Tallacootra	Tallacootra SZ	Retrogressed mafic granulite	cpx-hbl-gt-ep-plag-q-sphene	?1100-1200Ma	Petrology	36*	
44	231474	6564772	Lake Tallacootra	Tallacootra SZ	Retrogressed mafic granulite	cpx-hbl-gt-ep-plag-q-sphene	?1100-1200Ma	Petrology	33	
45	232570	6565098	Lake Tallacootra	Tallacootra SZ	Mylonite	q-f-bi	?1100-1200Ma	Petrology, kinematics	5	East up
46	232570	6565098	Lake Tallacootra	Tallacootra SZ	Syn-kinematic aplite	q-kf-plag-mus-gt	1175Ma	Petrology & Geochronology	<5	
47	232570	6565098	Lake Tallacootra	Tallacootra SZ	Retrogressed mafic granulite	cpx-cumm-hbl-gt-ep-plag-q	?1100-1200Ma	Petrology, P/T work	40*	
48	232570	6565098	Lake Tallacootra	Tallacootra SZ	Retrogressed mafic granulite	hbl-plag-q-sphene-ep	?1100-1200Ma	Petrology, P/T work	30*	
49	232570	6565098	Lake Tallacootra	Tallacootra SZ	Calc-silicate	cpx-calcite-hbl-gt-ep-q-plag-sph	?Archaean	Petrology, P/T work	15	
50	236168	6567859	E of Lake Tallacootra	Fowler	Retrogressed mafic granulites	cpx-opx-hbl-plag-q	Pal. Prot?	Petrology, P/T work	20-30*	
51	223918	6596242	N of Lake Ifould	Christie	Paragneiss	gt-bi-cd-sill-q-kf-plag-rutile	Archaean	Petrology	15*	
52	223918	6596242	N of Lake Ifould	Christie	Migmatitc paragneiss	gt-bi-cd-sill-q-kf-plag-rutile	Archaean	Petrology, P/T work	22	
53	223918	6596242	N of Lake Ifould	Christie	Pegmatite in shear zones	kf-mus-bi-q	?		<5	
54	223918	6596242	N of Lake Ifould	Christie	Pegmatite	kf-mus-bi-plag-q	2428 Ma	Geochronology	8	
55	223918	6596242	N of Lake Ifould	Christie	Migmatitic paragneiss	gt-bi-cd-sill-q-kf-plag-rutile	Archaean	Petrology, P/T work	19*	
56	214777	6594977	N of Lake Ifould	Christie	Partially retrogressed paragneiss	gt-bi-cd-sill-q-kf-plag-rutile	Archaean	Pterology	18*	
57	217006	6592347	N of Lake Ifould	Christie	Partially retrogressed paragneiss	gt-bi-cd-sill-q-kf-plag-rutile	Archaean	Petrology	16	
58	226137	6586169	Lake Ifould	Christie	Calc-silicate	cpx-hbl-ep-plag-q-sphene-gt	?Archaean	Petrology	40	
59	226876	6584711	Lake Ifould	Tallacootra SZ	Mylonite	q-f-bi-mus-ep	Pal. Prot?	Petrology, Kinematics	16*	East up
60	226892	6582401	Lake Ifould	Christie	Mafic dyke	hbl-plag-bi±q	Pal. Prot?	Petrology	32*	
61	225524	6583072	Lake Ifould	Christie	Foliated granite	q-kf-plag-bi	1677Ma	Geochronology	1000	
62	225477	6589493	Lake Ifould	Tallacootra SZ	Retrogressed gabbro	trem-cpx-plag-q	Pal. Prot?	Petrology	4000	
63	224736	6585602	Lake Ifould	Tallacootra SZ	Retrogressed granulite	bi-cd-plag-kf-q-chl	Archaean	Petrology	8*	
64	224079	6581710	Lake Ifould	Christie	Pegmatite	kf-q-bi	1666Ma	Geochronology	<5	
65	221683	6577598	Lake Ifould	Tallacootra SZ	Mylonitic granite gneiss	q-f-bi	Pal. Prot?	Petrology, Kinematics	7	East up
66	221683	6577598	Lake Ifould	Tallacootra SZ	Pelitic schist	gt-bi-mus-st-ky-sill-q-plag-kf	Mes. Prot?	Petrology, P/T work	12	
67	221092	6577533	Lake Ifould	Tallacootra SZ	Mafic schist	bi-hbl-plag-q-ep	Mes. Prot?	Petrology, P/T work	30*	
68	309381	6446192	Pt Sinclair	Nuyts	S-type granite	q-kf-plag-gt-bi-mus	Mes. Prot	Petrology	15	
69	309381	6446192	Pt Sinclair	Nuyts	Granite (enclave in WGC68)	q-kf-bi-mus-hbl	Mes. Prot	Petrology	36	
70	387687	6634747	Inglis R.H.	Nuyts	Granite	q-f-bi-magnetite	~1690Ma	Petrology	3600	
71	387756	6629512	SW of Inglis R.H.	Nuyts	Granite	q-f-bi	~1690Ma	-	2000	
72	377000	6634350	Mulgathing	Coorabie SZ	Felsic mylonite	q-f-sericite	?1150Ma	Petrology, kinematics	10*	W up, L=steep
73	377000	6634350	Mulgathing	Coorabie SZ	Felsic mylonite	q-f-sericite	?1150Ma	Petrology, kinematics	15*	W up, L=steep
74	377000	6634350	Mulgathing	Coorabie SZ	Brecciated ultramylonite	q-f-sericite....	?1150Ma	Petrology, kinematics	15*	W up, L=steep
75	377000	6634350	Mulgathing	Coorabie SZ	Felsic mylonite	q-f-sericite	?1150Ma	Petrology, kinematics	25*	W up, L=steep
76	377000	6634350	Mulgathing	Coorabie SZ	Felsic mylonite	q-f-sericite	?1150Ma	Petrology, kinematics	5	
77	377000	6634350	Mulgathing	Coorabie SZ	bag of (ultra)mylonites from float		?1150Ma	Show off!	20-40*	
78	356781	6644743	2km S of Mt Christie	Christie	Mafic granulite	opx-cpx-plag-q-bi	Archaean	Petrology, P/T work	40*	
79	356781	6644743	2km S of Mt Christie	Christie	Pelitic granulite	gt-cd-sill-sp-plag-kf-bi-q	Archaean	Petrology, P/T work	25*	
80	356781	6644743	2km S of Mt Christie	Christie	Granulite	gt-bi-kf-plag-q	Archaean	Petrology, P/T work	15*	
81	360200	6619150	Wynbring Rocks	Christie	Granite	q-kf-plag-bi	1672Ma	Geochronology	450	
82	325294	6437072	Pt Bell	Nuyts	Foliated granite	q-kf-plag-mus-bi-gt	Mes. Prot?	Petrology	8	
83	325294	6437072	Pt Bell	Nuyts	Weakly foliated granite	q-kf-plag-mus-bi-gt	Mes. Prot?	Petrology, kinematics	5	sinistral
84	323666	6437164	Pt Bell	Nuyts	m gr, q-kf-mu-bi-gt granite	q-kf-plag-mus-bi-gt	Mes. Prot?	-	220	
85	323666	6437164	Pt Bell	Nuyts	m gr, q-kf-mu-bi-gt granite	q-kf-plag-mus-bi-gt	Mes. Prot?	Petrology, kinematics	150	sinistral
86	323666	6437164	Pt Bell	Nuyts	m gr, q-kf-mu-bi-gt granite	q-kf-plag-mus-bi-gt	Mes. Prot?	Petrology, kinematics	150	sinistral
87	309381	6446192	Pt Sinclair	Nuyts	Layered gneiss (magic carpet xenolith)	bi-mus-gt-q-kf	?	Petrology	180	

88	309381	6446192	Pt Sinclair	Nuyts	Layered gneiss (xenolith)	gt-bi-mus-kf-q	?	Petrology	170	
89	232208	6567450	Lake Tallacootra	Tallacootra SZ	Retrogressed amphibolite	hbl-plag-ep-q-bi	?1100-1200Ma	Petrology, P/T work	2000	
90	232400	6568175	Lake Tallacootra	Tallacootra SZ	Retrogressed amphibolite	hbl-plag-ep-q-bi	?1100-1200Ma	Petrology, P/T work	40*	
91	230872	6563695	Lake Tallacootra	Tallacootra SZ	Retrogressed mafic granulite	cpx-hbl-plag-q-ep-cumm	?1100-1200Ma	Petrology, P/T work	20*	
92	229900	6562150	Lake Tallacootra	Tallacootra SZ	Mafic		?1100-1200Ma		32*	
93	229900	6562150	Lake Tallacootra	Tallacootra SZ	Retrogressed mafic granulite	cpx-gt-ep-plag-q±hbl	?Archaean	Petrology, P/T work	22*	
94	230380	6563627	Lake Tallacootra	Tallacootra SZ	Semipelitic schist	gt-bi-plag-q-kf	?1100-1200Ma	Petrology, P/T work	<5	
95	230380	6563627	Lake Tallacootra	Tallacootra SZ	Pelitic schist	bi-mus-ky-plag-kf	?1100-1200Ma	Petrology, P/T work	15	
96	230380	6563627	Lake Tallacootra	Tallacootra SZ	Pelitic schist	gt-bi-mus-q-f	?1100-1200Ma	Petrology, P/T work	10*	
97	230380	6563627	Lake Tallacootra	Tallacootra SZ	Pelitic schist		?1100-1200Ma		10*	
98	230380	6563627	Lake Tallacootra	Tallacootra SZ	Pelitic schist	gt-bi-mus-q-plag-kf	?1100-1200Ma	Petrology, P/T work	16*	
99	230814	6564567	Lake Tallacootra	Tallacootra SZ	Retrogressed mafic granulite	cpx-hbl-plag-q-sphene	?Archaean	Petrology, P/T work	40	
100	230814	6564567	Lake Tallacootra	Tallacootra SZ	Retrogressed mafic granulite		?Archaean		10*	
101	216451	6574985	Lake Ifould	Tallacootra SZ	Reworked pelitic granulite	gt-cd-sill-plag-kf-q, oa-st-bi-ky-q	?Archaean	Petrology, P/T work	58	
102	216451	6574985	Lake Ifould	Tallacootra SZ	Reworked pelitic granulite	gt-cd-sill-plag-kf-q, oa-st-bi-ky-q-sp	?Archaean	Petrology, P/T work	20	
103	216710	6575252	Lake Ifould	Tallacootra SZ	Reworked pelitic granulite	gt-cd-sill-plag-kf-q, oa-st-bi-ky-q-sp	?Archaean	Petrology, P/T work	15	
104	216832	6575523	Lake Ifould	Tallacootra SZ	Mafic gneiss	hbl-plag-q	?1100-1200Ma	Petrology, P/T work	25	
105	219495	6575939	Lake Ifould	Tallacootra SZ	V. fine grained dolerite	ol-plag-px-opaques	?1100-1200Ma	Petrology, P/T work	25*	
106	219495	6575939	Lake Ifould	Tallacootra SZ	Layered mylonite	bi-ep-plag-q, kf-plag-bi-q	?1100-1200Ma	Petrology	300*	
107	222931	6579203	Lake Ifould	Tallacootra SZ	Reworked pelitic granulite	gt-cd-sill-plag-kf-q, oa-st-bi-ky-q-sp	?Archaean	Petrology, P/T work	10*	
108	222931	6579203	Lake Ifould	Tallacootra SZ	V. fine grained dolerite	ol-plag-px-opaques	?1100-1200Ma	Petrology	420	
109	222288	6579189	Lake Ifould	Tallacootra SZ	Mafic boudin	cpx-hbl-plag-q	?1100-1200Ma	Petrology, P/T work	27	
110	221731	6577565	Lake Ifould	Tallacootra SZ	Mylonitic schist	gt-bi-plag-kf-ky-q	?1100-1200Ma	Petrology, kinematics	10*	East up
111	221731	6577565	Lake Ifould	Tallacootra SZ	Mylonitic schist	bi-plag-mus-q	?1100-1200Ma	Petrology, P/T work	10*	
112	223066	6579842	Lake Ifould	Tallacootra SZ	Retrogressed amphibolite	hbl-bi-ep-plag-q	?1100-1200Ma	Petrology, P/T work		
113	221731	6577565	Lake Ifould	Tallacootra SZ	Retrogressed mafic granulite	gt-hbl-cumm-plag-q-bi	?Archaean	Petrology, P/T work	50	
114	221731	6577565	Lake Ifould	Tallacootra SZ	Retrogressed mafic granulite	opx-cpx-hbl-ep-plag-q	?Archaean	Petrology, P/T work	60	
115	238120	6565926	Lake Tallacootra	Fowler	Felsic mylonite	q-kf-hem?	?1100-1200Ma	kinematics	600	?West up
116	238120	6565926	Lake Tallacootra	Fowler	Felsic mylonite	q-kf-hem?	?1100-1200Ma	kinematics	60	West up
117	238120	6565926	Lake Tallacootra	Fowler	Amphibolite	hbl-plag-q	?1100-1200Ma	Petrology	250*	
118	376976	6634095	Mulgathing	Coorabie SZ	Granitic protomylonite	q-kf-hem	?1150Ma	kinematics	20	?
119	376976	6634095	Mulgathing	Coorabie SZ	Mylonite	kf-q-hem	?1150Ma	kinematics	<5	W up, L=down dip
120	376976	6634095	Mulgathing	Coorabie SZ	Ultramylonite	kf-q-hem	?1150Ma	kinematics	70*	W up, dextral
121	376976	6634095	Mulgathing	Coorabie SZ	Mafic mylonite	bi-hbl-plag	?1150Ma	kinematics, petrology	<5	?
122	376976	6634095	Mulgathing	Coorabie SZ	Ultramylonite	q-kf-hem	?1150Ma	kinematics	75	W up, L=down dip
123	376976	6634095	Mulgathing	Coorabie SZ	Mafic mylonite	hbl-ep-plag-q-kf	?1150Ma	kinematics, petrology	250	W up, L=down dip
124	376976	6634095	Mulgathing	Coorabie SZ	Ultramylonite	q-kf-hem	?1150Ma	kinematics	55*	W up, L=steep
125	376976	6634095	Mulgathing	Coorabie SZ	Ultramylonite	q-kf-hem	?1150Ma	kinematics	180	W up, L=steep
126	373772	6636670	Mulgathing	Coorabie SZ	Mylonite		?1150Ma	kinematics	0	
127	371214	6629343	Mulgathing	Coorabie SZ	Mafic boudin	hbl-plag-sericite	?1150Ma	Petrology	30*	
128	371214	6629343	Mulgathing	Coorabie SZ	Mylonite	q-kf-bi-sericite	?1150Ma	kinematics		W up
129	371214	6629343	Mulgathing	Coorabie SZ	Mylonite		?1150Ma	kinematics	0	W up, dextral
130	371214	6629343	Mulgathing	Coorabie SZ	Mylonite	q-f-bi-sericite	?1150Ma	Petrology	<5	
131	373348	6624999	Mulgathing	Coorabie SZ	Breccia		?1150Ma		<5	
132	373533	6624916	Mulgathing	Coorabie SZ	Brecciated granite w. ?malachite		?1150Ma		15*	
133	373533	6624916	Mulgathing	Coorabie SZ	Silicified mylonite		?1150Ma		25*	

134	373533	6624916	Mulgathing	Coorabie SZ	Altered granite		?1150Ma		150*	
135	397000	6666350	Mulgathing	Coorabie SZ	Gneiss	q-f-bi	?1150Ma		600*	
136	400969	6671233	Mulgathing	Coorabie SZ	Mylonite	q-kf-bi	?1150Ma	kinematics	5*	W up, dextral
137	400969	6671233	Mulgathing	Coorabie SZ	Mafic boudin	hbl-plag	?1150Ma	Petrology, P/T work	200*	
138	402480	6671620	Mulgathing	Coorabie SZ	Kaolinised mylonite		?1150Ma		0	
139	400411	6670876	Mulgathing	Coorabie SZ	Mylonite	q-kf	?1150Ma	kinematics	<5	?
140	400411	6670876	Mulgathing	Coorabie SZ	Mylonite	q-kf	?1150Ma	kinematics	<5	?
141	367393	6615706	Mulgathing	Coorabie SZ	Silicified mylonite	q-kf-plag-Fe alteration	?1150Ma	kinematics	7	W up, dextral
142	367393	6615706	Mulgathing	Coorabie SZ	Brecciated mylonite		?1150Ma		10*	
143	367393	6615706	Mulgathing	Coorabie SZ	Mylonite		?1150Ma		20*	
144	367393	6615706	Mulgathing	Coorabie SZ	Fractured mylonite		?1150Ma		20*	
145	357495	6613553	Wynbring S	Christie	?Garnet		?		12*	
146	357495	6613553	Wynbring S	Coorabie SZ	Mylonite	q-kf-bi	?1150Ma	kinematics	0	Dextral
147	357495	6613553	Wynbring S	Christie	Breccia		?1150Ma		5*	
148	327054	6594867	White Gin RH	Fowler	Granite	q-kf-plag-bi	1690Ma	Geochronology	400	
149	318367	6594492	Barton S	Fowler	f-m gr granite		?		10	
150	314856	6595722	Barton S	Fowler	Mafic gneiss		?		10*	
151	314244	6595587	Barton S	Fowler	Granite gneiss		?		<5	
152	313263	6595267	Barton S	Colona SZ	Mylonite	q-kf-plag-bi	?1150Ma	kinematics	<5	W up, dextral
153	313263	6595267	Barton S	Colona SZ	Mylonite	q-kf-plag-bi	?1150Ma	kinematics	40*	W up, L=steep
154	313263	6595267	Barton S	Colona SZ	Mylonite	bi-q-f	?1150Ma	kinematics		W up, L=down dip
155	311376	6595654	Barton S	Colona SZ	Mylonite	q-kf-plag-bi-chl	?1150Ma	kinematics	<5	W up, L=down dip
156	311376	6595654	Barton S	Colona SZ	Mafic gneiss	hbl-plag-q	?1150Ma	Petrology	30	
157	311376	6595654	Barton S	Colona SZ	Mylonitic schist		?1150Ma			
158	306478	6595267	Barton S	Colona SZ	Mylonite		?1150Ma		0	
159	306478	6595267	Barton S	Colona SZ	Granite gneiss		?1150Ma		<5	
160	306387	6594834	Barton S	Colona SZ	Felsic gneiss	q-kf-plag-bi	?1150Ma	kinematics	0	?
161	283452	6613497	Barton S	Christie	Biotite schist	bi-q-plag-kf-ep	?Archaean	kinematics, PT work	27	W up
162	283452	6613497	Barton S	Christie	Granite gneiss	q-f-bi	?		0	
163	286130	6612680	Barton S	Christie	Mylonite	q-kf-plag-bi-ep	?	kinematics	15*	W up
164	286130	6612680	Barton S	Christie	Mylonite	q-bi-kf-ep-chl	?	kinematics	7	W up
165	286130	6612680	Barton S	Christie	Granite gneiss	q-kf-bi-mus-plag	1675Ma	Geochronology	410	
166	222800	6578000	Lake Ifould	Christie	Mafic gneiss	hbl-bi-plag-q	?	petrology	40*	
167	222222	6577823	Lake Ifould	Christie	Mafic/calc-silicate gneiss	hbl-ep-cpx-sphene-plag-q	?	petrology, PT work	35*	
168	222222	6577823	Lake Ifould	Christie	Mafic/calc-silicate gneiss	hbl-ep-cpx-sphene-plag-q	?	petrology, PT work	42*	
169	222336	6577911	Lake Ifould	Christie	Pelitic schist	gt-bi-plag-kf-q	?	petrology, PT work, kinematics	20	W up
170	222336	6577911	Lake Ifould	Christie	Pelitic schist	gt-bi-mus-plag-q	?	petrology, PT work, kinematics	22*	W up
171	222336	6577911	Lake Ifould	Christie	Pelitic schist	gt-bi-plag-q-tour	?	petrology, PT work, kinematics	10*	?
172	222336	6577911	Lake Ifould	Christie	Mylonitic pelitic schist	gt-bi-plag-kf-q-tour	?	petrology, PT work, kinematics	18*	?
173	222336	6577911	Lake Ifould	Christie	Pelitic schist		?		5*	
174	222336	6577911	Lake Ifould	Christie	Pelitic schist	gt-st-bi-plag-q	?	petrology, PT work, kinematics	15*	?
176	263343	6469912	Boree Rocks	Nuyts	Granite		?		2250	
177	246805	6463700	Coorabie Quarry	Nuyts	Granodiorite	q-plag-bi-opaque	?	petrology	5000	
178	224972	6596338	Lake Ifould N	Christie	Paragneiss	gt-cd-sill-bi-kf-q	Archaean	petrology	17	
179	224972	6596338	Lake Ifould N	Christie	Paragneiss		Archaean		30	
180	226801	6585726	Lake Ifould	Christie	Pegmatite		?		25	
181	226801	6585726	Lake Ifould	Christie	Mafic schist	bi-ep-plag-q	Mes. Prot	kinematics, petrology	2100	W up
182	222336	6577911	Lake Ifould	Christie	Retrogressed mafic granulite	gt-plag-hbl-cumm-bi-q	Archaean	petrology, PT work	40*	
183	387343	6473355	OTC hill	Nuyts	Felsic mylonite	q-kf-gt-hem	Mes. Prot	kinematics	<5	dextral
184	387343	6473355	OTC hill	Nuyts	Granite	q-kf-mag-plag	Mes. Prot	petrology	250	
185	336811	6479618	Munjeela RH	Nuyts	S-type granite	q-kf-plag-mus-bi-gt	?		23	
186	355522	6614747	Wynbring S	Christie	Gabbro	cpx-plag	?	Petrology	12*	
187	355522	6614747	Wynbring S	Christie	Retrogressed gabbro	ep-hbl-cpx-plag	?	Petrology	28*	
188	355522	6614747	Wynbring S	Christie	Leucogranite	q-kf-cpx	?	Petrology	17*	
189	356030	6613993	Wynbring S	Christie	Mafic	cpx-plag-ep	?	Petrology	38*	
190	338889	6629225	Wynbring N	Christie	granite		?		240	
192	246805	6463700	Coorabie Quarry	Nuyts	Granodiorite		~1540Ma?	Geochronology		
193	282444	6559947	Remote outcrop	Fowler	Granite gneiss		1566Ma	geochron	2000-3000	
195	231029	6564406	Lake Tallacootra	Tallacootra SZ	m gr q-plag-bi granitoid mylonite		?			
196	231029	6564406	Lake Tallacootra	Tallacootra SZ	f-m gr amphibolite gneiss		?			
197	231029	6564406	Lake Tallacootra	Tallacootra SZ	f gr bi-q-f mylonite		?			
198	216832	6575523	Lake Ifould	Christie	mafic granulite		?			
199	216832	6575523	Lake Ifould	Christie	reworked pelitic granulite		?			

200	216832	6575523	Lake Ifould	Christie	reworked pelitic granulite		?			
201	216832	6575523	Lake Ifould	Christie	f gr calc-silicate		?			
202	225524	6583072	Lake Ifould	Christie	granite gneiss		1630Ma			
203	286130	6612680	Barton S	Christie	c gr pegmatite		?			
204	311376	6595654	Barton S	Christie	Mylonite	q-plag-kf-bi	?	Kinematics		W up, dextral
205	287863	6612415	Barton S	Christie	Schist	gt-bi-plag-q	?	Petrology, P/T work		

Table A1.2 List of samples taken from drill core in the Nawa Subdomain, with brief descriptions. Thin sections exist for every sample in this list.

Drill Hole Name	Easting	Northing	Interval	Source	Lithology	Key Mineral Assemblages
Ooldea DDH2	189100	6611600	7 (RS9)	MESA	mafic	?inverted pyroxene
Ooldea DDH2	189100	6611600	7 (RS9)	MESA	mafic	cpx-opx
Ooldea DDH2	189100	6611600	37.2 (RS3)	MESA	Fe-Al gneiss	
Ooldea DDH2	189100	6611600	41.6 (RS4A)	MESA	BIF	
Ooldea DDH2	189100	6611600	41.6 (RS4B)	MESA	BIF	sp-q,sp+plag->sill
Ooldea DDH2	189100	6611600	43.2-43.3	JPT	BIF	cor-q
Ooldea DDH2	189100	6611600	43.2-43.3	JPT	mafic gneiss	
Ooldea DDH2	189100	6611600	46.3-46.4	JPT	Fe-aluminous gneiss	qt-sill-cd-bi±sa±sp
Ooldea DDH2	189100	6611600	46.9-47.0	JPT	BIF	?cor-q
Ooldea DDH2	189100	6611600	49.7-49.9	Oliver	BIF	?rutile, mesoperthite-antiperthite
Ooldea DDH2	189100	6611600	55.5-55.7	Oliver	BIF	sa-q±bi
Ooldea DDH2	189100	6611600	56.1-56.2	JPT	BIF	
Ooldea DDH2	189100	6611600	57.3 (RS10)	MESA	BIF	sa-q
Ooldea DDH2	189100	6611600	57.8-57.9	JPT	BIF	g-opx-plag-q
Ooldea DDH2	189100	6611600	64.0 (RS5)	MESA	mafic-intermediate ?intrusive	
Ooldea DDH2	189100	6611600	65.0-65.1	JPT	BIF	opx-sill-q±sp,sp-q
Ooldea DDH2	189100	6611600	65.9-66.0	JPT	BIF	cor-q,opx-sill-q,sp-q,sa-sp-sill-q
Ooldea DDH2	189100	6611600	66.1-66.2	JPT	BIF	good sp-q,sa-q
Ooldea DDH2	189100	6611600	67.0-67.1	JPT	BIF	
Ooldea DDH2	189100	6611600	71.3-71.4A	JPT	BIF	cor-q, spectacular folding
Ooldea DDH2	189100	6611600	71.3-71.4B	JPT	BIF	cor-q
Ooldea DDH2	189100	6611600	71.3-71.5 (RS11)	MESA	BIF	cor-q,sa-sp-q
Ooldea DDH2	189100	6611600	72.1 (RS16)	MESA	BIF	
Ooldea DDH2	189100	6611600	73.0-73.1	JPT	aluminous gneiss	opx-sill-q±sa±cd±gt,opx-sa-cd-Kf=osm?
Ooldea DDH2	189100	6611600	73.1 (RS17)	MESA	Fe-Al gneiss	opx-sill-q,g-sill-cd
Ooldea DDH2	189100	6611600	73.4-73.6	JPT	aluminous gneiss	opx-sill-q±sa±cd,sa-q,opx-sa-cd-Kf=osm?
Ooldea DDH2	189100	6611600	73.6-73.7	JPT	aluminous gneiss	opx-sill-q±sa±cd,sa-q,opx-sa-cd-Kf=osm?
Ooldea DDH2	189100	6611600	73.7-73.8	JPT	Fe-aluminous gneiss	gt-sill-cd-bi
Ooldea DDH2	189100	6611600	74.9-75.0	JPT	aluminous gneiss	opx-sill-q±sa±cd±gt,opx-sa-cd-Kf=osm?
Ooldea DDH2	189100	6611600	75.4-75.5	JPT	Fe-Al gneiss	opx-sill-q±sa±cd,sa-q,opx-sa-cd-Kf=osm?
Ooldea DDH2	189100	6611600	81.4-81.5	JPT	BIF,late shear zone	late shear zone/pseudotachylite
Ooldea DDH2	189100	6611600	87.4-87.5	MESA	Fe-Al gneiss	opx-sill-q-(bi),plag-Kf,sill-cd symplectites
Ooldea DDH2	189100	6611600	87.5-87.6	JPT	BIF	sa-q,opx-sill-q
Ooldea DDH2	189100	6611600	88.2-88.3	JPT	aluminous gneiss	opx-sill-q±sa±cd,sa-q,opx-sa-cd-Kf=osumilite?
Ooldea DDH2	189100	6611600	88.6-88.8	Oliver	aluminous gneiss	opx-sill-q
Ooldea DDH2	189100	6611600	89.1-89.2	JPT	aluminous gneiss	opx-sill-q±sa±cd,sa-q,opx-sa-cd-Kf=osumilite?
Ooldea DDH2	189100	6611600	89.8-89.9	JPT	aluminous gneiss	opx-sill-q,sa-q
Ooldea DDH2	189100	6611600	92.3-92.5	Oliver	BIF	
Ooldea DDH2	189100	6611600	93.6-93.7	JPT	aluminous gneiss	opx-sill-q±sa±cd,sa-q,opx-sa-cd-Kf=osumilite?
Ooldea DDH2	189100	6611600	94.1-94.2	JPT	BIF	
Ooldea DDH2	189100	6611600	94.1-94.2	JPT	aluminous gneiss	opx-sill-q±cd
Ooldea DDH2	189100	6611600	96.1-96.3	Oliver	BIF	sill-cd symplectites, relict ?sa-cd symplectites
Ooldea DDH2	189100	6611600	96.1-96.3	Oliver	BIF	
Ooldea DDH2	189100	6611600	99.1-99.3	MESA	BIF	great meso-antiperthite
Ooldea DDH2	189100	6611600	99.7-99.8	JPT	BIF	
Ooldea DDH2	189100	6611600	101.3-101.4	JPT	BIF	cor-q
Ooldea DDH2	189100	6611600	101.7-101.8	JPT	BIF	
Ooldea DDH2	189100	6611600	102.1-102.2	JPT	aluminous gneiss	cd-ex opx-sill-q, gt-cd-sill
Ooldea DDH2	189100	6611600	105.3-105.5	Oliver	BIF	
Ooldea DDH2	189100	6611600	105.8-105.9	JPT	BIF	
Ooldea DDH2	189100	6611600	106.0-106.1	JPT	Fe-Al gneiss	
Ooldea DDH2	189100	6611600	111.2-111.4	Oliver	BIF	
Ooldea DDH2	189100	6611600	111.2-111.4	Oliver	BIF	
Ooldea DDH2	189100	6611600	112.1 (RS6A)	MESA	BIF	
Ooldea DDH2	189100	6611600	112.1 (RS6B)	MESA	BIF	
Ooldea DDH2	189100	6611600	112.86-113.36	MESA	Fe-Al gneiss	opx-sill-q, sa-q?, sp-q
Ooldea DDH2	189100	6611600	112.86-113.36	MESA	mafic-intermediate ?intrusive	
Ooldea DDH2	189100	6611600	115.3-115.5	Oliver	BIF	opx-sill-q,?sp-q
Ooldea DDH2	189100	6611600	116.0-116.1	JPT	BIF	opx-sill-q±sp
Ooldea DDH2	189100	6611600	116.8-116.9	JPT	BIF	opx-sill-q
Ooldea DDH2	189100	6611600	118.4-118.6	JPT	BIF	
Ooldea DDH2	189100	6611600	120.5-120.6	JPT	Fe-Al gneiss	
Ooldea DDH2	189100	6611600	120.7-120.8	JPT	BIF	large relict/rotten opx?, g->cd+bi
Ooldea DDH2	189100	6611600	120.8-120.9	JPT	semi-BIF	good rutile
Ooldea DDH2	189100	6611600	123.5 (RS13)	MESA	semi-BIF	
Ooldea DDH2	189100	6611600	124.3-124.5	JPT	felsic gneiss/mylonite	extensive recrystallisation
Ooldea DDH2	189100	6611600	128.6-128.8	Oliver	BIF	

Ooldea DDH2	189100	6611600	129.0-129.1	JPT	aluminous gneiss	g-opx-plag-q±bi,g->bi+cd,opx->bi
Ooldea DDH2	189100	6611600	136.65 (RS7)	MESA	q-f gneiss	
Ooldea DDH2	189100	6611600	136-7-136.8	JPT	Fe-aluminous gneiss	ex-cd-gt-sill±opx
Ooldea DDH2	189100	6611600	138.5-138.6	JPT	felsic gneiss	
Ooldea DDH2	189100	6611600	141.8-141.9	JPT	BIF	extensive recryst of mag...unusual, shear bands
Ooldea DDH2	189100	6611600	149.7-149.9	Oliver	BIF	mesoperthite
Ooldea DDH2	189100	6611600	149.7-149.9	Oliver	BIF	unusual exsol lam. in mag - ?rutile
Ooldea DDH2	189100	6611600	152 (RS14A)	MESA	q-f gneiss	mesoperthite
Ooldea DDH2	189100	6611600	152 (RS14B)	MESA	BIF	mesoperthite
Ooldea DDH2	189100	6611600	153.8-153.9	JPT	Fe-leucogneiss	fresh retrograde assemblage
Ooldea DDH2	189100	6611600	157.3-157.4	JPT	felsic gneiss	mesoperthite
Ooldea DDH2	189100	6611600	161? (RS8B) #	Oliver	Fe-Al gneiss	
Ooldea DDH2	189100	6611600	162.8-163	Oliver	BIF	
Ooldea DDH2	189100	6611600	168.3 (RS15)	MESA	BIF	
Ooldea DDH2	189100	6611600	168.4-EOC	JPT	semi-BIF	g-opx-plag-q,early+late g,late opx
Lake Maurice East	157540	6718470	727.9-728.0	JPT	weathered pelitic mylonite	gt-sill-bi-?cd-mag
Lake Maurice East	157540	6718470	729.7-729.8	JPT	weathered pelitic mylonite	gt-sill-bi-?cd-mag
Lake Maurice East	157540	6718470	731.9-732.0	JPT	weathered pelitic mylonite	gt-sill-bi-?cd-mag
Lake Maurice East	157540	6718470	732.1-732.2	JPT	weathered pelitic mylonite	gt-sill-bi-?cd-mag
Lake Maurice East	157540	6718470	732.8-732.9	JPT	weathered pelitic mylonite	gt-sill-bi-?cd-mag
Lake Maurice East	157540	6718470	737.1-737.2	JPT	weathered pelitic mylonite	gt-sill-bi-?cd-mag-sapphirine?
Lake Maurice East	157540	6718470	737.5-737.6	JPT	weathered pelitic mylonite	gt-sill-bi-?cd-mag-sapphirine?
Lake Maurice East	157540	6718470	732.8-732.9	JPT	weathered pelitic mylonite	gt-sill-bi-?cd-mag
Maralinga 7	170280	6658650	1708'-1715'	JPT	mafic granulite + felsic gneiss	cpx-hbl
Maralinga 7	170280	6658650	1715'-1721'	JPT	mafic granulite	cpx-hbl
Ooldea DDH1	174900	6625170	288.25-288.35	JPT	felsic mylonite	
Ooldea DDH1	174900	6625170	288.7-288.8	JPT	felsic +pelitic mylonite	gt-sill-?cd-mag-bi,perthite
Ooldea DDH1	174900	6625170	289.1-289.2	JPT	felsic mylonite	gt,perthite
Ooldea DDH1	174900	6625170	290.1-290.2	JPT	felsic mylonite	gt,perthite
Ooldea DDH1	174900	6625170	291.15-291.25	JPT	felsic mylonite	gt,perthite
Ooldea DDH1	174900	6625170	292.65-292.75	JPT	semipelitic gneiss	gt-sill-bi-?cd-perthite-plag-q
Ooldea DDH1	174900	6625170	293.25-293.35	JPT	felsic mylonite	gt,perthite
Ooldea DDH1	174900	6625170	293.7-294.0	JPT	semipelitic gneiss	gt-sill-bi-?cd-perthite-plag-q
Ooldea DDH1	174900	6625170	295.0-295.1	JPT	felsic mylonite	gt,perthite
ORP2	169220	6625940	488-490	JPT	weathered pelitic gneiss	gt-?cd-sill-bi-mag
ORP2	169220	6625940	490-492	JPT	weathered pelitic gneiss	gt-?cd-sill-bi-mag
ORP2	169220	6625940	492-494	JPT	weathered pelitic gneiss	gt-?cd-sill-bi-mag
ORP2	169220	6625940	494-496	JPT	weathered pelitic gneiss	gt-?cd-sill-bi-mag

Table A1.3 List of samples taken from drill core in the Fowler Subdomain (in addition to numerous MESA samples and thin sections). Thin sections exist for most of the following samples.

#	Easting	Northing	Interval	Lithology	MINERALOGY
BAC1	237523	6581784	63	Biotite schist	
BAC2	238042	6581510	74	Biotite schist	
BAC8	244863	6576004	93	Highly weathered ?mafic	
BAC11	245397	6575524	93	Highly weathered schist	
BAC12	246300	6574950	32	Highly weathered gneiss, some opaques	
BAC13	246643	6574781	80	Garnet-sillimanite-biotite gneiss	
BAC14	247243	6574587	47	Amphibolite gneiss	
BAC15	247617	6574359	42	Cataclasite	
BAC16	247990	6574228	42	Weathered amphibolite gneiss	
BAC17	248124	6574215	43	Garnet-hornblende gneiss	
BAC18	248486	6574265	45	Garnet-biotite-sillimanite-magnetite gneiss	
BAC20	249458	6574007	65	Hornblende-biotite gneiss	
BAC21	249671	6573957	53	Quartz-feldspar-biotite gneiss	
BAC22	250109	6573738	60	Garnet-biotite-sillimanite-magnetite gneiss	
BAC23	250246	6573670	57	Garnet-biotite-sillimanite-magnetite gneiss	
BAC24	250432	6573633	46	Weathered quartz-feldspar-biotite gneiss	
BAC25	250801	6573565	36	Highly weathered ?mafic	
BAC26	251024	6573611	43	Garnet-hornblende-biotite gneiss	
BAC27	251701	6573402	37	Garnet-hornblende-biotite gneiss	
BAC28	251736	6573348	57	Garnet-biotite-sillimanite-magnetite gneiss	
BAC29	252244	6573163	33	Garnet-biotite-sillimanite-magnetite gneiss	
BAC30	252574	6573107	21	Amphibolite gneiss	
BAC31	252755	6573096	24	Sillimanite-biotite mylonite	
BAC33	253424	6573116	51	Garnet-biotite-sillimanite-magnetite gneiss	
BAC34	253611	6573168	16	Weathered biotite gneiss, some opaques	
BAC37	254155	6573146	27	Felsic gneiss	
BAC38	254482	6573167	23	Garnet-hornblende-biotite gneiss	
BAC39	255043	6573078	25	Cataclasite	
BAC40	255277	6573028	32	Weathered ?amphibolite, some opaques	
BAC41	255542	6572935	45	Garnet-biotite-sillimanite-magnetite gneiss	
BAC43	256897	6572530	26	Weathered ?amphibolite, some opaques	
BAC44	256997	6572469	41	Garnet-biotite-sillimanite-magnetite gneiss	
BAC46	257969	6572355	42	Garnet-biotite-sillimanite-magnetite gneiss	
BAC47	258544	6572268	61	Felsic gneiss + weathered biotite mylonite	
BAC50	260239	6571713	40	Weathered quartz-perthite-plag-biotite gneiss	
BAC54	262405	6571061	50	Weathered ?hornblende-biotite-magnetite gneiss	

BAC55	262540	6571020	35	Aplite	
BAC56	267880	6570440	93	Highly weathered ?mafic	
BAC57	271510	6569650	23	Cataclasite	
BAC58	272700	6569440	92	Biotite gneiss	
BAC59	273250	6569330	49	Quartz-feldspar-biotite gneiss	
BAC60	273450	6569320	66	Hornblende-biotite gneiss	
BAC61	274250	6569100	56	Hornblende-biotite gneiss	
BAC63	275500	6568880	27	Amphibolite	
NDR1	237935	6478041	40.8-40.9	Intermediate gneiss	gt-bi-plag-kf-q
NDR1	237935	6478041	41.3-41.4	Mafic granulite	gt-opx-cpx-scap-hbl-bi-plag-q
NDR2	237760	6478268	69.3-69.5	Metagabbro	cpx-opx-hbl-plag-q
NDR3	235560	6480710	41.7-41.8	Intermediate gneiss	gt-bi-plag-q
NDR5	240390	6474220	145.5-145.6	Pelitic schist	gt-bi-sill-kf-q
NDR7B	233010	6483610	118.6-118.7	Amphibolite	hbl-plag-q-bi
NDR13	221490	6496850	95.4-95.5	Weakly foliated granite	kf-q-bi-plag
Nundroo DDH1	238220	6477670	55.2-55.3	Intermediate gneiss	gt-hbl-bi-plag-q-scap
Nundroo DDH1	238220	6477670	57.2-57.3	Mafic granulite	gt-opx-cpx-scap-hbl-bi-plag-q
Nundroo DDH1	238220	6477670	57.55-57.75	Mafic gneiss	cpx-hbl-scap-plag-bi-q
Nundroo DDH1	238220	6477670	58.7-58.8	Mafic granulite + gt-bi gneiss	gt-cpx-opx-scap-hbl-bi-plag-q
Nundroo DDH1	238220	6477670	59.0-59.1	Intermediate gneiss	gt-bi-plag-q-scap
Nundroo DDH2	238320	6477590	130.2-130.3	Mylonite (late SZ)	hb-plag-bi-q-scap
Nundroo DDH2	238320	6477590	128.0-128.2	Granulite/Amphibolite	hbl-plag-q-opx-cpx
Nundroo DDH2	238320	6477590	139.4-139.5	Mafic granulite	gt-opx-cpx-hbl-bi-plag-q
Nundroo DDH2	238320	6477590	159.8-159.9	Mafic granulite	gt-opx-cpx-hbl-bi-plag-q
Nundroo DDH2	238320	6477590	160.0-160.1	Mafic granulite	gt-opx-cpx-hbl-bi-plag-q
Nundroo DDH2	238320	6477590	207.7-207.8	Metagabbro/granulite	opx-cpx-gt-hbl-plag-q-py
Nundroo DDH2	238320	6477590	243.2-243.3	Mafic granulite	gt-opx-cpx-hbl-plag-q
Nundroo DDH2	238320	6477590	252.1-252.2	Metagabbro	cpx-opx-plag-q
Nundroo DDH2	238320	6477590	261.7-261.8	Metagabbro/granulite	cpx-opx-gt-hbl-plag-q-bi-py
Nundroo DDH2	238320	6477590	265.6-265.7	Granulite/amphibolite	gt-opx-cpx-hbl-plag-q
Nundroo DDH2	238320	6477590	273.7-273.8	Granulite/amphibolite	gt-opx-cpx-hbl-plag-q
Nundroo DDH2	238320	6477590	300.9-301.0	Mafic granulite	gt-opx-cpx-plag-q-hbl
Nundroo DDH2	238320	6477590	306.0-306.1	Mafic granulite	gt-opx-cpx-plag-q-hbl
Nundroo DDH2	238320	6477590	320.8-320.9	Pelitic gneiss	gt-bi-sill-plag-q-?cd
Nundroo DDH2	238320	6477590	367.2-367.3	Pelitic gneiss	gt-bi-sill-plag-q
Nundroo DDH2	238320	6477590	74.2-74.3	Metadiorite	opx-cpx-plag-hbl-q
Nundroo DDH2	238320	6477590	94.7-94.8	Metagabbro	cpx-opx-hbl-plag-q-py
Nundroo DDH3	236275	6479922	72.6-72.7	Intermediate gneiss	gt-bi-kf-plag-q
Nundroo DDH3	236275	6479922	108.6-108.7	Intermediate gneiss	gt-bi-kf-plag-q
Nundroo DDH3	236275	6479922	110.1-110.2	Intermediate gneiss	gt-bi-kf-plag-q
Nundroo DDH3	236275	6479922	129.2-129.3	Amphibolite	gt-hbl-plag-q-bi
Nundroo DDH3	236275	6479922	158.4-158.5	Amphibolite	gt-hbl-plag-q-bi
Nundroo DDH3	236275	6479922	164.0-164.1	Intermediate gneiss	gt-bi-plag-q-scap
Nundroo DDH3	236275	6479922	211.8-211.9	Amphibolite	hbl-plag-q-bi
Nundroo DDH3	236275	6479922	218.5-218.6	Amphibolite + cataclasite	hbl-plag-q-bi
PIN-R4	223600	6560200	33.8-33.9	Amphibolite	hbl-plag-(bi)
PIN-R5	228500	6555500	88.9-89.0	Amphibolite	hbl-plag-(bi)
TAL4	245900	6561000	26.65-26.75	Gt-bi gneiss	gt-bi-kf-plag-q
TAL13	252200	6555700	24.8-24.9	Amphibolite	gt-hbl-bi-plag-q
TAL11	242000	6564200	26.7-26.8	Mafic granulite	cpx-opx-plag-q
TAL20	246900	6560100	57.8-57.9	Pelitic gneiss	gt-bi-sill-mag-?cd-kf-q
TAL5	245000	6561700	4.0-4.1	Mafic gneiss	cpx-opx-hbl-plag-q
TAL6	239500	6566200	57.4-57.5	Retrogressed amphibolite	hbl-bi-plag-q
TAL7	239100	6566500	99.1-99.2	Retrogressed amphibolite	hbl-bi-plag-q
TAL8	237300	6568100	18.1-18.2	Metagabbro	cpx-hbl-plag
TAL9	237000	6568400	22.2-22.3	Felsic gneiss	q-plag-kf-bi-q
TAL10	238100	6567400	54.2-54.3	Biotite gneiss	bi-plag-q
TAL16	255300	6553100	36.4-36.5	Granodiorite gneiss	q-plag-bi
TAL17	256600	6552000	43.9-44.0	Diorite gneiss	hbl-bi-plag-q
TAL18	251200	6556500	38.2-38.3	Diorite	hbl-bi-plag-q
TAL19	249300	6558100	42.2-42.3	Granodiorite	plag-q-bi
TAL21	243800	6562700	5.8-6.0	Felsic mylonite	q-f
625 14	225800	6563600	14	Felsic gneiss	q-plag-kf-bi

Appendix 2

MINERAL CHEMISTRY

This Appendix contains representative mineral analyses for samples used in thermobarometric and petrogenetic calculations. Analyses were performed on the Cameca SX51 Electron Microprobe, at CEMMSA, University of Adelaide, using an accelerating voltage of 15kV. Analyses have been recalculated for Fe^{3+} content using the AX computer program of Holland (1995).

A2.1 Nawa Subdomain

Table A2.1 Early, coarse grained, granular phases in the aluminous granulites (see Table 4.1 for osumilite compositions).

Sample	75.4-75.5	75.4-75.5	75.4-75.5	75.4-75.5
Mineral	hypersthene	hypersthene	cordierite	cordierite
SiO2	48.76	49.07	50.06	49.47
TiO2	0.02	0.06	0.02	0.00
Al2O3	9.59	9.22	32.93	33.05
Cr2O3	0.00	0.00	0.02	0.02
Fe2O3	2.05	1.44	0.50	0.52
FeO	13.38	13.42	1.78	1.87
MnO	2.49	2.71	0.46	0.35
MgO	23.76	23.82	12.28	12.09
CaO	0.05	0.03	0.00	0.00
Na2O	0.00	0.01	0.03	0.06
K2O	0.00	0.01	0.00	0.06
Totals	100.10	99.79	98.08	97.49
Oxygens	6	6	18	18
Si	1.767	1.782	5.029	5.003
Ti	0.001	0.002	0.002	0.000
Al	0.410	0.395	3.900	3.941
Cr	0.000	0.000	0.002	0.002
Fe3	0.056	0.039	0.037	0.040
Fe2	0.406	0.407	0.150	0.158
Mn	0.076	0.083	0.039	0.030
Mg	1.283	1.289	1.839	1.822
CA	0.002	0.001	0.000	0.000
Na	0.000	0.001	0.006	0.012
K	0.000	0.000	0.000	0.008
Sum	4.000	4.000	11.003	11.015
XMg	0.76	0.76	0.92	0.92

Table A2.2 Stage 2, fine grained reaction textures in the aluminous granulites.

Sample	88.2-88.3	75.4-75.5	93.6-93.7	88.2-88.3	88.2-88.3	93.6-93.7	93.6-93.7	93.6-93.7	88.2-88.3
Min	opx[1]	opx[1]	opx[1]	opx[1]	opx[2]	opx[2]	opx[2]	opx[2]	opx[3]
SiO2	50.46	50.16	47.61	50.78	49.77	49.68	50.35	49.71	50.00
TiO2	0.00	0.02	0.04	0.03	0.00	0.01	0.02	0.02	0.02
Al2O3	6.50	6.87	9.43	6.83	7.98	7.18	7.19	7.43	7.38
Cr2O3	0.04	0.05	0.03	0.01	0.04	0.01	0.00	0.02	0.08
Fe2O3	2.03	1.07	3.95	1.47	1.08	2.56	1.28	2.51	1.26
FeO	13.75	13.99	14.22	14.50	15.13	14.05	14.99	14.06	14.65
MnO	2.57	2.69	1.04	0.99	1.25	1.44	1.51	1.28	1.14
MgO	24.63	24.24	23.35	24.80	24.04	24.45	24.45	24.63	24.48
CaO	0.05	0.07	0.31	0.31	0.06	0.04	0.06	0.04	0.04
Na2O	0.00	0.00	0.12	0.09	0.02	0.04	0.00	0.02	0.01
K2O	0.01	0.00	0.04	0.07	0.03	0.03	0.02	0.02	0.09
Totals	100.03	99.17	100.16	99.90	99.40	99.48	99.87	99.73	99.14
Oxygens	6	6	6	6	6	6	6	6	6
Si	1.833	1.836	1.736	1.838	1.815	1.812	1.829	1.807	1.825
Ti	0.000	0.001	0.001	0.001	0.000	0.000	0.001	0.001	0.001
Al	0.278	0.297	0.406	0.292	0.343	0.309	0.308	0.318	0.318
Cr	0.001	0.001	0.001	0.000	0.001	0.000	0.000	0.001	0.002
Fe3	0.055	0.029	0.108	0.040	0.030	0.070	0.035	0.069	0.034
Fe2	0.418	0.428	0.434	0.439	0.462	0.429	0.455	0.427	0.447
Mn	0.079	0.083	0.032	0.030	0.038	0.044	0.046	0.039	0.035
Mg	1.333	1.322	1.269	1.338	1.307	1.329	1.323	1.334	1.331
CA	0.002	0.003	0.012	0.012	0.002	0.002	0.002	0.002	0.002
Na	0.000	0.000	0.009	0.006	0.001	0.003	0.000	0.001	0.001
K	0.000	0.000	0.002	0.003	0.001	0.001	0.001	0.001	0.004
Sum	4.000	4.000	4.010	4.000	4.000	4.000	4.000	4.000	4.000
XMg	0.73	0.72	0.73	0.74	0.72	0.74	0.73	0.74	0.73

Sample	93.6-93.7	93.6-93.7	88.2-88.3	88.2-88.3	93.6-93.7	93.6-93.7	75.4-75.5	93.6-93.7	93.6-93.7
Min	opx[3]	opx[3]	sa[4]	sa[4]	sa[4]	sa[4]	sa[5]	K-spar[6]	plag[7]
SiO2	49.00	49.45	14.32	14.65	15.14	12.59	13.37	65.30	58.13
TiO2	0.07	0.04	0.04	0.01	0.00	0.04	0.00	0.02	0.01
Al2O3	8.05	8.11	58.81	59.37	59.38	60.31	60.02	18.66	25.66
Cr2O3	0.04	0.02	0.00	0.00	0.00	0.03	0.00	0.01	0.04
Fe2O3	2.67	1.41	1.79	0.99	0.00	2.45	2.02	0.27	0.14
FeO	14.86	15.59	7.02	6.69	8.08	6.15	5.89	0.00	0.00
MnO	1.34	1.42	0.41	0.43	0.46	0.41	0.90	0.02	0.02
MgO	23.76	23.58	16.36	16.87	15.74	15.75	16.13	0.00	0.00
CaO	0.04	0.04	0.02	0.07	0.01	0.02	0.06	0.09	7.86
Na2O	0.01	0.01	0.01	0.03	0.00	0.00	0.00	1.82	6.27
K2O	0.00	0.01	0.09	0.01	0.07	0.00	0.03	13.60	0.09
Totals	99.83	99.67	98.87	99.12	98.88	97.76	98.42	99.80	98.22
Oxygens	6	6	20	20	20	20	20	8	8
Si	1.788	1.805	1.731	1.758	1.825	1.538	1.621	2.994	2.636
Ti	0.002	0.001	0.004	0.001	0.000	0.004	0.000	0.001	0.000
Al	0.346	0.349	8.383	8.401	8.437	8.688	8.578	1.009	1.372
Cr	0.001	0.001	0.000	0.000	0.000	0.003	0.000	0.000	0.001
Fe3	0.073	0.039	0.163	0.089	0.000	0.225	0.185	0.009	0.005
Fe2	0.453	0.476	0.710	0.672	0.814	0.629	0.597	0.000	0.000
Mn	0.041	0.044	0.042	0.044	0.047	0.042	0.092	0.001	0.001
Mg	1.292	1.283	2.948	3.018	2.827	2.868	2.914	0.000	0.000
CA	0.002	0.002	0.003	0.009	0.001	0.003	0.008	0.004	0.382
Na	0.001	0.001	0.002	0.007	0.000	0.000	0.000	0.162	0.551
K	0.000	0.000	0.014	0.002	0.011	0.000	0.005	0.796	0.005
Sum	4.000	4.000	14.000	14.000	13.962	14.000	14.000	4.976	4.953
XMg	0.72	0.71	0.80	0.81	0.77	0.81	0.81		

1=hypersthene in cordierite breakdown textures
2=hypersthene rimming cordierite breakdown textures
3=hypersthene in osumilite breakdown textures
4=sapphirine in osumilite breakdown textures
5=sapphirine rimming early hypersthene
6=K-feldspar in osumilite breakdown textures
7=Plagioclase in osumilite breakdown textures

Table A2.3 Stage 3 reaction products in the aluminous granulites (cordierite rims sapphirine in the osumilite breakdown textures).

Sample	93.6-93.7	93.6-93.7	93.6-93.7
Min	biotite	cordierite	cordierite
SiO2	38.92	49.65	49.43
TiO2	2.93	0.05	0.05
Al2O3	15.19	32.62	32.66
Cr2O3	0.03	0.01	0.05
Fe2O3	0.00	0.51	0.23
FeO	7.48	1.84	2.09
MnO	0.06	0.17	0.26
MgO	19.61	12.06	11.90
CaO	0.02	0.03	0.01
Na2O	0.14	0.07	0.06
K2O	9.89	0.13	0.02
Totals	94.28	97.14	96.76
Oxygens	11	18	18
Si	2.832	5.035	5.033
Ti	0.160	0.004	0.004
Al	1.303	3.900	3.920
Cr	0.002	0.001	0.004
Fe3	0.000	0.039	0.017
Fe2	0.455	0.156	0.178
Mn	0.004	0.015	0.022
Mg	2.127	1.823	1.806
CA	0.002	0.003	0.001
Na	0.020	0.014	0.012
K	0.919	0.017	0.003
Sum	7.824	11.006	11.000
XMg	0.82	0.91	0.90

Table A2.4 Miscellaneous analyses from the Moondrah Gneiss.

Sample	65.9-66.0	101.3-101.4	65.9-66.0	432.-43.3	101.3-101.4	73.6-73.7	129.0-129.1	168.4-EOC
Min	cor[1]	cor[1]	cor[1]	cor[1]	gt[2]	gt[3]	gt[4]	gt[4]
SiO2	0.04	0.05	0.00	0.03	38.97	39.75	39.26	37.53
TiO2	0.00	0.00	0.00	0.03	0.03	0.01	0.01	0.00
Al2O3	98.94	98.45	99.12	98.56	21.86	21.90	21.56	20.65
Cr2O3	0.00	0.01	0.02	0.06	0.00	0.02	0.00	0.00
Fe2O3	1.03	1.06	0.78	0.93	1.18	1.21	0.15	0.65
FeO	0.00	0.00	0.00	0.00	14.81	16.32	21.20	30.37
MnO	0.07	0.01	0.00	0.09	12.07	6.63	5.83	1.97
MgO	0.00	0.00	0.00	0.01	10.46	12.88	9.63	4.07
CaO	0.00	0.02	0.01	0.00	0.61	1.21	2.00	4.07
Na2O	0.01	0.03	0.00	0.00	0.03	0.00	0.02	0.01
K2O	0.03	0.02	0.02	0.00	0.01	0.00	0.01	0.00
Totals	100.11	99.65	99.95	99.71	100.03	99.93	99.68	99.32
Oxygens	30	30	30	30	12	12	12	12
Si	0.000	0.000	0.000	0.000	2.981	2.993	3.020	3.006
Ti	0.000	0.000	0.000	0.000	0.002	0.001	0.001	0.000
Al	0.994	0.996	0.995	0.994	1.972	1.944	1.955	1.950
Cr	0.000	0.000	0.000	0.000	0.000	0.001	0.000	0.000
Fe3	0.007	0.005	0.005	0.007	0.068	0.069	0.009	0.039
Fe2	0.000	0.000	0.000	0.000	0.947	1.028	1.364	2.034
Mn	0.000	0.000	0.002	0.000	0.782	0.423	0.380	0.134
Mg	0.000	0.000	0.000	0.000	1.193	1.445	1.104	0.486
CA	0.000	0.000	0.000	0.000	0.050	0.098	0.165	0.349
Na	0.000	0.000	0.000	0.000	0.004	0.000	0.003	0.002
K	0.000	0.000	0.000	0.000	0.001	0.000	0.001	0.000
Sum	1.003	1.002	1.002	1.003	8.000	8.000	8.000	8.000
XMg					0.40	0.48	0.37	0.16

Sample Min	57.8-57.9 gt[4]	73.6-73.7 sa[5]	73.6-73.7 sa[5]	88.2-88.3 sa[6]	73.6-73.7 bi[7]	129.0-129.1 bi[8]	73.6-73.7 sp[9]	116.0-116.0 sp[10]
SiO2	39.36	12.19	12.49	12.02	38.73	38.93	0.00	0.05
TiO2	0.00	0.00	0.01	0.02	2.13	3.45	0.00	0.04
Al2O3	21.83	61.36	60.99	60.84	16.99	14.99	64.46	63.18
Cr2O3	0.01	0.08	0.09	0.03	0.00	0.00	0.13	0.02
Fe2O3	0.13	3.88	4.36	4.12	0.86	0.00	0.00	1.07
FeO	18.17	5.14	4.93	5.33	4.38	8.55	12.48	18.12
MnO	8.90	0.52	0.57	0.50	0.07	0.10	1.48	1.46
MgO	10.20	16.14	16.45	15.79	21.69	19.48	17.41	14.24
CaO	1.29	0.01	0.03	0.02	0.00	0.00	0.02	0.01
Na2O	0.01	0.00	0.00	0.02	0.12	0.17	0.07	0.04
K2O	0.00	0.00	0.02	0.00	9.26	10.40	0.00	0.00
Totals	99.90	99.32	99.94	98.69	94.24	96.08	96.05	98.23
Oxygens	12	20	20	20	11	11	4	4
Si	3.012	1.467	1.495	1.459	2.771	2.806	0.000	0.001
Ti	0.000	0.000	0.001	0.002	0.115	0.187	0.000	0.001
Al	1.969	8.707	8.609	8.705	1.433	1.274	2.002	1.976
Cr	0.001	0.008	0.009	0.003	0.000	0.000	0.003	0.000
Fe3	0.007	0.351	0.393	0.376	0.046	0.000	0.000	0.021
Fe2	1.163	0.518	0.493	0.541	0.262	0.515	0.275	0.402
Mn	0.577	0.053	0.058	0.051	0.004	0.006	0.033	0.033
Mg	1.163	2.895	2.935	2.856	2.313	2.092	0.683	0.563
CA	0.106	0.001	0.004	0.003	0.000	0.000	0.001	0.000
Na	0.001	0.000	0.000	0.005	0.017	0.024	0.004	0.002
K	0.000	0.000	0.003	0.000	0.846	0.957	0.000	0.000
Sum	8.000	14.000	14.000	14.000	7.806	7.861	3.000	3.000
XMg	0.39	0.84	0.84	0.83	0.90	0.80	0.69	0.56

Sample Min	88.2-88.3 sill[11]	88.2-88.3 sill[11]	116.0-116.1 sill[12]	129.0-129.1 opx[13]	116.0-116.1 opx[14]	168.4-EOC opx[15]	57.8-57.9 opx[15]
SiO2	36.27	36.48	36.28	49.48	48.19	49.45	49.82
TiO2	0.01	0.02	0.00	0.07	0.03	0.00	0.09
Al2O3	60.45	61.01	61.37	6.34	7.82	1.83	7.71
Cr2O3	0.02	0.03	0.02	0.02	0.03	0.00	0.05
Fe2O3	1.94	1.58	1.81	2.51	3.54	0.69	2.64
FeO	0.00	0.00	0.00	16.47	13.75	30.99	14.22
MnO	0.00	0.07	0.00	1.55	1.88	0.75	1.85
MgO	0.00	0.03	0.01	23.00	23.51	15.15	24.30
CaO	0.00	0.01	0.00	0.12	0.08	0.30	0.08
Na2O	0.00	0.00	0.02	0.01	0.00	0.00	0.02
K2O	0.00	0.01	0.00	0.00	0.00	0.00	0.02
Totals	98.42	99.24	99.52	99.57	98.82	99.16	100.79
Oxygens	30	30	30	6	6	6	6
Si	6.009	5.995	5.951	1.825	1.779	1.947	1.798
Ti	0.001	0.002	0.000	0.002	0.001	0.000	0.002
Al	11.807	11.820	11.868	0.276	0.340	0.085	0.328
Cr	0.003	0.004	0.003	0.001	0.001	0.000	0.001
Fe3	0.089	0.083	0.095	0.070	0.098	0.021	0.072
Fe2	0.133	0.125	0.143	0.508	0.425	1.020	0.429
Mn	0.000	0.010	0.000	0.048	0.059	0.025	0.057
Mg	0.000	0.007	0.002	1.265	1.294	0.889	1.307
CA	0.000	0.002	0.000	0.005	0.003	0.013	0.003
Na	0.000	0.000	0.006	0.001	0.000	0.000	0.001
K	0.000	0.002	0.000	0.000	0.000	0.000	0.001
Sum	18.041	18.050	18.069	4.000	4.000	4.000	4.000
XMg				0.69	0.73	0.46	0.73

1=Stage 1 corundum intergrown with quartz and magnetite in ironstones, 2=Stage 1 garnet rimming corundum-magnetite-quartz intergrowth in ironstone, 3=Stage 1 garnet rimming sapphirine-spinel-quartz intergrowths in semipelitic gneiss, 4=Stage 1 garnet intergrown with hypersthene in a garnet-magnetite gneiss, 5=Stage 1 sapphirine blebs intergrown with magnetite surrounded by garnet in semipelitic gneiss, 6=Stage 1 sapphirine intergrown with magnetite surrounded by quartz in aluminous gneiss, 7=Stage 3 biotite in semipelitic garnet gneiss, 8=Stage 3 biotite after opx in magnetite gneiss, 9=Stage 1 spinel blebs in garnet in semipelitic gneiss, 10=Stage 3 spinel exsolution blebs from magnetite in magnetite gneiss, 11=Stage 1 sillimanite intergrown with magnetite, pseudomorphing spinel in aluminous gneiss, 12=Stage 1 sillimanite intergrown with hypersthene, quartz and magnetite in magnetite gneiss, 13=Stage 1 hypersthene intergrown with garnet in garnet gneiss, 14=Stage 1 hypersthene intergrown with sillimanite, magnetite and quartz in magnetite gneiss, 15=Stage 1 hypersthene intergrown with garnet in ironstone.

A2.2 Christie Subdomain

Table A2.4 Metapelitic granulites from the Christie Gneiss

Sample Min	WGC52A garnet[1]	WGC55 garnet[1]	WGC79 garnet[1]	WGC79 garnet[2]	WGC52A perthite[3]	WGC55 plagioclase[4]	WGC79 plagioclase[4]	WGC79 plagioclase[5]
SiO2	37.72	38.48	38.08	37.31	65.53	61.18	60.07	60.32
TiO2	0.06	0.03	0.02	0.00	0.01	0.01	0.01	0.02
Al2O3	21.28	21.80	21.70	21.07	18.67	24.07	24.46	24.53
Cr2O3	0.03	0.06	0.00	0.14	0.01	0.00	0.00	0.00
Fe2O3	2.20	1.71	2.08	0.94	0.02	0.00	0.00	0.01
FeO	29.35	29.04	28.79	34.33	0.00	0.00	0.00	0.00
MnO	0.47	0.34	0.72	1.37	0.02	0.00	0.00	0.00
MgO	7.90	8.67	8.30	4.32	0.00	0.00	0.00	0.00
CaO	0.87	0.94	0.97	0.84	0.22	5.80	6.28	6.63
Na2O	0.03	0.00	0.00	0.02	4.98	7.72	7.78	7.38
K2O	0.00	0.00	0.00	0.01	9.11	0.10	0.18	0.14
Totals	99.91	101.07	100.66	100.34	98.58	98.88	98.78	99.03
Oxygens	12	12	12	12	8	8	8	8
Si	2.951	2.959	2.948	2.978	2.995	2.739	2.703	2.705
Ti	0.004	0.002	0.001	0.000	0.000	0.000	0.000	0.001
Al	1.963	1.976	1.980	1.983	1.006	1.270	1.298	1.297
Cr	0.002	0.004	0.000	0.009	0.000	0.000	0.000	0.000
Fe3	0.130	0.099	0.121	0.056	0.001	0.000	0.000	0.000
Fe2	1.921	1.867	1.864	2.292	0.000	0.000	0.000	0.000
Mn	0.031	0.022	0.047	0.093	0.001	0.000	0.000	0.000
Mg	0.921	0.994	0.958	0.514	0.000	0.000	0.000	0.000
CA	0.073	0.078	0.081	0.072	0.011	0.278	0.303	0.319
Na	0.005	0.000	0.000	0.003	0.441	0.670	0.679	0.642
K	0.000	0.000	0.000	0.001	0.532	0.006	0.010	0.008
Sum	8.000	8.000	8.000	8.000	4.987	4.964	4.993	4.971
XMg	0.32	0.34	0.33	0.18				

Sample Min	WGC52A cordierite[6]	WGC55 cordierite[6]	WGC79 cordierite[6]	WGC79 cordierite[7]	WGC52A biotite[8]	WGC79 biotite[8]	WGC52A ilmenite	WGC79 spinel[9]
SiO2	49.72	49.43	49.54	49.07	36.24	36.28	0.06	0.01
TiO2	0.01	0.03	0.00	0.00	2.95	2.57	54.74	0.00
Al2O3	32.44	32.96	32.70	32.68	17.30	18.57	0.00	57.13
Cr2O3	0.00	0.03	0.00	0.00	0.06	0.04	0.00	1.27
Fe2O3	0.00	0.90	0.53	0.12	0.00	0.00	0.00	0.51
FeO	5.41	3.26	4.74	6.18	14.58	14.95	44.39	31.24
MnO	0.03	0.00	0.05	0.03	0.08	0.00	0.29	0.02
MgO	10.27	11.28	10.49	9.68	13.49	12.38	0.56	5.33
CaO	0.02	0.04	0.01	0.01	0.00	0.01	0.00	0.01
Na2O	0.08	0.06	0.09	0.04	0.12	0.08	0.00	0.06
K2O	0.01	0.00	0.00	0.00	9.70	10.03	0.00	0.00
Totals	97.99	97.99	98.15	97.80	94.53	94.92	100.04	95.58

Oxygens	18	18	18	18	11	11	3	4
Si	5.062	5.002	5.031	5.026	2.726	2.719	0.001	0.000
Ti	0.001	0.002	0.000	0.000	0.167	0.145	1.024	0.000
Al	3.894	3.932	3.915	3.946	1.534	1.641	0.000	1.962
Cr	0.000	0.002	0.000	0.000	0.004	0.002	0.000	0.029
Fe3	0.000	0.069	0.041	0.009	0.000	0.000	0.000	0.011
Fe2	0.461	0.276	0.402	0.529	0.917	0.937	0.923	0.761
Mn	0.003	0.000	0.004	0.003	0.005	0.000	0.006	0.000
Mg	1.558	1.701	1.588	1.478	1.512	1.383	0.021	0.231
CA	0.002	0.004	0.001	0.001	0.000	0.001	0.000	0.000
Na	0.016	0.012	0.018	0.008	0.017	0.012	0.000	0.003
K	0.001	0.000	0.000	0.000	0.932	0.960	0.000	0.000
Sum	10.998	11.000	11.000	11.000	7.813	7.800	1.975	3.000
XMg	0.77	0.86	0.80	0.74	0.62	0.60	0.02	0.23

1=garnet cores, 2=late secondary garnet, 3=integrated perthite composition from plagioclase + K-feldspar in mesoperthite, 4=plagioclase cores, 5=secondary plagioclase, 6=cordierite cores, 7=secondary cordierite, 8=early biotite cores, 9=early spinel.

Table A2.5 Mafic granulite interlayered with the Christie Gneiss

Sample Min	**WGC11 opx**	**WGC11 gt**	**WGC11 plag**	**WGC11 cumm[1]**
SiO2	50.92	37.98	51.03	53.51
TiO2	0.02	0.00	0.01	0.04
Al2O3	1.76	21.17	30.61	1.53
Cr2O3	0.02	0.01	0.01	0.02
Fe2O3	0.73	0.64	0.11	0.00
FeO	27.04	31.70	0.00	24.65
MnO	0.24	0.51	0.00	0.13
MgO	18.63	4.89	0.00	17.16
CaO	0.22	3.43	14.01	0.19
Na2O	0.03	0.02	3.43	0.03
K2O	0.00	0.00	0.03	0.01
Totals	99.61	100.34	99.24	97.27
Oxygens	6	12	8	23
Si	1.950	2.997	2.337	7.872
Ti	0.001	0.000	0.000	0.004
Al	0.079	1.970	1.653	0.265
Cr	0.001	0.001	0.000	0.002
Fe3	0.021	0.038	0.004	0.000
Fe2	0.866	2.092	0.000	3.033
Mn	0.008	0.034	0.000	0.016
Mg	1.063	0.575	0.000	3.762
CA	0.009	0.290	0.687	0.030
Na	0.002	0.003	0.305	0.009
K	0.000	0.000	0.002	0.002
Sum	4.000	8.000	4.988	14.995
XMg	0.55	0.21		0.55

1=retrograde cummingtonite after orthopyroxene

A2.3 Fowler Subdomain

Table A2.6 Lithomagnetic Association 1 mafic granulites (core mineral compositions)

Sample	NDR1 41m	NDDH1 57m	NDDH2 159m	NDDH2 160m	NDDH2 306m	NDR1 41m	NDDH2 159m	NDDH2 160m
Min	gt	gt	gt	gt	gt	opx	opx	opx
SiO2	37.90	38.30	38.43	38.08	38.01	50.80	50.73	50.60
TiO2	0.00	0.03	0.04	0.07	0.03	0.03	0.06	0.06
Al2O3	20.88	20.99	21.01	21.08	21.13	2.08	1.51	1.76
Cr2O3	0.02	0.02	0.01	0.04	0.07	0.01	0.02	0.00
Fe2O3	2.38	1.44	1.14	1.26	1.48	2.72	1.05	1.64
FeO	22.44	22.59	25.64	26.21	25.16	20.50	25.88	25.89
MnO	3.08	4.04	1.62	1.86	2.09	0.86	0.53	0.62
MgO	6.47	5.39	5.51	4.93	5.27	21.63	18.84	18.62
CaO	6.25	7.25	6.77	6.69	6.71	0.41	0.45	0.55
Na2O	0.04	0.03	0.04	0.03	0.03	0.07	0.03	0.02
K2O	0.01	0.03	0.01	0.00	0.02	0.00	0.00	0.02
Totals	99.48	100.12	100.22	100.25	100.02	99.11	99.10	99.77
Oxygens	12	12	12	12	12	6	6	6
Si	2.969	2.992	3.000	2.986	2.979	1.917	1.950	1.936
Ti	0.000	0.002	0.002	0.004	0.002	0.001	0.002	0.002
Al	1.928	1.934	1.934	1.948	1.952	0.093	0.069	0.079
Cr	0.001	0.001	0.001	0.003	0.004	0.000	0.001	0.000
Fe3	0.141	0.085	0.067	0.074	0.087	0.077	0.030	0.047
Fe2	1.470	1.476	1.674	1.719	1.649	0.647	0.832	0.829
Mn	0.204	0.268	0.107	0.124	0.139	0.027	0.017	0.020
Mg	0.755	0.627	0.641	0.576	0.616	1.216	1.079	1.062
CA	0.525	0.607	0.566	0.562	0.564	0.017	0.019	0.023
Na	0.006	0.005	0.006	0.005	0.005	0.005	0.002	0.002
K	0.001	0.003	0.001	0.000	0.002	0.000	0.000	0.001
Sum	8.000	8.000	8.000	8.000	8.000	4.000	4.000	4.000
XMg	0.26	0.21	0.21	0.19	0.21	0.64	0.55	0.55

Sample	NDDH2 306m	NDR1 41m	NDDH1 57m	NDDH2 159m	NDDH2 160m	NDDH2 306m	NDR1 41m	NDDH1 57m
Min	opx	cpx	cpx	cpx	cpx	cpx	plag	plag
SiO2	50.71	51.14	51.01	50.98	51.38	50.73	55.49	54.38
TiO2	0.07	0.04	0.28	0.22	0.20	0.19	0.03	0.00
Al2O3	1.65	1.70	3.15	2.66	2.52	2.31	26.92	28.88
Cr2O3	0.06	0.02	0.00	0.07	0.00	0.00	0.00	0.00
Fe2O3	1.09	1.86	1.21	1.78	2.37	2.56	0.34	0.19
FeO	25.75	21.97	8.75	9.12	8.53	7.26	0.00	0.00
MnO	0.66	1.07	0.42	0.18	0.27	0.33	0.00	0.00
MgO	18.85	21.12	12.49	12.19	12.39	12.44	0.00	0.00
CaO	0.46	0.34	21.18	21.18	22.12	22.35	10.13	11.91
Na2O	0.02	0.00	0.57	0.63	0.51	0.52	5.33	4.57
K2O	0.00	0.02	0.01	0.03	0.01	0.01	0.26	0.14
Totals	99.32	99.28	99.06	99.04	100.30	98.70	98.50	100.06
Oxygens	6	6	6	6	6	6	8	8
Si	1.945	1.935	1.926	1.932	1.924	1.926	2.534	2.454
Ti	0.002	0.001	0.008	0.006	0.006	0.006	0.001	0.000
Al	0.074	0.076	0.140	0.119	0.111	0.103	1.449	1.536
Cr	0.002	0.001	0.000	0.002	0.000	0.000	0.000	0.000
Fe3	0.031	0.053	0.034	0.051	0.067	0.073	0.012	0.006
Fe2	0.826	0.695	0.276	0.289	0.267	0.231	0.000	0.000
Mn	0.021	0.034	0.014	0.006	0.009	0.010	0.000	0.000
Mg	1.078	1.191	0.703	0.688	0.692	0.704	0.000	0.000
CA	0.019	0.014	0.857	0.860	0.887	0.909	0.496	0.576
Na	0.002	0.000	0.042	0.046	0.037	0.038	0.472	0.400
K	0.000	0.001	0.000	0.001	0.000	0.000	0.015	0.008
Sum	4.000	4.000	4.000	4.000	4.000	4.000	4.978	4.979
XMg	0.55	0.62	0.38	0.37	0.37	0.38		

Sample	NDDH2 159m	NDDH2 160m	NDDH2 306m	NDR1 41m	NDDH1 57m	NDDH2 159m	NDDH2 160m	NDDH2 306m
Min	plag	plag	plag	hbl	hbl	hbl	hbl	hbl
SiO2	56.65	57.31	56.87	41.97	42.48	41.38	42.37	41.57
TiO2	0.01	0.00	0.02	1.79	1.63	2.25	1.79	2.28
Al2O3	26.62	26.51	26.95	11.45	11.88	12.09	11.49	11.87
Cr2O3	0.00	0.01	0.04	0.02	0.00	0.00	0.00	0.04
Fe2O3	0.09	0.24	0.16	2.87	2.84	2.62	2.73	1.89
FeO	0.00	0.00	0.00	11.23	12.08	13.99	14.14	13.90
MnO	0.02	0.07	0.09	0.13	0.25	0.13	0.17	0.22
MgO	0.00	0.00	0.00	12.04	11.62	10.13	10.47	10.61
CaO	9.18	9.24	9.64	11.67	11.57	11.05	11.51	11.60
Na2O	5.89	5.87	5.95	1.21	1.15	1.50	1.43	1.37
K2O	0.26	0.34	0.19	1.60	1.86	1.30	1.27	1.48
Totals	98.71	99.59	99.92	95.98	97.35	96.44	97.39	96.83
Oxygens	8	8	8	23	23	23	23	23
Si	2.572	2.581	2.557	6.339	6.347	6.282	6.371	6.288
Ti	0.000	0.000	0.001	0.203	0.183	0.257	0.202	0.259
Al	1.425	1.407	1.428	2.039	2.093	2.163	2.037	2.116
Cr	0.000	0.000	0.001	0.002	0.000	0.000	0.000	0.005
Fe3	0.003	0.008	0.005	0.326	0.319	0.299	0.309	0.216
Fe2	0.000	0.000	0.000	1.418	1.509	1.776	1.779	1.758
Mn	0.001	0.003	0.003	0.017	0.031	0.017	0.022	0.029
Mg	0.000	0.000	0.000	2.710	2.586	2.291	2.347	2.391
CA	0.447	0.446	0.464	1.889	1.851	1.797	1.855	1.880
Na	0.518	0.512	0.519	0.354	0.332	0.443	0.418	0.402
K	0.015	0.019	0.011	0.309	0.354	0.253	0.244	0.287
Sum	4.981	4.977	4.990	15.606	15.607	15.578	15.584	15.630
XMg				0.45	0.43	0.39	0.39	0.39

Sample	NDR1 41m	NDDH1 57m	NDR1 41m	NDDH2 306m
Min	scap	scap	bi	ilmenite
SiO2	44.92	46.78	36.26	0.05
TiO2	0.03	0.05	4.76	48.85
Al2O3	25.94	26.55	14.45	0.01
Cr2O3	0.00	0.03	0.14	0.01
Fe2O3	0.00	0.00	0.00	5.74
FeO	0.16	0.42	13.76	42.13
MnO	0.02	0.04	0.03	0.45
MgO	0.00	0.00	14.75	0.78
CaO	17.58	17.69	0.00	0.01
Na2O	3.33	3.13	0.04	0.00
K2O	0.07	0.12	10.01	0.00
Totals	92.05	94.81	94.21	98.04
Oxygens	0	0	11	3
Si	7.112	7.217	2.744	0.001
Ti	0.004	0.006	0.271	0.943
Al	4.842	4.828	1.289	0.000
Cr	0.000	0.004	0.008	0.000
Fe3	0.000	0.000	0.000	0.111
Fe2	0.021	0.055	0.871	0.904
Mn	0.003	0.005	0.002	0.010
Mg	0.000	0.000	1.664	0.030
CA	2.982	2.925	0.000	0.000
Na	1.022	0.935	0.006	0.000
K	0.014	0.024	0.967	0.000
Sum	16.000	16.000	7.823	2.000
XMg			0.66	

Table A2.7 Litho-magnetic Association 2 amphibolites (core mineral compositions)

Sample Min	WGC19 gt	WGC20 gt	NDDH3 158m gt	WGC19 hbl	WGC20 hbl	NDDH3 158m hbl	WGC19 plag	WGC20 plag
SiO2	37.94	37.93	37.94	41.57	40.36	41.78	58.22	56.72
TiO2	0.08	0.03	0.00	1.20	1.60	1.07	0.00	0.03
Al2O3	20.55	20.59	20.95	12.61	13.07	12.22	26.34	26.76
Cr2O3	0.00	0.00	0.05	0.00	0.00	0.01	0.02	0.00
Fe2O3	0.73	1.31	1.51	2.37	2.33	4.29	0.17	0.06
FeO	28.04	27.86	24.62	16.26	17.71	13.18	0.00	0.00
MnO	2.27	1.28	4.16	0.10	0.11	0.25	0.04	0.00
MgO	3.90	3.97	4.27	8.58	7.45	10.21	0.00	0.00
CaO	6.32	7.03	6.77	11.42	11.44	11.45	8.85	9.69
Na2O	0.01	0.03	0.04	1.43	1.33	1.16	6.15	5.87
K2O	0.00	0.00	0.02	1.10	1.39	1.64	0.09	0.18
Totals	99.84	100.03	100.32	96.64	96.78	97.25	99.88	99.31
Oxygens	12	12	12	23	23	23	8	8
Si	3.012	3.001	2.986	6.344	6.217	6.301	2.605	2.563
Ti	0.005	0.002	0.000	0.138	0.185	0.121	0.000	0.001
Al	1.924	1.921	1.944	2.269	2.374	2.172	1.390	1.425
Cr	0.000	0.000	0.003	0.000	0.000	0.001	0.001	0.000
Fe3	0.044	0.078	0.089	0.272	0.270	0.487	0.006	0.002
Fe2	1.862	1.844	1.620	2.075	2.281	1.662	0.000	0.000
Mn	0.153	0.086	0.277	0.013	0.014	0.032	0.002	0.000
Mg	0.461	0.468	0.501	1.951	1.710	2.294	0.000	0.000
CA	0.538	0.596	0.571	1.867	1.888	1.851	0.424	0.469
Na	0.002	0.005	0.006	0.423	0.397	0.338	0.534	0.514
K	0.000	0.000	0.002	0.214	0.273	0.315	0.005	0.010
Sum	8.000	8.000	8.000	15.567	15.611	15.575	4.966	4.985
XMg	0.19	0.20	0.17	0.48	0.43	0.39		

Sample Min	NDDH3 158m plag	BAC17 gt	BAC17 hbl	BAC17 plag	BAC26 bi	BAC26 plag	BAC26 gt	BAC26 hbl
SiO2	58.23	38.57	43.99	53.19	36.92	58.39	37.30	41.12
TiO2	0.00	0.04	1.19	0.00	4.13	0.00	0.06	1.37
Al2O3	25.61	21.46	11.23	28.66	14.86	25.25	20.79	12.79
Cr2O3	0.05	0.00	0.01	0.03	0.00	0.00	0.00	0.00
Fe2O3	0.30	1.44	3.56	0.21	0.80	0.13	2.90	3.62
FeO	0.00	23.32	9.18	0.00	16.50	0.00	22.63	12.71
MnO	0.08	1.43	0.11	0.05	0.21	0.01	5.41	0.33
MgO	0.18	6.89	13.55	0.00	12.58	0.00	4.41	10.29
CaO	7.17	7.08	11.86	12.12	0.09	7.86	6.67	11.39
Na2O	6.39	0.00	1.52	4.58	0.19	6.73	0.02	1.44
K2O	0.59	0.01	0.81	0.04	7.26	0.16	0.02	1.30
Totals	98.61	100.24	97.02	98.88	93.56	98.52	100.21	96.36
Oxygens	8	12	23	8	11	8	12	23
Si	2.636	2.979	6.472	2.434	2.803	2.645	2.945	6.236
Ti	0.000	0.002	0.132	0.000	0.236	0.000	0.004	0.156
Al	1.367	1.954	1.947	1.546	1.330	1.348	1.935	2.286
Cr	0.002	0.000	0.001	0.001	0.000	0.000	0.000	0.000
Fe3	0.010	0.084	0.393	0.007	0.045	0.005	0.173	0.413
Fe2	0.000	1.507	1.131	0.000	1.048	0.000	1.494	1.611
Mn	0.003	0.094	0.014	0.002	0.014	0.000	0.361	0.043
Mg	0.012	0.793	2.972	0.000	1.424	0.000	0.518	2.324
CA	0.348	0.586	1.869	0.594	0.007	0.381	0.564	1.851
Na	0.561	0.000	0.435	0.407	0.028	0.591	0.003	0.424
K	0.034	0.001	0.153	0.002	0.704	0.009	0.002	0.252
Sum	4.973	8.000	15.519	4.993	7.639	4.979	8.000	15.597
XMg		0.27	0.50			0.57		0.40

Sample	BAC38	BAC38	BAC38	BAC38	TAL13	TAL13	TAL13	TAL13
Min	gt	cpx	plag	hbl	hbl	gt	bi	plag
SiO2	37.33	50.52	57.10	40.04	41.03	37.85	35.40	59.76
TiO2	0.08	0.24	0.00	2.09	1.79	0.03	5.16	0.02
Al2O3	20.54	2.37	26.33	12.46	11.96	20.41	14.14	24.53
Cr2O3	0.01	0.02	0.06	0.00	0.02	0.03	0.00	0.00
Fe2O3	2.71	2.78	0.29	2.40	2.74	1.32	0.00	0.18
FeO	25.12	9.91	0.00	17.70	17.81	26.49	21.30	0.00
MnO	1.48	0.11	0.00	0.07	0.39	3.27	0.15	0.03
MgO	3.01	10.59	0.00	7.74	7.94	3.20	10.24	0.00
CaO	9.91	22.45	8.98	11.36	11.05	7.53	0.00	6.43
Na2O	0.00	0.64	5.96	1.11	1.56	0.00	0.06	7.57
K2O	0.01	0.00	0.27	1.97	1.56	0.04	9.56	0.19
Totals	100.20	99.63	98.99	96.94	97.86	100.19	96.01	98.71
Oxygens	12	6	8	23	23	12	11	8
Si	2.956	1.923	2.585	6.186	6.273	3.005	2.724	2.693
Ti	0.005	0.007	0.000	0.243	0.206	0.002	0.299	0.001
Al	1.917	0.106	1.405	2.269	2.156	1.910	1.283	1.304
Cr	0.001	0.001	0.002	0.000	0.002	0.002	0.000	0.000
Fe3	0.162	0.080	0.010	0.279	0.315	0.079	0.000	0.006
Fe2	1.663	0.316	0.000	2.287	2.277	1.759	1.371	0.000
Mn	0.099	0.004	0.000	0.009	0.051	0.220	0.010	0.001
Mg	0.355	0.601	0.000	1.782	1.809	0.379	1.174	0.000
CA	0.841	0.916	0.436	1.881	1.811	0.640	0.000	0.310
Na	0.000	0.047	0.523	0.333	0.461	0.000	0.009	0.661
K	0.001	0.000	0.016	0.389	0.304	0.004	0.940	0.011
Sum	8.000	4.000	4.976	15.657	15.667	8.000	7.810	4.987
XMg	0.12	0.33		0.30	0.30	0.13	0.46	

Table A2.8 Lithomagnetic Association 2 garnet-biotite gneiss

Sample	NDR3 41m	NDDH1 59m	NDDH3 164m	NDR3 41m	NDDH1 59m	NDDH3 164m	NDR3 41m	NDDH1 59m
Min	gt	gt	gt	bi	bi	bi	plag	plag
SiO2	37.31	38.03	37.52	35.55	36.91	36.84	57.80	55.96
TiO2	0.01	0.01	0.01	2.87	5.41	3.55	0.05	0.01
Al2O3	20.91	20.94	20.88	15.91	14.62	14.72	25.88	26.78
Cr2O3	0.00	0.00	0.00	0.00	0.09	0.03	0.02	0.00
Fe2O3	2.07	1.72	1.17	0.00	0.00	0.00	0.10	0.12
FeO	24.06	23.91	24.70	18.20	16.34	18.52	0.00	0.00
MnO	6.97	4.28	4.14	0.25	0.10	0.12	0.03	0.00
MgO	4.04	5.40	4.36	11.74	12.92	12.64	0.00	0.00
CaO	4.67	5.82	6.40	0.04	0.03	0.00	8.37	9.69
Na2O	0.05	0.02	0.00	0.12	0.04	0.20	6.41	5.49
K2O	0.03	0.02	0.00	9.82	9.95	9.82	0.23	0.31
Totals	100.10	100.15	99.19	94.52	96.43	96.46	98.90	98.36
Oxygens	12	12	12	11	11	11	8	8
Si	2.964	2.983	2.985	2.736	2.755	2.776	2.613	2.553
Ti	0.001	0.001	0.001	0.166	0.304	0.201	0.002	0.000
Al	1.959	1.937	1.958	1.444	1.286	1.307	1.380	1.441
Cr	0.000	0.000	0.000	0.000	0.005	0.002	0.001	0.000
Fe3	0.124	0.101	0.070	0.000	0.000	0.000	0.003	0.004
Fe2	1.598	1.568	1.644	1.172	1.020	1.167	0.000	0.000
Mn	0.469	0.285	0.279	0.017	0.006	0.008	0.001	0.000
Mg	0.478	0.631	0.517	1.347	1.438	1.420	0.000	0.000
CA	0.397	0.489	0.546	0.003	0.002	0.000	0.405	0.473
Na	0.008	0.003	0.000	0.018	0.006	0.030	0.562	0.486
K	0.003	0.002	0.000	0.965	0.948	0.945	0.013	0.018
Sum	8.000	8.000	8.000	7.868	7.772	7.856	4.981	4.976
XMg	0.16	0.21	0.17	0.53	0.58	0.55		

Sample Min	NDDH3 164m plag	NDDH3 164m Kspar	NDDH1 59m scap	TAL4 bi	TAL4 plag	TAL4 gt	TAL4 Kspar
SiO2	59.40	64.58	46.00	36.76	57.40	38.52	62.97
TiO2	0.00	0.02	0.00	4.41	0.00	0.04	0.00
Al2O3	25.59	18.54	25.77	14.69	25.45	21.65	17.95
Cr2O3	0.02	0.00	0.00	0.05	0.00	0.00	0.00
Fe2O3	0.29	0.24	0.00	0.00	0.07	1.66	0.07
FeO	0.00	0.00	0.15	14.29	0.00	23.47	0.00
MnO	0.01	0.00	0.00	0.05	0.04	1.73	0.00
MgO	0.00	0.03	0.00	14.19	0.00	7.92	0.00
CaO	7.55	0.05	17.47	0.01	8.29	5.25	0.08
Na2O	6.82	1.14	3.38	0.04	6.43	0.00	0.88
K2O	0.24	15.41	0.09	9.95	0.20	0.01	15.36
Totals	99.91	100.04	92.86	94.45	97.88	100.25	97.33
Oxygens	8	8	0	11	8	12	8
Si	2.651	2.981	7.223	2.775	2.622	2.967	2.990
Ti	0.000	0.001	0.000	0.251	0.000	0.002	0.000
Al	1.346	1.009	4.770	1.307	1.370	1.966	1.005
Cr	0.001	0.000	0.000	0.003	0.000	0.000	0.000
Fe3	0.010	0.008	0.000	0.000	0.002	0.096	0.002
Fe2	0.000	0.000	0.020	0.902	0.000	1.512	0.000
Mn	0.000	0.000	0.000	0.003	0.002	0.113	0.000
Mg	0.000	0.002	0.000	1.596	0.000	0.910	0.000
CA	0.361	0.003	2.940	0.001	0.405	0.433	0.004
Na	0.590	0.102	1.029	0.006	0.570	0.000	0.081
K	0.013	0.909	0.018	0.959	0.012	0.001	0.931
Sum	4.972	5.015	16.000	7.802	4.983	8.000	5.013
XMg				0.64		0.31	

Table A2.9 Lithomagnetic Association 2 pelitic gneisses/schists

Sample Min	NDDH2 320m gt	NDDH2 320m plag	NDDH2 320m Kspar	NDDH2 320m bi	BAC13 Kspar	BAC13 plag	BAC13 gt	BAC13 bi
SiO2	37.91	62.58	64.96	36.28	63.49	57.05	38.81	38.86
TiO2	0.07	0.00	0.00	3.80	0.00	0.00	0.00	1.66
Al2O3	21.29	23.90	18.64	17.03	18.13	26.45	21.79	17.24
Cr2O3	0.00	0.01	0.00	0.00	0.00	0.02	0.02	0.00
Fe2O3	0.78	0.11	0.06	0.00	0.03	0.06	1.66	1.54
FeO	29.22	0.00	0.00	14.07	0.00	0.00	21.63	7.85
MnO	1.77	0.04	0.00	0.01	0.00	0.00	4.60	0.00
MgO	7.08	0.00	0.00	13.41	0.01	0.00	9.55	19.49
CaO	1.38	5.54	0.05	0.00	0.05	9.38	2.34	0.00
Na2O	0.00	7.86	0.94	0.16	1.08	6.24	0.00	0.09
K2O	0.00	0.14	15.11	9.73	14.84	0.13	0.03	10.15
Totals	99.49	100.18	99.78	94.49	97.66	99.33	100.43	96.89
Oxygens	12	8	8	11	8	8	12	11
Si	2.985	2.762	2.994	2.724	2.993	2.576	2.970	2.764
Ti	0.004	0.000	0.000	0.215	0.000	0.000	0.000	0.089
Al	1.976	1.244	1.013	1.507	1.008	1.408	1.966	1.446
Cr	0.000	0.000	0.000	0.000	0.000	0.001	0.001	0.000
Fe3	0.046	0.004	0.002	0.000	0.001	0.002	0.096	0.082
Fe2	1.924	0.000	0.000	0.883	0.000	0.000	1.385	0.467
Mn	0.118	0.002	0.000	0.001	0.000	0.000	0.298	0.000
Mg	0.831	0.000	0.000	1.500	0.001	0.000	1.090	2.066
CA	0.116	0.262	0.003	0.000	0.003	0.454	0.191	0.000
Na	0.000	0.673	0.084	0.024	0.099	0.546	0.000	0.013
K	0.000	0.008	0.889	0.932	0.893	0.008	0.003	0.922
Sum	8.000	4.954	4.985	7.786	4.998	4.995	8.000	7.850
XMg	0.28			0.63			0.37	0.82

Sample Min	BAC18 Kspar	BAC18 plag	BAC18 gt	BAC18 bi	BAC23 Kspar	BAC23 gt	BAC23 ilmenite	BAC23 bi
SiO2	64.13	59.48	38.33	36.48	64.92	39.90	0.07	38.95
TiO2	0.00	0.00	0.02	3.89	0.00	0.00	7.57	2.13
Al2O3	18.33	25.16	21.36	16.21	18.38	22.35	0.31	17.32
Cr2O3	0.00	0.05	0.02	0.10	0.02	0.05	0.08	0.00
Fe2O3	0.11	0.12	0.70	0.00	0.02	0.00	81.97	0.00
FeO	0.00	0.00	28.39	13.43	0.00	20.13	6.57	7.81
MnO	0.07	0.00	2.03	0.04	0.02	3.92	0.00	0.08
MgO	0.00	0.00	6.85	14.97	0.00	11.84	0.12	18.65
CaO	0.02	7.46	2.36	0.00	0.06	1.95	0.01	0.06
Na2O	1.06	7.09	0.02	0.08	1.29	0.00	0.02	0.14
K2O	15.74	0.24	0.03	10.31	15.36	0.00	0.00	9.89
Totals	99.48	99.61	100.10	95.52	100.08	100.14	96.73	95.04
Oxygens	8	8	12	11	8	12	3	11
Si	2.983	2.663	2.996	2.714	2.993	3.006	0.002	2.807
Ti	0.000	0.000	0.001	0.218	0.000	0.000	0.155	0.115
Al	1.006	1.328	1.968	1.422	0.999	1.985	0.010	1.472
Cr	0.000	0.002	0.001	0.006	0.001	0.003	0.002	0.000
Fe3	0.004	0.004	0.041	0.000	0.001	0.000	1.676	0.000
Fe2	0.000	0.000	1.856	0.836	0.000	1.268	0.149	0.470
Mn	0.003	0.000	0.135	0.003	0.001	0.250	0.000	0.005
Mg	0.000	0.000	0.798	1.660	0.000	1.329	0.005	2.003
CA	0.001	0.358	0.197	0.000	0.003	0.158	0.000	0.005
Na	0.096	0.615	0.003	0.012	0.115	0.000	0.001	0.020
K	0.935	0.014	0.003	0.979	0.904	0.000	0.000	0.910
Sum	5.027	4.984	8.000	7.849	5.016	8.000	2.000	7.807
XMg			0.27	0.66		0.44	0.03	0.81

Sample Min	BAC28 gt	BAC28 bi	BAC28 Kspar	BAC28 plag	BAC41 Kspar	BAC41 gt	BAC41 bi
SiO2	38.66	39.79	64.48	59.65	65.10	37.10	36.64
TiO2	0.00	1.59	0.00	0.01	0.00	0.01	2.48
Al2O3	21.72	19.71	18.33	25.42	18.42	20.95	17.02
Cr2O3	0.05	0.03	0.02	0.00	0.01	0.00	0.01
Fe2O3	0.79	0.00	0.00	0.08	0.01	2.74	0.00
FeO	11.41	6.30	0.00	0.00	0.00	20.96	11.28
MnO	17.60	0.29	0.11	0.00	0.00	9.05	0.15
MgO	7.74	17.41	0.00	0.00	0.04	6.62	16.02
CaO	2.29	0.05	0.03	7.31	0.01	1.84	0.03
Na2O	0.05	0.12	1.49	7.24	1.32	0.02	0.12
K2O	0.01	9.78	15.12	0.08	14.98	0.00	10.23
Totals	100.31	95.09	99.60	99.80	99.91	99.28	93.99
Oxygens	12	11	8	8	8	12	11
Si	2.990	2.828	2.988	2.662	2.998	2.941	2.737
Ti	0.000	0.085	0.000	0.000	0.000	0.001	0.139
Al	1.980	1.652	1.001	1.337	1.000	1.958	1.499
Cr	0.003	0.002	0.001	0.000	0.000	0.000	0.001
Fe3	0.046	0.000	0.000	0.003	0.000	0.163	0.000
Fe2	0.738	0.375	0.000	0.000	0.000	1.389	0.705
Mn	1.153	0.018	0.004	0.000	0.000	0.608	0.009
Mg	0.892	1.845	0.000	0.000	0.003	0.782	1.784
CA	0.190	0.004	0.002	0.350	0.000	0.156	0.002
Na	0.008	0.017	0.134	0.627	0.118	0.003	0.017
K	0.001	0.887	0.895	0.005	0.881	0.000	0.976
Sum	8.000	7.712	5.025	4.983	5.001	8.000	7.870
XMg	0.30	0.82				0.27	0.71

A2.4 Tallacootra Shear Zone

Table A2.10 Reworked pelitic granulites and schists

Sample Min	WGC38 st	WGC38 bi	WGC38 mus	WGC38 plag	WGC42 gt	WGC42 bi	WGC42 plag	WGC66b st
SiO2	27.29	35.28	46.35	61.89	36.96	35.29	61.31	27.36
TiO2	0.64	2.40	0.62	0.00	0.00	1.88	0.03	0.53
Al2O3	52.91	18.54	36.07	23.35	20.66	17.42	24.30	52.91
Cr2O3	0.01	0.00	0.10	0.00	0.02	0.06	0.04	0.17
Fe2O3	0.00	0.00	0.00	0.07	0.13	0.00	0.00	0.00
FeO	12.00	18.01	1.08	0.00	30.81	21.39	0.00	13.57
MnO	0.27	0.11	0.06	0.00	6.72	0.23	0.02	0.25
MgO	1.75	10.50	0.52	0.00	2.01	7.96	0.00	1.86
CaO	0.02	0.01	0.00	5.11	2.23	0.03	6.59	0.00
Na2O	0.04	0.14	1.05	8.18	0.03	0.09	7.27	0.02
K2O	0.00	9.67	9.50	0.06	0.00	9.60	0.19	0.01
Totals	94.93	94.67	95.36	98.66	99.57	93.96	99.75	96.68
Oxygens	46	11	11	8	12	11	8	46
Si	7.746	2.693	3.065	2.772	3.007	2.763	2.726	7.691
Ti	0.137	0.138	0.031	0.000	0.000	0.111	0.001	0.112
Al	17.706	1.669	2.812	1.233	1.982	1.608	1.274	17.534
Cr	0.002	0.000	0.005	0.000	0.001	0.004	0.001	0.038
Fe3	0.000	0.000	0.000	0.002	0.008	0.000	0.000	0.000
Fe2	2.849	1.150	0.060	0.000	2.096	1.401	0.000	3.190
Mn	0.065	0.007	0.003	0.000	0.463	0.015	0.001	0.060
Mg	0.740	1.195	0.051	0.000	0.244	0.929	0.000	0.779
CA	0.006	0.001	0.000	0.245	0.194	0.003	0.314	0.000
Na	0.022	0.021	0.135	0.710	0.005	0.014	0.627	0.011
K	0.000	0.943	0.802	0.003	0.000	0.960	0.011	0.004
Sum	29.274	7.816	6.964	4.967	8.000	7.807	4.954	29.418
XMg	0.20	0.51			0.09	0.40		0.19

Sample Min	WGC66b mus	WGC66b bi	WGC66b gt	WGC66b plag	WGC98 gt	WGC98 bi	WGC98 plag	WGC98 mus
SiO2	46.64	36.16	37.00	61.61	36.48	34.31	60.89	47.76
TiO2	0.12	1.57	0.03	0.00	0.03	1.76	0.00	0.58
Al2O3	36.33	18.81	20.59	23.81	20.50	18.85	23.39	35.54
Cr2O3	0.00	0.10	0.06	0.03	0.04	0.15	0.00	0.10
Fe2O3	0.00	0.00	0.88	0.31	0.90	2.97	0.03	0.00
FeO	1.03	16.56	30.91	0.00	30.24	15.12	0.00	1.09
MnO	0.00	0.04	5.74	0.00	4.85	0.11	0.06	0.04
MgO	0.54	11.78	2.71	0.00	3.29	12.08	0.00	0.79
CaO	0.01	0.04	2.01	5.57	1.87	0.04	5.41	0.00
Na2O	1.14	0.25	0.03	7.95	0.05	0.13	7.80	0.92
K2O	9.54	9.50	0.00	0.14	0.00	7.78	0.09	9.70
Totals	95.36	94.82	99.96	99.42	98.25	93.30	97.67	96.53
Oxygens	11	11	12	8	12	11	8	11
Si	3.080	2.727	2.991	2.746	2.985	2.621	2.758	3.117
Ti	0.006	0.089	0.002	0.000	0.002	0.101	0.000	0.028
Al	2.828	1.672	1.962	1.251	1.977	1.697	1.249	2.734
Cr	0.000	0.006	0.004	0.001	0.003	0.009	0.000	0.005
Fe3	0.000	0.000	0.053	0.010	0.055	0.170	0.001	0.000
Fe2	0.057	1.045	2.090	0.000	2.069	0.966	0.000	0.059
Mn	0.000	0.003	0.393	0.000	0.336	0.007	0.002	0.002
Mg	0.053	1.324	0.326	0.000	0.401	1.375	0.000	0.077
CA	0.001	0.003	0.174	0.266	0.164	0.003	0.263	0.000
Na	0.146	0.037	0.005	0.687	0.008	0.019	0.685	0.116
K	0.805	0.915	0.000	0.008	0.000	0.759	0.005	0.808
Sum	6.975	7.820	8.000	4.970	8.000	7.729	4.963	6.948
XMg	0.48	0.56	0.12		0.14	0.59		

Sample Min	WGC101 gt	WGC101 oa	WGC101 bi	WGC101 st	WGC101 oa	WGC101 st	WGC101 bi
SiO2	37.11	40.21	37.55	27.78	37.45	27.28	37.95
TiO2	0.00	0.00	1.43	0.16	0.02	0.08	0.57
Al2O3	20.86	20.26	18.83	51.82	22.72	52.90	19.37
Cr2O3	0.06	0.00	0.44	0.00	0.04	0.04	0.02
Fe2O3	0.12	3.00	1.62	0.00	1.51	0.00	2.18
FeO	32.48	16.70	9.71	12.97	21.40	13.24	11.12
MnO	1.27	0.18	0.04	0.06	0.51	0.11	0.00
MgO	5.35	13.97	16.65	2.68	10.13	2.56	15.90
CaO	0.84	0.15	0.00	0.00	0.10	0.01	0.00
Na2O	0.00	2.06	0.56	0.00	2.13	0.00	0.41
K2O	0.00	0.00	8.80	0.02	0.00	0.02	8.37
Totals	98.08	96.53	95.64	95.49	96.01	96.24	95.90
Oxygens	12	23	11	46	23	46	11
Si	3.000	5.901	2.717	7.871	5.650	7.685	2.742
Ti	0.000	0.000	0.078	0.034	0.002	0.017	0.031
Al	1.988	3.505	1.606	17.310	4.041	17.570	1.650
Cr	0.004	0.000	0.025	0.000	0.005	0.009	0.001
Fe3	0.007	0.331	0.088	0.000	0.172	0.000	0.119
Fe2	2.196	2.050	0.588	3.074	2.700	3.120	0.672
Mn	0.087	0.022	0.002	0.014	0.065	0.026	0.000
Mg	0.645	3.055	1.795	1.132	2.277	1.075	1.712
CA	0.073	0.024	0.000	0.000	0.016	0.003	0.000
Na	0.000	0.587	0.079	0.000	0.624	0.000	0.057
K	0.000	0.000	0.813	0.007	0.000	0.007	0.772
Sum	8.000	15.475	7.791	29.443	15.551	29.512	7.757
XMg	0.22	0.60	0.75	0.27	0.45	0.25	0.72

Table A2.11 WGC46 (Lake Tallacootra Aplite) and WGC47c (Lake Tallacootra reworked mafic granulite).

Sample Min	WGC46 gt	WGC46 plag	WGC46 K-spar	WGC46 mus	WGC47c plag	WGC47c gt	WGC47c hbl
SiO2	36.40	66.94	64.67	47.71	55.87	37.65	41.72
TiO2	0.00	0.02	0.00	0.21	0.00	0.03	0.41
Al2O3	20.37	20.99	17.95	35.19	28.21	20.70	14.18
Cr2O3	0.02	0.00	0.00	0.02	0.00	0.00	0.00
Fe2O3	0.12	0.09	0.18	0.00	0.00	0.00	0.85
FeO	26.86	0.00	0.00	2.26	0.00	26.83	19.65
MnO	14.20	0.07	0.04	0.06	0.00	1.20	0.03
MgO	0.68	0.00	0.02	0.55	0.00	1.11	5.86
CaO	0.73	1.95	0.00	0.01	10.99	11.24	11.71
Na2O	0.03	9.95	0.34	0.32	5.15	0.03	1.20
K2O	0.00	0.10	16.99	11.11	0.03	0.00	0.50
Totals	99.40	100.11	100.20	97.45	100.25	98.79	96.11
Oxygens	12	8	8	11	8	12	23
Si	3.006	2.927	2.999	3.121	2.505	3.030	6.427
Ti	0.000	0.001	0.000	0.010	0.000	0.002	0.047
Al	1.983	1.082	0.981	2.714	1.491	1.964	2.575
Cr	0.001	0.000	0.000	0.001	0.000	0.000	0.000
Fe3	0.007	0.003	0.006	0.000	0.000	0.000	0.098
Fe2	1.855	0.000	0.000	0.124	0.000	1.806	2.531
Mn	0.993	0.003	0.002	0.003	0.000	0.082	0.004
Mg	0.084	0.000	0.001	0.054	0.000	0.133	1.345
CA	0.065	0.091	0.000	0.001	0.528	0.969	1.933
Na	0.005	0.843	0.031	0.041	0.448	0.005	0.358
K	0.000	0.006	1.006	0.928	0.002	0.000	0.098
Sum	8.000	4.955	5.026	6.996	4.974	7.989	15.417
XMg	0.03					0.07	0.35

Appendix 3

THERMOBAROMETRY

Table A3.1 Thermocalc results for the Christie Gneiss

Sample		**WGC52a**	**WGC52a**	**WGC52a**	**WGC52a**	**WGC52a**	**WGC52a**	**WGC52a**	**WGC52a**	**WGC52a**
Mineral		gt-cd-sill	gt-cd-sill	gt-cd-sill	gt-cd-sill	gt-cd-sill	gt-cd-sill	gt-cd-sill	gt-cd-sill	gt-cd-sill
Ass'blage		plag-q	plag-q	plag-q	bi-plag-q	bi-plag-q	bi-plag-q	bi-perth-q	bi-perth-q	bi-perth-q
aH2O		0.1	0.3	0.5	0.1	0.3	0.5	0.1	0.3	0.5
Average		702±119	716±122	729±126	690±99	699±101	708±105	751±137	754±139	757±140
PT (°C,kb)		4.7±0.7	5.2±0.8	5.7±0.9	4.6±0.7	5.1±0.7	5.6±0.8	4.9±0.9	5.4±1.0	5.8±1.0
Ave P (kb)	650°C									
	700°C	4.7±0.4	5.1±0.4	5.5±0.4	-	5.1±0.3	5.5±0.4	4.6±0.4	5.0±0.4	5.4±0.5
	750°C	4.9±0.4	5.3±0.4	5.7±0.4	-	5.4±0.4	5.8±0.4	4.8±0.4	5.3±0.4	5.7±0.5
	800°C	5.2±0.4	5.5±0.4	5.9±0.4	-	5.7±0.4	6.0±0.4	5.1±0.4	5.5±0.4	5.9±0.5
	850°C	5.4±0.4	5.8±0.4	6.1±0.5	-	5.9±0.5	6.3±0.5	5.4±0.4	5.8±0.4	6.2±0.5
Ave T (°C)	3kb									
	4kb	703±119	707±119	710±119	747±96	725±102	719±105	779±110	779±110	779±110
	5kb	707±119	713±120	715±120	789±95	733±103	726±105	788±110	788±110	788±110
	6kb	713±120	719±120	722±121	832±117	742±103	734±105	796±110	796±110	796±110
	7kb	720±121	727±121	729±121	874±137	750±103	741±105	804±110	804±110	804±110

Sample		**WGC55**	**WGC55**	**WGC55**	**WGC55**	**WGC55**	**WGC55**	**WGC55**	**WGC55**	**WGC55**
Mineral		gt-cd-plag-q	gt-cd-plag-q	gt-cd-plag-q	gt-cd-plag	gt-cd-plag	gt-cd-plag	gt-cd-plag-bi-ru	gt-cd-plag-bi-ru	gt-cd-plag-bi-ru
Ass'blage		sill-ilm-ru	sill-ilm-ru	sill-ilm-ru	sill-q	sill-q	sill-q	sill-q-ilm	sill-q-ilm	sill-q-ilm
aH2O		0.1	0.3	0.5	0.1	0.3	0.5	0.1	0.3	0.5
Average		664±174	633±129	608±108	575±93	594±122	610±153	596±104	570±81	548±71
PT (°C,kb)		5.1±1.2	5.3±0.9	5.4±0.8	4.6±0.6	5.2±0.8	5.7±1.1	4.7±0.8	4.9±0.7	5.1±0.6
Ave P (kb)	650°C									
	700°C	5.3±0.6	5.5±0.5	5.8±0.5	5.2±0.6	5.6±0.6	6.1±0.7	5.2±0.4	5.6±0.4	5.9±0.5
	750°C	5.5±0.6	5.8±0.6	6.0±0.6	5.4±0.8	5.8±0.8	6.2±1.0	5.5±0.5	5.8±0.5	6.1±0.6
	800°C	5.8±0.7	6.1±0.7	6.3±0.7	5.6±0.9	6.0±1.0	6.4±1.1	5.8±0.6	6.1±0.6	6.4±0.7
	850°C	6.1±0.8	6.3±0.8	6.5±0.8	5.8±1.1	6.2±1.2	6.6±1.3	6.1±0.7	6.4±0.7	6.7±0.8
Ave T (°C)	3kb									
	4kb	-	-	-	-	-	-	-	500±103	523±55
	5kb	-	-	-	-	-	-	529±108	666±93	633±53
	6kb	-	-	-	-	-	-	649±111	825±102	737±63
	7kb	-	-	-	-	-	-	771±114	-	833±78

Sample		**WGC 79**	**WGC 79**	**WGC 79**	**WGC 79**	**WGC 79**	**WGC 79**	**WGC 11**
Mineral		gt-cd-sp-sill	gt-cd-sp-sill	gt-cd-sp-sill	gt-bi-sill-	gt-bi-sill-	gt-bi-sill-	gt-opx-plag-q
Ass'blage		plag-cor	plag-cor	plag-cor	plag-q-cd	plag-q-cd	plag-q-cd	
aH2O		0.1	0.3	0.5	0.1	0.3	0.5	0
Average		708±95	747±103	785±110	518±81	525±82	532±85	586±120
PT (°C,kb)		4.1±0.6	4.6±0.7	5.1±0.8	3.1±0.6	3.6±0.7	4.0±0.7	4.2±1.4
Ave P (kb)	650°C				3.9±0.3	4.6±0.4	4.3±0.4	
	700°C	4.1±0.3	4.4±0.4	4.7±0.4	4.2±0.4	4.9±0.5	4.6±0.5	5.2±1.0
	750°C	4.3±0.4	4.6±0.4	4.9±0.4	4.5±0.5	5.2±0.6	4.9±0.6	5.7±1.1
	800°C	4.6±0.4	4.9±0.4	5.1±0.4	4.8±0.6	5.4±0.7	5.2±0.7	6.2±1.3
	850°C	4.8±0.4	5.1±0.4	5.4±0.4	-	-	-	6.6±1.6
Ave T (°C)	3kb				501±78	530±107	531±108	
	4kb	694±112	702±113	-	534±77	535±108	536±108	-
	5kb	704±112	713±113	-	565±76	539±108	540±108	-
	6kb	714±113	724±114	-	592±75	544±108	545±109	-
	7kb	724±113	735±114	-	-	-	-	-

Table A3.2 Results of conventional geothermobarometry for the Christie Gneiss.

Sample		**WGC 11**	**WGC 52A**
Mineral Assemblage		gt-opx-plag-q	gt-cd-sill plag-q
Average P (kb)	700°C	5.0±1.0*	4.8#
	750°C	5.3±1.1*	5.3#
	800°C	5.6±1.3*	5.9#
	850°C	5.9±1.5*	6.4#
Average T (°C)	4kb	683±32+	755@
	5kb	690±32+	761@
	6kb	697±33+	767@
	7kb	703±33+	772@

*=average of 6 garnet-orthopyroxene barometers (Newton & Perkins, 1982; Bohlen et al., 1983; Ganguly & Saxena, 1984; Harley, 1984; Perkins & Chipera, 1985; Bhattacharya et. al, 1991)

#,@=Perchuk & Lavrent'eva (1981)

+=average of 3 geothermometers (Harley, 1984; Lee & Ganguly, 1988; Bhattacharya et. al, 1991)

Table A3.3 Thermobarometric results for mafics in the Nundroo Block

NDR1 41m					
Assemblage	gt-opx-plag-q				
Barometers	Calibration/T (°C)	700	750	800	850
gt-opx	Newton & Perkins (1982)	7.4	7.6	7.8	8.0
	Bhattacharya et. al (1991)	7.4	7.9	8.4	8.9
	Perkins & Chipera (1985)	9.6	9.6	9.6	9.6
	Ganguly & Saxena (1984)	7.3	7.8	8.2	8.6
	Bohlen et. al (1983)	8.0	8.8	9.3	10.0
	Thermocalc	7.1±1.1	7.5±1.2	7.9±1.2	8.2±1.3
Thermometers	Calibration/P (kb)	7	8	9	10
gt-opx	Harley (1984)	645	650	655	660
	Bhattacharya et. al (1991)	741	751	761	771
	Lee & Ganguly (1988)	811	816	821	827

Nundroo DDH2 159m					
Assemblage	gt-opx-cpx-plag-q				
Barometers	Calibration/T (°C)	700	750	800	850
gt-opx	Newton & Perkins (1982)	6.8	7.0	7.2	7.3
	Bhattacharya et. al (1991)	7.4	7.9	8.4	8.9
	Perkins & Chipera (1985)	9.4	9.4	9.4	9.4
	Harley (1984)	8.2	8.7	9.1	9.6
	Ganguly & Saxena (1984)	6.9	7.3	7.7	8.1
	Bohlen et. al (1983)	8.0	8.4	8.8	9.2
gt-cpx	Newton & Perkins (1982)	5.6	5.8	6.1	6.4
	Moecher et. al (1988)	6.9	7.5	8.1	8.7
gt-opx-cpx	Bohlen et. al (1983)	7.6	8.5	9.5	10.5
	Thermocalc	7.3±0.9	7.7±0.9	8.2±1.0	8.7±1.2
Thermometers	Calibration/P (kb)	7	8	9	10
gt-opx	Harley (1984)	617	622	627	632
	Bhattacharya et. al (1991)	720	729	739	749
	Lee & Ganguly (1988)	760	765	770	775

Nundroo DDH2 160m					
Assemblage	gt-opx-cpx-hbl-plag-q				
Barometers	Calibration/T (°C)	700	750	800	850
gt-opx	Newton & Perkins (1982)	7.5	7.7	7.9	8.1
	Bhattacharya et. al (1991)	7.5	8.0	8.5	9.0
	Perkins & Chipera (1985)	9.5	9.5	9.5	9.5
	Harley (1984)	8.4	8.8	9.2	9.7
	Ganguly & Saxena (1984)	6.9	7.4	7.9	8.2
	Bohlen et. al (1983)	7.3	8.0	8.6	9.1
gt-cpx	Newton & Perkins (1982)	5.8	6.1	6.4	6.7
	Moecher et. al (1988)	6.8	7.4	8.0	8.7
gt-opx-cpx	Bohlen et. al (1983)	7.7	8.7	9.7	10.7
gt-hbl	Kohn & Spear (1990)	7.8	8.0	8.2	8.4
	Thermocalc	7.3±0.9	7.7±0.9	8.1±1.0	8.6±1.0

Thermometers	Calibration/P (kb)	7	8	9	10
gt-opx	Harley (1984)	678	683	688	693
	Bhattacharya et. al (1991)	775	786	796	807
	Lee & Ganguly (1988)	834	840	845	851
gt-hbl	Graham & Powell (1984)	699	699	699	699

Nundroo DDH2 306m					
Assemblage	gt-opx-cpx-hbl-plag-q				
Barometers	Calibration/T (°C)	700	750	800	850
gt-opx	Newton & Perkins (1982)	7.3	7.5	7.7	7.9
	Bhattacharya et. al (1991)	7.3	7.8	8.3	8.8
	Perkins & Chipera (1985)	9.4	9.4	9.4	9.4
	Harley (1984)	8.4	8.9	9.3	9.8
	Ganguly & Saxena (1984)	6.9	7.3	7.8	8.1
	Bohlen et. al (1983)	7.5	8.0	8.5	9.0
gt-cpx	Newton & Perkins (1982)	5.7	5.9	6.2	6.5
	Moecher et. al (1988)	6.8	7.3	8.1	8.7
gt-opx-cpx	Bohlen et. al (1983)	7.7	8.7	9.6	10.6
gt-hbl	Kohn & Spear (1990)	7.6	7.8	7.9	8.1
	Thermocalc	7.5±1.4	7.9±1.4	8.3±1.4	8.7±1.4
Thermometers	Calibration/P (kb)	7	8	9	10
gt-opx	Harley (1984)	673	678	683	688
	Bhattacharya et. al (1991)	771	781	792	802
	Lee & Ganguly (1988)	835	840	846	851
gt-hbl	Graham & Powell (1984)	694	694	694	694
Average PT (Thermocalc)	828±111 8.6±1.8				

NDR3 41m					
Assemblage	gt-bi-plag-q				
Thermocalc	600	650	700	750	800
Average P	4.4±2.5	4.9±1.9	5.4±1.7	5.9±1.8	6.4±1.9

Nundroo DDH1 57m					
Assemblage	gt-cpx-hbl-scap-plag-q				
Barometers	Calibration/T (°C)	700	750	800	850
gt-cpx	Newton & Perkins (1982)	5.1	5.3	5.6	5.8
	Moecher et. al (1988)	6.1	6.8	7.3	7.8
gt-hbl	Kohn & Spear (1990)	6.8	6.9	7.1	7.2
	Thermocalc	7.5±1.6	7.7±1.4	8.0±1.5	8.3±1.8
Thermometers	Calibration/P (kb)	7	8	9	10
gt-hbl	Graham & Powell (1984)	656	656	656	656
	Thermocalc	760±39	764±38	767±40	771±44
Thermocalc	774±42				
Average PT	7.9±1.6				

Nundroo DDH3 164m								
Assemblage	gt-bi-plag-q							
Thermocalc								
Average P	600	650	700	750	800	850		
	5.3±1.9	5.9±1.6	6.4±1.7	6.9±1.7	7.5±1.8	8.0±1.9		
Average T	4	5	6	7	8	9		
	795±151	804±151	812±152	821±152	829±153	838±154	(too high)	GTB results in 600-700 degree range
Average PT	837±181							
	7.9±2.7							

Appendix 4

GEOCHRONOLOGICAL DATA

In this study, selective framework geochronology has been based on Pb-Pb and U-Pb dating of zircons. Zircons are a physically robust, common accessory mineral in many crustal rocks, and are widely used for U-Pb geochronology. Zircons have a low solubility at crustal melting temperatures (Watson & Harrison, 1983), so often survive high grade reworking in either magmatic or metamorphic systems. Such "inherited" zircons can act as nucleation sites for further zircon growth resulting in compositional, isotopic and/or temporal zoning within single crystals which can often be related to the tectonic evolution of a rock, or a terrane. Hence isotopic analysis of zircons provides a powerful means for understanding the absolute temporal evolution of a terrane. However, it is vital to recognise the presence of temporal zonation within a zircon population, which is clearly impossible using conventional zircon dissolution techniques.

In recent years, SHRIMP (Sensitive High Resolution Ion Microprobe - Compston et. al, 1984) has become the benchmark for U-Pb geochronology of zircons and other accessory minerals, since it can rapidly sample accurately targeted 15-30 μm spots on a polished zircon grain, thereby resolving most growth phases within a single zircon crystal and/or population. Importantly, SHRIMP analysis is not confined to zircons, and other U-Pb-bearing accessory phases (e.g. monazite, sphene) can also be dated. The main drawbacks of SHRIMP are that it is very expensive and difficult to get machine time. The Kober Technique (Kober, 1986, 1987) provides and alternative analytical technique for zircon geochronology, which is also capable of resolving complex zircon populations using a cheaper, more widely available thermal ionisation mass spectrometer (TIMS) (Dougherty-Page & Foden, 1996; Bartlett et. al, in press). Using the Kober Technique, single zircons are analysed via a series of incremental heating steps (ideally) corresponding to concentric layers within each crystal. Hence the Kober Technique is also capable of resolving isotopic and/or temporal heterogeneities within single zircon crystals. It is important to recognise the limitations of the Kober Technique compared with the SHRIMP (see Table A1 below). In both techniques it is vital to have a detailed understanding of the zircon morphology and structure from transmitted and reflected light photographs, as well as cathodoluminescence (CL) and SEM images.

SHRIMP	**Kober Technique**
• able to analyse small (15-30 μm) spots on a single zircon grain	• able to analyse potentially narrow "onion skin" rings of a single zircon grain
• high precision analysis of U and Pb isotopes	• high precision analysis of Pb isotopes only
• minimal destruction of zircons	• zircons are destroyed
• can measure variations in discordance	• incapable of measuring discordance (hence Pb-loss via radiation damage to zircons)
• expensive (collaborative rate ~$2500 per sample)	• relatively cheap (in house rate ~$100 per sample excluding labour)
• able to avoid damaged parts of zircons	• fractured or damaged zircons likely to give spurious (mixed) ages
• much better sample selection and targeting resolution using photographs and images of the analysed zircons	• sample selection relies on inherently less reliable grain picking under a binocular microscope
• can resolve any zircon structure greater than the spot size	• unlikely to detect zircon structure unless it is approximately concentric
• difficult to get machine time	• easy to get machine time

Both the SHRIMP and Kober Technique have been used for zircon geochronology in this study. The Kober Technique provided cheap, fast reconnaissance geochronology and is readily accessible within the Department of Geology & Geophysics, University of Adelaide using a Finnigan MAT261 TIMS. Key samples were then analysed using the SHRIMP at the Research School of Earth Sciences, Australian National University, Canberra. Results are summarised in the relevant chapters. The detailed geochronological data for relevant samples is presented below:

WGC46 - Lake Tallacootra Aplite SHRIMP zircon analyses

												Ages (in Ma)				
Grain	U/ppm	Th/ppm	Th/U	204/206	f206	206/238	±	207/235	±	207/206	±	206/238	207/235	207/206	±	% CONC
1.1	204	113	0.56	0.000044	0.00071	0.2935	0.0095	3.856	0.170	0.0953	0.0025	1659	1605	1534	50	108
2.1	10	12	1.16	0.000010	1.50E-03	0.3252	0.0558	5.702	1.251	0.1272	0.0149	1815	1932	2059	222	88
3.1	40	49	1.23	0.000169	0.00237	0.5267	0.0438	11.82	1.25	0.1627	0.0091	2727	2590	2484	97	110
4.1	76	39	0.51	-	-0.00174	0.4881	0.0500	10.64	1.23	0.1581	0.0068	2563	2492	2435	75	105
5.1	228	163	0.71	0.000351	0.00556	0.2642	0.0117	3.610	0.226	0.0991	0.0039	1511	1552	1607	75	94
6.1	180	97	0.54	0.000070	0.00112	0.2638	0.0160	3.553	0.247	0.0977	0.0027	1509	1539	1580	52	96
7.1	288	49	0.17	0.000073	0.00114	0.3252	0.0093	4.958	0.167	0.1106	0.0016	1815	1812	1809	27	100
8.1	61	108	1.77	-	-0.00174	0.1989	0.0113	2.350	0.187	0.0857	0.0042	1169	1228	1331	98	88
9.1	235	163	0.70	0.000159	0.00252	0.3242	0.0153	4.483	0.288	0.1003	0.0038	1810	1728	1630	72	111
10.1	207	103	0.50	0.000317	0.00532	0.1874	0.0149	2.009	0.230	0.0778	0.0057	1107	1119	1141	152	97
11.1	161	227	1.41	0.000319	0.00536	0.2029	0.0089	2.119	0.167	0.0757	0.0046	1191	1155	1088	126	110
11.2	15	48	3.19	0.001468	0.02065	0.2406	0.0365	4.792	1.190	0.1445	0.0258	1390	1783	2281	346	61
12.1	158	71	0.45	0.000350	0.00587	0.2106	0.0164	2.243	0.236	0.0773	0.0047	1232	1195	1128	127	109
13.1	378	430	1.14	0.002949	0.04702	0.0429	0.0027	0.340	0.184	0.0574	0.0305	271	297	508	2012	53
14.1	42	56	1.32	0.001562	0.02623	0.1081	0.0090	1.141	0.312	0.0766	0.0192	661	773	1110	603	60
15.1	253	207	0.82	0.000648	0.01013	0.2649	0.0103	3.897	0.284	0.1067	0.0061	1515	1613	1744	108	87
16.1	919	880	0.96	0.004615	0.07211	0.2051	0.0082	2.931	0.501	0.1036	0.0167	1203	1390	1690	332	71
17.1	341	304	0.89	0.000118	0.00185	0.3126	0.0180	4.480	0.298	0.1039	0.0028	1753	1727	1696	51	103
18.1	112	185	1.66	0.000010	0.00016	0.2101	0.0124	2.415	0.169	0.0834	0.0026	1229	1247	1278	62	96
19.1	172	93	0.54	0.000123	0.00207	0.2025	0.0068	2.158	0.120	0.0773	0.0031	1189	1168	1129	82	105
19.3	26	10	0.38	0.000010	0.00016	0.1404	0.0141	1.760	0.251	0.0909	0.0081	847	1031	1444	180	59
21.1	166	135	0.82	0.000039	0.00063	0.1717	0.0080	1.993	0.117	0.0842	0.0026	1021	1113	1297	60	79
22.1	75	75	1.00	0.000118	0.00197	0.1821	0.0098	1.986	0.166	0.0791	0.0045	1078	1111	1175	118	92
23.1	79	126	1.60	0.000010	0.00017	0.1970	0.0077	2.193	0.125	0.0808	0.0030	1159	1179	1215	74	95
24.1	111	70	0.63	0.000157	0.00264	0.1967	0.0133	1.907	0.190	0.0703	0.0046	1157	1084	938	139	123
25.1	352	460	1.31	0.000060	0.00095	0.2416	0.0078	3.275	0.137	0.0983	0.0022	1395	1475	1593	43	88

WGC61 - Lake Ifould Granite SHRIMP zircon analyses

												Ages (in Ma)				
Grain	U/ppm	Th/ppm	Th/U	204/206	f206	206/238	±	207/235	±	207/206	±	206/238	207/235	207/206	±	% conc
1.1	74	91	1.23	0.000047	0.00074	0.3180	0.0104	4.539	0.189	0.1035	0.0023	1780	1738	1688	41	105
2.1	70	70	1.00	0.000010	1.60E-03	0.3145	0.0083	4.488	0.157	0.1035	0.0021	1763	1729	1688	38	104
3.1	49	46	0.94	-	-0.00053	0.3032	0.0122	4.258	0.201	0.1019	0.0021	1707	1685	1658	39	103
4.1	91	93	1.02	0.000070	0.0011	0.3004	0.0085	4.326	0.149	0.1045	0.0017	1693	1698	1705	30	99
5.1	72	89	1.24	-	-0.00053	0.3066	0.0111	4.432	0.230	0.1048	0.0035	1724	1718	1711	62	101
6.1	124	78	0.63	0.000137	0.00216	0.2453	0.0141	3.361	0.218	0.0994	0.0024	1414	1495	1612	45	88
7.1	136	118	0.86	0.000127	0.00201	0.3038	0.0100	4.161	0.157	0.0993	0.0015	1710	1666	1612	28	106
8.1	99	73	0.74	0.000028	0.00045	0.3114	0.0069	4.383	0.124	0.1021	0.0015	1747	1709	1663	28	105
9.1	63	91	1.46	0.000039	0.00061	0.3087	0.0087	4.343	0.157	0.1021	0.0020	1734	1702	1662	36	104
10.1	144	142	0.99	0.000040	0.00064	0.3010	0.0073	4.303	0.120	0.1037	0.0012	1696	1694	1691	21	100
10.2	290	106	0.37	0.000665	0.01049	0.1309	0.0056	1.821	0.100	0.1009	0.0029	793	1053	1641	55	48
11.1	105	67	0.64	0.000077	0.00122	0.3151	0.0065	4.343	0.120	0.1000	0.0016	1766	1702	1623	31	109
12.1	77	44	0.57	0.000288	0.00455	0.3148	0.0181	4.205	0.294	0.0969	0.0032	1764	1675	1565	64	113
13.1	133	119	0.89	-	-0.00053	0.3109	0.0120	4.402	0.197	0.1027	0.0019	1745	1713	1674	34	104
14.1	449	392	0.87	0.002155	0.03401	0.1084	0.0034	1.503	0.095	0.1006	0.0051	663	932	1635	98	41
15.1	130	66	0.51	-	-0.00084	0.2915	0.0068	4.153	0.136	0.1033	0.0021	1649	1665	1685	37	98
16.1	92	30	0.33	0.000047	0.00075	0.2987	0.0072	4.204	0.128	0.1021	0.0016	1685	1675	1663	30	101
17.1	100	44	0.44	0.000122	0.00193	0.2922	0.0072	4.091	0.127	0.1016	0.0016	1652	1653	1653	30	100
18.1	82	63	0.77	0.000049	0.00077	0.2935	0.0132	4.244	0.213	0.1049	0.0019	1659	1683	1712	33	97
19.1	59	60	1.01	0.000147	0.00231	0.3069	0.0111	4.396	0.214	0.1039	0.0030	1726	1712	1695	53	102
20.1	45	48	1.06	-	-0.00032	0.3056	0.0127	4.412	0.215	0.1047	0.0022	1719	1715	1710	38	101

WGC81 - Wynbring Rocks granite SHRIMP zircon analyses

												Ages (in Ma)				
Grain	U/ppm	Th/ppm	Th/U	204/206	f206	206/238	±	207/235	±	207/206	±	206/238	207/235	207/206	±	%conc
1.1	281	243	0.87	0.001461	0.02306	0.2853	0.0079	3.979	0.147	0.1011	0.0021	1618	1630	1645	40	98
1.2	15	18	1.19	-	-0.00138	0.3083	0.0164	4.553	0.285	0.1071	0.0029	1732	1741	1751	51	99
2.1	90	71	0.79	0.000021	0.00033	0.3059	0.0175	4.367	0.264	0.1035	0.0014	1721	1706	1688	25	102
3.1	638	566	0.89	0.000335	0.00529	0.3022	0.0053	4.295	0.085	0.1031	0.0007	1702	1692	1681	13	101
4.1	321	318	0.99	0.000017	0.00027	0.2810	0.0069	3.997	0.106	0.1031	0.0007	1597	1634	1681	13	95
5.1	179	162	0.91	0.000163	0.00258	0.2775	0.0068	4.000	0.108	0.1046	0.0010	1579	1634	1706	17	93
6.1	181	159	0.88	0.000263	4.15E-02	0.2916	0.0069	4.172	0.127	0.1038	0.0017	1650	1669	1693	30	98
7.1	98	90	0.91	0.000694	0.01095	0.2941	0.0080	4.271	0.203	0.1053	0.0037	1662	1688	1720	67	97
8.1	360	275	0.76	0.000916	0.01446	0.2802	0.0060	3.863	0.177	0.1000	0.0038	1592	1606	1624	72	98
9.1	266	194	0.73	0.009277	1.46E-00	0.1531	0.0045	2.726	0.201	0.1292	0.0083	918	1336	2087	118	44
9.2	107	89	0.83	0.000125	0.00197	0.3011	0.0079	4.268	0.133	0.1028	0.0014	1697	1687	1676	26	101
10.1	702	290	0.41	0.000191	0.00301	0.2901	0.0052	4.087	0.084	0.1022	0.0009	1642	1652	1664	16	99
11.1	188	107	0.57	0.005117	0.08075	0.1820	0.0035	2.572	0.229	0.1025	0.0087	1078	1293	1670	165	65
12.1	619	532	0.86	0.002703	0.04266	0.2738	0.0067	3.816	0.168	0.1011	0.0034	1560	1596	1644	64	95
13.1	645	717	1.11	0.000565	0.00892	0.3003	0.0064	4.170	0.097	0.1007	0.0007	1693	1668	1638	13	103
14.1	226	181	0.80	0.002062	0.03253	0.2687	0.0072	3.732	0.146	0.1007	0.0025	1534	1578	1638	47	94
15.1	318	297	0.94	0.000182	0.00287	0.2859	0.0099	4.020	0.149	0.1020	0.0010	1621	1638	1661	18	98
16.1	461	415	0.90	0.000340	0.00536	0.2820	0.0058	3.955	0.094	0.1017	0.0010	1601	1625	1656	18	97
17.1	537	323	0.60	0.000544	0.00858	0.2768	0.0047	3.874	0.080	0.1015	0.0010	1575	1608	1652	18	95
18.1	686	643	0.94	0.002712	0.0428	0.2506	0.0083	3.508	0.147	0.1015	0.0022	1442	1529	1652	42	87
19.1	148	215	1.46	-	-0.00138	0.3051	0.0066	4.329	0.108	0.1029	0.0011	1717	1699	1677	19	102
20.1	531	447	0.84	0.002076	3.28E-01	0.2558	0.0052	3.734	0.106	0.1059	0.0019	1468	1579	1730	32	85

WGC148 - White Gin Rockhole granite SHRIMP zircon analyses

												Ages (in Ma)				
Grain	U/ppm	Th/ppm	Th/U	204/206	f206	206/238	±	207/235	±	207/206	±	206/238	207/235	207/206	±	% conc
1.1	205	129	0.63	0.000008	0.00013	0.2972	0.0056	4.258	0.136	0.1039	0.0024	1678	1685	1695	44	99
2.1	104	62	0.60	0.000249	0.00394	0.2917	0.0091	4.083	0.173	0.1015	0.0025	1650	1651	1652	47	100
3.1	269	164	0.61	0.000010	0.00016	0.3003	0.0064	4.207	0.104	0.1016	0.0011	1693	1675	1654	19	102
4.1	284	144	0.51	0.004088	0.06452	0.1691	0.0036	2.398	0.137	0.1028	0.0052	1007	1242	1676	96	60
5.1	101	65	0.65	0.000010	0.00016	0.2979	0.0072	4.241	0.130	0.1033	0.0016	1681	1682	1684	30	100
6.1	184	81	0.44	0.000292	0.00461	0.2845	0.0077	4.055	0.144	0.1034	0.0021	1614	1645	1686	38	96
7.1	253	162	0.64	0.000010	1.60E-03	0.2910	0.0093	4.160	0.149	0.1037	0.0013	1646	1666	1691	23	97
8.1	164	110	0.67	0.000033	0.00052	0.3045	0.0086	4.305	0.136	0.1025	0.0012	1714	1694	1670	21	103
9.1	157	112	0.71	0.000102	0.00161	0.2869	0.0093	4.099	0.151	0.1036	0.0014	1626	1654	1690	25	96
10.1	230	129	0.56	0.000026	4.10E-03	0.3023	0.0073	4.293	0.123	0.1030	0.0013	1703	1692	1679	23	101
11.1	181	98	0.54	0.000043	0.00068	0.2679	0.0133	3.814	0.205	0.1033	0.0016	1530	1596	1683	29	91
12.1	146	98	0.67	0.000071	0.00111	0.3037	0.0046	4.254	0.089	0.1016	0.0013	1710	1685	1654	23	103
13.1	171	112	0.66	0.000058	0.00091	0.3040	0.0052	4.238	0.094	0.1011	0.0012	1711	1681	1644	23	104
14.1	217	109	0.50	0.000033	0.00051	0.2993	0.0078	4.208	0.120	0.1020	0.0009	1688	1676	1660	16	102
15.1	129	71	0.55	0.000007	1.00E-03	0.3082	0.0068	4.353	0.108	0.1024	0.0010	1732	1704	1669	17	104
16.1	118	81	0.69	0.000057	0.00089	0.3028	0.0105	4.321	0.164	0.1035	0.0012	1705	1697	1688	22	101
17.1	187	117	0.62	0.000024	0.00038	0.2984	0.0057	4.260	0.098	0.1035	0.0011	1684	1686	1688	20	100

WGC165 - Barton South Rockhole granite SHRIMP zircon analyses

												Ages (in Ma)				
Grain	U/ppm	Th/ppm	Th/U	204/206	f206	206/238	±	207/235	±	207/206	±	206/238	207/235	207/206	±	% conc
1.1	129	63	0.49	0.000014	0.00022	0.3100	0.0081	4.392	0.135	0.1028	0.0014	1740	1711	1675	25	104
2.1	164	76	0.47	0.000065	0.00103	0.2932	0.0129	4.156	0.200	0.1028	0.0015	1658	1665	1675	27	99
3.1	106	44	0.41	0.000147	0.00232	0.2803	0.0111	4.075	0.187	0.1054	0.0020	1593	1649	1722	35	93

WGC190 - Wynbring West granite SHRIMP zircon analyses

												Ages (in Ma)				
Grain	U/ppm	Th/ppm	Th/U	204/206	f206	206/238	±	207/235	±	207/206	±	206/238	207/235	207/206	±	% conc
1.1	336	409	1.22	0.031174	0.44263	0.1653	0.0189	3.435	0.804	0.1507	0.0287	986	1513	2354	368	42
1.2	308	399	1.29	0.017841	0.25332	0.3134	0.0094	6.560	0.455	0.1518	0.0089	1757	2054	2367	104	74
2.1	35	41	1.18	0.000231	0.00361	0.2823	0.0144	4.150	0.253	0.1066	0.0029	1603	1664	1743	51	92
3.1	62	86	1.39	0.000242	0.0038	0.3035	0.0119	4.378	0.207	0.1046	0.0023	1709	1708	1708	41	100
4.1	28	16	0.58	0.000840	1.31E-01	0.2750	0.0138	4.125	0.380	0.1088	0.0078	1566	1659	1779	136	88
5.1	324	141	0.43	0.000019	0.00026	0.4581	0.0171	10.456	0.649	0.1655	0.0075	2431	2476	2513	78	97
6.1	234	150	0.64	0.000457	0.00718	0.2635	0.0087	3.742	0.148	0.1030	0.0019	1508	1580	1679	34	90
7.1	55	32	0.59	-	-0.00138	0.2949	0.0110	4.546	0.207	0.1118	0.0024	1666	1739	1828.9	40	91

WGC192 - Coorabie Quarry granodiorite SHRIMP zircon analyses

												Ages (in Ma)				
Grain	U/ppm	Th/ppm	Th/U	204/206	f206	206/238	±	207/235	±	207/206	±	206/238	207/235	207/206	±	% conc
1.1	1129	361	0.32	0.000319	0.00509	0.1997	0.0087	2.343	0.122	0.0851	0.0021	1174	1225	1317	47	89
2.1	363	444	1.22	0.000006	9.00E-04	0.3137	0.0089	4.420	0.163	0.1022	0.0021	1759	1716	1665	38	106
3.1	1594	224	0.14	0.000950	0.01515	0.1721	0.0073	2.000	0.106	0.0843	0.0023	1023	1115	1299	54	79
4.1	128	146	1.14	0.000078	0.00122	0.2881	0.0110	4.040	0.186	0.1017	0.0022	1632	1642	1656	40	99
5.1	1302	671	0.52	0.003470	0.05175	0.1386	0.0111	2.441	0.229	0.1277	0.0051	837	1255	2067	73	41
6.1	720	374	0.52	0.002195	0.03273	0.1490	0.0100	2.484	0.214	0.1209	0.0056	895	1267	1970	85	46
6.2	479	670	1.40	0.000049	0.00079	0.2657	0.0078	3.502	0.128	0.0956	0.0017	1519	1528	1540	34	99
7.1	112	154	1.37	0.001737	0.02591	0.1457	0.0069	2.357	0.170	0.1174	0.0057	877	1230	1916	90	46
8.1	168	138	0.82	0.000721	0.01075	0.1908	0.0087	3.470	0.261	0.1319	0.0072	1126	1521	2124	99	53
9.1	188	408	2.17	0.000357	0.00568	0.2725	0.0103	3.554	0.203	0.0946	0.0036	1553	1539	1520	74	102
10.1	62	115	1.85	0.000162	0.00255	0.1107	0.0038	1.566	0.076	0.1026	0.0031	677	957	1671	56	41
11.1	140	328	2.34	0.000010	0.00016	0.2618	0.0145	3.528	0.250	0.0977	0.0037	1499	1534	1581	72	95
12.1	447	396	0.88	0.001044	0.01557	0.1857	0.0100	2.941	0.247	0.1149	0.0067	1098	1393	1878	108	59
13.1	406	264	0.65	0.005724	0.08536	0.3019	0.0174	5.202	0.559	0.1250	0.0105	1701	1853	2028	156	84

WGC193 - Unnamed rockhole granite, SHRIMP zircon analyses

												Ages (in Ma)				
Grain	**U/ppm**	**Th/ppm**	**Th/U**	**204/206**	**f206**	**206/238**	**±**	**207/235**	**±**	**207/206**	**±**	**206/238**	**207/235**	**207/206**	**±**	**% conc**
1.1	164	154	0.94	0.000078	0.00124	0.2507	0.0085	3.404	0.144	0.0985	0.0021	1442	1505	1596	40	90
2.1	67	47	0.71	0.000766	1.22E-01	0.2735	0.0242	3.561	0.409	0.0944	0.0060	1558	1541	1517	124	103
3.1	142	93	0.65	0.000013	0.00021	0.3140	0.0096	4.389	0.158	0.1014	0.0016	1760	1710	1649	29	107
4.1	431	405	0.94	0.001677	0.02679	0.2042	0.0087	2.975	0.259	0.1056	0.0075	1198	1401	1725	136	69
5.1	736	1011	1.37	0.000061	0.00097	0.2642	0.0123	3.538	0.170	0.0971	0.0007	1511	1536	1570	14	96
6.1	386	364	0.94	0.000069	0.0011	0.2745	0.0074	3.545	0.113	0.0937	0.0013	1563	1537	1502	27	104
7.1	386	408	1.06	0.000184	0.00294	0.2580	0.0140	3.445	0.206	0.0968	0.0019	1480	1515	1564	36	95
8.1	624	656	1.05	0.000010	0.00016	0.2780	0.0117	3.730	0.164	0.0973	0.0008	1582	1578	1573	16	101
8.2	65	61	0.94	0.000342	0.00546	0.2858	0.0143	3.957	0.274	0.1004	0.0042	1621	1625	1631	80	99
9.1	182	144	0.79	-	-0.00054	0.2800	0.0136	3.682	0.195	0.0954	0.0015	1591	1567	1535	30	104
10.1	280	359	1.28	0.000107	0.0017	0.2591	0.0106	3.477	0.165	0.0974	0.0019	1485	1522	1574	37	94
11.1	299	501	1.68	0.001229	0.01964	0.2441	0.0181	3.581	0.472	0.1064	0.0107	1408	1545	1739	196	81
12.1	574	499	0.87	0.000196	0.00313	0.2472	0.0155	3.253	0.278	0.0955	0.0049	1424	1470	1537	99	93
12.2	106	95	0.89	0.000343	0.00548	0.2909	0.0196	4.041	0.356	0.1008	0.0049	1646	1643	1638	94	101
13.1	808	332	0.41	0.000069	0.0011	0.2735	0.0047	3.626	0.078	0.0962	0.0011	1558	1555	1551	21	101
14.1	1196	813	0.68	0.001319	0.02108	0.1463	0.0056	1.980	0.109	0.0982	0.0035	880	1109	1590	67	55
15.1	406	441	1.09	0.000010	0.00016	0.2838	0.0050	3.815	0.082	0.0975	0.0010	1610	1596	1577	20	102
16.1	226	274	1.21	0.000067	0.00107	0.2940	0.0119	4.005	0.190	0.0988	0.0020	1662	1635	1601	38	104
17.1	524	435	0.83	0.000139	0.00222	0.2523	0.0088	3.338	0.129	0.0960	0.0013	1450	1490	1547	25	94
17.2	61	78	1.27	0.000361	0.00576	0.2807	0.0138	3.759	0.258	0.0971	0.0041	1595	1584	1570	81	102
18.1	152	73	0.48	0.000138	0.00221	0.2874	0.0085	3.761	0.147	0.0949	0.0021	1629	1585	1526	43	107

BAC23 - Pelitic gneiss, SHRIMP zircon analyses

												Ages (in Ma)				
Grain	**U/ppm**	**Th/ppm**	**Th/U**	**204/206**	**f206**	**206/238**	**±**	**207/235**	**±**	**207/206**	**±**	**206/238**	**207/235**	**207/206**	**±**	**% conc**
1.1	133	62	0.47	0.000020	0.00031	0.3092	0.0123	4.541	0.196	0.1065	0.0013	1737	1739	1741	23	100
8.1	102	11	0.11	-	-0.00023	0.2875	0.0148	4.084	0.221	0.1031	0.0011	1629	1651	1680	20	97
8.2	626	243	0.39	0.000937	0.01473	0.0797	0.0072	1.135	0.109	0.1033	0.0026	494	770	1683	48	29
9.1	114	15	0.13	0.000040	0.00063	0.3147	0.0106	4.441	0.173	0.1024	0.0016	1764	1720	1667	29	106
10.1	100	15	0.15	-	-2.80E-03	0.2911	0.0116	3.928	0.171	0.0978	0.0013	1647	1619	1583	24	104
11.1	122	26	0.22	0.000046	0.00074	0.2848	0.0077	3.807	0.121	0.0969	0.0014	1616	1594	1566	27	103
15.1	137	40	0.30	0.000010	0.00016	0.3159	0.0177	4.677	0.271	0.1074	0.0011	1770	1763	1755	18	101

BAC23 - Pelitic gneiss, SHRIMP monazite analyses

												Ages (in Ma)				
Grain	**U/ppm**	**Th/ppm**	**Th %**	**Th/U**	**ThO/Th**	**206/238**	**±**	**207/235**	**±**	**207/206**	**±**	**206/238**	**207/235**	**207/206**	**±**	**%conc**
1.1	4424	721,070	7.21	163.0	13.314	0.2842	0.0158	4.171	0.265	0.1065	0.0026	1612	1668	1740	46	93
2.1	4580	209,000	2.09	45.6	15.102	0.2934	0.0095	4.212	0.141	0.1041	0.0006	1659	1676	1699	10	98
2.2	4153	625,310	6.25	150.6	15.35	0.3033	0.0154	4.513	0.237	0.1079	0.0009	1708	1733	1765	16	97
3.1	5694	916,740	9.17	161.0	15.454	0.2971	0.0147	4.311	0.221	0.1052	0.0009	1677	1695	1718	16	98
4.1	4431	617,910	6.18	139.4	15.403	0.3038	0.0123	4.453	0.190	0.1063	0.0010	1710	1722	1737	17	98
5.1	5117	1,043,800	10.44	204.0	14.906	0.3113	0.0189	4.619	0.297	0.1076	0.0016	1747	1753	1759	27	99
6.1	3729	504,140	5.04	135.2	14.189	0.2881	0.0186	4.120	0.281	0.1037	0.0016	1632	1658	1691	29	97
7.1	4882	333,610	3.34	68.3	15.582	0.3046	0.0109	4.418	0.166	0.1052	0.0008	1714	1716	1718	14	100
8.1	6087	888,860	8.89	146.0	16.173	0.2909	0.0143	4.277	0.231	0.1066	0.0018	1646	1689	1743	31	95
9.1	6006	942,810	9.43	157.0	15.651	0.2910	0.0151	4.272	0.234	0.1065	0.0014	1647	1688	1740	23	95
10.1	6002	742,120	7.42	123.7	16.73	0.2737	0.0162	3.952	0.252	0.1047	0.0018	1559	1624	1710	32	91
11.1	4624	343,190	3.43	74.2	15.814	0.2823	0.0111	4.044	0.167	0.1039	0.0009	1603	1643	1695	16	95
12.1	5327	562,550	5.63	105.6	16.259	0.2895	0.0145	4.154	0.218	0.1041	0.0011	1639	1665	1698	19	97
12.2	4940	345,530	3.46	69.9	15.784	0.2911	0.0115	4.241	0.176	0.1057	0.0009	1647	1682	1726	15	95
13.1	3686	179,880	1.80	48.8	16.045	0.2802	0.0099	4.008	0.147	0.1037	0.0007	1593	1636	1692	12	94
14.1	5292	999,400	9.99	188.9	16.176	0.2837	0.0133	4.145	0.206	0.1059	0.0013	1610	1663	1731	22	93

NDR13 - Granite, SHRIMP zircon analyses

												Ages (in Ma)				
Grain	**U/ppm**	**Th/ppm**	**Th/U**	**204/206**	**f206**	**206/238**	**±**	**207/235**	**±**	**207/206**	**±**	**206/238**	**207/235**	**207/206**	**±**	**% conc**
1.1	215	120	0.56	-	-0.00138	0.2920	0.0058	3.900	0.085	0.0969	0.0007	1652	1614	1565	13	106
2.1	141	79	0.57	0.000020	3.20E-03	0.2906	0.0071	3.972	0.109	0.0991	0.0010	1645	1628	1608	19	102
3.1	95	44	0.46	-	-0.00138	0.2905	0.0059	3.939	0.094	0.0984	0.0010	1644	1622	1593	19	103
4.1	90	49	0.55	0.000100	0.0016	0.2894	0.0069	3.844	0.118	0.0963	0.0016	1639	1602	1554	31	105
5.1	136	56	0.41	-	-0.00138	0.2827	0.0061	3.830	0.093	0.0982	0.0009	1605	1599	1591	16	101
6.1	101	51	0.50	0.000055	0.00088	0.2825	0.0102	3.834	0.148	0.0984	0.0009	1604	1600	1595	18	101
7.1	129	87	0.67	0.000003	4.00E-04	0.2699	0.0120	3.653	0.179	0.0982	0.0015	1541	1561	1589	29	97
8.1	35	43	1.23	-	-0.00138	0.3042	0.0093	4.362	0.179	0.1040	0.0025	1712	1705	1697	44	101
9.1	121	63	0.52	0.000078	0.00124	0.2913	0.0062	3.905	0.100	0.0972	0.0012	1648	1615	1572	23	105
10.1	183	107	0.59	0.000062	9.90E-03	0.2877	0.0060	3.860	0.088	0.0973	0.0006	1630	1605	1573	12	104
11.1	115	61	0.53	0.000071	0.00114	0.2785	0.0057	3.785	0.090	0.0986	0.0010	1584	1590	1597	19	99
12.1	149	82	0.55	0.000047	0.00074	0.2788	0.0060	3.776	0.091	0.0983	0.0009	1585	1588	1591	17	100
13.1	147	65	0.44	0.000182	0.0029	0.2505	0.0058	3.391	0.096	0.0982	0.0013	1441	1502	1589	25	91
14.1	121	66	0.54	-	-0.00138	0.2848	0.0053	3.901	0.085	0.0994	0.0009	1615	1614	1612	17	100
15.1	155	125	0.81	0.000119	0.0019	0.2610	0.0070	3.576	0.108	0.0994	0.0011	1495	1544	1612	20	93
16.1	170	100	0.59	0.000029	0.00046	0.2880	0.0069	3.878	0.104	0.0977	0.0009	1632	1609	1580	17	103
17.1	113	61	0.53	0.000050	0.0008	0.2790	0.0062	3.777	0.102	0.0982	0.0013	1586	1588	1590	24	100
18.1	157	103	0.66	0.000030	0.00047	0.2851	0.0060	3.799	0.090	0.0967	0.0008	1617	1593	1561	15	104
19.1	162	82	0.50	0.000121	0.00193	0.2736	0.0069	3.666	0.105	0.0972	0.0010	1559	1564	1571	20	99
20.1	198	99	0.50	0.000071	1.14E-02	0.2771	0.0058	3.726	0.093	0.0975	0.0011	1577	1577	1578	21	100

Nundroo DDH2 - Pegmatite, SHRIMP zircon analyses

												Ages (in Ma)				
Grain	**U/ppm**	**Th/ppm**	**Th/U**	**204/206**	**f206**	**206/238**	**±**	**207/235**	**±**	**207/206**	**±**	**206/238**	**207/235**	**207/206**	**±**	**%conc**
1.1	1826	1116	0.61	0.001283	0.02068	0.2090	0.0043	2.455	0.083	0.0852	0.0021	1224	1259	1320	48	93
2.1	325	118	0.36	0.000006	1.00E-03	0.2546	0.0053	3.273	0.078	0.0932	0.0009	1462	1475	1493	18	98
3.1	2340	406	0.17	0.000087	0.00139	0.2546	0.0073	3.274	0.097	0.0933	0.0004	1462	1475	1493	9	98
4.1	769	562	0.73	-	-0.00138	0.2600	0.0047	3.361	0.072	0.0938	0.0009	1490	1495	1503	18	99
5.1	939	435	0.46	0.000007	0.00011	0.2440	0.0048	3.131	0.068	0.0931	0.0007	1407	1440	1489	14	95
6.1	1238	515	0.42	0.000007	0.00012	0.2522	0.0058	3.230	0.076	0.0929	0.0003	1450	1464	1486	6	98
7.1	1148	183	0.16	0.000056	0.0009	0.2473	0.0076	3.163	0.099	0.0928	0.0004	1425	1448	1483	8	96
8.1	1814	480	0.26	0.000005	7.00E-04	0.2530	0.0079	3.253	0.103	0.0933	0.0003	1454	1470	1493	5	97
9.1	421	196	0.47	0.000022	0.00035	0.2555	0.0047	3.253	0.067	0.0923	0.0006	1467	1470	1474	13	100
10.1	462	214	0.46	0.000005	8.00E-04	0.2655	0.0055	3.378	0.076	0.0923	0.0006	1518	1499	1473	13	103
11.1	120	69	0.57	0.000091	0.00146	0.2820	0.0065	3.772	0.103	0.0970	0.0012	1602	1587	1567	23	102
12.1	544	229	0.42	0.000010	0.00017	0.2628	0.0050	3.335	0.075	0.0920	0.0010	1504	1489	1468	20	103
13.1	177	170	0.96	0.000042	0.00068	0.2649	0.0052	3.403	0.081	0.0932	0.0010	1515	1505	1492	21	102
14.1	270	388	1.44	-	-0.00138	0.2640	0.0054	3.445	0.080	0.0946	0.0009	1510	1515	1521	17	99
15.1	1353	508	0.38	0.000008	0.00013	0.2556	0.0050	3.282	0.073	0.0931	0.0008	1467	1477	1491	16	98
16.1	530	184	0.35	0.000059	0.00095	0.2630	0.0188	3.414	0.256	0.0942	0.0014	1505	1508	1511	29	100
17.1	1285	429	0.33	0.000009	0.00015	0.2307	0.0221	3.057	0.304	0.0961	0.0017	1338	1422	1551	33	86
18.1	971	679	0.70	0.000192	0.0031	0.2646	0.0196	3.313	0.310	0.0908	0.0044	1513	1484	1443	95	105
19.1	1191	481	0.40	-	-0.00138	0.2527	0.0174	3.295	0.231	0.0946	0.0007	1453	1480	1520	14	96
20.1	2117	368	0.17	0.000018	3.00E-03	0.2351	0.0492	2.868	0.664	0.0885	0.0068	1361	1374	1393	154	98

WGC46 - Lake Tallacootra Aplite, zircon evaporation results

Grain	208/206	±	204Pb/206	±	207Pb/206	±	Th/U	AGE	±
ZR8,HS1,B1	0.306866	0.002729	0.000177	0.000114	0.081286	0.000164	0.873	1167.1	55.5
ZR9,HS2,B1	0.344554	0.001081	0.000615	0.000053	0.088150	0.000611	0.942	1184.2	56.8
ZR7,HS1,B1*	0.394648	0.004152	0.000005	0.000003	0.079503	0.000191	1.141	1183.3	5.9
ZR6,HS1,B1*	0.290930	0.004990	0.000005	0.000003	0.078748	0.000365	0.842	1164.5	10.3
ZR4,HS1,B1*	0.492331	0.001806	0.000151	0.000085	0.081128	0.000130	1.413	1172.4	41.8
ZR5,HS1,B1	0.449445	0.008603	0.000171	0.000065	0.081810	0.001788	1.286	1182.4	73.4

* multiple mounts of 6 zircons each (21 zircons in total analysed)

WGC54 - Ifould north pegmatite, inherited metamorphic zircon evaporation results

	208/206	±	204Pb/206	±	207Pb/206	±	Th/U	AGE	±
ZR2,HS2,B1	0.141280	0.001726	0.000013	0.000007	0.156941	0.000177	0.413	2421.5	3.3
ZR2,HS3,B1	0.156414	0.000083	0.000022	0.000021	0.157510	0.000077	0.340	2426.3	4.7
ZR2,HS4,B1	0.158980	0.000142	0.000065	0.000065	0.157305	0.000104	0.371	2418.3	13.3
ZR2,HS5,B1	0.161064	0.000325	0.000010	0.000010	0.157236	0.000237	0.361	2425.1	4.4
ZR5,HS1,B1	0.154422	0.000436	0.000031	0.000031	0.157410	0.000065	0.354	2424.1	6.5
ZR10,HS2,B1	0.129352	0.000765	0.000005	0.000003	0.156742	0.000228	0.404	2420.4	3.1
ZR10,HS3,B1	0.152144	0.000221	0.000005	0.000003	0.157299	0.000082	0.333	2426.4	1.4
ZR10,HS4,B1	0.158007	0.000611	0.000005	0.000003	0.157505	0.000179	0.423	2428.6	2.4
ZR11,HS1,B1	0.126786	0.000230	0.000006	0.000003	0.157143	0.000112	0.410	2424.6	1.8
ZR11,HS2,B1	0.137309	0.000537	0.000006	0.000003	0.156856	0.000149	0.400	2421.5	2.2
ZR11,HS3,B1	0.134615	0.000182	0.000005	0.000003	0.156890	0.000336	0.415	2422.0	4.1

WGC54 - Ifould north pegmatite, prismatic zircon evaporation results

	208/206	±	204Pb/206	±	207Pb/206	±	Th/U	AGE	±
ZR6,HS3,B1	0.196703	0.001336	0.000826	0.000065	0.167196	0.000398	0.353	2421.2	36.1
ZR8,HS2,B1	0.171942	0.000210	0.000011	0.000018	0.158359	0.000419	0.449	2436.9	7.7
ZR8,HS3,B1	0.163749	0.000267	0.000091	0.000012	0.158077	0.000091	0.443	2423.0	5.2
ZR9,HS2,B1	0.140664	0.002567	0.000209	0.000007	0.159243	0.000062	0.423	2419.4	6.9
ZR9,HS3,B1	0.171566	0.000367	0.000201	0.000006	0.159540	0.000300	0.435	2423.8	9.1
ZR9,HS4,B1	0.181098	0.000028	0.000174	0.000027	0.159883	0.000047	0.449	2431.2	9.2
ZR15,HS5,b1	0.215337	0.001601	0.001297	0.000058	0.173908	0.000428	0.431	2429.9	48.5
ZR15,HS6,B1	0.190863	0.000947	0.000710	0.000094	0.165803	0.000383	0.459	2421.9	37.7
ZR13,HS3,B1	0.179232	0.000137	0.000015	0.000037	0.158603	0.000031	0.462	2439.0	6.6
ZR14,HS1,B1	0.175703	0.000791	0.000373	0.000024	0.162124	0.000349	0.451	2428.2	16.8
ZR14,HS2,B1	0.178801	0.000235	0.000258	0.000013	0.160346	0.000104	0.470	2424.7	9.6

WGC61 - Lake Ifould granite, zircon evaporation results

	208/206	±	204Pb/206	±	207Pb/206	±	Th/U	AGE	±
ZR1,HS2,Block 1	0.197289	0.000662	0.000011	0.000020	0.103523	0.000096	0.842	1685.0	7.5
ZR1,HS3,Block 1	0.206568	0.000399	0.000009	0.000023	0.103481	0.000089	0.873	1684.9	8.2
ZR1,HS4,Block 1	0.218433	0.000262	0.000108	0.000067	0.103888	0.000164	1.404	1667.7	24.9
ZR2,HS1,Block 1	0.203275	0.000506	0.000007	0.000006	0.102973	0.000107	1.286	1676.2	3.8
ZR2,HS2,Block 1	0.246460	0.000693	0.000039	0.000025	0.103072	0.000013	1.141	1670.1	8.4
ZR2,HS3,Block 1	0.307982	0.001176	0.000021	0.000007	0.103101	0.000127	0.942	1674.9	4.7
ZR3,HS1,Block 1	0.285633	0.000927	0.000020	0.000004	0.103135	0.000112	1.012	1676.0	3.7
ZR3,HS2,Block 1	0.296256	0.001708	0.000007	0.000008	0.103533	0.000121	0.973	1686.3	4.4
ZR3,HS3,Block 1	0.242169	0.001499	0.000005	0.000003	0.103660	0.000129	1.112	1689.0	3.1
ZR4,HS2,Block 1	0.203275	0.000506	0.000005	0.000000	0.103575	0.000114	1.003	1687.5	2.2
ZR4,HS3,Block 1	0.307982	0.001176	0.000005	0.000003	0.103603	0.000014	0.909	1687.9	1.1

WGC64 - Lake Ifould pegmatite, zircon evaporation results

	208/206	±	204Pb/206	±	207Pb/206	±	Th/U	AGE	±
ZR1,HS2,Block 1			0.000105	0.000057	0.103308	0.000154		1657.9	21.9
ZR2,HS1,Block 1			0.000048	0.000008	0.102898	0.000022		1664.8	4.0
ZR2,HS2,Block 1			0.000054	0.000005	0.102767	0.000020		1660.8	3.3
ZR3,HS1,Block 1			0.000050	0.000050	0.102730	0.000220		1661.2	19.4
ZR3,HS2,Block 1			0.000009	0.000016	0.103037	0.000060		1677.0	5.7
ZR4,HS1,Block 1			0.000092	0.000015	0.103452	0.000081		1663.8	8.2
ZR5,HS1,Block 1			0.000080	0.000018	0.103378	0.000169		1665.4	10.4
ZR6,HS2,Block 1			0.000042	0.000012	0.102996	0.000036		1667.9	5.4
ZR7,HS2,Block 1			0.000050	0.000027	0.103380	0.000124		1672.9	11.2
ZR7,HS3,Block 1			0.000005	0.000003	0.103603	0.000014		1687.9	1.1
ZR8,HS2,Block 1			0.000005	0.000000	0.103575	0.000114		1687.5	2.2

WGC148 - White Gin Rockhole granite, zircon evaporation results

	208/206	±	204Pb/206	±	207Pb/206	±	Th/U	AGE	±
ZR1,HS2,B1	0.228581	0.000394	0.000030	0.000021	0.103557	0.000171	0.636	1680.9	9.8
ZR1,HS3,B1	0.221044	0.008310	0.000033	0.000039	0.104652	0.000202	0.724	1699.9	15.1
ZR4,HS3,B1	0.192889	0.000261	0.000005	0.000003	0.103962	0.000150	0.538	1694.3	3.5
ZR3,HS2,B1	0.285598	0.000737	0.000840	0.000036	0.115025	0.000084	0.663	1688.3	38.7
ZR3,HS3,B1	0.285829	0.000441	0.000389	0.000055	0.110074	0.000100	0.614	1709.7	28.6
ZR2,HS1,B1	0.237788	0.001027	0.000012	0.000024	0.104069	0.000107	0.763	1694.4	8.9

WGC192 - Coorabie Quarry granodiorite, zircon evaporation results

	208/206	±	204Pb/206	±	207Pb/206	±	Th/U	AGE	±
ZR1,HS1,B1	0.199576	0.001501	0.001223	0.000173	0.110926	0.000506	0.450	1508.4	109.9
ZR7,HS3,B1	0.237135	0.000018	0.000278	0.000111	0.099999	0.000010	0.644	1550.4	43.1
ZR7,HS2,B1	0.247808	0.001699	0.000241	0.000051	0.100948	0.000249	0.676	1578.9	27.2
ZR4,HS1,B1	0.435839	0.011752	0.002363	0.000310	0.130040	0.002884	1.029	1580.6	239.2
ZR6,HS1,B1	0.390688	0.000303	0.002537	0.000089	0.132910	0.000110	0.881	1590.8	133.6
ZR7,HS1,B1	0.323536	0.000569	0.001204	0.000471	0.115222	0.000608	0.805	1599.2	204.4
ZR2,HS3,B1	0.270862	0.000656	0.000005	0.000003	0.098790	0.000267	0.761	1599.7	5.9
ZR2,HS2,B1	0.249256	0.000584	0.000005	0.000003	0.098868	0.000219	0.700	1601.1	5.0
ZR3,HS1,B1	0.194058	0.000479	0.000012	0.000012	0.099291	0.000171	0.544	1607.3	7.0
ZR3,HS2,B1	0.285598	0.000737	0.000840	0.000036	0.115025	0.000084	0.724	1688.3	38.7
ZR4,HS3,B1	0.192889	0.000261	0.000005	0.000003	0.103962	0.000150	0.538	1694.3	3.5
ZR2,HS1,B1	0.237788	0.001027	0.000012	0.000024	0.104069	0.000107	0.663	1694.4	8.9
ZR1,HS3,B1	0.204758	0.000489	0.000007	0.000007	0.104817	0.000120	0.570	1708.9	4.2
ZR3,HS3,B1	0.285829	0.000441	0.000389	0.000055	0.110074	0.000100	0.763	1709.7	28.6

WGC193 - Unnamed rockhole granite, zircon evaporation results

	208/206	±	204Pb/206	±	207Pb/206	±	Th/U	AGE	±
ZR9,HS2,B1	0.319517	0.003229	0.000463	0.000044	0.102860	0.000117	0.861	1556.5	30.5
ZR9,HS1,B1	0.264394	0.003004	0.000356	0.000067	0.101501	0.000324	0.714	1558.7	37.6
ZR13,HS2,B1	0.259829	0.000223	0.000080	0.000011	0.098609	0.000065	0.725	1576.5	7.0
ZR13,HS1,B1	0.251856	0.000594	0.000119	0.000099	0.099257	0.000223	0.698	1578.5	37.4
ZR12,HS2,B1	0.264269	0.000416	0.000050	0.000050	0.098367	0.000172	0.740	1579.8	19.6
ZR12,HS3,B1	0.264299	0.000408	0.000005	0.000003	0.098047	0.000138	0.743	1585.6	3.5
ZR13,HS6,B1	0.241786	0.000376	0.000098	0.000007	0.099386	0.000069	0.672	1586.7	6.4
ZR12,HS1,B1	0.271951	0.001013	0.000005	0.000003	0.098188	0.000186	0.765	1588.3	4.4
ZR13,HS4,B1	0.256754	0.001412	0.000068	0.000054	0.099149	0.000210	0.716	1590.0	22.0
ZR13,HS3,B1	0.260804	0.000247	0.000013	0.000044	0.098889	0.000122	0.732	1599.4	15.4
ZR8,HS1,B1	0.199076	0.002406	0.000084	0.000006	0.099967	0.000063	0.552	1601.3	5.5
ZR13,HS5,B1	0.250920	0.000342	0.000058	0.000058	0.100026	0.000252	0.700	1609.2	23.3
ZR13,HS7,B1	0.228982	0.000046	0.000063	0.000003	0.101004	0.000009	0.637	1626.1	2.9
ZR10,HS3,B1	0.188567	0.000229	0.000157	0.000026	0.102479	0.000060	0.515	1629.5	13.2
ZR10,HS2,B1	0.197217	0.001129	0.000054	0.000008	0.101218	0.000174	0.548	1632.3	7.0
ZR8,HS2,B1	0.168683	0.000492	0.000053	0.000005	0.101643	0.000089	0.468	1640.6	4.7
ZR3,HS3,B1	0.199660	0.000566	0.000135	0.000016	0.102804	0.000113	0.547	1641.3	10.7
ZR7,HS1,B1	0.168912	0.000064	0.000007	0.000010	0.101546	0.000091	0.472	1650.3	4.7
ZR7,HS2,B1	0.154266	0.000096	0.000011	0.000020	0.102315	0.000038	0.431	1663.3	6.7
ZR2,HS2,B1	0.219930	0.001104	0.000060	0.000060	0.103293	0.000284	0.610	1668.9	23.6

Ooldea DDH2 153-154m - inherited zircon evaporation results

	208/206	±	204Pb/206	±	207Pb/206	±	Th/U	AGE	±
zr11,hs2,b1	0.148752	0.000224	0.000005	0.000003	0.157002	0.000327	0.391	2423.2	4.0
zr11,hs3,b1	0.152291	0.000074	0.000033	0.000023	0.157698	0.000143	0.398	2426.9	6.0
zr11,hs4,b1	0.152023	0.000002	0.000006	0.000003	0.157126	0.000131	0.399	2424.4	2.0
zr11,hs5,b1	0.157974	0.000210	0.000005	0.000003	0.156727	0.000097	0.415	2420.2	1.6
zr11,hs6,b1	0.166050	0.000628	0.000005	0.000003	0.157328	0.000196	0.436	2426.7	2.6
zr12,hs2,b1	0.135763	0.023524	0.000547	0.000020	0.164334	0.000341	0.328	2428.3	20.6
zr12,hs3,b1	0.172267	0.000345	0.000455	0.000005	0.163173	0.000197	0.311	2428.4	14.2
zr12,hs4,b1	0.169759	0.000454	0.000368	0.000026	0.162084	0.000232	0.415	2428.4	15.8
zr12,hs5,b1	0.164079	0.000544	0.000081	0.000026	0.158683	0.000370	0.416	2431.0	10.0

Ooldea DDH2 153-154m - metamorphic zircon evaporation results

	208/206	±	204Pb/206	±	207Pb/206	±	Th/U	AGE	±
ZR13,HS3,B1	0.020112	0.000257	0.000203	0.000203	0.104401	0.000269	0.078	1653.4	69.4
ZR13,HS4,B1	0.023433	0.000198	0.000005	0.000003	0.104086	0.000210	0.095	1696.5	4.5
ZR13,HS5,B1	0.032595	0.000139	0.000005	0.000003	0.104011	0.000065	0.113	1695.2	2.0
ZR13,HS6,B1	0.041909	0.000376	0.000046	0.000046	0.103939	0.000114	0.037	1683.9	16.1
ZR14,HS1,B1	0.038258	0.000484	0.000005	0.000003	0.104136	0.000151	0.036	1697.4	3.5
ZR14,HS2,B1	0.034262	0.000450	0.000009	0.000009	0.103396	0.000077	0.038	1683.4	4.1
ZR14,HS3,B1	0.028742	0.000051	0.000006	0.000003	0.103699	0.000057	0.080	1689.4	1.9
ZR14,HS4,B1	0.027918	0.000057	0.000005	0.000003	0.103308	0.000094	0.091	1682.7	2.5
ZR16,HS3,B1*	0.013689	0.000073	0.000005	0.000003	0.103655	0.000304	0.065	1688.9	6.2
ZR16,HS4,B1*	0.013278	0.000026	0.000005	0.000003	0.103620	0.000013	0.106	1688.2	1.1
ZR16,HS5,B1*	0.013233	0.000102	0.000005	0.000003	0.103642	0.000039	0.043	1688.6	1.5

* multiple zircon mount containing 6 small zircons

Appendix 5

GEOCHEMISTRY

All data from MESA unless otherwise specified

RS#	144	151	158	161	167	169	171	176	178
Hole #	**Nundroo DDH1**	**Nundroo DDH2**	**Nundroo DDH2**	**Nundroo DDH2**	**Nundroo DDH2**	**Nundroo DDH2**	**Nundroo DDH2**	**Nundroo DDH2**	**Nundroo DDH2**
From (m)	58.8	52	88	116	160	183	230	252	263
To (m)	59.4	53	89	117	161	184	231	253	264
Lithology	gt-bi gneiss granulite	50% reworked granulite	60% reworked granulite	75% reworked granulite	unreworked granulite	<20% reworked gabbro/ granulite	65% reworked granulite	c gr gabbro-> granulite-> amphib	30% reworked granulite
SiO2	65.3	46.2	48.4	49.5	48.7	59.3	47.9	48.5	50
TiO2	0.91	6.85	1.22	0.3	1.42	1.04	0.98	1.47	1.42
Al2O3	14.9	16.2	14.3	12.3	13.6	17.3	14.8	16.5	14.9
Fe2O3	6.45	12.5	13.3	10.3	16.4	8	11.9	11.7	14.1
MnO	0.15	0.15	0.2	0.18	0.24	0.1	0.19	0.17	0.2
MgO	1.91	3.92	8.05	13.4	6.6	3.04	9.3	5.2	4.9
CaO	4.62	8.95	10.9	11.3	10.6	6.65	11.4	10.8	10.4
Na2O	2.96	3.66	2.94	1.87	2.74	4.34	3.04	3.96	3.68
K2O	2.38	0.89	0.8	0.48	0.29	0.39	0.41	0.49	0.37
P2O5	0.48	0.68	0.12	0.01	0.15	0.21	0.29	0.73	0.17
LOI	0.71	0.74	0.55	1.1	0.08	0.63	0.64	1.15	0.63
TOTAL	100.8	100.7	100.8	100.7	100.8	101	100.9	100.7	100.8
Rb (DL=2)	78	2	2	2	2	2	2	2	2
Ba	610	250	200	40	45	240	45	280	310
Th (DL=4)	38	4	4	4	4	6	4	4	4
U (DL=4)	4	4	4	4	4	4	4	4	4
Nb	46	50	40	32	34	38	34	40	32
La	290	90	80	60	90	90	60	200	60
Ce	420	50	70	30	30	60	30	270	20
Pb									
Sr	340	500	260	62	115	460	220	600	165
Zr	880	165	36	10	56	260	86	320	64
Y	54	20	32	10	32	10	18	38	32

RS#	208	213	222	217	221	226	231	239	241
Hole #	**Nundroo DDH2**	**Nundroo DDH2**	**Nundroo DDH2**	**Nundroo DDH2**	**Nundroo DDH2**	**Nundroo DDH2**	**Nundroo DDH3**	**Nundroo DDH3**	**Nundroo DDH3**
From (m)	293	307	348	320	339	359	72	104	115
To (m)	294	308	349	321	340	360	73	105	116
Lithology	amphib	20% reworked granulite	10% reworked gabbro-> granulite	gt-sill metapelite	gt-sill metapelite	gt-sill metapelite	gt-bi gneiss	gt-bi gneiss	bi-?opx gneiss
SiO2	47.8	48.7	50.6	67	69.1	64.3	55.3	52.5	46.6
TiO2	1.55	0.72	1.49	0.61	0.57	0.89	0.69	0.61	1.8
Al2O3	14.7	14	14	16.4	14.7	15	14.7	13.5	15.8
Fe2O3	15.4	13.2	15.9	5.2	4.62	7.9	18.1	22.4	13.3
MnO	0.23	0.18	0.27	0.19	0.15	0.51	0.72	1.02	0.17
MgO	5.55	8.4	5.9	1.6	1.16	2.64	3.56	4.3	4.8
CaO	11.4	11.8	9.45	1.76	1.58	2.66	1.29	3.1	7.95
Na2O	2.56	2.54	2.26	2.66	2.94	2.34	1.16	0.38	3.36
K2O	0.72	0.33	0.56	4.6	5.25	3.5	3.98	1.35	3.58
P2O5	0.17	0.16	0.21	0.16	0.14	0.2	0.05	0.33	0.93
LOI	0.78	0.71	0.21	0.67	0.57	0.87	0.84	0.59	1.39
TOTAL	100.9	100.7	100.8	100.9	100.8	100.8	100.4	100.1	99.7
Rb (DL=2)	2	2	2	120	130	94	140	90	62
Ba	65	35	170	770	800	870	580	230	1980
Th (DL=4)	4	4	4	10	8	8	26	18	4
U (DL=4)	4	4	4	4	4	4	4	4	4
Nb	38	32	36	42	42	46	15	14	10
La	50	60	70	120	110	120	70	20	110
Ce	30	20	30	90	90	100	100	50	180
Pb									
Sr	220	100	140	220	220	220	150	32	1680
Zr	60	32	70	230	260	200	195	130	230
Y	36	20	34	36	32	38	38	36	26

RS#	245	247	251	253	256	259	103	104	105
Hole #	**Nundroo DDH3**	**Nundroo DDH3**	**Nundroo DDH3**	**Nundroo DDH3**	**Nundroo DDH3**	**Nundroo DDH3**	**Nundroo NDR1**	**Nundroo NDR2**	**Nundroo NDR3**
From (m)	125	129	164	187	207.8	228.9	40.6	69	41.3
To (m)	126	130	165	188	208.8	229.9	41.6	70	42.3
Lithology	hbl-bi gneiss	gt-hbl-bi amphib	gt-bi gneiss	hbl-bi gneiss	amphib gneiss	amphib	gt-bi gneiss +granulite	gabbro-> granulite-> amphib	gt-bi gneiss
SiO2	56.1	56	55.3	56.2	50.1	40.7	59.2	54	60.3
TiO2	0.8	0.81	0.82	0.8	0.97	1.7	1.27	0.62	0.67
Al2O3	16.8	15.9	15.7	17	18.6	15.1	14.5	18	15.7
Fe2O3	8.45	10.3	12.1	7.8	9.55	16.8	10	7.17	7.35
MnO	0.14	0.31	0.46	0.13	0.17	0.25	0.29	0.12	0.16
MgO	3.3	3.52	3.7	3.58	4.54	8	4.9	3.56	3.44
CaO	5.7	4.38	3.74	5.95	8.3	10.4	5.4	9.1	3.96
Na2O	3.56	2.86	2.6	3.66	4.12	2.12	2.24	4.78	2.78
K2O	2.68	2.92	3.1	2.58	1.79	2.28	2.22	0.72	4.1
P2O5	0.24	0.35	0.14	0.24	0.36	0.57	0.22	0.15	0.12
LOI	0.85	0.76	0.62	0.71	0.65	1.54	0.71	1.71	1.09
TOTAL	98.6	98.1	98.3	98.7	99.2	99.5	100.95	99.93	99.67
Rb (DL=2)	98	135	150	96	56	72	64	2	110
Ba	780	840	970	850	470	600	460	240	740
Th (DL=4)	4	24	4	4	4	4	4	4	4
U (DL=4)	4	4	4	4	4	4	4	4	4
Nb	9	12	11	9	9	16	42	36	40
La	40	60	50	40	30	120	100	70	90
Ce	70	90	80	80	70	210	70	70	50
Pb							60	30	40
Sr	590	460	420	700	680	240	210	430	260
Zr	175	200	190	155	230	430	175	100	140
Y	16	20	26	18	30	46	24	24	34

RS#	108	109	110	129	132	134	136	140	106
Hole #	**Nundroo NDR6**	**Nundroo NDR7**	**Nundroo NDR8**	**Nundroo NDR9**	**Nundroo NDR10**	**Nundroo NDR11**	**Nundroo NDR13**	**Nundroo NDR15**	**Nundroo NDR4**
From (m)	63.8	116.6	64	113	17.5	84.5	94.2	25	85
To (m)	64.9	118.7	64.7	115	18.5	88.6	94.7	26.1	86
Lithology	g'diorite gneiss	amphib	g'diorite gneiss	g'diorite gneiss	amphib	mylonit'd amphib	foliated granite	layered amphib	weathered mylonitic mafic
SiO2	61.1	47.6	64.1	71.9	49.9	46.5	66.8	52.2	51.2
TiO2	0.67	1.28	0.44	0.17	1.35	1.13	0.6	1.88	1.65
Al2O3	16.7	17.9	15.7	13.2	12.7	13.4	12.9	13.7	13.6
Fe2O3	6.1	11.7	6.15	3.16	14.00	8.50	4.52	15.70	15.00
MnO	0.11	0.17	0.08	0.03	0.25	0.13	0.09	0.22	0.25
MgO	2.28	5.9	2.7	0.3	8.25	2.1	0.6	4.06	5.8
CaO	5.1	9.4	3.92	1.13	8.45	10	1.62	7.4	7.2
Na2O	4.18	3.5	3.1	3.18	2.16	2.42	3.24	3.3	2.36
K2O	3.04	1.74	2.84	5.75	2.34	3.42	6.45	1.25	0.86
P2O5	0.18	0.48	0.13	0.04	0.27	0.81	0.14	0.14	0.15
LOI	1.39	1.12	1.67	2.02	0.93	10.2	1.08	0.76	2.54
TOTAL	100.85	100.79	100.83	100.88	100.6	98.61	98.04	100.61	100.61
Rb (DL=2)	58	13	88	250	40	68	120	6	3
Ba	980	580	520	440	470	1040	1040	185	135
Th (DL=4)	8	4	22	32	4	8	4	4	4
U (DL=4)	4	4	4	4	4	4	4	4	4
Nb	38	42	44	40	46	54	48	38	38
La	120	90	100	90	150	140	120	100	60
Ce	90	70	80	70	200	140	100	60	<20
Pb	30	30	45	55	30	45	30	25	25
Sr	410	1120	430	96	200	520	270	125	100
Zr	250	145	100	135	170	420	520	115	60
Y	26	32	14	10	68	22	40	48	68

RS#	107	138							
Hole #	**Nundroo NDR5**	**Nundroo NDR14**	**Colona COL8D**	**Colona COL8D**	**Colona COL11D**	**Colona COL16D**	**Colona COL20D**	**Colona COL21D**	**Colona COL21D**
From (m)	45	20	54.35	58.46	55.05	63.90	44.10	32.50	39.50
To (m)	45.8	20.9	54.60	58.68	55.30	64.25	44.38	32.78	39.84
Lithology	gt-sill-bi pelitic gneiss	altered breccia	meta-gabbro	Meta-gabbro	Meta-gabbro-	Meta-gabbro	Tonalite gneiss	bi-hbl gneiss	q-f-bi-ep gneiss
SiO2	64.7	68.5	49.40	47.60	57.60	45.50	63.30	50.60	69.20
TiO2	0.6	0.76	0.85	0.75	0.79	1.04	0.96	1.42	0.48
Al2O3	16	12.9	21.30	20.30	17.00	18.60	12.50	17.70	14.90
Fe2O3	5.45	4.86	11.00	11.80	8.55	13.60	12.20	12.60	4.58
MnO	0.13	0.14	0.17	0.15	0.15	0.26	0.34	0.23	0.08
MgO	1.77	1.15	3.44	4.12	3.32	5.30	2.86	4.32	1.32
CaO	1.93	1.53	8.50	9.30	6.75	9.55	1.81	6.45	3.52
Na2O	3.28	2.86	4.18	3.70	3.24	3.34	1.80	3.70	3.84
K2O	5.75	5.45	0.97	0.55	1.53	0.95	2.72	2.16	1.42
P2O5	0.02	0.18	0.39	0.27	0.25	0.40	0.04	0.16	0.09
LOI	0.84	2.6	1.06	1.36	0.97	0.78	0.59	0.73	0.59
TOTAL	100.47	100.93	101.26	99.90	100.15	99.32	99.12	100.07	100.02
Rb (DL=2)	180	250	22	11	58	24	115	56	52
Ba	780	510	340	195	690	560	1080	530	550
Th (DL=4)	4	20	4	4	4	4	52	4	4
U (DL=4)	4	4	4	4	4	4	4	4	4
Nb	50	50	5	3	5	6	8	13	5
La	130	100	30	20	20	30	110	<20	20
Ce	120	80	60	50	40	60	190	40	30
Pb	50	55	10	10	15	10	15	15	20
Sr	150	86	1080	1160	640	750	210	370	290
Zr	200	270	20	12	105	140	310	80	125
Y	80	52	15	18	16	28	26	24	6

Hole #	**Colona COL21D**	**Colona COL25D**	**Colona COL25D**	**Colona COL43D**	**Colona COL43D**	**Colona COL43D**	**Colona COL43D**	**Colona COL43D**	**Colona COL43D**
From (m)	43.55	55.64	56.25	52.35	56.05	57.81	61.50	64.00	67.05
To (m)	43.83	55.85	56.50	52.63	56.38	58.20	61.70	64.38	67.40
Lithology	bi -amphi	Meta-gabbro	Meta-gabbro	Meta-gabbro	Meta-diorite	Meta-gabbro + Meta-diorite	Meta-gabbro + Micro-diorite	Meta-gabbro + Meta-diorite	Meta-diorite
SiO2	46.80	47.00	52.40	54.30	58.70	46.70	51.00	42.50	54.50
TiO2	1.12	0.88	0.42	1.03	0.93	1.28	1.13	1.29	0.36
Al2O3	15.40	19.10	24.10	16.30	16.20	17.70	18.90	16.00	22.00
Fe2O3	13.80	11.70	4.34	11.20	8.50	14.10	11.10	18.60	5.20
MnO	0.27	0.18	0.07	0.20	0.17	0.27	0.29	0.29	0.13
MgO	8.00	5.65	2.46	3.74	3.12	5.20	4.12	6.30	2.16
CaO	10.30	9.55	9.80	6.65	5.70	8.65	7.10	10.80	8.05
Na2O	2.60	3.32	4.42	3.18	3.22	2.98	3.84	1.86	4.66
K2O	1.21	1.00	0.99	1.36	1.60	1.51	1.47	0.69	0.88
P2O5	0.13	0.17	0.00	0.38	0.22	0.61	0.47	0.04	0.41
LOI	0.86	1.69	1.39	0.64	0.58	0.83	0.58	1.22	0.69
TOTAL	**100.49**	**100.24**	**100.39**	**98.98**	**98.94**	**99.83**	**100.00**	**99.59**	**99.04**
Rb (DL=2)	22	17	18	38	54	44	36	17	22
Ba	130	260	280	710	700	440	490	210	470
Th (DL=4)	4	4	4	4	4	4	4	4	4
U (DL=4)	4	4	4	4	4	4	4	4	4
Nb	7	3	3	5	6	9	7	4	2
La	<20	20	<20	30	30	40	30	<20	30
Ce	30	40	40	50	50	90	60	40	40
Pb	10	10	10	10	10	20	15	15	15
Sr	165	720	950	580	570	620	810	380	930
Zr	58	24	14	200	125	88	66	24	58
Y	24	22	16	18	12	36	10	15	6

Hole #	**Colona COL44D**	**Colona COL44D**	**Colona COL44D**	**Colona COL44D**	**Colona COL45D**
From (m)	54.05	57.00	66.30	70.50	88.50
To (m)	54.16	57.20	66.50	70.85	91.50
Lithology	Metagabbro + Metadiorite	Metagabbro	bi-plag schist	Metadiorite	?
SiO2	52.40	47.80	69.40	47.80	40.20
TiO2	0.27	1.05	0.54	1.70	0.57
Al2O3	20.10	17.20	13.80	14.20	10.80
Fe2O3	8.15	12.70	3.98	15.40	24.80
MnO	0.22	0.24	0.07	0.30	0.21
MgO	4.18	5.25	1.53	4.70	7.25
CaO	7.80	9.40	4.18	8.50	1.21
Na2O	4.04	3.08	3.00	2.52	0.52
K2O	1.12	1.02	1.11	1.86	0.87
P2O5	0.50	0.21	0.11	1.26	0.65
LOI	0.83	0.77	0.58	0.81	11.50
TOTAL	**99.61**	**98.72**	**98.30**	**99.05**	**98.58**
Rb (DL=2)	28	13	36	90	150
Ba	340	220	570	550	570
Th (DL=4)	4	4	4	4	22
U (DL=4)	4	4	4	4	4
Nb	<2	8	2	9	16
La	20	20	<20	50	40
Ce	30	60	30	90	80
Pb	10	15	10	15	10
Sr	860	320	420	540	74
Zr	8	84	120	94	270
Y	8	25	<4	30	12

Sample #	**4A***	**29b***	**45a***	**47***	**60***	**66f***	**85***
Lithology	**Quartz Diorite**	**Granodiorite**	**Leuco-Monzanite**	**Granite**	**Granodiorite**	**Granodiorite**	**Granite**
SiO2	53.37	69.97	75.99	73.26	65.1	65.65	74.17
TiO2	0.75	0.35	0.04	0.29	0.54	1.05	0.22
Al2O3	18.49	16.09	13.86	13.8	17.21	15.24	13.03
Fe2O3	3.58	1.2	0.15	1.15	2.32	3.29	1.27
FeO	4.68	0.95	0.14	0.78	2.02	2.8	0.54
MnO	0.15	0.02	0.01	0.03	0.1	0.07	0.04
MgO	4.41	0.86	0.41	1.13	1.96	1.46	0.57
CaO	8.24	3.32	1.42	1.93	4.15	3.96	1.32
Na2O	3.83	5.12	3.21	3.05	4.57	4.27	3.22
K2O	1.32	1.17	4.1	4.14	1.58	1.48	4.69
P2O5	0.18	0.14	0.13	0.1	0.19	0.23	0.09
TOTAL	99.59	99.3	99.47	99.75	99.97	99.83	99.23
Zr	104	174	62	235	116	282	156
Nb	5.4	4.2	0	6.2	4	17.2	0.9
Y	26.2	3	4	13.3	7	21.3	9.9
V	126	32	5	14	83	57	15
Sc	26	3.9	2.3	2.1	4.1	9	1.7
Cr	41	15	5	5	5	13	5
Ni	35	10	5	4	7	11	6
Ce	94	84	22	151	47	119	120
Nd	47	29	0	37	10	40	37
La	44	57	7	121	28	76	71
Rb	21	21.1	44	50	48	29.9	59
Sr	1017	610	319	782	707	629	227
Ba	289	922	1039	3621	551	1039	772

* Ifould Complex samples from Taylor (1987)

SCALE 1:500,000

5 0 5 10 15 20 25

KILOMETERS

Transverse Mercator Projection
Australian Geodetic Datum 1984, AMG Zone 53

6650000mN
625
600
575
550
525
500
475
6450000mN

175000mE
200
225
250
275
300
325
350000mE

SOUTH AUSTRALIA

Fowler, Barton, Nuyts (part), Nullarbor (part) and Ooldea (part) 1:250,000 map sheets

WESTERN GAWLER CRATON

INTERPRETIVE GEOLOGICAL MAP

Jon Teasdale, December 1997

Trend Lines (structural & lithological trends)

Geological boundaries

	NAWA SUBDOMAIN	CHRISTIE SUBDOMAIN	FOWLER SUBDOMAIN	WILGENA SUBDOMAIN	NUYTS SUBDOMAIN
		GAIRDNER DYKE SWARM: Narrow (<100m wide), linear, strongly magnetised, ~1.0-0.8Ga mafic dykes up to 200km long.			
		Undifferentiated “bullseye” magnetic highs, probably associated with strongly magnetised mafic plugs.			
MESOPROTEROZOIC		Large, complex, ?granitoid plutons.			
MESOPROTEROZOIC		SZ_3 - Karari Fault Zone, which juxtaposes the Nawa and Christie Subdomains and truncates SZ_2 shear zones.			
MESOPROTEROZOIC		SZ_2 - Northeast trending, regional scale, weakly magnetised, anastamosing, systems of major shear zones, notably the ~1.18Ga Tallacootra and Coorabie Shear Zone systems.			
MESOPROTEROZOIC			Narrow (50-500m), linear, demagnetised, anastamosing shear zones (1-20km scale).		
MESOPROTEROZOIC		SZ_1 - East-west trending, regional scale, demagnetised shear zones responsible for the early juxtaposition of the Wilgena and Nuyts Subdomains, and the Christie and Fowler Subdomains.			
MESOPROTEROZOIC	Undifferentiated, late, ?post-kinematic intrusives.		ASSOCIATION 3: Variably deformed, weakly-moderately magnetised, I-type granitoids of varying age and origin (~1.7-1.5Ga).		MUNJEELA SUITE: Large, unmagnetised plutons of S-type granite.
PALAEOPROTEROZOIC	Undifferentiated, weakly magnetised, dominantly felsic gneisses surrounding the Moondrah Gneiss.	Early shear zones.	ASSOCIATION 2: Moderately-strongly magnetised, well foliated, metapelitic and amphibolite gneiss of varying age (~1.7-1.49Ga). Amphibolites derived from hydration of Assocation 1 gabbros and granulites.	HILTABA SUITE: Large, moderately magnetised, elliptical plutons and batholiths of ~1.59Ga A-type granitoids. Comagmatic with the voluminous Gawler Range Volcanics.	ST PETER SUITE: ~1.62Ga, comagmatic, composite, granitoid plutons with abundant mafic enclaves.
PALAEOPROTEROZOIC	MOONDRAH GNEISS: Ultrahigh-T, intensely deformed, strongly magnetised, ~1.69-1.65Ga, metasedimentary granulites.	IFOULD COMPLEX: Strongly magnetised, variably deformed, mafic-felsic, I-type, comagmatic, ~1.67Ga intrusives. Some weakly magnetised plutons (inset).	ASSOCIATION 1: Mafic-intermediate, strongly magnetised, ~1.73Ga, gabbroic intrusives, variably overprinted by high-P, granulite facies metamorphism at ~1.54Ga.	Moderately magnetised, variably deformed, ~1.69Ga felsic intrusives (e.g. Symon’s Granite).	Undifferentiated early shear zones of varying age.
PALAEOPROTEROZOIC					Undifferentiated, weakly magnetised basement dominated by granitoids.
ARCHAEAN		MULGATHING COMPLEX: Dominated by coarse grained, weakly magnetised metapelitic granulites (Christie Gneiss) and banded iron formation (inset). Age of original sedimentation ~3.0-2.6Ga, high grade metamorphism and complex deformation during the ~2.4Ga Sleafordian Orogeny.			Undifferentiated, strongly magnetised basement dominated by intermediate-mafic intrusives.